ACTA UNIVERSITATIS UPSALIENSIS
Uppsala Dissertations from the Faculty of Science and Technology
148

Viktor Thorén

Hadron Physics in a Polarized World

Exploring Electromagnetic Interactions with Spin Observables

UPPSALA
UNIVERSITET

Dissertation presented at Uppsala University to be publicly examined in 101195, Ångströmlaboratoriet, Lägerhyddsvägen 1, Uppsala, Friday, 1 April 2022 at 13:15 for the degree of Doctor of Philosophy. The examination will be conducted in English. Faculty examiner: Professor David Ireland (University of Glasgow).

Abstract
Thorén, V. 2022. Hadron Physics in a Polarized World. Exploring Electromagnetic Interactions with Spin Observables. *Uppsala Dissertations from the Faculty of Science and Technology* 148. 174 pp. Uppsala: Acta Universitatis Upsaliensis. ISBN 978-91-513-1415-0.

The electromagnetic interactions of hadrons serve as a valuable probe of the nature of the strong force at low energies and simultaneously allow for tests of fundamental discrete symmetries. In this thesis, I show how polarization observables can be used to gain an in-depth understanding of these processes and present two analyses of data from the BESIII experiment where such observables have been studied.

In the first part of the thesis, I report on a study of the rare decay $\eta' \to \pi^+\pi^-e^+e^-$ based on a sample of 1.3×10^9 $e^+e^- \to J/\psi$ events using the $J/\psi \to \gamma\eta'$ radiative decay as a source of η' mesons. The branching fraction is measured to be $(2.42\pm0.05_{\text{stat.}}\pm0.08_{\text{syst.}})\times10^{-3}$ with statistical precision a factor of two better than the previous best measurement. Furthermore, I investigate the possibility of a CP-violating contribution to the decay beyond the standard model which would lead to an asymmetry in the angle between the decay planes of the e^+e^-- and $\pi^+\pi^-$-pairs. The asymmetry is measured to be $(2.9\pm3.7_{\text{stat.}}\pm1.1_{\text{syst.}})$%, consistent with zero in agreement with the standard model expectation of no CP-violation.

In the second part of the thesis, the reaction $e^+e^- \to \Lambda$ anti-Λ is studied at five center-of-mass energies from 2.3864 GeV to 3.0800 GeV. A combination of fully and partially reconstructed events is used to measure the Born cross section for the process and determine the ratio and the relative phase of the timelike electromagnetic form factors of the Λ hyperon.

Finally, I present a benchmark test of the tracking software for the planned upgrade of the BESIII detector with a new cylindrical gas electron-multiplier tracker.

Keywords: Hadron, Hyperon, Meson, Polarization, Spin observables, Electromagnetic interactions, BESIII

Viktor Thorén, Department of Physics and Astronomy, Nuclear Physics, Box 516, Uppsala University, SE-751 20 Uppsala, Sweden.

ISSN 1104-2516
ISBN 978-91-513-1415-0
URN urn:nbn:se:uu:diva-466892 (http://urn.kb.se/resolve?urn=urn:nbn:se:uu:diva-466892)

To Olga

Contents

Part I:
Introduction

1. Introduction

The basic purpose of any fundamental research is to improve our understanding of the world that we live in. On one hand this spurs further discoveries and can eventually help make our lives easier. On the other hand, we seek answers to our existential questions that can help us find our place in a larger cosmic order. In this context, this thesis investigates some of the most basic building blocks of our universe.

At a fundamental level, all matter the we deal with in our daily lives is made up of quarks held together by the strong force within composite objects known as hadrons. Due to the very nature of the strong force it is a challenge to understand the interactions between the quarks and the origin of the properties of the observed hadrons. Almost all visible mass in the universe is generated by these interactions, but the mechanism responsible for this is not fully clear.

Another related enigma is why the universe is made up of matter at all, and not antimatter. This is one of the observations that the standard model of particle physics can not explain. A necessary component of the answer is the violation of *CP*-symmetry. However, the mechanism included in the standard model can not explain the disparity between matter and antimatter that we can observe. One possible solution to this conundrum is that there are other mechanisms for *CP*-violation beyond the standard model that we have yet to discover.

The electromagnetic interactions of hadrons serve as an important laboratory for investigations of both the strong force and *CP*-symmetry. Their properties depend on the complex internal structure of the hadrons and if measured can be used to further our knowledge of how this structure comes about. A particularly powerful observable that can unlock an in-depth understanding of these processes is the polarization of the photons and hadrons involved, *i.e.* the degree to which the spins of these particles are aligned in a certain direction. The polarization is challenging to measure and is therefore relatively unexplored, but the information it provides helps disentangle the different components of the interactions. It can also facilitate the identification of contributions from rare beyond-standard-model processes that would otherwise not be possible to resolve.

In this thesis, data on e^+e^--collisions from the BESIII experiment are analyzed along two lines of inquiry that involve polarization in the electromagnetic interactions of hadrons. The first is the study of rare decays of light mesons in search of new mechanisms for *CP*-violation and for testing the predictions of effective field theories that describe the strong interaction at low

energies. The second is the study of the internal electromagnetic structure of hyperons, baryons that contain at least one strange quark, with the goal of achieving a more complete understanding of how matter is formed.

1.1 Structure of this Thesis

This thesis is divided into three distinct parts. Part I describes the current state of the field and how the research presented in this thesis can improve our understanding of *CP*-violation and the strong interaction at low energies. The theoretical frameworks used to interpret the experimental results, as well as the BESIII experiment and the related software tools used in this work are also described. Thus, Part I describes work performed by others. Parts II and III on the other hand describe the research undertaken by the author of this thesis. Results and methods discussed therein are the work of the author unless explicitly stated otherwise. Part II describes a study of the rare decay $\eta' \to \pi^+\pi^- e^+ e^-$ resulting in a measurement of the branching fraction and a search for a beyond standard model source of *CP*-violation. Part III describes a measurement of the energy dependence of the timelike form factors of the Λ hyperon in the range 2.3864 GeV to 3.0800 GeV as well as tests of how well the software for a planned upgrade of the BESIII experiment can reconstruct hyperons.

2. The Standard Model

The elementary particles that make up the observable universe and the electromagnetic, weak, and strong interactions between them are described by the standard model (SM) of particle physics. The mathematical foundation of the SM is its Lagrangian. Physical conservation laws appear as symmetries of this Lagrangian because, according to the Noether theorem [1], any transformation that leaves the Lagrangian invariant corresponds to a conserved quantity. To respect conservation of energy, momentum, and angular momentum, the Lagrangian is invariant under the Poincaré group, *i.e.* space-time translations, rotations and boosts.

The particle content of the SM, shown in Fig. 2.1, can be broadly divided into *fermions* and *bosons*. The fermions are the particles that make up matter. They have half-integer spin and their name is derived from the fact that they obey Fermi statistics. Furthermore, they are subject to the Pauli exclusion principle according to which identical fermions can not occupy the same quantum state. The bosons mediate the interactions between the fermions and get their name because they obey Bose-Einstein statistics. The electromagnetic and weak interactions are unified into one single electroweak theory [2, 3, 4] with four force-carrying gauge bosons. The photon, γ, mediates the electromagnetic interaction, and $W^{\pm}$ and Z^0 mediate the weak interaction. While the photon is massless, the weak bosons are heavy with masses $M_W \approx 80$ GeV/c^2 and $M_Z \approx 91$ GeV/c^2. The final ingredient is the Higgs boson that gives the fermions their masses. The third force of the SM, the strong interaction, is the focus of this thesis. It is mediated by massless gluons (named for "glue").

2.1 Leptons and Quarks

There are two types of fermions: leptons and quarks. The leptons are grouped into three families each with one charged and one neutral particle. These are the electron (e) and electron-neutrino (ν_e), the muon (μ) and the muon-neutrino (ν_μ), and the tauon (τ) and the tauon-neutrino (ν_τ). For each lepton, there is a corresponding antilepton with opposite quantum numbers. All leptons interact weakly, and the electron, muon, and tauon that have charge $Q = -1$ also interact electromagnetically. In the SM, the lepton number is a conserved quantity. It is defined as

$$L = n_l - n_{\bar{l}}, \tag{2.1}$$

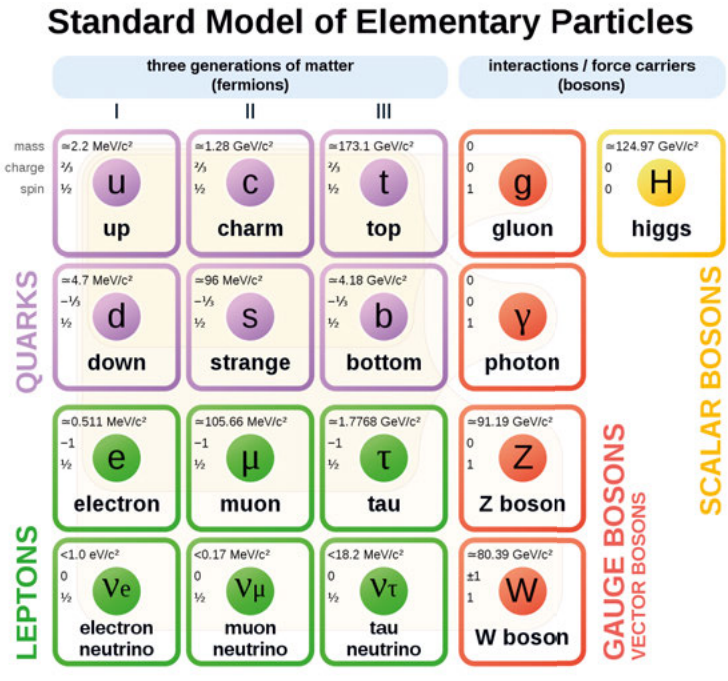

Figure 2.1. Particle content of the SM. Figure from Ref [5].

where n_l is the number of leptons, and $n_{\bar{l}}$ is the number of antileptons. The same holds for the number of leptons of each type, the *lepton flavor*. Neutrino oscillations violate lepton flavor conservation, but this is a feature that can not be described within the SM.

The quarks, unlike the leptons, carry color charge and interact via the strong force as well as the weak and electromagnetic forces. They come in three generations, each comprising two different flavors. The first generation is made up of the *up* and *down* quarks, the second of the *charm* and *strange* quarks, and the third of the *top* and *bottom* quarks. The up, charm, and top quarks are collectively referred to as the *up-type* quarks and have electric charge $Q = \frac{2}{3}$. Similarly, the down, strange, and bottom quarks are referred to as the *down-type* quarks and have electric charge $Q = -\frac{1}{3}$. Furthermore, the quarks have flavor quantum numbers that are conserved in the electromagnetic and strong interactions. For each type of quark, there is a corresponding antiquark with the same mass but opposite charges. The quarks do not carry lepton number, but instead baryon number given by

$$B = \frac{1}{3}(n_q - n_{\bar{q}}) \tag{2.2}$$

where n_q is the number of quarks and $n_{\bar{q}}$ is the number of antiquarks. Baryon number is conserved in the SM, and no deviations from this expectation have

been observed in experiment. A consequence of this is that the lightest baryon, the proton, must be stable. Indeed, based on the complete absence of proton decays in experiment, the mean proton lifetime is estimated to be longer than 10^{29} years [6]. Finally, quarks carry any of three color charges: *red*, *blue*, and *green*. Antiquarks carry corresponding anticolors. The combination of all three colors or of a color and its anticolor is *colorless* or *white*. This concept is an analogy with the more well-known electric charge and has nothing to do with the visual appearance of quarks, which we know nothing about.

2.2 The Strong Interaction

Arguably, the least understood part of the SM is the strong interaction that acts on objects that carry color charge, and is mediated by gluons. The gluons are massless particles that carry both color and anticolor at once, and form an octet of states with different charges. The fact that they carry the strong color charge means that gluons, unlike photons which are electrically neutral, can interact directly with each other as well as with the quarks. The theory that describes the strong interaction is quantum chromodynamics (QCD).

The QCD Lagrangian contains seven parameters: the six quark masses, and the coupling constant α_s, which gives the strength of the interaction. The energy behavior of this coupling, which is caused by the self-interactions of the gluons, gives QCD some of the properties that make it challenging to understand.

It suits our classical intuition for physics well to imagine that a force between any two objects (*e.g.* electrical charges) becomes weaker as the distance between them increases and vice versa. In the quantum world, the momentum transferred in an interaction, q^2, and the distance at which it occurred are considered equivalent following de Broglie. For the electromagnetic interaction, the coupling constant takes its well-known value of $\alpha_e \sim \frac{1}{137}$ for zero momentum transfer, but with larger momenta or shorter distances, it grows larger and eventually goes to infinity. The coupling constant of the weak interaction, α_W, likewise grows with the momentum transfer. This type of energy dependent interaction strength is known as a *running coupling constant*. This can be understood as a screening effect due to vacuum polarization. At large distances, virtual electron-positron pairs created spontaneously screen a particle, lowering the effective charge and thus the strength of the interaction. The larger the distance, the smaller the effective charge becomes.

The strong force on the other hand exhibits the opposite running behavior, growing stronger for lower momentum transfers and larger distances, see Fig. 2.2. This is because the self-interactions of the gluons lead to an antiscreening effect, increasing the effective charge at larger distances. To first

order, the coupling constant is given by

$$\alpha_s(q^2) = \frac{4\pi}{\beta_0 \ln\left(\frac{q^2}{\Lambda^2}\right)}, \tag{2.3}$$

where $\beta_0 = 11 - \frac{2}{3}n_f$, n_f is the number of quark flavors, and Λ is the QCD scale which is around 300 MeV. Clearly α_s approaches 0 when $q^2 \to \infty$ and diverges when $q^2 \to \Lambda^2$, and as such Λ^2 represents the location of the *Landau pole*, where a perturbative expansion in the coupling constant breaks down.

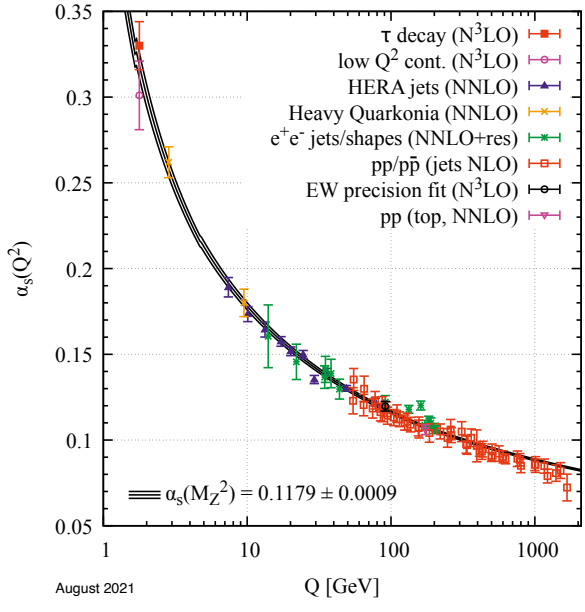

Figure 2.2. Energy dependence of the QCD coupling constant. The points with error bars represent experimental measurements, and black lines represent the world average and its uncertainty. Figure from Ref. [6].

For large momentum transfers, or equivalently short distances, the coupling is weak and the quarks and gluons are expected to behave as free particles, though this has yet to be observed. This concept is known as *asymptotic freedom* [7, 8]. The small value of the coupling ($\alpha_s \sim 0.1$ in the range 0.1-1 TeV) furthermore allows for a perturbative expansion which has been successfully used to predict a wide variety of observables in high-energy e^+e^-- and $p\bar{p}$-collisions measured at *e.g.* the LEP [9], Tevatron [10], or HERA [11] colliders.

At sufficiently low energies ($\lesssim 1$ GeV) on the other hand, the coupling is so strong that the color-charged objects (quarks and gluons) do not exist as free particles, but are confined inside colorless composite particles called hadrons. This phenomenon is known as *confinement*. The relevant degrees

of freedom when studying the strong interaction at these energies are thus not the elementary particles, but the hadrons. The large value of the coupling furthermore means that the perturbative approach that works so well for high energies can not be used to make predictions at low energies. In order to describe physics at this energy scale, one must resort to other approaches like effective field theories or lattice QCD.

2.3 Discrete Symmetries

In addition to the continuous spacetime, flavor, and gauge symmetries mentioned, our classical intuition tells us that there should also be three fundamental discrete symmetries: parity (P), charge conjugation (C), and time reversal (T). However, as we shall see, none of them are actually respected by nature.

Parity symmetry means that the laws of physics should remain the same under an inversion of all spatial coordinates around the origin ($\vec{r} \to -\vec{r}$). This was believed to be a fundamental symmetry of nature until 1957 when Wu showed that electrons from the β-decay of polarized Co^{60} were not emitted with the same rates at angles θ and $180^\circ - \theta$ [12]. Thus parity is violated in the weak interaction, as suggested by Lee and Yang the year before [13].

Charge conjugation transforms particles into their antiparticles, or for some neutral particles into themselves. Intuitively, one might expect particles and antiparticles to obey the same rules, and that C would be therefore a fundamental symmetry of nature. This is, however, not the case. It was argued by Lee, Oehme, and Yang that the observed parity-violation must mean that the C-symmetry was likewise broken in the weak interaction [14].

It was therefore suggested that the combination of parity and charge conjugation CP might be a true symmetry of nature. Also this claim was soon refuted by the results of the Fitch-Cronin experiment [15] which showed that the K_L meson decays into two pions, even though this is forbidden by CP-conservation. This was later explained through a complex phase in the Cabibbo-Kobayashi-Maskawa (CKM) mixing matrix that governs the flavor-changing mechanism of the weak interaction which is now part of the SM.

There are two different mechanisms responsible for CP-violation: The first is indirect CP-violation, which occurs due to the mixing of particle and antiparticle states with different CP-eigenvalues. This is only possible for neutral mesons that are not their own antiparticle. The other type is direct CP-violation which is caused by the interference of CP-odd and CP-even transitions in decays. This is possible for both baryons and mesons, charged and neutral. In general, weak CP-violation is a combination of both of these mechanisms. CP is in principle also broken in the strong interaction via the so-called θ-term of the QCD Lagrangian. This term induces an electric dipole moment for the neutron, but precise experimental measurements, most recently by the nEDM experiment [16], have found that if it exits, the neutron

electric dipole moment must be incredibly small. This means that the size of *CP*-violation in the strong interaction must likewise be very small, and that the value of the parameter θ must be $\lesssim 1 \times 10^{-10}$, see *e.g.* Ref. [17] and references therein. The question of why the *CP*-violation in the strong interaction is so small is known as the strong *CP* problem.

To our current best understanding, supported by experimental observations, the combination of parity, charge conjugation, and time-reversal, *CPT*, is a fundamental symmetry of nature and inviolate in the SM. In fact, Lee, Oehme, and Yang [14] showed that it is impossible to create a local Lorentz-invariant quantum field theory that does not conserve *CPT*. This is known as the *CPT*-theorem. A necessary consequence of this is that whenever *CP*-symmetry is violated, so is *T*-symmetry and vice versa.

As suggested by Sakharov [18], the violation of *CP*, as well as *C* and baryon number *B*, are necessary ingredients for explaining *baryogenesis*, *i.e.* why there is more matter than antimatter in the observable universe. However, knowing that *CP* violation does occur is not the end of the story. In order to fully understand baryogenesis, we must also understand the mechanisms of *CP*-violation as it occurs within the SM, or perhaps beyond it. Indeed, the *CP*-violation seen so far is restricted to flavor-changing interactions in the *K*- [15, 19, 20, 21, 22, 23], *D*- [24] and *B*-meson [25, 26] systems, but the really crucial ingredient in baryogenesis is *CP*-violation in baryon decays of which there are not yet any conclusive observations. Furthermore, the size of *CP*-violations that have been observed and are currently known are too small to explain the matter-antimatter asymmetry, and one possible explanation is that there are additional sources of *CP*-violation beyond the SM and the CKM mechanism.

2.4 Composite Particles - Hadrons

In the 1950s and 1960s, several different experiments observed a wide range of new, strongly interacting particles that were initially believed to be elementary. The apparent large variety of species among them led Robert Oppenheimer to refer to them as the subnuclear zoo. Gell-Mann [27] and Ne'eman [28] showed that these particles could be organized into multiplets based on SU(3) symmetry in a scheme that became known as the *eightfold way*. This organization could subsequently be justified through the realization that the particles of the subnuclear zoo were composite objects made up of a fixed set of building blocks, quarks, combined in different ways [29, 30]. This idea was used to predict states whose quantum numbers were identified with the experimentally observed particles. The model that describes the properties of hadrons based on the constituent quarks in this way is called the *quark model*. Here it is used to describe the static properties of hadrons made up of up, down, and strange quarks, following Gell-Mann, and not so much their dynamics. Because the

masses of the u, d, and s quarks are not identical, the SU(3) symmetry of the eightfold way is not is not exact, but broken to some extent.

All hadrons that have been observed so far can be classified into two basic categories: baryons, with baryon number $B = 1$ and mesons with $B = 0$. They are classified and named according to the additive flavor quantum numbers as well as the isospin of the constituent quarks. Isospin can be seen as a flavor quantum number for the up- and down- quarks. Both have total isospin $I = \frac{1}{2}$, but differ in the projection on the third component I_3: up has $I_3 = \frac{1}{2}$ and down has $I_3 = -\frac{1}{2}$. The difference between isospin and the other flavor quantum numbers is that isospin adds like angular momentum so that a given combination of quarks can produce several particles with different isospin states and different properties. The hadrons are further classified according to their total angular momentum J and parity P given in spectroscopic notation J^P. The total angular momentum is given by

$$|L-S| \leq J \leq |L+S|, \tag{2.4}$$

where L is the orbital angular momentum, and S depends on the spin configuration of the individual quarks. The parity is given by the product of the intrinsic quark parities, chosen to be positive for quarks and negative for antiquarks, multiplied by a factor that depends on the orbital angular momentum

$$P(L) = (-1)^L. \tag{2.5}$$

Let us now discuss the mesons, *i.e.* the hadrons that have baryon number $B = 0$. Typically, this means that they consist of a quark and an antiquark. For the meson to be a colorless object these must carry a color and the corresponding anticolor. The spins of the constituent quarks can be either parallel or antiparallel, and as a result, the mesons are bosons with integer spin. Since quarks and antiquarks have opposite intrinsic parity, the parity of the mesons depends on the orbital angular momentum L as

$$P(L) = (-1)^{L+1}. \tag{2.6}$$

The mesons without orbital angular momentum ($L = 0$) have odd parity, and they are therefore known as pseudoscalar and vector mesons. The neutral mesons are furthermore eigenstates of C-parity, with values given by

$$C = (-1)^{L+S}. \tag{2.7}$$

For zero orbital angular momentum, the three lightest quarks, u, d, and s, can be organized into an octet and a singlet of meson states. For both pseudoscalars and vectors there are isoscalar states (with $I_3 = 0$) and the same J^{PC}, that mix with one another to produce the physically observable particles. For the pseudoscalars we have

$$\begin{aligned} \eta &= \cos\theta_P \eta_8 - \sin\theta_P \eta_1 \\ \eta' &= \sin\theta_P \eta_8 + \cos\theta_P \eta_1, \end{aligned} \tag{2.8}$$

where η_8, η_1 are the isoscalar pseudoscalar octet and singlet states and θ_P is the pseudoscalar mixing angle. For the vector mesons, the corresponding relations are

$$\begin{aligned} \phi &= \cos\theta_V \psi_8 - \sin\theta_V \psi_1 \\ \omega &= \sin\theta_V \psi_8 + \cos\theta_V \psi_1 \end{aligned} \tag{2.9}$$

where ψ_8, ψ_1 are the isoscalar vector octet and singlet states and θ_V is the vector mixing angle. The pseudoscalar and vector nonets are shown in Fig. 2.3. If the heavier charm and bottom quarks are also considered, there are many more possible combinations. Of particular importance for this work is the vector charmonium ($c\bar{c}$) state J/ψ. Experiments using e^+e^--annihilation are typically run at the mass of such neutral $q\bar{q}$ resonances since this yields an environment with well-defined quantum numbers and particle-antiparticle symmetric conditions for high-rate production of a large range of interesting states.

The eight lightest pseudoscalars play a special role in our understanding of low-energy QCD as the massless pseudo-Goldstone bosons of the broken chiral symmetry. The η', on the other hand, is much heavier, as consequence of the chiral anomaly.

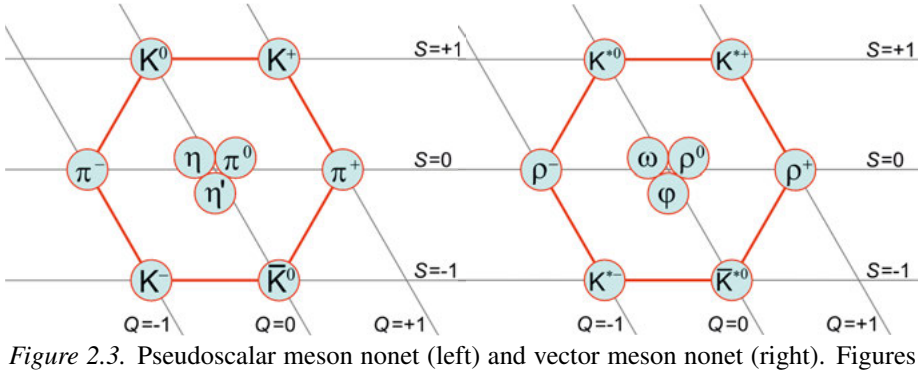

Figure 2.3. Pseudoscalar meson nonet (left) and vector meson nonet (right). Figures from Refs. [31] and [32].

For non-zero orbital angular momentum, other types of mesons known as the scalar ($J^P = 0^+$), axial-vector ($J^P = 1^+$), and tensor ($J^P = 2^+$) mesons are possible. It is also possible to form excited pseudoscalar and vector mesons with the same quantum numbers as those shown in Fig. 2.3, but with higher masses. Finally, a number of more exotic mesons that consist of two quark-antiquark pairs, known as tetraquarks, have been observed. The first of these was discovered independently by the BESIII [33] and Belle [34] experiments.

The other major category of hadrons is Baryons, *i.e.* particles that have baryon number $B = 1$. The most common baryons are made of three quarks with total spin of either 1/2 or 3/2. Each quark must have a unique color charge, and this allows several same-flavor quarks to occupy the same spin state without violating the Pauli exclusion principle. The constituents of (anti)

baryons all have the same intrinsic parity, and the parity of the composite object is therefore given by

$$P = \begin{cases} (-1)^L & \text{for baryons} \\ (-1)^{L+1} & \text{for antibaryons} \end{cases} \tag{2.10}$$

Unlike in the meson sector, the neutral baryons are not their own antiparticles, and therefore they are not eigenstates of C-parity. The lightest and most commonly occurring baryons are made up of the u, d, and s quarks with no orbital angular momentum ($L = 0$). These form an octet of spin 1/2 states and a decuplet of spin 3/2 states as shown in Fig. 2.4.

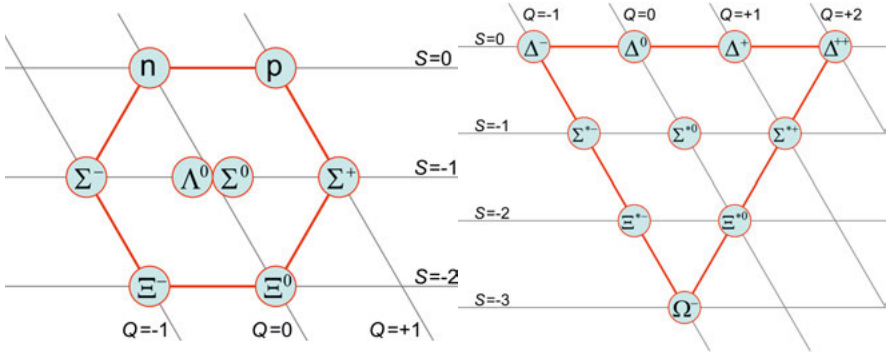

Figure 2.4. Spin-1/2 baryon octet (left) and spin-3/2 baryon decuplet (right). Figures from Refs. [35] and [36].

The baryons are classified according to their quark content and total isospin. Any baryon that consist of three up and/or down quarks is called N ($I = 0$) or Δ ($I = 3/2$). Those with two up and/or down quarks are known as Λ ($I = 0$) or Σ ($I = 1$), and finally those with only one up or down quark are known as Ξ ($I = 1/2$). The exceptions to this naming scheme are the proton and neutron that have their historical names.

There is furthermore a multitude of excited states with non-zero orbital angular momentum. These are named following the convention outlined above, followed by their mass to distinguish them from the ground state baryons. For example, the excited uds-state with $I = 0$ are called $\Lambda(1405)$, $\Lambda(1520)$ etc. If we also include the charm and bottom quarks, yet more baryon states are possible. These are named like the other baryons, but with a subscript to indicate the number of charm or bottom quarks. For example, a state with quark content udc and $I = 0$ is called Λ_c^+

Finally, there are also more exotic baryons beyond the typical three-quark structure. The LHCb experiment has recently found evidence for "pentaquark" states made up of three quarks and a quark-antiquark-pair [37].

3. The Strong Interaction at Low Energies

Making predictions based on QCD at low energies is difficult because the large coupling constant does not permit a perturbative expansion. One of the main challenges is to understand how the strong interaction confines quarks in hadrons and give these the properties that we can observe. Indeed, the inner workings of even the most ubiquitous hadrons, the nucleons, remain mysterious to this date. These have been studied extensively for over a century, but the mechanisms that give them their mass and spin [38] are not yet fully understood. The intrinsic properties of the constituent quarks provide less than $\sim 10\%$ of the mass [39] and ca. 33% of the spin [40]. The rest must be dynamically generated, but how is not yet firmly established. The proton charge radius too has been the topic of intense discussion. A measurement based on muonic hydrogen [41] yielded results that were inconsistent with others based on atomic hydrogen [42, 43, 44, 45] and electron-nucleon scattering [46, 43]. This situation persisted until 2019 when two new experiments using the latter two approaches [47, 48] both observed values consistent with the previous results from muonic hydrogen. The reason for the discrepancy is not yet entirely clear.

To be able to describe the strong interaction in the non-perturbative regime, one must generally resort to effective field theories or models that only describe the strong interaction in this particular energy range, and are not applicable at higher energies. Experimental measurements of the properties and decays of hadrons test the validity of these models, and serve as a guide for their further development. In the following, the effective field theories and other approaches relevant for this work and important features of QCD at low energies are described.

3.1 Chiral Perturbation Theory

In order to build an effective theory for the strong interaction at low energies where quarks are confined inside hadrons, it is useful to start from the symmetries of QCD. In particular, one can note that in the limit where the quark masses are vanishingly small (the chiral limit), the QCD Lagrangian has a chiral symmetry, i.e. left- and right-handed quarks behave the same way. If we restrict ourselves to only considering the three lightest quarks u, d, and s, reality should not be too far from the chiral limit since their masses are much smaller than the typical energy scale of the region we are interested in ~ 1

GeV. By studying the experimentally measured hadron spectrum, one can deduce that the chiral symmetry must be spontaneously broken. This generates eight massless Goldstone bosons that can be identified as the lightest pseudoscalar mesons. Because we know that the pseudoscalars are not, in fact, massless, the chiral symmetry must also be explicitly broken. This is realized by introducing the masses through a perturbative expansion in the small quark masses. The low energy effective field theory for the strong interaction constructed in this way is called chiral perturbation theory (χPT).

To determine which of an infinite number of interaction terms contribute to a given process at a certain order in the expansion, the terms are ordered by the power of the momentum and quark masses. The expansion holds for momenta smaller than the chiral symmetry breaking scale $\Lambda_\chi \approx 1$ GeV. Heavier particles, *e.g.* η' or ρ^0, do not appear explicitly in the chiral Lagrangian, but their interactions with the lightest pseudoscalars are incorporated through low-energy constants that multiply the interaction terms. These constants are determined empirically by comparison with experimental data.

3.2 Vector Meson Dominance

Past studies of the electromagnetic structure of the proton and neutron [49] resulted in the idea that neutral vector particles might be important in mediating the interactions of photons with hadrons [50, 51]. This led Sakurai to propose the existence of vector mesons [52], and, in turn, to the notion of vector meson dominance (VMD). That is, the idea that the photon-hadron interaction is dominated by the exchange of neutral vector mesons, and in particular ρ^0 . In modern language, VMD can refer to several different approaches that describe the photon-hadron interaction in terms of vector mesons.

One frequently used framework is the hidden local symmetry (sometimes referred to as hidden gauge) model where VMD is reproduced assuming that the ρ^0 is a dynamical gauge boson corresponding to a hidden local symmetry of the chiral Lagrangian [53].

VMD fails to reproduce results from deep-inelastic-scattering measurements [54], but remains successful at low energies where pQCD is not applicable. In particular, it is a useful tool for describing the electromagnetic structure of both baryons(*e.g.* [55]) and pseudoscalar mesons (*e.g.* [56]).

3.3 Axial Anomaly

A symmetry of a classical theory that is broken upon quantization is known as an anomalous symmetry. An important example of this occurs in massless electrodynamics. The classical theory has two conserved currents; the standard vector (electrical) current, and an axial vector current. In the quantized

theory, the latter is no longer conserved, and this anomaly leads to the *triangle* diagrams, shown in Fig. 3.1, responsible for the decays $\pi^0, \eta^{(\prime)} \to 2\gamma$ which would otherwise be forbidden [57, 58]. Similarly in QCD, an anomalous axial symmetry of the chiral Lagrangian leads to extra gluonic interaction terms for the flavor singlet state that can explain why the η' is so massive compared to the other pseudoscalars [59].

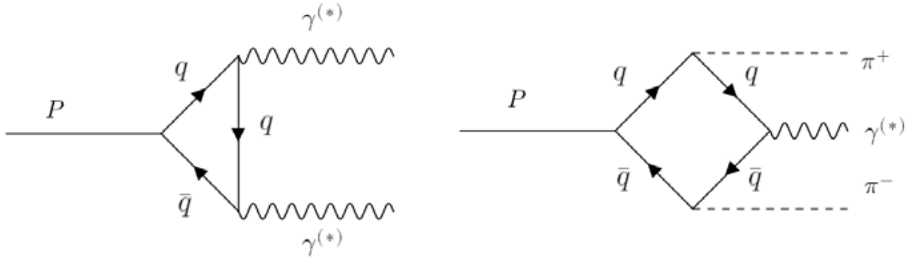

Figure 3.1. Triangle (left) and box (right) anomaly contribution to the interaction of a pseudoscalar *P* with photons.

Effects of anomalies are summarized in the Wess-Zumino-Witten (WZW) Lagrangian, which contains not only the aforementioned triangle but also the *box*, *pentagon* and further higher anomalies [60, 61]. The box anomaly, shown in Fig. 3.1, describes the interaction of a photon and three pseudoscalars. While the $\pi^0 \to \gamma\gamma$ decay is dominated by the anomaly, the anomalous contribution to other decays can be small and in general requires high precision experiments to be observed.

3.4 Lattice QCD

A complementary approach to effective field theories is the discretized version of QCD known as lattice QCD [62]. In this approach, the quarks are placed at sites in discretized space-time connected by the gluon fields, and to make predictions, ones solve the path integrals over the lattice. Because this involves a large number of variables it is computationally heavy and must necessarily be done using MC integration. The precision of these calculations is limited by available computing resources, and this means that lattice QCD predictions, unlike those from other approaches discussed here, have statistical uncertainties alongside systematic uncertainties.

In the 21st century, lattice QCD has become a competitive tool used for precise calculations of a wide range observables, including the strong coupling constant and the quark masses. For a complete review, see Ref. [63]. There are ongoing attempts to use lattice QCD to determine the properties of hadrons and, for example, much progress has been made recently regarding spin of the nucleons [64] and the electric dipole moment of the neutron [65].

3.5 Electromagnetic Form Factors

Much can be learned about hadrons and what goes on inside them by studying their electromagnetic interactions. Whereas the coupling of a photon to point particles is straightforward to describe in QED, the situation is much more complex when dealing with hadrons because of their non-trivial internal structure. The deviation of hadrons from a point-like structure is quantified in terms of scalar functions called *form factors* $F(q^2)$. As an example, the cross section for the scattering of an electron off a hadron can be described as

$$\frac{d\sigma}{dq^2} = \left|\frac{d\sigma}{dq^2}\right|_{pointlike} |F(q^2)|^2, \tag{3.1}$$

where the first part of the right hand side is the cross section for scattering off a pointlike particle. In general, the form factors describe any interaction between a photon and two hadrons as shown in Fig. 3.2 where the "blob" represents the form factors. The diagram can be turned so that it instead represents a decay or a scattering process, but the same form factors apply in all cases. If the two hadrons are of the same type or a particle-antiparticle pair, the form factors are called *elastic*, and if not they are called *transition* form factors. For example, the transition form factors describe interactions where $h_1 = \pi^0$ and $h_2 = \rho^0$ or $h_1 = \Sigma^0$ and $h_2 = \Lambda$.

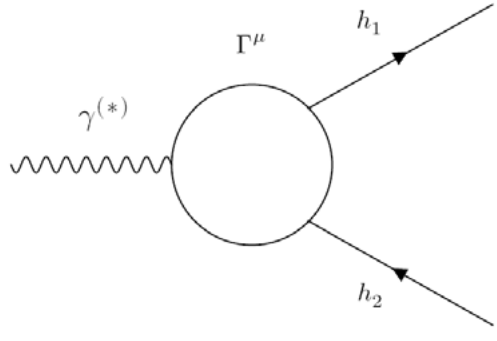

Figure 3.2. Feynman diagram for the interaction of a photon and two hadrons h_1 and h_2. The white "blob" represents the form factors that describe the interaction.

The form factors replace an exact description of the complex internal structure or the full set of intermediate processes that contribute to a reaction and simply give the momentum transfer (q^2) dependence. This is something that can be readily measured, and the form factors are therefore an excellent tool for phenomenological studies. Predictions can be made based on any of the different approaches described in this chapter, and these in turn can be tested.

Different regions of the momentum transfer range can be explored in different types of reactions. A first subdivision of the form factors is made based on the sign of q^2. For momentum transfers $q^2 < 0$ the corresponding form

factors are referred to as *spacelike*. This corresponds to scattering processes $e^- h_1 \to e^- h_2$ that can be either elastic or inelastic. The spacelike form factors are closely related to the internal spatial structure of the hadrons involved. The other category is the *timelike* momentum transfers, $q^2 > 0$. This corresponds either to annihilation of an e^+e^--pair into a pair of hadrons or decays of the type $h_1 \to \gamma^{(*)} h_2$. This thesis deals with both transition form factors of mesons and elastic form factors of baryons at timelike momentum transfers.

Angular momentum conservation and charge conjugation symmetry mean that only certain combinations of mesons can couple to a photon. The simplest possibility is two charged pseudoscalars, *e.g.* $\pi^+\pi^-$, for which the vertex function is given by

$$\Gamma^{\mu}_{\pi^+\pi^-\gamma} = (p_+ + p_-)^{\mu} F_V(q^2), \tag{3.2}$$

where p_+ and p_- are the four-momenta of the positive and negative pion, respectively, $q = p_+ - p_-$, and $F_V(q^2)$ is the so-called pion vector form factor. A slightly more involved case that we will consider in this work is the coupling between a photon, a pseudoscalar meson, and a vector meson ($PV\gamma$) as shown in Fig. 3.3.

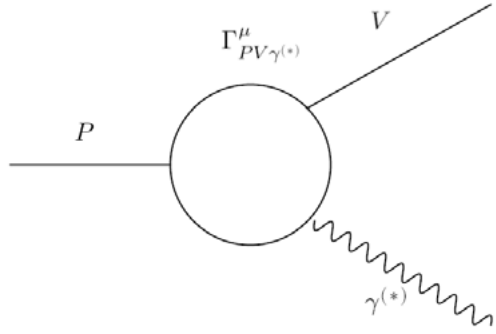

Figure 3.3. Feynman diagram for the interaction of a photon, a pseudoscalar meson, and a vector meson. The white "blob" represents the form factors for that describe the interaction.

For this interaction, the most general expression for the vertex function is

$$\begin{aligned}
&\Gamma^{\mu}_{PV\gamma^{(*)}} = \\
&p_+^{\mu}\left(E_1(p_+ - p_- - p)\cdot q - E_2 q^2\right) + p_-^{\mu}\left(E_1(p_+ - p_- + p)\cdot k + E_2 q^2\right) \\
&+ q^{\mu} E_2(p_+ - p_-)\cdot q + M\varepsilon^{\mu\nu}{}_{\alpha\beta}(p_+ - p_-)_{\nu} q^{\alpha} p^{\beta},
\end{aligned} \tag{3.3}$$

where we have assumed that the vector meson with four-momentum p decays into two charged pseudoscalars with four-momenta p_+ and p_-. The four-momentum of the photon is q. There are three independent form factors E_1,

E_2, and M that are functions of q^2 and p^2. The first two are electric form factors that violate parity, and the last is a magnetic form factor that conserves parity. For real photons, E_2 does not contribute to the reaction because $q^2 = 0$ and $\varepsilon_\gamma \cdot q = 0$. It can also be useful to define the linear combinations E_+ and E_- as

$$\begin{aligned} E_+ &= -(E_1\, 2p_- \cdot k + E_2 q^2) \\ E_- &= E_1\, 2p_+ \cdot k + E_2 q^2. \end{aligned} \tag{3.4}$$

In VMD models, the meson transition form factors are calculated through the pole approximation [66] given by

$$F(q^2) = \sum_V \frac{M_V^2}{M_V^2 - q^2 - iM_V\Gamma_V(q^2)} \approxeq \frac{1}{1 - q^2/M_V^2}, \tag{3.5}$$

where the index V runs over all kinematically allowed vector mesons and M_V and Γ_V are the corresponding mass and width. In the final expression on the right hand side, M_V can be seen as the effective mass of the different vector mesons that contribute. By fitting the expression above to data, M_V can be determined to give an idea of which vector mesons are most important for the reaction.

Let us now consider the interaction of a photon and two spin-1/2 baryons of the same type as shown in Fig. 3.4. Whether in elastic scattering $e^- B \to e^- B$ or annihilation $e^+e^- \to B\bar{B}$ through the exchange of a single photon, the matrix element for this interaction is given by

$$\Gamma^\mu = \gamma^\mu F_1(q^2) + \frac{i\sigma^{\mu\nu} q_\nu}{2M} F_2(q^2), \tag{3.6}$$

where M is the mass of the baryon and $F_1(q^2)$ and $F_2(q^2)$ are the Dirac and Pauli electromagnetic form factors.

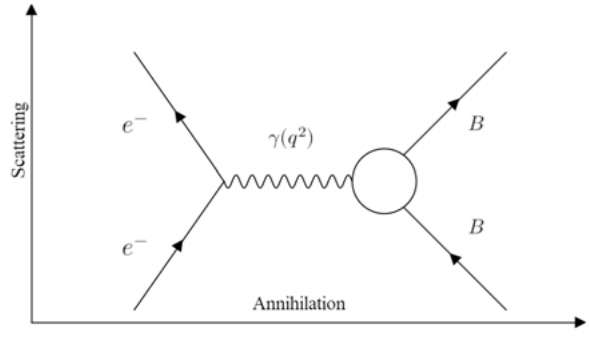

Figure 3.4. One-photon exchange diagram for elastic scattering $e^- B \to e^- B$ or annihilation $e^+e^- \to B\bar{B}$.

By taking linear combinations of these two, we can define the Sachs electric and magnetic form factors [67, 68] that offer a more straightforward interpretation of experimental results. They are given by

$$G_E(q^2) = F_1 + \frac{q^2}{4M^2}F_2 \tag{3.7}$$

$$G_M(q^2) = F_1 + F_2. \tag{3.8}$$

In the Breit frame, where the momentum transfer is completely space-like, G_E and G_M correspond to the Fourier transforms of the charge and magnetic moment distributions. They are normalized such that

$$\begin{aligned} G_E(0) &= Q \\ G_M(0) &= \mu, \end{aligned} \tag{3.9}$$

where Q is the total charge and μ is the magnetic moment. In the spacelike region, the form factors are real-valued.

Since the first experiments by Hofstadter in the 1950s [69], the spacelike form factors of the nucleons have been studied extensively via electron-nucleon scattering experiments where the electric and magnetic form factors were separated using the Rosenbluth method [70] (for a review see *e.g.* [71, 72]). Modern facilities with high-intensity, polarized electron beams have enabled measurements on the basis of polarization observables (see *e.g.* [72]) that have led to important advances in separating the electric and magnetic form factors from each other. In particular, it has been found that the electric form factor of the proton decreases faster than expected for $q^2 < -2$ GeV^2, indicating that it crosses zero around -15 GeV^2 [73].

In the timelike region, the form factors are complex functions

$$\begin{aligned} G_E(q^2) &= |G_E(q^2)|e^{i\Phi_E} \\ G_M(q^2) &= |G_M(q^2)|e^{i\Phi_M} \end{aligned} \tag{3.10}$$

with a relative phase $\Delta\Phi = \Phi_E - \Phi_M$. In general, a non-zero relative phase between the form factors can lead to polarization of the final state baryons even if the initial state is unpolarized [74]. If this polarization can be measured, so can the relative phase. The timelike form factors are not directly related to the electromagnetic structure, but rather to the time evolution of the charge and magnetization densities [75]. They provide snapshots of the production processes and give information on how intermediate hadronic states contribute to the reactions [76]. Extensive experimental efforts are ongoing to measure the timelike nucleon form factors in e^+e^-- or $p\bar{p}$-annihilation experiments. Recently, the BESIII experiment has measured the moduli of the timelike electromagnetic form factors of both the proton [77] and neutron [78] with a precision similar to that achieved in the spacelike region. However, a complete measurement of the timelike form factor must include a determination of the relative

phase and for the nucleons this has not yet been realized. A measurement of the relative phase in $p\bar{p}$-annihilation would require a polarized initial state, either in the form of a polarized $\bar{p}$-beam, a polarized target, or both [79, 80]. Another option would be to use $e^+e^- \to p\bar{p}$ with unpolarized beams and measure the polarization of the proton with a polarimeter. Efforts to develop a polarized ^{3}He target are ongoing within the PANDA collaboration [81], and a polarized antiproton beam is being developed by the PAX collaboration [82]. For hyperons, on the other hand, the polarization can be measured without the need for a dedicated polarimeter and a complete measurement of the timelike form factors can be performed at existing experiments. The possibilities and prospects for studies of the form factors of hyperons are discussed further in Chapter 5.

4. Meson Decays

Precise tests of the predictions from effective field theories can be made by measuring the decays of light pseudoscalar mesons. These processes also provide opportunities for studying *CP*-violation. In this chapter I will discuss how *CP*-violation has been observed in the flavor-changing decays of neutral kaons and show how analogous methods can be used to look for beyond SM sources of *CP*-violation in flavor-conserving processes.

4.1 *CP*-Violation in Kaon Decays

CP-violation was first observed in the decay of the neutral kaon into two pions. This is a process where both the direct and indirect mechanisms mentioned in Section 2.3 contribute. The indirect component is due to the mixing of the *CP*-eigenstates and the direct component is due to the interference of the tree-level and penguin diagram [83] contributions. The former means that both K_S and K_L can decay into the two pion final state, and the latter leads to an observable difference in the decay rates to the $\pi^0\pi^0$ and $\pi^+\pi^-$ final states. The presence of direct *CP*-violation has been established by comparing the decay rates of K_L and K_S into two pions [19, 20, 21]

$$\begin{aligned} \eta_{+-} &= \frac{\Gamma(K_L \to \pi^+\pi^-)}{\Gamma(K_S \to \pi^+\pi^-)} = \varepsilon + \varepsilon' \\ \eta_{00} &= \frac{\Gamma(K_L \to \pi^0\pi^0)}{\Gamma(K_S \to \pi^0\pi^0)} = \varepsilon - 2\varepsilon' \end{aligned} \tag{4.1}$$

where ε and ε' represent the degree of indirect and direct *CP*-violation, respectively.

In addition, *CP*-violation has been observed in angular variables in the decay $K_L \to \pi^+\pi^- e^+ e^-$ [22, 23]. There are four possible contributions to the decay amplitude that are illustrated in Fig. 4.1. The dominating contribution is expected to be a *CP*-conserving magnetic ($M1$) transition, while the second most important is a directly *CP*-violating flavor-changing process with bremsstrahlung. The other two contributions come from indirectly *CP*-violating electric dipole ($E1$) photon emission and a *CP*-conserving $K_L \to \gamma^* K_S$ contribution, the latter sometimes referred to as the charge radius process. The interference between the CP-conserving and CP-violating amplitudes generates an angular distribution proportional to $\sin 2\varphi$, where φ is the angle

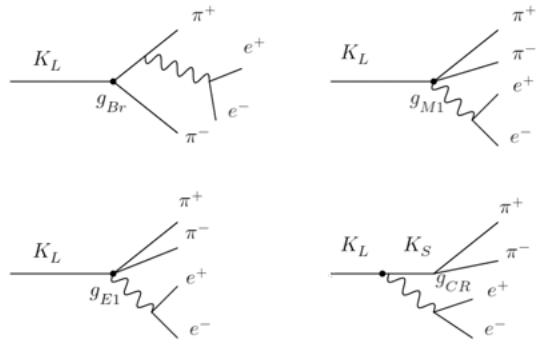

Figure 4.1. Contributions to the decay $K_L \to \pi^+\pi^- e^+ e^-$.

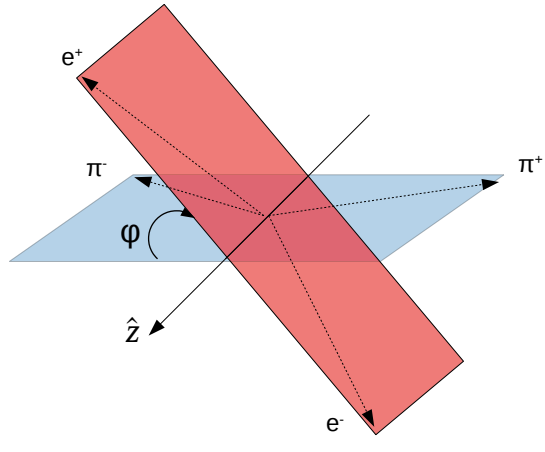

Figure 4.2. Illustration of the angle φ between the decay planes of the $\pi^+\pi^-$- and e^+e^--pairs. The unit vector $\hat{z}$ is given by the sum of the momenta of the electron and positron. Figure from Ref. [84].

between the decay planes of the $\pi^+\pi^-$-pair and the e^+e^--pair as shown in Fig. 4.2.

The KTeV and NA48 experiments observed asymmetries at the level of $(13.6 \pm 2.5 \pm 1.2)\%$ [22] and $(13.9 \pm 2.7 \pm 2.0)\%$ [23], respectively, consistent with the SM CKM mixing matrix mechanism [85]. This does not, however, preclude the presence of an additional *CP*-violating contribution from an electric dipole transition on the percent-level.

4.2 The Process $P \to \pi^+\pi^- l^+ l^-$

So far, *CP*-violation has only been observed in flavor-changing decays of strange, charm [24] and beauty mesons [25, 26], and the effects have been found to be consistent with the SM CKM-mechanism. For a complete picture, it is also interesting to search for *CP*-violation in flavor-conserving processes. One possibility for exploring this topic that has been discussed since the 1970s is to study photon polarization in meson decays [86]. In particular, the process $\eta^{(\prime)} \to \pi^+\pi^-\gamma$ has been suggested as a good candidate. This decay could proceed via an intermediate *CP*-violating decay $\eta^{(\prime)} \to \pi^+\pi^-$ followed by the emission of a bremsstrahlung photon. Because there is no change of flavor, the SM electroweak contribution to this process is expected to be vanishingly small $\mathscr{B}_{EW}(\eta' \to \pi^+\pi^-) \leq 3 \times 10^{-29}$ [87]. The contribution from *CP*-violation in the strong interaction is likewise small. The branching fraction for $\eta' \to \pi^+\pi^-$ due to strong *CP*-violation is constrained by the value of θ to be of the order $\mathscr{O}(10^{-17})$ or smaller [87]. The most stringent experimental limit set so far is $\mathscr{B}(\eta' \to \pi^+\pi^-) \leq 1.8 \times 10^{-5}$ at 90% C.L. [88]. The SM mechanisms for *CP*-violation clearly contribute very little to this decay, and this means that interactions beyond the SM can in principle have a sizeable and detectable contribution. In the following, we will discuss what such a contribution could look like.

If the two-pion system is in a p-wave, the decay $P \to \pi^+\pi^-\gamma^{(*)}$ is equivalent to having the pseudoscalar couple to a photon and a vector meson as discussed in Section 3.5. The decay is thus described by three independent form factors: two electric and one magnetic. The two-pion system in a p-wave is odd under *C*. Since the neutral pseudoscalars are even and the photon is odd under *C*, this means that the decay does not violate *C*. As a consequence, the magnetic form factor, which conserves *P*, also conserves *CP*. The electric form factors violate *P* and therefore violate also *CP*. The magnetic transition is the dominating contribution and can accurately predict the experimentally measured decay width for decays of both η and η' [89, 90, 91]. In a vector meson dominance picture, it can be factorized into three separate parts, see Fig. 4.3. The contact term represents the contribution from the axial anomaly, in this case the box anomaly shown in Fig. 3.1. The other two diagrams give the VMD interactions where the pseudoscalar does not interact directly with photons. The electric transition includes any *CP*-odd beyond SM interactions. We will return to the specific form of this interaction and the corresponding form factor later.

For now, let us discuss the formalism for the decay $P \to \pi^+\pi^-\gamma^{(*)}$ in the most general way possible. We begin by defining the relevant kinematic variables. In the rest frame of the decaying particle *P*, the momentum direction of the photon, with four-momentum k and three-momentum $\mathbf{k}$, is taken as the z-axis. We further define p_+ and p_- as the four-momentum vectors of the π^+ and π^- in the rest frame of the $\pi^+\pi^-$ system. $\mathbf{p}_+$ and $\mathbf{p}_-$ are the corresponding three-momentum vectors. For the case when the photon is virtual

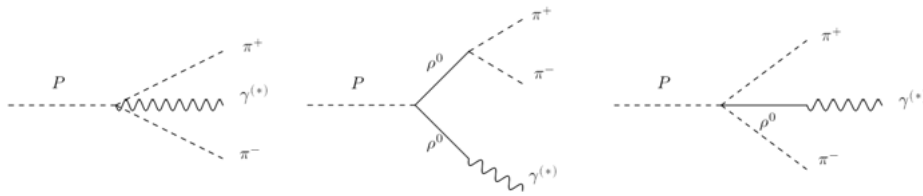

Figure 4.3. Contact term corresponding to the axial anomaly (left) and vector meson dominance contributions (middle and right) to the decay $P \to \pi^+\pi^-\gamma^{(*)}$.

and decays into a lepton-antilepton pair ($l\bar{l}$), we define four-momenta k_+ and k_- for the decay products. The corresponding three-momenta are $\mathbf{k}_+$ and $\mathbf{k}_-$. The angle θ_p is the angle between $\mathbf{p}_+$ and the z-axis in the $\pi^+\pi^-$ rest frame, given by

$$\theta_p = \arccos\left(\frac{\mathbf{p}_+ \cdot \hat{\mathbf{k}}}{|\mathbf{p}_+|}\right). \tag{4.2}$$

When relevant, θ_k is the angle between $\mathbf{k}_-$ and the P momentum in the $l\bar{l}$ rest frame

$$\theta_l = \arccos\left(\frac{-\mathbf{k}_- \cdot \hat{\mathbf{k}}}{|\mathbf{k}_-|}\right) \tag{4.3}$$

The dominating magnetic form factor can be factorized into parts that depend on the properties of the decaying particle, and intermediate vector meson contributions respectively. For η', it is given by [92]

$$M(s_{\pi\pi}, s_{ll}) = \frac{e}{8\pi^2 f_\pi^3}\frac{1}{\sqrt{3}}\left(\frac{f_\pi}{f_8}\sin\theta_{mix} + 2\sqrt{2}\frac{f_\pi}{f_0}\cos\theta_{mix}\right) \times VMD(s_{\pi\pi}, s_{ll}), \tag{4.4}$$

where $s_{\pi\pi}$ is the squared invariant mass of the $\pi^+\pi^-$-pair and s_{ll} is that of the photon, $f_\pi = 92.4$ MeV is the pion decay constant, $f_8 = 1.3 f_\pi$ and $f_0 = 1.04 f_\pi$ are the pseudoscalar octet and singlet decay constants respectively, and θ_{mix} is the pseudoscalar mixing angle. The VMD factor accounts for the different contributions illustrated in Fig. 4.3 and is given by

$$\begin{aligned} VMD(s_{\pi\pi}, s_{ll}) = 1 &- \frac{3}{4}(c_1 - c_2 + c_3) + \frac{3}{4}(c_1 - c_2 - c_3)\frac{m_V^2}{m_V^2 - s_{ll} - i m_V \Gamma(s_{ll})} \\ &+ \frac{3}{2}c_3 \frac{m_V^2}{m_V^2 - s_{ll} - i m_V \Gamma(s_{ll})}\frac{m_V^2}{m_V^2 - s_{\pi\pi} - i m_V \Gamma(s_{\pi\pi})}. \end{aligned} \tag{4.5}$$

Here it is assumed that the vector meson is ρ^0 and Γ is its total width

$$\Gamma(s) = g_{mv}\left(\frac{s}{m_V^2}\right)\left(\frac{1-\frac{4m^2}{s}}{1-\frac{4m^2}{m_V^2}}\right)^{3/2}\Theta(s-4m^2), \tag{4.6}$$

where $g_{mV} = 149.1$ MeV is the on-shell width of ρ^0, m_V is ρ^0 mass, m is the mass of the pion, and Θ is the Heaviside step function. The parameters c_{1-4} are model dependent and determine the contributions of the different interaction terms illustrated in Fig. 4.3. In the case of full vector meson dominance, where photons and hadrons only couple via vector mesons, one would have $c_3 = 1$, $c_1 - c_2 = \frac{1}{3}$. However the contact term, *i.e.* the box anomaly, is required by χPT. The box anomaly predicts the low energy limit $VMD(s_{\pi\pi} = 0, s_{ll} = 0) = 1$. In the hidden gauge model this is realized by $c_3 = c_1 - c_2 = 1$ [93, 94, 95]. Evidence for the presence of the box anomaly has been seen in the decay $\eta' \to \pi^+\pi^-\gamma$ where it causes a shift of the peak in the $\pi^+\pi^-$ invariant mass by about 20 MeV/c^2 [96, 97, 98, 99, 100, 101, 102]. The model parameters have also been determined by a fit to data on hadronic cross sections in e^+e^--annihilation from mainly the CMD-2 experiment. The best fit yields $c_3 = 0.927 \pm 0.010$, $c_1 - c_2 = 1.168 \pm 0.069$ [103].

Recalling the vertex function from Eq. 3.3, and remembering that the electric form factor E_2 does not contribute when the photon is real we are now ready to express the squared amplitude. In the rest frame of the decaying pseudoscalar P, it is given by

$$\begin{aligned}|\mathscr{A}_{P\to\pi\pi\gamma}|^2 = m_P^{-4}E_\gamma^2\Big(&|M|^2|\hat{\mathbf{k}}\cdot(\boldsymbol{\varepsilon}\times\mathbf{p}_+)|^2 + |E_1|^2|(\boldsymbol{\varepsilon}\cdot\mathbf{p}_+)|^2 \\ &+ E_1^* M\left[\hat{\mathbf{k}}\cdot(\mathbf{p}_+\times\boldsymbol{\varepsilon})\right](\boldsymbol{\varepsilon}\cdot\mathbf{p}_+)^* \\ &+ M^* E_1\left[\hat{\mathbf{k}}\cdot(\mathbf{p}_+\times\boldsymbol{\varepsilon})\right]^*(\boldsymbol{\varepsilon}\cdot\mathbf{p}_+)\Big),\end{aligned} \tag{4.7}$$

where $\boldsymbol{\varepsilon}$ is the photon polarization vector. The interference terms depend on the T-odd product $\hat{\mathbf{k}}\cdot(\mathbf{p}_+\times\boldsymbol{\varepsilon})$ which, according to the CPT theorem, must also be CP-odd. If one sums over polarizations, the interference terms vanish, resulting in

$$|\mathscr{A}_{P\to\pi^+\pi^-\gamma}|^2(E_\gamma,\theta_\pi) = \frac{E_\gamma^2\left(1-2E_\gamma/m_P\right)\beta_\pi^2\sin^2\theta_\pi}{4m_P^2}\left(|M|^2+|E_1|^2\right), \tag{4.8}$$

where $\beta_\pi = \sqrt{1-\frac{4m_\pi^2}{s_{\pi\pi}}}$. It is clear therefore that CP-violating contributions to the decay can not be measured except by explicitly studying the photon

polarizations. The Stokes vector for the polarization has the components

$$
\begin{aligned}
S_1(E_\gamma, \theta_\pi) &= \frac{2\,\mathrm{Re}(E_1^* M)}{|E_1|^2 + |M|^2} \\
S_2(E_\gamma, \theta_\pi) &= \frac{2\,\mathrm{Im}(E_1^* M)}{|E_1|^2 + |M|^2} \\
S_3(E_\gamma, \theta_\pi) &= \frac{|E_1|^2 - |M|^2}{|E_1|^2 + |M|^2}
\end{aligned}
\tag{4.9}
$$

Clearly S_1 and S_2, known as the linear and circular polarizations, are related to the interference and would be zero in the absence of the electric transition. It has been shown that an unconventional, structure dependent interaction, illustrated in Fig. 4.4, could induce an electric dipole-type transition [104]. Here, unconventional means that the strength of the interaction is unconstrained by experimental knowledge of $\eta' \to \pi^+\pi^-$ and the neutron EDM. It could in principle have a significant contribution to the decay, and possibly generate linear polarizations up to 21% in decays of η and about 4% in decays of η', compared to an SM expectation of less than 10^{-6} in both cases. A similar analysis for the decay $K_L \to \pi^+\pi^-\gamma$ has been performed in Ref. [105].

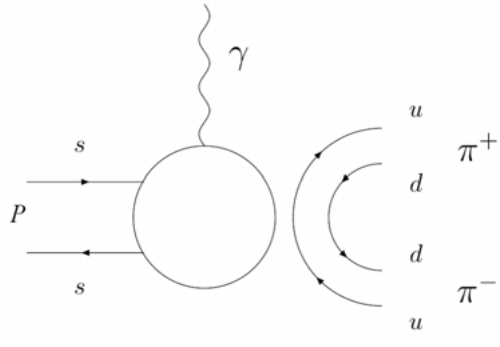

Figure 4.4. Illustration of the contribution from the unconventional operator to the decays $\eta' \to \pi^+\pi^-\gamma^{(*)}$. Figure adapted from Ref. [104].

However, experimental facilities where large samples of η/η' are produced are typically not equipped with polarimeters and such a measurement can not be performed at present. Let us discuss alternative methods for extracting the polarization that are possible at experiments that detect charged particles. The first option is to consider polarized real photons that convert into an e^+e^--pair in the detector material. The differential cross section for pair production depends on the photon polarization [106], and it has been suggested [107] that the angle-dependent rate of conversion events could therefore be used to measure the polarization. The second method, and the one that will be used in this work, is to consider the case when the photon is virtual and decays into an e^+e^--pair. In this case, the polarization is translated into a correlation between

the angular distributions of the e^+e^-- and $\pi^+\pi^-$-pairs [108]. We can express the decay rate in terms of *CP*-even and *CP*-odd components as

$$\begin{aligned} d\Gamma(P \to \pi^+\pi^- e^+e^-) = &\left(d\Gamma(P \to \pi^+\pi^- e^+e^-)\right)_{CP-\text{even}} \\ &+ \left(d\Gamma(P \to \pi^+\pi^- e^+e^-)\right)_{CP-\text{odd}}. \end{aligned} \tag{4.10}$$

The *CP*-even component, integrated over the angles θ_p and θ_k, is given by

$$\begin{aligned} \left(\frac{d\Gamma(P \to \pi^+\pi^- e^+e^-)}{ds_{ll}ds_{\pi\pi}d\varphi}\right)_{CP-\text{even}} &= C_{kin.}|M|^2 s_{\pi\pi}\beta_\pi^3\lambda^{3/2}(m_P^2, s_{\pi\pi}, s_{ll}) \\ &\times \beta_l \frac{3-\beta_l^2}{2}\sin^2\varphi, \end{aligned} \tag{4.11}$$

where λ is the Källén function, $\beta_l = \sqrt{1-\frac{4m_l^2}{s_{ll}}}$, $C_{kin.}$ is a kinematic factor and M is the same magnetic form factor as above. Terms that depend on the electric form factors squared have been omitted because their contributions are expected to be negligible. The *CP*-odd component, likewise integrated over θ_p and θ_l, is given by

$$\begin{aligned} \left(\frac{d\Gamma(P \to \pi^+\pi^- e^+e^-)}{ds_{ll}ds_{\pi\pi}d\varphi}\right)_{CP-\text{odd}} &= C_{kin.}\text{Re}\left(M(E_+^* - E_-^*)\right) \\ &\times \frac{\lambda(m_P^2, s_{\pi\pi}, s_{ll})}{s_{ll}} s_{\pi\pi}\beta_\pi^3 \sin 2\varphi, \end{aligned} \tag{4.12}$$

where E_+ and E_- are the linear combinations of the form factors E_1 and E_2 defined in Eq. 3.4. Both terms depend on φ, which is the angle between the decay planes of the e^+e^-- and $\pi^+\pi^-$-pairs, illustrated in Fig. 4.2. While the *CP*-even term is symmetric with respect to φ, the *CP*-odd term is antisymmetric. In order to study the *CP*-odd contribution to the decay rate, we can thus define the asymmetry

$$\begin{aligned} \mathscr{A}_{CP} &= <\text{sgn}(\sin 2\varphi)> = \frac{1}{\Gamma}\int_0^{2\pi}\frac{d\Gamma}{d\varphi}\text{sgn}(\sin 2\varphi)\,d\varphi \\ &= \frac{C_{kin.}}{\Gamma} \\ &\times \int \frac{s_{\pi\pi}\beta_\pi^3\lambda(m_P^2, s_{\pi\pi}, s_{ll})}{s_{ll}}\text{Re}\left(M(E_+^* - E_-^*)\right)\sin^2\theta_\pi\, ds_{\pi\pi}ds_{ll}. \end{aligned} \tag{4.13}$$

From the expression above, we can see that that the size of the asymmetry is proportional to the size of the electric form factors $E_\pm$. The presence of the type of four-quark operator illustrated in Fig. 4.4 would lead to electric form

factors of the form

$$E_+ \propto \frac{eF(s)G}{m_P^3}(s_{ll} + 2k \cdot p_-)$$
$$E_- \propto \frac{eF(s)G}{m_P^3}(s_{ll} + 2k \cdot p_+), \tag{4.14}$$

where $F(s) \simeq 0.19$ is a form factor for the transition $P \to \gamma$ and G is a dimensionless real parameter. When it was first suggested, it was argued that this operator would neither lead to a neutron EDM nor contribute to $\eta' \to \pi^+\pi^-$ and that G could be of the order 1. This would mean a negligible impact on the decay rate, but could lead to an asymmetry $\mathscr{A}_{CP}$ on the percent level [108]. More recently, it has been suggested that such an operator must also give rise to interactions that do contribute to the neutron EDM, and that the electric form factors must be much smaller than previously thought, $E/M < 10^{-11}$ [109].

The asymmetry was measured in the decay $\eta \to \pi^+\pi^-e^+e^-$ by the KLOE [110] and WASA-at-COSY [111] experiments to be $\mathscr{A}_\varphi = (-0.6 \pm 2.5_{stat.} \pm 0.7_{syst.}) \times 10^{-2}$ and $\mathscr{A}_\varphi = (-1.1 \pm 6.6_{stat.} \pm 0.2_{syst.}) \times 10^{-2}$, respectively. Both measurements are consistent with zero and the SM expectation of practically no *CP*-violation. The focus of this work is to measure the asymmetry in the decay $\eta' \to \pi^+\pi^-e^+e^-$, which has never been studied before. While the polarization induced by the *CP*-violating contribution is predicted to have a maximum value of 4% in this case compared to 21% in the decay of η, the branching fraction for $\eta' \to \pi^+\pi^-e^+e^-$ is almost one order of magnitude larger than its η counterpart and an observation may still be possible.

Aside from the possible contribution of beyond SM sources of *CP*-violation, it is interesting to test the different models that describe the strong interaction contributions to the decay. The most straightforward test is to measure the partial decay width, but with large data samples, the structure of the magnetic form factors could be tested by studying the $s_{\pi\pi}$ and s_{ll} distributions. In addition to the vector meson dominance models with the box anomaly shown explicitly above, calculations have been performed at one-loop order in a chiral unitary approach that combines chiral perturbation theory and final-state interactions [91]. As above, the anomaly is accounted for by the WZW action. This model depends on five parameters that have been determined by fits to data on $\eta^{(\prime)} \to \pi^+\pi^-\gamma$.

The focus for this work is on a measurement of the branching fraction of the decay $\eta' \to \pi^+\pi^-e^+e^-$. Predictions from the aforementioned models are given in Table 4.1. The chiral unitary approach and modified VMD model both have uncertainties due to parameters estimated by fitting data. Both VMD models furthermore have uncertainties due to the experimentally determined universal vector coupling constant g.

On the experimental side, the decay $\eta' \to \pi^+\pi^-e^+e^-$ was first observed by the CLEO experiment in 2009 [112] via the process $\psi(2S) \to \pi^+\pi^-J/\psi$ followed by $J/\psi \to \gamma\eta'$. The analysis found $7.9^{+3.9}_{-2.7}$ signal events and the branch-

Table 4.1. *Predictions for the $\eta' \to \pi^+\pi^- e^+ e^-$ branching fraction.*

	$\mathrm{B}(\eta' \to \pi^+\pi^- e^+ e^-)\ (10^{-3})$
Unitary χPT [91]	$2.13^{+0.17}_{-0.31}$
Hidden gauge [92]	2.17 ± 0.21
Modified VMD [92]	2.27 ± 0.13

ing fraction was determined to be $(2.5^{+1.2}_{-0.9} \pm 0.5) \times 10^{-3}$. The most precise measurement until now was made by the BESIII experiment in 2013 [113] using a data set of $(225.3 \pm 2.8) \times 10^6$ J/ψ events. The branching fraction was determined to be $(2.11 \pm 0.12(stat.) \pm 0.15(syst.)) \times 10^{-3}$ from 429 ± 24 signal events.

5. Hyperons

Hyperons are baryons that contain at least one strange quark alongside up and/or down quarks. In this way, they can be considered siblings of the nucleons. Because they are similar to the nucleons, studies of hyperons are a complementary approach to understanding the structure of matter and how quarks form hadrons in general. At the same time, the unique properties of hyperons give access to new information that is not available for the nucleons. The mass of the strange quark is close to the QCD scale and by studying hyperons one can thus probe the strong interaction in the confinement domain. The heavier strange quark mass also means that compared to the proton, a smaller portion of the hyperon mass is dynamically generated and this can perhaps help us understand the mechanisms behind the observable masses of hadrons.

From SU(3) symmetry emerges twelve hyperons with $L = 0$, six with spin 1/2 and six with spin 3/2, see Fig. 2.4. This works focuses on the lightest of these, Λ, with quark contents (uds). Its properties, listed in Table 5.1, are similar to those of the proton; the spin-parity are the same, and the mass is slightly larger. Unlike the proton however, the Λ hyperon is unstable and to be studied experimentally it must be reconstructed from its decay products.

Table 5.1. *Measured properties of the Λ hyperon [6].*

Quark content	uds
Mass	1.116 GeV
J^P	$\frac{1}{2}^+$
τ	2.6×10^{-10} s
$c\tau$	7.8 cm

5.1 Hyperon Decays

Depending on their quantum numbers and mass, hyperons can either decay via the weak, electromagnetic, and/or strong interactions. For Λ, there are no possible final states with mass $< m_\Lambda$ into which it can decay while still satisfying baryon number and strangeness conservation. Therefore it must decay weakly and as a consequence, the Λ hyperon has a relatively long lifetime of 2.6×10^{-10} s. In an experiment, this means that a Λ hyperon will travel a measurable distance before decaying which complicates the process of reconstructing it. The Σ^0 hyperon, in contrast, can decay electromagnetically into $\Lambda\gamma$ and hence it has a much shorter lifetime of the order 10^{-20} s.

All known decay modes of Λ and their branching fractions are listed in Table 5.2. In this work, only the two dominating hadronic weak decays into a nucleon and a pion will be considered. The contributions from weak radiative and leptonic decays are small enough to be considered negligible.

Table 5.2. *Known decay modes of the Λ hyperon and their branching fractions [6].*

Mode	$\mathscr{B}$
$\Lambda \to p\pi^-$	63.9%
$n\pi^0$	35.8%
$n\gamma$	1.75×10^{-3}
$p\pi^-\gamma$	8.4×10^{-4}
$pe^-\nu_e$	8.32×10^{-4}
$p\mu^-\nu_\mu$	1.57×10^{-4}

For all hyperon decays, transitions corresponding to a change in isospin of 3/2 are strongly suppressed relative to those where the change is 1/2 [114]. This phenomenological selection rule is known as the isospin-1/2 or $\Delta I = 1/2$ rule. This leads to the prediction that the branching fractions for the dominating decay modes of Λ should be related to each other by $\mathscr{B}(\Lambda \to p\pi^-)/(\mathscr{B}(\Lambda \to p\pi^-) + \mathscr{B}(\Lambda \to n\pi^0)) = \frac{2}{3}$. Including a phase space factor and radiative corrections, the expected ratio rises to 0.674. The experimentally observed ratio of 0.641 ± 0.005 [6] significantly disagrees with this prediction, but still shows that the contribution from the $\Delta I = 3/2$ transition is small .

The weak decay of a spin-$\frac{1}{2}$ hyperon into a baryon and a meson is characterized by two spin transitions S and P, where the former is parity-violating and the latter is parity-conserving. The amplitude is given by

$$\mathscr{A} = S + P\boldsymbol{\sigma} \cdot \hat{n}, \tag{5.1}$$

where $\hat{n}$ is the direction of the final baryon in the rest frame of the decaying hyperon, and S and P can be expressed as

$$S = |S|\exp(i\xi_S)\exp(i\delta_S) \tag{5.2}$$
$$P = |P|\exp(i\xi_P)\exp(i\delta_P). \tag{5.3}$$

The arguments $\xi_{S,P}$ and $\delta_{S,P}$ are weak and strong phases respectively. Both have isospin components corresponding to $\Delta I = 1/2$ and $\Delta I = 3/2$, but due to the isospin-1/2 rule, it will be sufficient to consider the former in this presen-

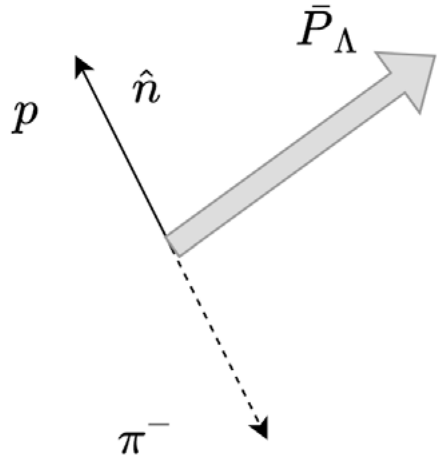

Figure 5.1. Illustration of the vectors $\hat{n}$ and $\bar{P}_B$ for the decay $\Lambda \to p\pi^-$ given in the rest frame of the decaying Λ.

tation. The decays are described by three parameters defined as [115]

$$\alpha_\Lambda = \frac{2\mathrm{Re}(S^*P)}{|S|^2+|P|^2} \tag{5.4}$$

$$\beta_\Lambda = \frac{2\mathrm{Im}(S^*P)}{|S|^2+|P|^2} = \sqrt{1-\alpha_\Lambda^2}\sin\phi_\Lambda \tag{5.5}$$

$$\gamma_\Lambda = \frac{\left(|S|^2-|P|^2\right)}{\left(|S|^2+|P|^2\right)} = \sqrt{1-\alpha_\Lambda^2}\cos\phi_\Lambda. \tag{5.6}$$

Note that the definitions of these parameters are analogous to the components of the photon polarization in Eq. 4.9. Experimentally, one studies the parameters α_Λ and ϕ_Λ. The decay asymmetry parameter, α_Λ, lies in the range $-1 \leq \alpha_\Lambda \leq 1$, and is related to the daughter baryon angular distribution via

$$\frac{d\Gamma}{d\Omega} = \frac{1}{4\pi}(1+\alpha_\Lambda \hat{n}\bar{P}_\Lambda), \tag{5.7}$$

where $\hat{n}$ is the flight direction of the daughter baryon, and $\bar{P}_\Lambda$ is the polarization vector of the decaying hyperon as illustrated in Fig. 5.1. This relationship means that the hadronic weak decays of hyperons are "self-analyzing". That is, the angular distribution of the daughter baryon can be used to determine the polarization of the decaying hyperon without the need for a dedicated polarimeter.

The parameter ϕ_Λ , $-\pi \leq \phi_\Lambda \leq \pi$, relates the polarization of the decaying hyperon P_Λ to that of its daughter P_b

$$P_b \cdot \hat{z} = \frac{\alpha_\Lambda + P_\Lambda \cdot \hat{z}}{1 + \alpha_\Lambda P_\Lambda \cdot \hat{z}} \tag{5.8}$$

$$P_b \times \hat{z} = |P_\Lambda| \sqrt{1 - \alpha_\Lambda^2} \frac{\sin\phi_\Lambda \hat{x} + \cos\phi_\Lambda \hat{y}}{1 + \alpha_D P_\Lambda \cdot \hat{z}} \tag{5.9}$$

That is, the transverse polarization of the daughter baryon is rotated by an angle ϕ_Λ with respect to the polarization of its parent. A simultaneous measurement of the decay parameters of a hyperon and the corresponding antihyperon allows for a test of *CP*-symmetry. If *CP* is conserved, one expects $\alpha = -\bar{\alpha}$ and one can construct the *CP* test

$$A_{CP} = \frac{\alpha_\Lambda + \bar{\alpha}_\Lambda}{\alpha_\Lambda - \bar{\alpha}_\Lambda} \tag{5.10}$$

where a non-zero value would indicate *CP*-violation. Throughout this work, however, *CP*-conservation will be assumed.

The decay asymmetry parameter for Λ, α_Λ, was measured in a series of experiments in the 1960s and 70s [116, 117, 118, 119, 120] . The PDG-average of $\alpha_\Lambda = 0.642 \pm 0.013$ that was established after these measurements was in place for the last forty years, and was used in all measurements relating to Λ polarization up until now.

Recently, the BESIII experiment measured the value of α_Λ through the reaction $e^+e^- \to J/\psi \to \Lambda\bar{\Lambda}$ following the procedure outlined below, taking into account the correlations between the spins of hyperon and antihyperon. The result, $0.754 \pm 0.003 \pm 0.002$ [121], is 17% larger than the old PDG average and has led to a reevaluation of the contributing measurements. The CLAS experiment has since performed a re-analysis of its data on $\gamma p \to \Lambda K$ and measured the decay parameter to be $\alpha_\Lambda = 0.721 \pm 0.006 \pm 0.005$ [122]. Another independent measurement is provided by a BESIII analysis of $\Xi \to \Lambda\pi \to p\pi\pi$ that yielded the value $\alpha_\Lambda = 0.760 \pm 0.006 \pm 0.003$ [123]. The two measurements from BESIII are consistent with each other, but not with the result from CLAS. Nevertheless, all three point to a true value of α_Λ larger than the old PDG average. An analysis of $\Lambda_b \to J/\psi\Lambda$ from the LHCb experiment [124] found that the BESIII-value gave a better description of data than the old PDG average, which supports the aforementioned conclusion.

In this work, the focus is on the form factors of Λ, and the data samples used are far too small to provide competitive measurements of the decay parameters. Therefore, *CP*-conservation is assumed so that $\alpha_\Lambda = -\bar{\alpha}_\Lambda$, and its value is fixed to 0.754.

5.2 Hyperon Form Factors

Measurements of the electromagnetic form factors of hyperons are interesting from the point of view of extending our understanding of the internal structure of hadrons to a more general picture beyond just the nucleon. To what extent do the electromagnetic properties of the hyperons follow from SU(3) symmetry, and do new effects come into play when strangeness and the larger strange quark mass are involved? The electromagnetic form factors of the whole baryon octet have been investigated on the basis of chiral perturbation theory, see *e.g.* [125], as well as lattice QCD, see *e.g* [126].

Because of the short-lived nature of hyperons, it is difficult to study their properties in scattering experiments. It is not feasible to create a hyperon target, and making a hyperon beam with sufficiently high intensity is very challenging. Therefore there is little experimental data on their spacelike electromagnetic form factors, and the charge and magnetization densities inside them are largely unknown. What is known so far comes from one measurement of the charge radius of the Σ^--hyperon [127], which gives the value its electric form factor at $q^2 = 0$. Modern, high-intensity e^+e^--annihilation experiments do however allow us access to the timelike form factors of hyperons. Their self-analyzing hadronic weak decays enable measurements of their polarization. This means that, unlike for nucleons, the relative phase between the timelike hyperon electromagnetic form factors can be extracted experimentally.

While we can only measure the timelike form factors of hyperons, there is still hope that we can learn something about their spacelike structure. Dispersion relations, see *e.g.* Ref. [128], can provide a description of the form factors in the spacelike and timelike regions simultaneously. It has been shown that for the proton, this approach can reproduce experimental results in both regions as well as the expected behavior at $q^2 = 0$ and in the asymptotic limit [129]. For hyperons in particular, this means that data on the timelike form factors can be used to determine the experimentally inaccessible spacelike form factors. Recently, the authors of Ref. [130] showed how data on the timelike form factor, and in particular the relative phase $\Delta\Phi$, can be directly related to predictions of the electromagnetic structure of Λ. The q^2-dependence of $\Delta\Phi$ is especially interesting. For each time the sinus of the relative phase crosses zero, there must be a corresponding zero crossing for the electric form factor in the spacelike region. Furthermore, the spacelike and timelike form factors G_E and G_M must become equal in the asymptotic limit, *i.e.* for $q^2 \to \infty$. This follows from analyticity and the Phragmén-Lindelöf theorem. Therefore the relative phase must become either zero or an integer multiple of π [131, 132]. Finding the scale where the asymptotic behavior sets in would provide a clear constraint for the dispersive calculations.

By studying the relative phase over a wide range of momentum transfers, and particularly if the asymptotic scale can be identified, it is possible to pin

down the spacelike structure of Λ despite the fact that it can not be measured at present. This information allows for the extraction of both dynamical and static properties of the Λ-hyperon such as the charge radius which is hitherto unknown.

5.3 Formalism for The Process $e^+e^- \to Y\bar{Y}$

The production of a hyperon-antihyperon pair in e^+e^--annihilation via single-photon exchange has been investigated in great detail and a theoretical formalism for describing the process is well established [74, 133, 134, 135, 136]. It has recently been shown that the same formalism also describes the production via the decay of vector charmonia, *e.g.* $J/\psi, \psi(2S)$ [137], and this fact has been utilized with great success for high precision measurements of hyperon decays at the BESIII experiment (see *e.g.* Ref. [121]). The cross section depends on the two complex form factors G_E and G_M and can be expressed in terms of three observable parameters: $|G_M|$, the ratio $R = |G_E|/|G_M|$ and the relative phase $\Delta\Phi$. To describe the angular distributions of the hyperons and their daughter baryons, only the latter two are needed. The form factor ratio is related to the hyperon scattering angle distribution, and the relative phase to the hyperon polarization.

In this section I will present the formalism and show how the angular distributions of the hyperon-antihyperon pair and their decay products can be related to the form factor parameters R and $\Delta\Phi$. To begin with, I will give the singly-differential cross-section to illustrate the relationship between the parameter R and the hyperon scattering angle. I will also show how the total, momentum transfer dependent cross section is related to the form factors. Then I will give the most general possible description of the production and decay of any spin-1/2 baryon-antibaryon pair and their subsequent decays. This part will in particular illustrate the relationship between the parameter $\Delta\Phi$ and the polarizations of and spin correlations between the hyperon and antihyperon. Lastly, I will give explicit expressions for the angular distribution that can be used to extract both parameters from data.

The one-dimensional differential cross section for the e^+e^--annihilation into a baryon-antibaryon pair, $e^+e^- \to B\bar{B}$, can be expressed as

$$\frac{d\sigma(q^2)}{d\Omega} = \frac{\alpha^2\beta}{4q^2}\left(\frac{1}{\tau}|G_E|^2\sin^2\theta + |G_M|^2(1+\cos^2\theta)\right), \tag{5.11}$$

where $\alpha \approx 1/137$ is the fine structure constant, $\tau = q^2/4m_B^2$, m_B is the baryon mass, β is the baryon velocity $\beta = \sqrt{1-1/\tau}$, and θ is the scattering angle of the baryon with respect to the electron beam direction. This can be rewritten

as

$$\frac{d\sigma(q^2)}{d\cos\theta} = \frac{2\pi\alpha^2\beta}{4q^2}\left((1+\cos^2\theta)+\frac{1}{\tau}R^2\sin^2\theta\right)|G_M|^2, \tag{5.12}$$

where $R = \left|G_E(q^2)/G_M(q^2)\right|$ is the ratio of the form factors. At the production threshold, the electric and magnetic form factors are equal by construction and therefore $R = 1$.

The angular dependence can be further simplified as

$$\frac{d\sigma(q^2)}{d\cos\theta} = \frac{2\pi\alpha^2\beta}{4q^2(\tau+R^2)}\left(1+\eta\cos^2\theta\right), \tag{5.13}$$

where $\eta = \frac{\tau-R^2}{\tau+R^2}$, $-1 < \eta < 1$. From a measured angular distribution parameter, the ratio of electromagnetic form factors can thus be determined as

$$R = \sqrt{\tau}\sqrt{\frac{1-\eta}{1+\eta}}. \tag{5.14}$$

If the e^+ and e^- beams are unpolarized, the (anti)baryon can only be polarized in the direction perpendicular to the production plane. This polarization is given by

$$P_y(\cos\theta) = \frac{\sqrt{1-\eta^2}\cos\theta\sin\theta}{1+\eta\cos^2\theta}\sin(\Delta\Phi). \tag{5.15}$$

Clearly, a non-zero relative phase will lead to a non-zero transverse polarization. The total cross section, integrated over all angles, is given by

$$\sigma(q^2) = \frac{4\pi\alpha^2\beta}{3q^2}\left(\frac{1}{2\tau}|G_E|^2+|G_M|^2\right), \tag{5.16}$$

which can be used to define an effective form factor

$$|G_{eff}(q^2)| = \sqrt{\frac{2\tau|G_M|^2+|G_E|^2}{2\tau+1}} = \sqrt{\frac{\sigma(q^2)}{\left(1+\frac{1}{2\tau}\right)\left(\frac{4\pi\alpha^2\beta}{3q^2}\right)}}. \tag{5.17}$$

5.3.1 Joint Angular Distributions

Now we turn to the task providing a description of the full angular distribution of the process $e^+e^- \to \Lambda\bar{\Lambda}$. Let us begin by defining the reference system. We start from the center-of-mass system, where the momenta are defined as

$$\begin{aligned} \boldsymbol{p}_\Lambda &= -\boldsymbol{p}_{\bar{\Lambda}} = \boldsymbol{p} \\ \boldsymbol{k}_{e^-} &= -\boldsymbol{k}_{e^+} = \boldsymbol{k} \end{aligned} \tag{5.18}$$

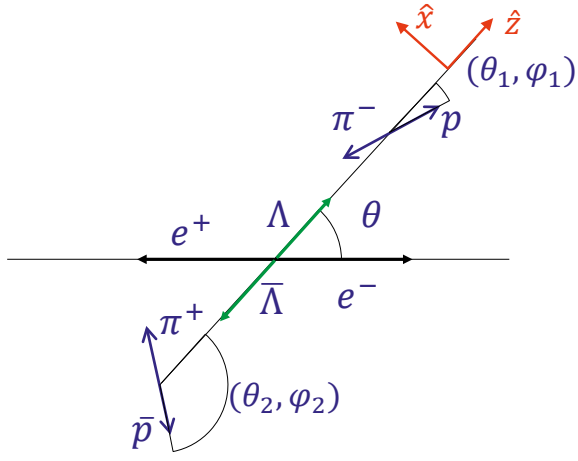

Figure 5.2. Definition of the coordinate system and angles used to describe the process $e^+e^- \to \Lambda\bar{\Lambda}$.

and the scattering angle is given by

$$\cos\theta = \hat{\boldsymbol{p}} \cdot \hat{\boldsymbol{k}}. \tag{5.19}$$

We define a right-handed coordinate system with the basis vectors

$$\begin{aligned} \boldsymbol{e}_z &= \hat{\boldsymbol{p}}, \\ \boldsymbol{e}_x &= \frac{1}{\sin\theta}\left(\hat{\boldsymbol{p}} \times \hat{\boldsymbol{k}}\right) \times \hat{\boldsymbol{p}} \\ \boldsymbol{e}_y &= \frac{1}{\sin\theta}\left(\hat{\boldsymbol{p}} \times \hat{\boldsymbol{k}}\right). \end{aligned} \tag{5.20}$$

This coordinate system, illustrated in Fig. 5.2, is used to define the spherical angles $\Omega_1 : (\theta_1, \phi_1)$ of the proton in the Λ rest frame and those of the antiproton $\Omega_2 : (\theta_2, \phi_2)$ in the $\bar{\Lambda}$ rest frame. The reaction is completely described by the five-dimensional vector $\xi = (\theta, \Omega_1, \Omega_2)$.

In Ref. [138], a modular formalism for describing the production and subsequent decay of any baryon-antibaryon pair is developed. The spin state is encoded in the spin density matrix which, for a spin-1/2 baryon-antibaryon pair is given by

$$\rho_{B\bar{B}} = \sum_{\mu,\bar{\nu}=0}^{3} C_{\mu\nu}^{1/2} \sigma_\mu^B \otimes \sigma_\nu^{\bar{B}}, \tag{5.21}$$

where σ_μ^B are the spin-1/2 basis matrices for baryon B in its helicity frame

$$\sigma_0^B = \mathbb{1} \tag{5.22}$$

$$\sigma_1^B = \sigma_x = \begin{pmatrix} 0 & 1 \\ 1 & 0 \end{pmatrix} \tag{5.23}$$

$$\sigma_2^B = \sigma_y = \begin{pmatrix} 0 & -i \\ i & 0 \end{pmatrix} \tag{5.24}$$

$$\sigma_3^B = \sigma_z = \begin{pmatrix} 1 & 0 \\ 0 & -1 \end{pmatrix}. \tag{5.25}$$

The coefficient matrix $C_{\mu\nu}$ contains the polarization P and spin correlations C and is given by

$$\begin{aligned} C_{\mu\nu}^{1/2} &= 3\frac{1+\eta\cos^2\theta}{3+\eta}\begin{pmatrix} 1 & 0 & P_y & 0 \\ 0 & C_{xx} & 0 & C_{xz} \\ P_y & 0 & C_{yy} & 0 \\ 0 & C_{xz} & 0 & C_{zz} \end{pmatrix} \\ &= \frac{3}{3+\eta}\begin{pmatrix} 1+\eta\cos^2\theta & 0 & \beta_\psi \sin\theta\cos\theta & 0 \\ 0 & \sin^2\theta & 0 & \gamma_\psi\sin\theta\cos\theta \\ \beta_\psi\sin\theta\cos\theta & 0 & -\eta\sin^2\theta & 0 \\ 0 & \gamma_\psi\sin\theta\cos\theta & 0 & \eta+\cos^2\theta \end{pmatrix}, \end{aligned} \tag{5.26}$$

where $\beta_\psi = \sqrt{1-\eta^2}\sin(\Delta\Phi)$ and $\gamma_\psi = \sqrt{1-\eta^2}\cos(\Delta\Phi)$. The spin correlations are transformed to the decay products of the baryons via the 4×4 decay matrices $a_{\mu\nu}$

$$\sigma_\mu^B \to \sum_{\nu=0}^{3} a_{\mu,\nu}^D \sigma_\nu^b. \tag{5.27}$$

The full angular distribution is finally given by

$$\mathscr{W}(\xi,\omega) = \mathrm{Tr}\rho_{b\bar{b}} \propto \sum_{\mu,\nu=0}^{3} C_{\mu\nu} a_{\mu 0}^B a_{\nu 0}^{\bar{B}}. \tag{5.28}$$

For a spin 1/2 baryon like Λ the decay matrix is is given by

$$a_{\mu 0} = \begin{pmatrix} 1 \\ \alpha_\Lambda\cos\phi_b\sin\theta_b \\ \alpha_\Lambda\sin\theta_b\sin\phi_b \\ \alpha_\Lambda\cos\theta_b \end{pmatrix}, \tag{5.29}$$

where α_Λ is the decay parameter defined in Eq. 5.6. Finally, the differential cross section can be written as

$$\frac{d\sigma}{d\cos\theta d\Omega_1 d\Omega_2} = \frac{\mathscr{W}(\xi)}{\mathscr{N}}, \tag{5.30}$$

where the normalization factor $\mathscr{N}$ is given by

$$\mathscr{N} = \int \mathscr{W}(\xi) d(\cos\theta) d\Omega_1 d\Omega_2. \tag{5.31}$$

Let us now write out the full expression for the angular distribution in the process $e^+e^- \to \Lambda\bar{\Lambda}$. The function $\mathscr{W}$ can be expressed in terms of a set of seven functions $\mathscr{F}_k(\xi)$

$$\begin{aligned}
\mathscr{F}_0(\xi) &= 1 \\
\mathscr{F}_1(\xi) &= \sin^2\theta \sin\theta_1 \sin\theta_2 \cos\phi_1 \cos\phi_2 + cos^2\theta \cos\theta_1 \cos\theta_2 \\
\mathscr{F}_2(\xi) &= \sin\theta \cos\theta (\sin\theta_1 \cos\theta_2 \cos\phi_1 + \cos\theta_1 \sin\theta_2 \cos\phi_2) \\
\mathscr{F}_3(\xi) &= \sin\theta \cos\theta \sin\theta_1 \sin\phi_1 \\
\mathscr{F}_4(\xi) &= \sin\theta \cos\theta \sin\theta_2 \sin\phi_2 \\
\mathscr{F}_5(\xi) &= \cos^2\theta \\
\mathscr{F}_6(\xi) &= \cos\theta_1 \cos\theta_2 - \sin^2\theta \sin\theta_1 \sin\theta_2 \sin\phi_1 \sin\phi_2
\end{aligned} \tag{5.32}$$

as

$$\begin{aligned}
\mathscr{W}(\xi) = {} & \mathscr{F}_0(\xi) + \eta \mathscr{F}_5(\xi) \\
& - \alpha_\Lambda^2 \left(\mathscr{F}_1(\xi) + \sqrt{1-\eta^2} \cos(\Delta\Phi) \mathscr{F}_2(\xi) + \eta \mathscr{F}_6(\xi) \right) \\
& + \alpha_\Lambda \sqrt{1-\eta^2} \sin(\Delta\Phi) (\mathscr{F}_3(\xi) - \mathscr{F}_4(\xi))
\end{aligned} \tag{5.33}$$

Here, *CP*-conservation: $\alpha_\Lambda = -\alpha_{\bar{\Lambda}}$ is assumed. When only one of the hyperons is reconstructed, it is still possible to extract some information about η and $\Delta\Phi$. After integrating over the angles of the proton or antiproton, only three out of seven functions are non-zero,

$$\begin{aligned}
\mathscr{F}_0(\xi) &= 1 \\
\mathscr{F}_1(\xi) &= \sin\theta \cos\theta \sin\theta_1 \sin\phi_1 \\
\mathscr{F}_2(\xi) &= \cos^2\theta
\end{aligned} \tag{5.34}$$

$\mathscr{F}_1(\xi)$ can be further simplified by realizing that

$$\begin{aligned}
\sin\theta_1 \sin\phi_1 &= \frac{p_x}{|p| \cos\phi_1} \sin\phi_1 \\
&= \frac{p_x}{|p|} \tan\phi = \frac{p_x}{|p|} \frac{p_y}{p_x} = \frac{p_y}{|p|}.
\end{aligned} \tag{5.35}$$

Then one can define

$$\frac{p_y}{|p|} := \cos\theta_p, \tag{5.36}$$

where θ_p is the angle between the y-axis and the proton momentum. That is, only two angles are needed to describe the decay distribution. The set of functions that describe the single-hyperon case becomes

$$\begin{aligned}\mathscr{F}_0(\xi) &= 1 \\ \mathscr{F}_1(\xi) &= \sin\theta\cos\theta\cos\theta_p \\ \mathscr{F}_2(\xi) &= \cos^2\theta,\end{aligned} \tag{5.37}$$

and the decay distribution simplifies to

$$\begin{aligned}\mathscr{W}_{\Lambda/\bar{\Lambda}}(\xi) = \mathscr{F}_0(\xi) + \eta\mathscr{F}_2(\xi) \\ + \alpha_{\Lambda/\bar{\Lambda}}\sqrt{1-\eta^2}\sin(\Delta\Phi)\mathscr{F}_1(\xi).\end{aligned} \tag{5.38}$$

Note that the phase only appears as $\sin(\Delta\Phi)$. Therefore, when only Λ or $\bar{\Lambda}$ is reconstructed, the value of $\Delta\Phi$ will be ambiguous: either $\Delta\Phi$ or $180^\circ - \Delta\Phi$.

Alternatively, the angular distribution can be expressed in terms of the polarizations P and spin correlations C

$$\begin{aligned}\mathscr{W}(\xi) = \mathscr{I}(\theta)\Bigg(1 + \alpha_\Lambda\sum_\nu P_\nu(\theta)\cos\theta_\nu + \alpha_{\bar{\Lambda}}\sum_\mu P_\mu(\theta)\cos\bar{\theta}_\mu + \\ \alpha_\Lambda\alpha_{\bar{\Lambda}}\sum_{\bar{\mu}\nu} C_{\mu\nu}(\theta)\cos\bar{\theta}_\mu\cos\theta_\nu\Bigg),\end{aligned} \tag{5.39}$$

where the indices $\bar{\mu},\nu$ represent the coordinate axes x, y, and z defined in equation 5.20, and $\cos\theta_\nu$ and $\cos\bar{\theta}_\mu$ are the corresponding direction cosines of the proton and antiproton. The expression above can be rewritten in a more compact form as

$$\mathscr{W}(\xi) = \left(1 + \eta\cos^2\theta\right)\sum_{\mu\nu} C_{\mu\nu}(\theta)\hat{n}_\mu\hat{n}_\nu, \tag{5.40}$$

where $\mu = 0,x,y,z$, $\hat{n}_0 = 1, \hat{n}_x = \cos\bar{\theta}_x, \hat{n}_y = \cos\bar{\theta}_y, \hat{n}_z = \cos\bar{\theta}_z$, and $\nu = 0,x,y,z$, $\hat{n}_0 = 1, \hat{n}_x = \cos\theta_x, \hat{n}_y = \cos\theta_y, \hat{n}_z = \cos\theta_z$. From this expression, it is straightforward to define method-of-moments estimates of the spin correlations and polarizations.

5.4 State of the Art

Hyperon form factors are relatively unexplored compared to nucleon form factors, but a number of measurements of primarily the form factor ratio R have been performed in recent years. These measurements are done using two main experimental techniques. One is the initial-state radiation (ISR) technique

where the accelerator is run with high-intensity at a fixed center-of-mass energy, but where one makes use of the fact that in a portion of events, either (or both) of the beams radiates bremsstrahlung photons, effectively lowering the center-of-mass energy. In this way, one can achieve a continuous distribution of data over the desired energy range. However, the probability for emitting an ISR photon goes to zero as the energy of the photon becomes large, and this means that it is challenging to collect sufficiently large data samples. The ISR method is illustrated in Fig. 5.3.

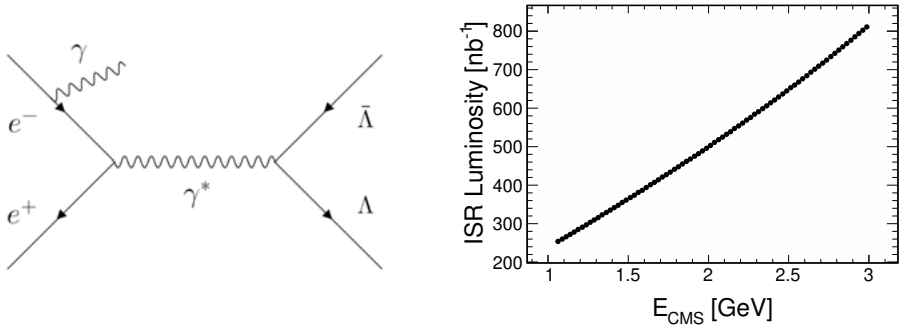

Figure 5.3. **Left:** Illustration of the ISR process. The electron radiates off a photon before the collision with the positron, lowering the energy available for the $\Lambda\bar{\Lambda}$-pair. **Right:** The luminosity of an ISR sample collected by the BaBar experiment as a function of the effective center-of-mass energy. The distribution of energies is approximately continuous, but the luminosity falls off as the energy carried off by the photon increases. Figure produced with data from Ref. [139].

The other method is the energy scan technique, illustrated in Fig. 5.4, where the center-of-mass energy of the accelerator is varied and data collected at discrete energy points. This method allows for a larger, controlled luminosity at the expense of only giving data in discrete bins.

The BaBar experiment has measured the cross section for $e^+e^- \to \Lambda\bar{\Lambda}$, as well as the effective form factor of Λ in the time-like region, covering a wide energy range from close to the production threshold up to 3.4 GeV using the initial state radiation technique [140]. Furthermore, the ratio of the electric to the magnetic form factor $R = G_E/G_M$ for Λ was measured in two mass ranges: from threshold to 2.4 GeV/c^2 and from 2.4 to 2.8 GeV/c^2 and the results were $R = 1.73^{+0.99}_{-0.57}$ and $R = 0.71^{+0.66}_{-0.71}$ respectively.

The CLEO-c experiment has studied the reaction $e^+e^- \to \Lambda\bar{\Lambda}$ at the $\psi(3770)$ and $\psi(4170)$ masses [141]. Based on pQCD predictions, it is argued that the contribution of resonant production is negligibly small, and that these data therefore probe the electromagnetic form factor. Because of the limited size of the data sample the measurement of the form factor ratio R only considered two limiting cases $R = 1$ and $R = 0$. Data were found to be consistent

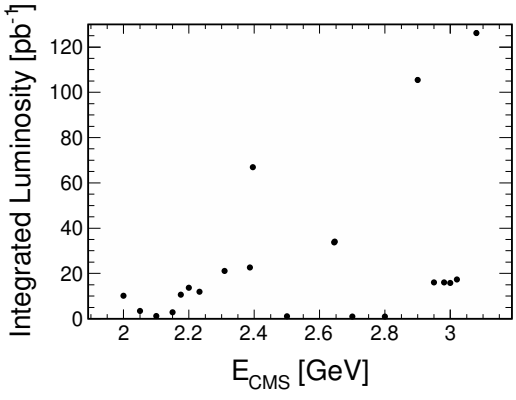

Figure 5.4. Luminosity as a function of the center-of-mass energy for an energy scan sample collected at the BESIII experiment. Data are collected in discrete bins, but the luminosity can be chosen freely according to the specific needs of the experiment.

with $R = 0$ and G_M was determined under that assumption. However, a recent measurement from the BESIII experiment [142] has found that the branching fraction for the decay $\psi(3770) \to \Lambda\bar{\Lambda}$ is at least an order of magnitude larger than was assumed in the CLEO-c analysis. This results calls the CLEO-c conclusions about the form factors of Λ into question.

Using energy scan data collected in 2011 and 2012, the BESIII experiment has measured the cross section of $e^+e^- \to \Lambda\bar{\Lambda}$ and the effective form factor of Λ at center-of-mass energy 2.2324, 2.4, 2.8, and 3.08 GeV [143]. In 2015, an additional set of high-luminosity scan data samples were collected in this region. The largest of these samples, at 2.396 GeV, was used to perform the first complete measurement of the Λ timelike electromagnetic form factors, including the relative phase, by exploiting the self-analyzing weak decay of Λ [144]. Several comparatively large data samples have not yet been used to study the reaction $e^+e^- \to \Lambda\bar{\Lambda}$. At higher energies, a recent analysis has measured a non-zero phase and form factor ratio at $\sqrt{s} = 3.773$ GeV/c^2 [145], calling for a reevaluation of the CLEO-c results.

BESIII has furthermore employed the spin correlation and polarization analysis used in this work to completely determine the form factors for the processes $e^+e^- \to J/\psi \to \Lambda\bar{\Lambda}$ [121], $\Sigma^+\bar{\Sigma}^-$ [146], $\Xi^-\bar{\Xi}^+$ [123] and $\psi(2S) \to \Sigma^+\bar{\Sigma}^-$ [146]. In particular, these were the first observations of hyperon polarization in these processes which, in turn, allowed for measurements of the decay parameters of both hyperons and antihyperons. Comparisons of the hyperon and antihyperon decay parameters give precise tests of *CP*-symmetry.

On the theory side, predictions for the ratio R and relative phase $\Delta\Phi$ of Λ have been made using meson exchange models [76] and dispersive approaches [130] that agree with the current experimental knowledge dominated

by results from BESIII. Further experimental input, especially on the q^2 dependence of the phase, will be of great importance for future developments. The current experimental status for the timelike form factors of Λ is shown in Fig. 5.5 together with the predictions from meson exchange models.

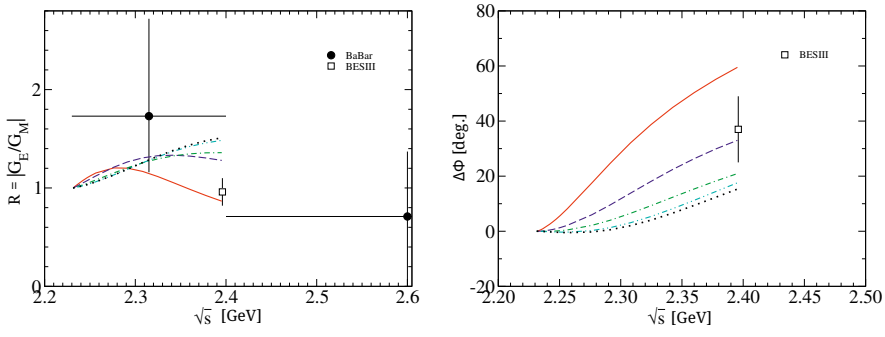

Figure 5.5. Currently published data and model predictions for the ratio $R = |G_E/G_M|$ (left) and the relative phase (right). Figure adapted from Ref. [76].

6. Scientific Questions for This Thesis

In this thesis, electromagnetic interactions of hadrons and in particular associated polarization observables are studied to reveal new insights about the matter-antimatter asymmetry in the universe and the internal structure of matter. Specifically, I seek to answer the following questions:

Are there beyond SM contributions to the decay $\eta' \to \pi^+\pi^- e^+ e^-$ that violate *CP*-symmetry? Can effective field theories for the strong interaction accurately predict the branching fraction of this decay?

What is the energy dependence of the timelike electromagnetic form factors of the Λ hyperon, and in particular, the relative phase $\Delta\Phi$ between electric and magnetic form factors? Do the values of $\Delta\Phi$ indicate that the form factors cross zero in the spacelike region? Can we learn something about the spacelike structure of hyperons by studying their timelike structure?

In connection with the hyperon studies, can the software for the planned upgrade of the BESIII detector reconstruct hyperon events with high precision and efficiency?

7. The BESIII Experiment

The Beijing Spectrometer (BESIII) collaboration comprises around 500 scientists from 72 institutions in 15 different countries across Europe, Asia, and the Americas. BESIII is a multi-purpose detector for hadron physics experiments located at the Beijing Electron-Positron Collider (BEPCII) in Beijing, China that has been running since 2008 and as the name implies is the third major upgrade since the original BES detector located at this site. BEPCII provides e^+e^--collisions at energies ranging from 2 GeV, close to the threshold for production of hyperon-antihyperon pairs, to 4.95 GeV covering the J/ψ and $\psi(2S)$ resonances as well as exotic XYZ-states. The energy range covered with BESIII at BEPCII is shown in Fig. 7.1. Table 7.1 lists the wide range of data sets collected at BESIII each year since the start of the experiment.

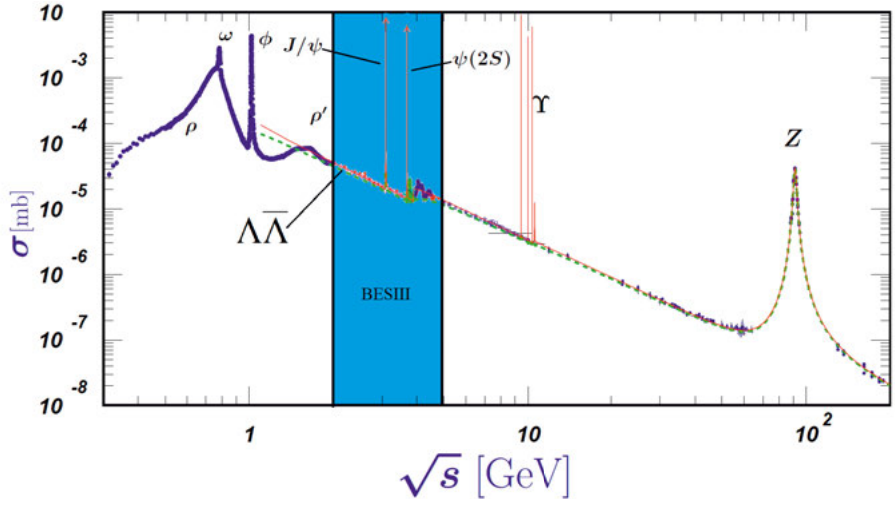

Figure 7.1. Hadronic cross section in e^+e^- annihilation. The region accessible with BESIII at BEPCII is highlighted in blue. Figure adapted from Ref [6].

7.1 The Beijing Electron-Positron Collider

The Beijing electron-positron collider (BEPCII) is a dual ring collider operating at beam energies from 1 up to 2.5 GeV. The e^+ and e^- beams always have

Table 7.1. *Data taken year by year with the BESIII detector since its inauguration in 2009.*

Year	Type of Data	E_{cms} (GeV)	Luminosity/ Number of Events
2009	J/ψ	3.097	0.225×10^9
2009	$\psi(2S)$	3.686	0.107×10^9
2010-2011	$\psi(3770)$	3.770	2.9 fb^{-1}
2011	$\psi(4040)$	4.009	0.5 fb^{-1}
2011	τ scan	~ 3.554	0.024 fb^{-1}
2012	J/ψ	3.0971	1.087×10^9
2012	$\psi(2S)$	3.686	0.341×10^9
2013	$Y(4260), Y(4360)$	4.23, 4.26, 4.36	2.9 fb^{-1}
2014	Scan	3.85-4.59	0.8 fb^{-1}
2015	Scan	2.0-3.08	0.5 fb^{-1}
2016	$D_s^{\pm} D_s^{*\mp}$	4.18	3.1 fb^{-1}
2017	Scan	4.19-4.28	3.8 fb^{-1}
2018	J/ψ	3.097	4.6×10^9
2018	$\psi(3686)$ scan	~ 3.686	0.5 fb^{-1}
2019	J/ψ	3.097	4.2×10^9
2019	Scan	4.13-4.44	3.8 fb^{-1}
2020	Scan	4.61-4.7	3.8 fb^{-1}
2021	$\psi(2S)$	3.686	2.5×10^9

the same energy. Its performance is optimized for running at 1.89 GeV, where it is designed to reach a luminosity of 1.0×10^{33} cm^{-2}s^{-1} [147]. For three months per year, the electron ring is used as a source of synchrotron radiation.

The beams begin their life at the thermionic triode electron gun [148] that generates a 10 A beam with a pulse length of 1 ns. Positrons are created by first accelerating electrons up to 240 MeV and letting them hit a 10 mm diameter, 8 mm thick tungsten target [149]. Positrons produced in the resulting interaction are collected with a solenoid magnetic field and accelerated further. This system produces positrons at a rate of 50 mA/min. A 202 m long linear accelerator accelerates the beams up to a maximum energy of 1.3 GeV, whereafter they are injected into the storage rings with a circumference of 237.5 m, one for electrons and one for positrons. Kicker magnets at the injection point ensure that the injected bunches are in phase with the stored beam. The rings each hold 93 bunches with a spacing of 8 ns, and the maximum current is 910 mA. Four RF cavities in the rings accelerate the stored beams up to the desired energy. A total of 357 magnets shape and steer the beams as they propagate along the rings [150]. The layout of the two storage rings is shown in Fig. 7.2.

The BESIII detector is located at one of two interaction points where the electron and positron beams cross at an angle of 2×11 mrad. Superconducting

Table 7.2. *Design parameters of the BEPCII beams at the BESIII interaction point [150].*

Parameter	Value
Bunch length (σ_z)	1.5 cm
Bunch width (σ_x)	$\sim 380\ \mu$m
Bunch height (σ_y)	$\sim 5.7\ \mu$m
Relative Energy spread	5×10^{-4}

insertion magnets just before the interaction point ensure that the beam keeps the desired shape despite the competing influence of the detector magnet. Key beam parameters at the interaction point are listed in Table 7.2 [150].

The lifetime of the beam in the storage rings is around 2.7 hours, but the accelerator is generally operated in so-called top-off mode, where the beam currents are always kept within certain upper and lower limits. This allows for keeping the average luminosity above 60% of the peak value at all times. This is not to be confused with the top-up mode [151] that was implemented in 2019. In the latter scheme, the beams are refilled every 90 seconds to ensure a current that is constant within 1.5%. This leads to an increase of the luminosity by 20 to 30% compared to the top-off mode.

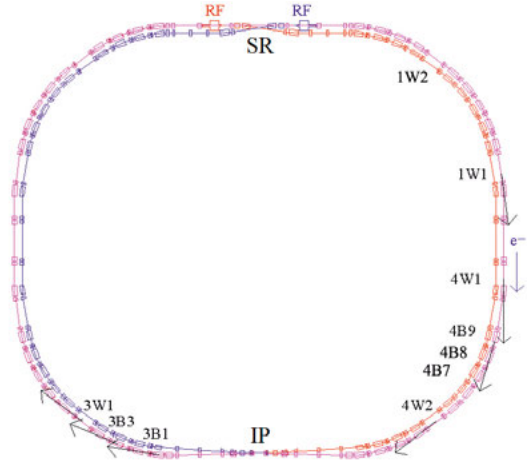

Figure 7.2. Layout of the BEPCII storage rings. "RF" stands for the superconducting radiofrequency cavities that accelerate the beams up to full energy and "SR" shows the point where synchrotron radiation is extracted. The BESIII detector is located at the interaction point labeled "IP". Figure adapted from Ref. [152].

7.2 Interaction Region

In order to minimize the amount of secondary interactions, the beam pipe in the interaction region, shown in Fig. 7.3, must be made as thin as possible. At the same time, the beam pipe needs to be a able to withstand the heating caused by interactions with the beam. Therefore, BESIII makes use of a jacketed pipe with inner (0.6 mm) and outer walls (0.8 mm) made of beryllium, which has low density and atomic number. The volume between them is filled a high purity mineral oil for cooling. The inner surface of the inner wall that faces the beam is coated with a 14.6 μm gold layer for absorption of synchrotron radiation photons and beam particles. In total, this design and choice of materials means that particles produced at the IP must pass through 1.04% of a radiation length to reach the detector [153].

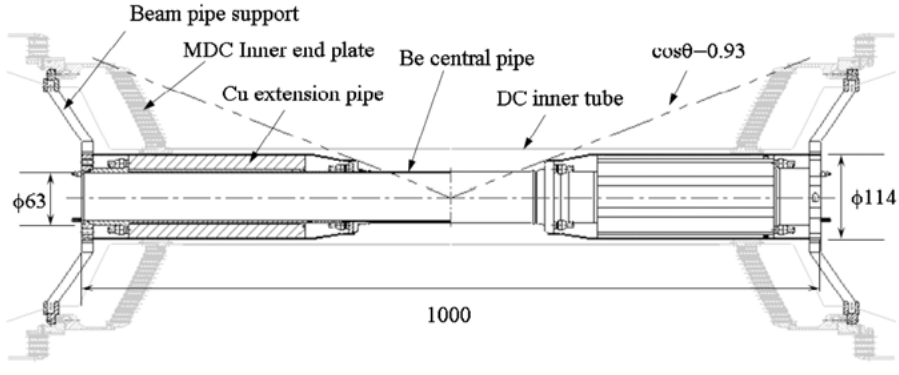

Figure 7.3. Cross-section view of the beam pipe in the interaction region. Figure from Ref. [153].

7.3 The BESIII Detector

The BESIII detector consists of several subdetectors that serve different purposes. From the beam pipe and outwards, these are (see Fig. 7.4): a multilayer drift chamber for tracking of charged particles, a time-of-flight system, an electromagnetic calorimeter for photon detection and energy measurement, and a muon detector. In the following sections, each of these components will be described in greater detail.

The following right-handed coordinate system is adopted by the BESIII experiment [155]:

- The positive x-axis points toward the center of the BEPCII storage rings.
- The positive y-axis points vertically upward.
- The positive z-axis points in the direction of the positron beam, and is parallel to the solenoid magnetic field.

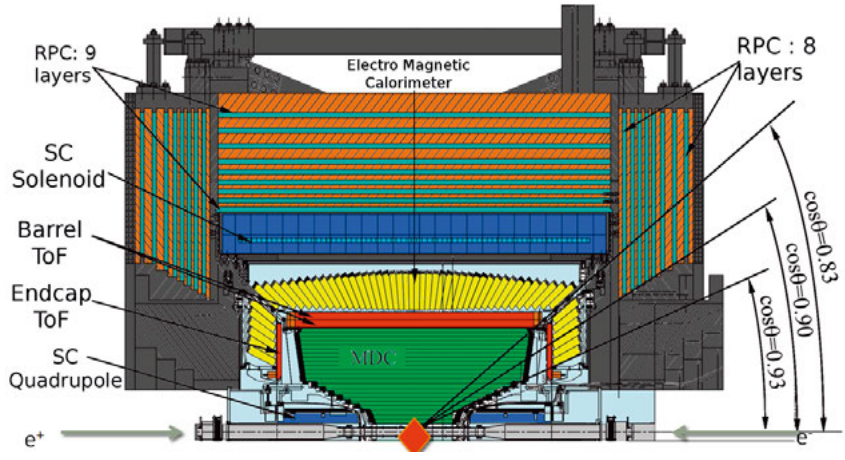

Figure 7.4. Cross-section view of the upper half of the BESIII detector. The detector is mirrored around the beam pipe [154].

7.3.1 Multilayer Drift Chamber

The multilayer drift chamber (MDC) is responsible for tracking charged particles to determine their momentum and position. In particular, we want to know the kinematics of particles at the point where they were produced, *i.e.* the production vertex. For this purpose, the MDC is used as the innermost subdetector.

The MDC covers 93% of the solid angle and consists of an inner and outer part. These share a common gas volume filled with a mixture of He and C_3H_8 in proportions 60/40%. The inner part is designed in such a way that it can be replaced to mitigate the effects of radiation damage as the detector ages. The inner radius is 60 mm and the outer radius is 800 mm. The longest extent in the beam direction is 2.4 m. Wires are stretched along the length of the chamber in a drift cell pattern, see Fig. 7.5, with high-voltage anode or sense wires surrounded by an almost square formation of eight cathode or field shaping wires that generate an electric field. There are a total of 6796 sense wires made of gold-plated tungsten organized in 43 circular layers. The field shaping wires are made of gold-plated aluminium. There are both axial layers, parallel to the beam axis, and stereo layers with a small tilt relative to the beam axis. Such stereo layers allow for a determination of the z-position in addition to the xy-position. The 8 layers of the inner part are all stereo layers, and have a smaller cell size of 12×12 mm^2 compared 16.2×16.2 mm^2 in the outer part. In the outer part there is a mix of in total 16 stereo and 19 axial layers. A set of four consecutive layers with the same stereo angle is referred to as a superlayer. A highly uniform magnetic field along the beam axis provided by a superconducting solenoid that surrounds the whole detector causes the

trajectories of charged particles to curve in the *xy*-plane [156]. A 3D-drawing of the MDC is shown in Fig. 7.5.

The operating principle of the detector is the following: As charged particles travel through the gas mixture they will ionize atoms along the way, resulting in pairs of electrons and positive ions. The electric field causes the electrons to drift toward the sense wires and generate an electric pulse. The velocity at which electrons travel toward the sense wire depends on the strength of the electric field and is thus well known. The time of arrival of these signals with respect to the time of the collision is given by the detector clock. By taking into account the time of flight of particles from the IP to the cell and the time for signal propagation in the wires, the time from ionization to signal, the drift time, can be determined. Since both time and velocity are known, the position at which ionization occurred can be determined. By subsequently measuring the curvature of charged particle trajectories one can determine the momentum since the magnetic field strength is precisely known. Furthermore, the pulse height of each hit gives a measure of the energy deposited in the interaction and can be used to identify particles. The charged particle track information collected by the MDC is also used for the hardware trigger and online software event filter and to extrapolate tracks to other subdetectors.

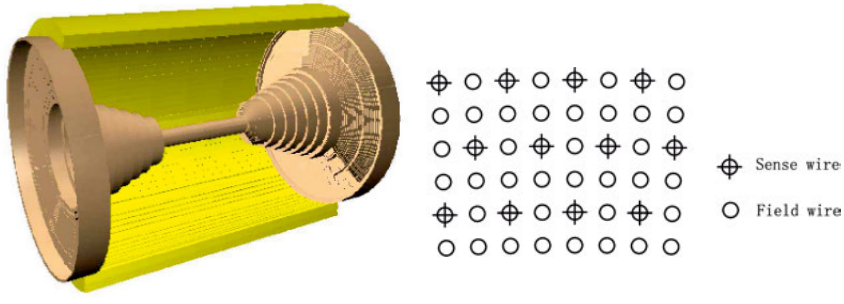

Figure 7.5. 3D drawing of the multilayer drift chamber (left). The beam pipe runs along the central axis and is attached to support structures at both endcaps. The wires are stretched between the endcaps parallel to or with a small stereo angle with respect to the beam pipe. Sense and field wires are organized in a structure of almost square drift cells (right). Figures from Refs. [156] and [157] respectively.

The single-wire spatial resolution is designed to be <120 μm in the *xy*-plane, and < 2 mm in *z*-direction. The transverse momentum resolution that can be achieved is 0.5% at 1 GeV/c, and the dE/dx resolution $< 6\%$, allowing for 3σ K/π separation up to 770 MeV/c.

7.3.2 Time of Flight System

The time-of-flight (TOF) detector, placed between the MDC and the EMC, provides a precise measurement of the time of arrival of charged particles. This can be used to determine the flight time from their origin. Comparing this value with the expected value for different particle species allows for particle identification. The TOF detector also provides fast signals for the trigger that can help to reject events from cosmic background radiation.

The TOF system is based on plastic scintillator counters connected to fine-mesh photomultiplier tubes that turn the scintillator light into electric signals. These are chosen for the high light yield that can be achieved with a relatively small detector and for yielding fast signals that can provide precise timing measurements. In the barrel there are two cylindrical layers, each consisting of 88 Saint-Gobain BC-408 scintillators that cover the solid angle $|\cos\theta| < 0.83$. These are connected to PMTs at the each end of the detector. The two endcap TOF systems cover the solid angle $0.85 < |\cos\theta| < 0.95$ and each consists of 48 Saint-Gobain BC-404 type fan-shaped crystals that are read out with PM tubes at the center of the detector. The precise time measurement from the TOF system can be combined with the momentum and the length of the trajectory measured by the MDC to estimate the mass in order to identify a given particle. The TOF setup employed at BESIII allows for a total time resolution of around 100 ps, and a separation efficiency for K/π of about 95% up to 900 MeV/c.

7.3.3 Electromagnetic Calorimeter

The role of the electromagnetic calorimeter (EMC) is to provide precise measurements of the energies of photons and electrons. It consists of in total 6272 CsI(Tl) scintillator crystals read out by silicon photodiodes. The crystals are organized into one barrel and two endcap sections, covering in total 93% of the solid angle. The barrel has an inner radius of 940 mm, a length of 2750 mm and covers the angular range $|\cos\theta| < 0.83$. It is made up of 44 rings that each contains 120 crystals. Except for the two most central rings, these are inclined so that they point toward $z = \pm 50$ mm. The endcaps have an inner radius of 50mm and cover the range $0.85 < |\cos\theta| < 0.93$. Each is made up of six layers with increasing numbers of crystals that are all pointing toward $z = \pm 100$ mm. A drawing of the EMC is shown in Fig. 7.6.

As a high-energy photon or electron hits the detector, it will generate a shower of secondary electrons and positrons that will spread out before they are eventually absorbed. The signature of such events are therefore clusters of crystal hits centered on the one that was first struck. The total energy of the incident particle can be deduced by combining the energy deposits of all hits belonging to a certain cluster.

The EMC can measure photon and electron energies ranging from 20 MeV up to 2 GeV with a resolution of $\sim 2.3\%/\sqrt{E(\mathrm{GeV})}$. The shower position resolution in the *xy*-plane is $\sigma_{xy} \leq 6$ mm $/\sqrt{E(\mathrm{GeV})}$.

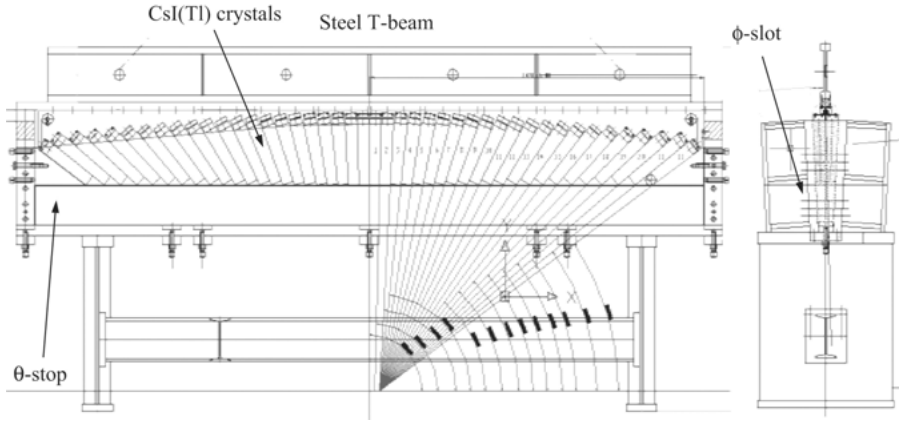

Figure 7.6. Schematic drawing of the electromagnetic calorimeter of BESIII [153].

7.3.4 Muon Chamber

Distinguishing muons and pions from each other is a challenging task due to the similarity of their masses. To achieve better separation, BESIII makes use of a special muon chamber (MUC) as its outermost sub-detector. This detector consists of resistive plate chambers filled with an argon/F134a/isobutane mixture (50/42/8%) that are inserted into the steel plates of the magnetic flux return yoke that surrounds the whole detector. Like the TOF and EMC systems, it is made up of a barrel and two endcap parts, and the total coverage corresponds to 89% of the solid angle. There are 8 detecting layers in the endcaps and 9 in the barrel, and each layer consists of two RPC layers and one pickup strip layer. Between these layers, the iron of the yoke acts as an absorber that slows the muons down and increases the chance of a detector interaction. A drawing of the MUC is shown in Fig. 7.7.

One expects that most hadrons and electrons are absorbed by the either the calorimeter or the iron yoke before reaching the MUC. Muons on the other hand are expected to penetrate through the iron because they are more massive than electrons and do not interact strongly. Any signal in the MUC is therefore most likely to have come from a muon. If they do manage to reach the first layers of the MUC, hadrons are unlikely to be able to penetrate any deeper. Therefore the penetration depth, *i.e.* the number of layers of the MUC that have a signal, can be used to distinguish between true and fake muon signals.

The MUC is effective for a minimum muon momentum of 0.4 GeV/*c* and can achieve muon identification efficiencies over 90% for momenta over 0.5

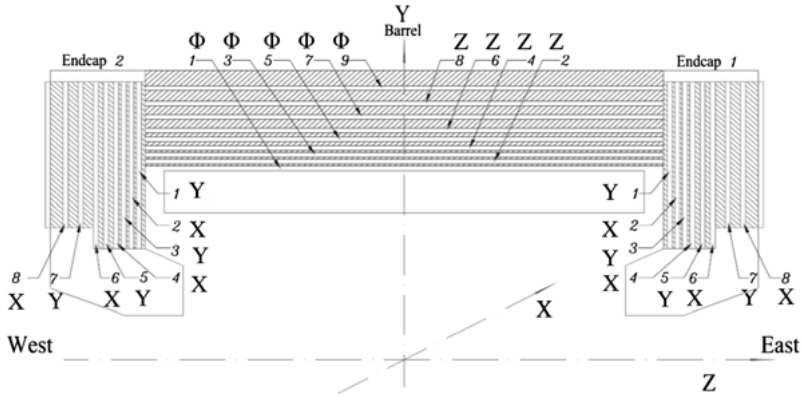

Figure 7.7. Schematic drawing of the muon chamber of BESIII [153].

GeV/c. The percentage of pions misidentified as muons is below 10% for the majority of the expected momentum and angular range. The resolution for the position measurement from one layer is 1.2 cm.

7.3.5 Superconducting Solenoid

A superconducting solenoid provides a highly uniform magnetic field for momentum measurements in the drift chamber. The field strength has been set to 1 T for all data taking periods except for the 2012 campaign at the J/ψ resonance when it was set to 0.9 T. The non-uniformity of the magnetic field is 13%. The magnetic field has been measured with a precision of < 1 mT and position resolution < 1 mm in the axial and radial direction and $< 0.1^\circ$ in φ. These measurements also include the magnetic field from the superconducting insertion quadrupoles.

7.3.6 Online Luminosity Monitoring

During data taking, the luminosity is monitored online using Bhabha scattering events, $e^+e^- \to e^+e^-\gamma$. Most photons from such events are emitted at small angles, < 1 mrad, relative to the beam axis. To detect them, two detectors are placed on either side of the interaction point in the otherwise empty space between the magnets immediately outside the BESIII vacuum chamber. These detectors consist of a tungsten target that converts the Bhabha photons into electrons and positrons. These subsequently travel trough a block of fused silica where they generate Cherenkov photons that are read out by two PMTs. The count rates in these detectors can be converted into a measurement of the luminosity in real time [153].

7.3.7 Trigger

The data acquisition system of BESIII is designed to handle event rates of up to 4 kHz. The rate of good physics events when running at the J/ψ resonance is expected to be 2 kHz, while the rate from cosmic background is expected to be 2 kHz and that from beam loss background is expected to be 40 MHz [153, 158]. The latter refers to particles that escape the magnetic field and collide with the detector instead of circulating along the rings. In order to achieve tolerable rates, BESIII makes use of a two-level trigger system that is able to reject the vast majority of background events while retaining close to 100% of the interesting events. The first level (L1) is a hardware trigger and the second level (unintuitively referred to as L3) is an online software event filter [159].

The bunch spacing of the beams of BEPCII is 8 ns, but the timing properties of the detectors and the time evolution of physics events mean that the hardware trigger must necessarily be considerably slower. Several factors contribute to this. Long-lived particles in interesting physics events do not decay immediately after production, and give a natural spread of 30 ns in the TOF measurement. In addition, the average drift time in the MDC is 400 ns. The slowest signal by far, and the main limiting factor for the trigger, is the calorimeter signal with a rise time of 1.5 μs and decay time 3 μs. To be able to include the energy deposit in the EMC in the L1 trigger, the trigger signal is therefore set to arrive with a fixed latency of 6.4 μs.

The final decision in the hardware trigger is based on a combination of information from the MDC, TOF, and EMC subdetector systems. The fastest signals come from the TOF system that reports the number of hits in the barrel and endcap and whether there are any back-to-back hits. For MDC hits, a fast track segment finding procedure is performed, and the number of tracks, as well as their length and position are reported to the trigger. The last system to provide information is the EMC, that generates signals based on the number of clusters as well as the position and energy deposit of each cluster. Finally, hits in all three detectors are matched with each other, and the number of matched tracks is used to make the L1 decision. The trigger selection criteria are optimized using MC simulations. A block diagram of the L1 trigger system is shown in Fig. 7.8.

Simulations show that the efficiency of the global hardware trigger reaches 99.8% for $J/\psi \rightarrow$ anything, 99.5% for $\psi' \rightarrow$ anything, and 99.9% for $\psi(3770) \rightarrow$ anything. After the L1 trigger, the background rates are reduced to about 1.85 kHz for lost beam particles and 200 Hz for cosmic rays. Trigger efficiencies well above 99% for all types of physics events at the J/ψ and ψ' resonances were experimentally confirmed in 2009 [160] and 2018 data [161].

The L1 trigger accept signal gives the green light for event building and processing by the software event filter. To meet the requirements of the DAQ system, the latency for this procedure must be less than 5 ms. The total energy deposited in the EMC and, depending on the energy, either a fast reconstruc-

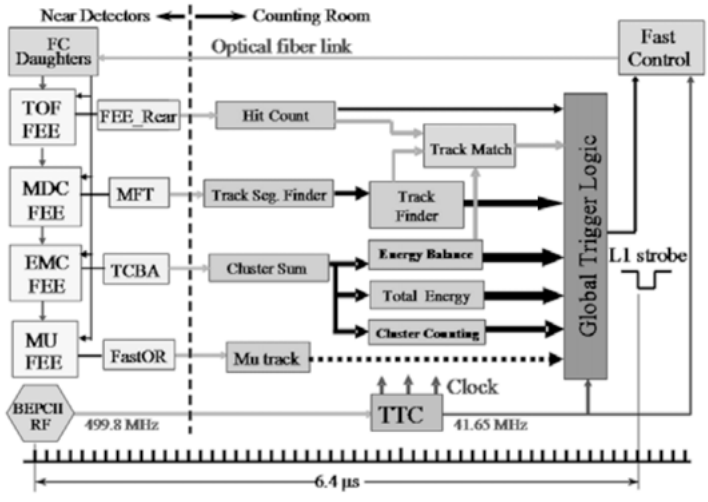

Figure 7.8. Block diagram of the trigger system. Figure from Ref. [153].

tion of MDC tracks or the EMC cluster position, along with the TOF and number of hits in the MUC is used to classify events into five physics categories: e^+e^-, $\mu^+\mu^-$, $\gamma\gamma$, $\tau^+\tau^-$ and hadron events while tuning selection criteria so that as many background events as possible are rejected. This procedure yields filtering efficiencies above 99% for all types of physics events while suppressing 70% of the cosmic ray background and 50% of the beam related background. In the background scenario described above, this puts the total event rate well within the acceptable limit of 4 kHz, and the average CPU time required for the filtering procedure is 1.5 ms. In addition, the selection criteria on the total energy deposit is straightforward to tune so that the event rate remains acceptable even in more extreme background scenarios.

Events that pass both the hardware trigger and online event filter are fed to the DAQ system where data from the different subdetectors are assembled into events. The average size for an event is 14 kB which means that data must be written to disk with a rate of 42 MB/s [153].

Event Start Time

The detector clock used for time measurements in all subdetectors and the entire trigger system is synchronized with the accelerator RF and operates at a frequency of 41.65 MHz. This corresponds to cycles of 24 ns between trigger signals. In that time, three beam bunches pass the IP so that there can be a delay of up to 16 ns between the start of the trigger cycle and the bunch collision that produces an event that should be recorded. The trigger start time is given by the L1 trigger signal. However, it is more important to know the time of the bunch collision, referred to as the event start time T_{EST} (see Fig. 7.9). Depending on the subdetector information available, the start time

is calculated with data from either the MDC or TOF as

$$T_{EST} = TDCM - T_{ev}, \tag{7.1}$$

where $TDCM$ is detector clock time associated with a hit signal, and T_{ev} is the time from the collision to the considered detector hit. A fast MDC track reconstruction and PID is performed to estimate the flight time to the position of the hit whereafter T_{ev} can be calculated by taking into account the signal processing latency for either MDC or TOF. A second, refined determination of T_{EST} is performed offline as part of the full event reconstruction. This algorithm achieves an error rate, defined as the fraction of events that are associated with the wrong beam bunch, of less than 1% [162].

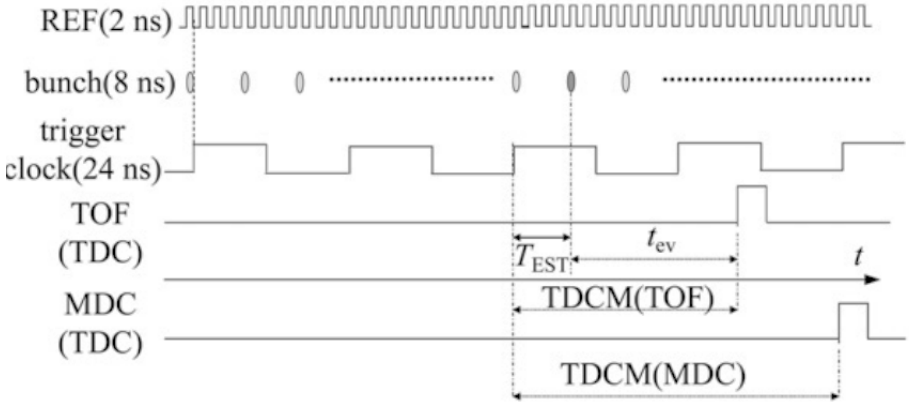

Figure 7.9. Definition of the event start time T_{EST} as the time from the trigger signal to the bunch collision that generated a good event. Figure from Ref. [162].

7.4 New Cylindrical GEM Inner Tracker

Years of running with high intensity beam related backgrounds have lead to aging problems for the inner part of the drift chamber with a gain decrease up to 29% for the first layers. This in turn leads to deteriorated performance both in terms of hit efficiency and spatial resolution. The gain of the first layer decreases by about 4% every year, and for the longevity of the experiment it is crucial to plan for and start preparing a replacement ahead of time.

To this end, the inner part of the drift chamber will be replaced by a new detector. This is an opportunity to improve the performance compared to the current design and therefore, the new detector will not be a drift chamber but a cylindrical gas electron-multiplier inner tracker (CGEM-IT). The main advantage of this new system is that it allows for better resolution in the position measurement, in particular in the z-direction. The new detector must fulfill the following criteria:

- Cover a polar angle range of $|\cos\theta| < 0.93$ and fit within the available volume from 59 to 183.5 mm in the radial direction.
- Achieve spatial resolution of better than 120 μm in the $r-\varphi$(xy)-plane and better than 1 mm in the z-direction. This is similar to the current MDC in the $r-\varphi$-plane, but a factor of two better in the z-direction.
- Have a material budget less than 1.5% of a radiation length X_0.
- Work for counting rates > 4 kHz/cm^2

The design for the new CGEM-IT builds on knowledge from the KLOE-2 experiment that built the only other existing cylindrical GEM tracker [163]. The core component of a gas electron multiplier detector is a thin ($\sim$ µm) polymer film coated on either side with a conducting metal, typically copper. This film is etched with a high density of holes in a regular pattern. An example of this structure is shown in Fig. 7.10. The film is placed in an inert gas and a voltage difference is applied between the outer metal layers. This creates a strong electric field in the holes, such that electrons knocked out of the gas by ionizing radiation will drift toward these and acquire sufficient energy to cause an avalanche of secondary electrons. The amplified current produced in this way can either be read out at the surface of the foil by an electrode, or transferred to a second foil for further amplification if needed [164, 165].

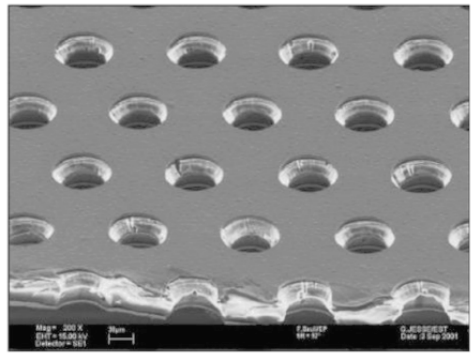

Figure 7.10. Electron microscope image of a GEM foil with the hole structure clearly visible. Figure from Ref. [165].

The BESIII CGEM-IT will consist of three GEM foils in a cylindrical geometry. The GEM foils consist of a 50 µm layer of Kapton coated in copper. The holes are biconical in shape with a diameter of 70 µm at the surface and 50 µm at the center (it has been shown that a hole size approximately equal to the foil thickness gives optimal amplification [165]). The voltage difference between the copper electrodes is 300-500 V, resulting in a field of about 100 kV/cm in the holes and a corresponding amplification factor of a few thousand. The entire detector will have an inner radius of 78 mm and an outer radius of 179 mm. The GEM layers are placed within 2 mm of each other, see Fig. 7.11, and the detector volume will be filled with a gas mixture consisting

of argon and isobutane in proportions 90% and 10% respectively [166]. The total material budget for the detector corresponds to about 1% of one radiation length [167].

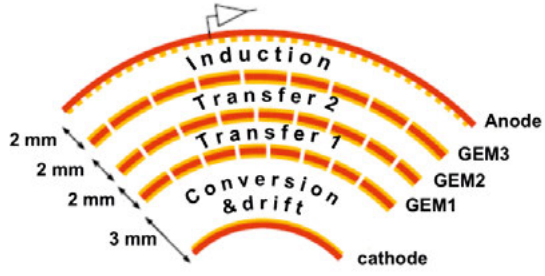

Figure 7.11. Schematic drawing of the three layer CGEM-IT for BESIII. Figure from Ref. [167].

The readout anode of each GEM foil consists of two sets of copper strips; one parallel to the detector axis providing the xy-position, and the other with a stereo angle w.r.t the first, giving the z-position. Larger stereo angles are possible in the GEM detector compared to the drift chamber, where it is limited to be within a few degrees so as not to distort the electric field. As a consequence, the z-position resolution of the CGEM-IT is expected to be more than two times better compared to the current inner tracker. The overall spatial resolution of the CGEM-IT is expected to be $<$100 μm [167].

8. Software

All offline analysis for the BESIII experiment is carried out within the framework of the BESIII Offline Software System (BOSS) [168]. It is based on the Gaudi architecture [169] developed for the LHCb experiment, and includes functionality from many external libraries like ROOT [170], CLHEP [171], and CERNLIB [172]. The main tasks performed by BOSS are event generation, simulations of the detector geometry, particle transport, digitization of simulated detector signals, and finally event selection and parameter estimation.

Prior to version 6.6.5 the BOSS framework runs in Scientific Linux SLC5. Later versions have been updated to run in versions up to and including SLC7. The work presented in this thesis has been performed in BOSS versions 6.6.4p01 and 6.6.5p01.

8.1 Event Generation

Many different MC generators are available within BOSS to serve the diverse physics goals of the BESIII experiment. The KKMC [173] generator is used to model the production of J/ψ in e^+e^--annihilation, taking into account the beam energy spread and initial state radiation. Final state radiation is handled by the PHOTOS [174] generator.

Most decays are modeled with a customized implementation of EvtGen [175, 176] that includes a wide range of models, and also provides an interface for user-defined models. Radiative decays of J/ψ into hadrons are modeled with the helicity amplitude model (HELAMP) within EvtGen that generates angular distributions based on the spin of the decay daughters [177]. In addition, EvtGen comprises a phase space model, PHSP, that allows for the generation of any decay with flat angular distributions. Finally, specific models for the processes $\eta' \to \pi^+\pi^-\gamma$ and $\eta' \to \pi^+\pi^- e^+e^-$ based on observed [102] and VMD amplitudes [92] are included.

Hadronic channels produced in the continuum well below the J/ψ resonance are modeled with the Continuum Exclusive Generator (ConExc) [178], that includes angular distributions as well as ISR and vacuum polarization. The probability for emission of an ISR photon is calculated using the structure function method of Ref. [179]. Furthermore, ConExc, uses experimentally measured cross sections as input to estimate the ISR correction factor for the reconstruction efficiency. In this work, the ConExc generator is used to model the reaction $e^+e^- \to \Lambda\bar{\Lambda}$.

For qualitative studies of background contributions in a given analysis of data taken at the J/ψ resonance, so-called *inclusive* samples are used. These include all known decay modes with branching fractions set according to the PDG [6] as well as unknown decays of charmonia generated with `LUNDCHARM` [180]. At energies below 3 GeV, similar samples based on measured hadronic cross sections are used, but since there is much less data available in this energy range they are less finely tuned. The event generation step outputs the positions and kinematics of the generated particles to be further processed in the detector simulation.

8.2 Detector Simulation

Particle transport and simulations of how particles interact with the detector material are performed with the BESIII Object Oriented Simulation Tool (BOOST) [181] based on GEANT4 [182] with the detector geometry implemented [183] in Geometry Description Markup Language (GDML) [184]. This step simulates the motion of particles in the magnetic field, their energy loss and scattering as they hit the detector as well as reactions that result in secondary particles. The `QGSP_BERT_HP` physics list for which processes to simulate and how to model them is used as it has been found to describe data best [185]. Of all the different interactions with the detector material, the production of e^+e^- pairs in the trough the conversion of a real photon is of particular importance for this work. In GEANT, this is implemented via the Bethe-Heitler cross section [186]. For photon energies $E_\gamma > 50$ MeV, it can be expressed as

$$\frac{d\sigma_{pairprod.}}{dE_e} = \frac{4r_e^2\alpha Z^2}{E_\gamma^3} \times \left(E_+^2 + E_-^2 + \frac{2}{3}E_+E_-\right)\left[\ln\left(\frac{2E_+E_-}{E_\gamma}\right) - \frac{1}{2}\right], \quad (8.1)$$

where $E_+(E_-)$ is the positron (electron) energy, r_e is the electron radius, α is the fine structure constant, and Z is the atomic number of the nucleus where pair production occurs.

The detector simulation step generates a set of true MC hits and energy deposits with perfect resolution in the subdetectors that are subsequently converted into realistic detector signals by the digitization algorithm. The digitized hits are subjected to a trigger simulation and if they pass are saved as recorded events. At this stage the data is saved in *raw data* format that contains all available information on each event, including hits in all subdetectors. A schematic view of how data flows in the detector simulations is shown in Fig. 8.1.

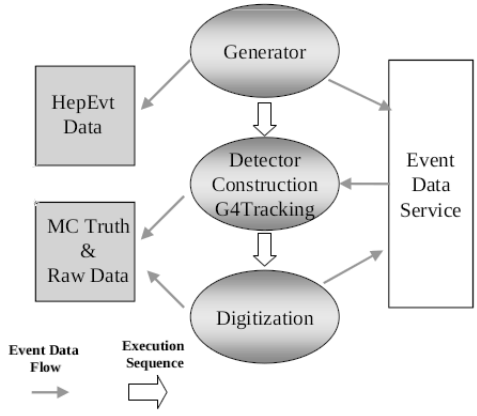

Figure 8.1. Data flow in the BESIII simulation software. Figure from [168].

8.3 Reconstruction

Full reconstruction is performed offline, taking into account the run conditions and calibration constants collected run-by-run from a central database. Reconstructed data can be saved in two different ways based on `ROOT` trees. The most frequently used one is *Data-Summary-Tape* that contains reconstructed particles, but not raw hits in order to save disk space. The other format, *reconstructed data*, is an accumulation of all available information, including raw hits.

8.3.1 MDC Tracking

As a charged particle moves in a uniform magnetic field it traces a helix. The coordinates of points along the helix are given by

$$\begin{aligned} x &= x_0 + d_p \cos\phi_0 + \frac{\alpha}{\kappa}\left(\cos\phi_0 - \cos(\phi_0+\phi)\right) \\ y &= y_0 + d_p \sin\phi_0 + \frac{\alpha}{\kappa}\left(\sin\phi_0 - \sin(\phi_0+\phi)\right) \\ z &= z_0 + d_z \cos\phi_0 + \frac{\alpha}{\kappa}\tan\lambda\cdot\phi\,, \end{aligned} \tag{8.2}$$

where d_p is the signed distance from the helix to the reference point in the xy-direction, ϕ_0 is the azimuthal angle of the pivot w.r.t the helix center, $\kappa = 1/P_t$ with sign according to the charge of the particle, d_z is the signed distance from the reference point in the z-direction, and λ the dip angle/slope of the track. The default choice of reference point is the origin. It is the task of the tracking algorithm to identify tracks and determine these parameters based on the hits collected by the MDC.

The track finding algorithm consists of several parts that are suited to finding tracks in different momentum ranges. These are performed in sequence, so

that hits that could not be matched to a track track in one step are studied again in the next. When a track is found, its constituent hits are not considered in the subsequent steps. The first step of the track finding procedure is the pattern recognition algorithm [187] that looks for track segments in every superlayer of the MDC by comparing the wire hit patterns to eight four-hit templates and twenty three-hit templates. Track segments that match one of the patterns are kept for further analysis.

The next step is the track segment finder (TSF) [188] that looks for tracks in all superlayers of the MDC where three out of four constituent layers received a hit. Hit positions (x,y) in the transverse plane are transformed into coordinates (X,Y) by a conformal map such that tracks that intersect the IP are transformed into lines, while drift circles are transformed into circles tangential to this line. Hits that do not belong to the track will in general not give circles tangent to the line. A set of lines are fitted to the two outermost drift circles, whereafter the inner circles are added to discriminate between them. Any lines that are tangential to the inner circles are valid candidates. Track segments found in this way are matched to those in other superlayers through their position and direction. Finally, the hits in the stereo layers are added and the least squares method is used to fit a helix of the track.

A recent addition to the BESIII track finding algorithm is the Hough Transform method, that aims to improve performance for low momentum tracks that were previously lost by the pattern recognition or TSF algorithms [189]. The conformal transformation described above is followed by the Hough transform

$$\rho = X\cos\alpha + Y\sin\alpha, \tag{8.3}$$

where (X,Y) are the coordinates of a hit in the conformal plane, $\alpha \in [0,\pi]$, and $\rho \in [-0.1,0.1]$ (cm^{-1}). Each point in the conformal plane is transformed into a sinusoid in the $\alpha-\rho$ parameter space. This is done for all hits belonging to a certain track candidate. If they do indeed belong to the same track, they will intersect at one point. The coordinates of this point give the parameters that describe a line through all hits. In practice, this is done by filling a two-dimensional histogram with the curves corresponding to all hits and finding the bin (parameter combination) with the highest concentration of curves.

Once a track has been found using any of the aforementioned methods, the helix parameters are updated using a Kalman filter algorithm where multiple scattering, energy loss, non-uniformity of the magnetic field and wire sag effects are taken into account as additional terms in the covariance matrix [190]. For physics analysis, the tracking algorithm returns the momentum of tracks at the point of closest approach to the pivot point by default. However, the user can specify a new reference point in order to extract the momentum at a different point along the helix.

8.3.2 EMC Shower Reconstruction

The energy deposit in each crystal of the EMC can be derived from the pulse height and the relevant calibration constants. Hits are subsequently formed into clusters around the crystals with the largest energy deposit, known as the seed. If the seed is unique, one shower corresponding to one single particle is formed. If there are more than one, the cluster is split and several particles are generated. The energy of the shower is determined by summing the energy deposits of the crystals in the cluster and the position is calculated as the mean of the position of all crystals in the cluster weighted according to their individual energy deposits.

8.3.3 TOF

Each hit in the TOF system is first matched with an MDC track. This track provides a measure of the particle momentum and velocity. Having determined the event start time using the procedure described in Section 7.3.7, the time of flight can be determined by taking into account the speed of light in the scintillators, and the latency of the readout electronics. In addition to the time measurement, the pulse height gives a measurement of the energy deposit that can be added to the EMC measurement for improved resolution.

8.3.4 Muon Track Finder

The MUC reconstruction begins by collecting hits into track candidates that are subsequently compared to the tracks reconstructed by the MDC. A second search, that immediately tries to match MUC hits to extrapolated MDC tracks is performed to find low momentum tracks that did not lead to enough hits [191]. For example, the penetration depth, the goodness-of-fit of the track, and how well it matches its corresponding MDC track can be used for particle identification.

8.4 Analysis

8.4.1 Particle Identification

All subdetectors provide some information that can be used for particle identification. Generally, the time-of-flight and dE/dx are sufficient for separating different species of hadrons [192]. It is also possible to include the energy deposit and shower shape in the EMC, as well as detailed information from the MUC. This includes *e.g.* the penetration depth or the degree of match between an MDC and an MUC track. In this work, PID based on TOF and dE/dx has been used.

The probability that the measured time of flight was caused by a particle of species p is given by

$$\mathscr{P}(t;p) = \frac{1}{\sqrt{2\pi}\sigma_t}\exp\left[-\frac{1}{2}\left(\frac{t-t_p}{\sigma_t}\right)^2\right], \tag{8.4}$$

where $\sigma_t \sim 80$ ps. Equivalently for the energy deposit dE/dx

$$\mathscr{P}(\mathrm{dE/dx};p) = \frac{1}{\sqrt{2\pi}\sigma_E}\exp\left[-\frac{1}{2}\left(\frac{\mathrm{dE/dx}-(\mathrm{dE/dx})_p}{\sigma_E}\right)^2\right], \tag{8.5}$$

where $\sigma_E \sim 6.5\%$. Each of these probabilities is converted to a χ^2-value and these can in turn be summed to yield a new combined $\chi^2 = \sum_{i=1}^{n}\chi_i^2$. This value gives a combined probability $\mathscr{P}(\chi^2|n)$ that the particle is of species p.

8.4.2 Vertex Fit

A vertex fit, that constrains a set of particles to originate from a common vertex, is a powerful tool both for improving the momentum resolution and for rejecting background events with different topologies. The motion of particles in the magnetic field is well known and gives constraint equations

$$\begin{aligned}
\vec{p} &= -(\vec{p}_0\times\hat{h})\times\hat{h}\cos\rho s - \vec{p}_0\times\hat{h}\sin\rho s + (\vec{p}_0\cdot\hat{h})\hat{h}) \\
\vec{x} &= \vec{x}_0 - \frac{(\vec{p}_p\times\hat{h})\times\hat{h}}{a}\sin\rho s - \frac{\vec{p}_0\times\hat{h}}{a}(1-\cos\rho s) + \frac{(\vec{p}_0\cdot\hat{h})s}{p}\hat{h} \\
\vec{p} &= \vec{p}_0 - a(\vec{x}-\vec{x}_0)\times\hat{h}
\end{aligned} \tag{8.6}$$

where $\vec{p}_0, \vec{x}_0$ are the momentum at and the position of the vertex, $\vec{p}, \vec{x}$ are the momentum and position at any given point along the track, a is the magnetic field strength (constant), $\hat{h}$ is a unit vector along the magnetic field, s is the arc length along the track from $\vec{x}_0$ to $\vec{x}$, and $\rho = a/s$. A common vertex can then be found by requiring that $\vec{x}_0$ is the same for two or more tracks. The vertex fit algorithm in BOSS implements these constraints using the Lagrange multiplier method [193] and outputs the vertex position as well as updated four-momenta for the particles.

In the analysis of long-lived particles that travel a measurable distance before decaying, a vertex fit to the final state particles yields the decay vertex, but it is also useful to know where the decaying particle was produced. This is achieved by a secondary vertex fit where the long-lived particle reconstructed in the primary vertex fit is constrained to originate from the interaction region measured during data taking. If the long-lived particle is charged, its motion in the magnetic field is subjected to the same constraints as above. If it is neutral, its motion is simply given by a straight line. The main result of the secondary vertex fit is an estimate of the decay length.

8.4.3 Kinematic Fit

e^+e^--collisions provide a clean and well-known initial state that allows for powerful kinematic constraints on the reconstructed particles. Similar to the vertices, the BESIII software implements fitting under kinematic constraints using Lagrange multipliers. In this work, the four-momenta of the relevant particles are constrained to the four-momentum of the initial e^+e^--system. If all final state particles are produced at the interaction point, they can safely be used as input to the kinematic fit. If not, *e.g.* if they are produced in the decay of a long-lived particle, it is more suitable to use the reconstructed momentum of the decaying particle(s) as input. The constraint equations are given by

$$\begin{aligned} p_x - p_{cx} &= 0 \\ p_y - p_{cy} &= 0 \\ p_z - p_{cz} &= 0 \\ E - E_c &= 0 \end{aligned} \tag{8.7}$$

where p_c and E_c are the constraint momenta and energy respectively. The fit takes as input the four-vectors of all involved particles. Missing particles with known masses can be included as *missing tracks*. The latter option allows for testing how well partially reconstructed events fit a hypothesized topology and can help reject background events.

Part II:
Analysis of the Rare Decay $\eta' \to \pi^+\pi^- e^+ e^-$

9. Analysis Strategy

This chapter describes a study of the decay $\eta' \to \pi^+\pi^- e^+ e^-$ based on a data sample of 1.3 billion J/ψ events collected by the BESIII detector: 224 million collected in 2009 and 1.09 billion collected in 2012. The purpose of the measurement is to determine the branching fraction and measure the asymmetry in the $\sin 2\varphi$ distribution where φ is the angle between the decay planes of the e^+e^-- and $\pi^+\pi^-$-pairs. In the following, I will discuss the strategy for the measurement of these two quantities.

9.1 *CP*-Asymmetry

If the *CP*-violating contribution to the decay $\eta' \to \pi^+\pi^- e^+ e^-$ discussed in Section 4.2 exists, the interference term in the decay rate depends on $\sin 2\varphi$, where φ is the angle between the decay planes shown in Fig. 4.2. Since $\sin 2\varphi$ is an odd function, the differential decay rate becomes asymmetric. The size of the asymmetry, which can be expressed as

$$\begin{aligned} \mathscr{A}_{CP} &= < \mathrm{sgn}(\sin 2\varphi) > \\ &= \frac{1}{\Gamma}\int_0^{2\pi} \frac{d\Gamma}{d\varphi}\,\mathrm{sgn}(\sin 2\varphi)\,d\varphi, \end{aligned} \tag{9.1}$$

gives a measure of the size of the interference term. Experimentally, the quantity $\sin 2\varphi$ can be calculated using the final state particle momenta following a procedure described in Ref. [110]. The orientation of the decay planes is given by the unit normal vectors

$$\hat{n}_e = \frac{\mathbf{p}_{e^+} \times \mathbf{p}_{e^-}}{|\mathbf{p}_{e^+} \times \mathbf{p}_{e^-}|} \text{ and } \hat{n}_\pi = \frac{\mathbf{p}_{\pi^+} \times \mathbf{p}_{\pi^-}}{|\mathbf{p}_{\pi^+} \times \mathbf{p}_{\pi^-}|}\,, \tag{9.2}$$

where $\mathbf{p}_{\pi^\pm}$ and $\mathbf{p}_{e^\pm}$ are the three-momenta of the pions and electrons in the η' rest frame, respectively. In this frame, both normal vectors are perpendicular to the $\hat{z}$-axis, defined as the momentum direction of the virtual photon (see Fig. 4.2)

$$\hat{z} = \frac{\mathbf{p}_{e^+} + \mathbf{p}_{e^-}}{|\mathbf{p}_{e^+} + \mathbf{p}_{e^-}|}. \tag{9.3}$$

It follows from the properties of the dot and cross products that

$$\hat{n}_e \cdot \hat{n}_\pi = \cos\varphi \text{ and } \hat{n}_e \times \hat{n}_\pi = \sin\varphi \cdot \hat{z}\,, \tag{9.4}$$

where φ is the angle between the normal vectors, or equivalently the angle between the decay planes. Then $\sin\varphi$ is given by

$$\sin\varphi = (\hat{n}_e \times \hat{n}_\pi) \cdot \hat{z} \tag{9.5}$$

and the final expression for $\sin 2\varphi$ is

$$\sin 2\varphi = 2\sin\varphi\cos\varphi = 2\left[(\hat{n}_e \times \hat{n}_\pi) \cdot \hat{z}\right](\hat{n}_e \cdot \hat{n}_\pi)\ . \tag{9.6}$$

The asymmetry can then be calculated by counting the number of events with $\sin 2\varphi > 0$ and $\sin 2\varphi < 0$ as

$$\mathscr{A}_\varphi = \frac{N_+ - N_-}{N_+ + N_-}. \tag{9.7}$$

Here N_+ and N_- are the true numbers of events with $\sin 2\varphi > 0$ and $\sin 2\varphi < 0$, respectively. These quantities differ from what is measured in experiment in two ways. Firstly, the limited efficiency of the event selection procedure means that only a fraction of the true events are reconstructed. This effect is only important if the efficiency is different in the two regions. In the following, it is assumed to be identical with value ε in both regions. It will be shown that if this is true, it does not affect the value of the determined asymmetry. The second more important effect is that a limited momentum resolution may cause an event with $\sin 2\varphi < 0$ to be reconstructed as $\sin 2\varphi > 0$ and vice versa. This will affect the value of the asymmetry and must be corrected for. Let us now derive a formula for an unbiased estimate of the asymmetry, corrected for the migration. We define the number of reconstructed events N_{R+} and N_{R-} with $\sin 2\varphi_R > 0$ and $\sin 2\varphi_R < 0$, respectively, where φ_R is the reconstructed angle. Furthermore, α_1 represents the fraction of events that migrated from $\sin 2\varphi > 0$ to $\sin 2\varphi_R < 0$ while α_2 represents the fraction that migrated from $\sin 2\varphi < 0$ to $\sin 2\varphi_R > 0$. The number of reconstructed events can be expressed in terms of the number of true events as

$$\begin{aligned} N_{R+} &= \varepsilon(1-\alpha_1)N_+ + \varepsilon\alpha_2 N_- \\ N_{R-} &= \varepsilon\alpha_1 N_+ + \varepsilon(1-\alpha_2)N_-. \end{aligned} \tag{9.8}$$

An estimate of the asymmetry based on the numbers of reconstructed events is given by

$$\mathscr{A}_{\varphi,R} = \frac{N_{R+} - N_{R-}}{N_{R+} + N_{R-}}. \tag{9.9}$$

Inserting Eq. 9.8 into Eq. 9.9 yields

$$\mathscr{A}_{\varphi,R} = \frac{\varepsilon\left((1-2\alpha_1)N_+ - (1-2\alpha_2)N_-\right)}{\varepsilon\left(N_+ + N_-\right)}, \tag{9.10}$$

where the efficiency ε cancels out. Then an expression for $\mathscr{A}_\varphi$ can be derived

$$\mathscr{A}_\varphi = \frac{\alpha_1 - \alpha_2}{1 - \alpha_1 - \alpha_2} + \frac{\mathscr{A}_{\varphi,R}}{1 - \alpha_1 - \alpha_2} + \mathscr{O}(\mathscr{A}_{\varphi,R}^2), \tag{9.11}$$

where the higher order terms have been neglected. If $\alpha_1 = \alpha_2 =: \alpha$, the expression above simplifies to

$$\mathscr{A}_\varphi = \frac{\mathscr{A}_{\varphi,R}}{1 - 2\alpha} = \frac{1}{1 - 2\alpha} \frac{N_{R+} - N_{R-}}{N_{R+} + N_{R-}}. \tag{9.12}$$

The correction factor also affects the uncertainty, so that

$$\sigma_{\mathscr{A}_\varphi} = \frac{d\mathscr{A}_\varphi}{d\mathscr{A}_{\varphi,R}} \sigma_{\mathscr{A}_{\varphi,R}} = \frac{1}{1 - 2\alpha} \sigma_{\mathscr{A}_{\varphi,R}}, \tag{9.13}$$

where the uncertainty $\sigma_{\mathscr{A}_{\varphi,R}}$ is given by the error propagation procedure

$$\begin{aligned} \sigma_{\mathscr{A}_{\varphi,R}} &= \sqrt{\left(\frac{\partial \mathscr{A}_{\varphi,R}}{\partial N_{R+}}\right)^2 \sigma_{N_{R+}}^2 + \left(\frac{\partial \mathscr{A}_{\varphi,R}}{\partial N_{R-}}\right)^2 \sigma_{N_{R-}}^2} \\ &= \sqrt{\left(\frac{1}{N_{R+} + N_{R-}}\right)^2 \sigma_{N_{R+}}^2 + \left(\frac{-1}{N_{R+} + N_{R-}}\right)^2 \sigma_{N_{R-}}^2} \\ &= \frac{\sqrt{\sigma_{N_{R+}}^2 + \sigma_{N_{R-}}^2}}{(N_{R+} + N_{R-})}. \end{aligned} \tag{9.14}$$

Because N_{R+} and N_{R-} are the efficiency uncorrected numbers of events, their uncertainties are simply $\sqrt{N_{R+}}$ and $\sqrt{N_{R-}}$. The expression above simplifies to

$$\begin{aligned} \sigma_{\mathscr{A}_{\varphi,R}} &= \frac{\sqrt{N_{R+} + N_{R-}}}{(N_{R+} + N_{R-})} \\ &= \frac{1}{\sqrt{N_{R+} + N_{R-}}} = \frac{1}{\sqrt{N_R}}, \end{aligned} \tag{9.15}$$

where N_R is the total number of reconstructed events. The final expression for the uncertainty of the corrected asymmetry, $\sigma_{\mathscr{A}_\varphi}$, is then

$$\sigma_{\mathscr{A}_\varphi} = \frac{1}{(1 - 2\alpha)\sqrt{N_R}}. \tag{9.16}$$

9.2 Monte Carlo Simulations

The Monte Carlo simulations of the processes studied and the signals they give in the detector are an important part of the analysis. They are used both

to investigate which background processes can be misidentified as the signal reaction and to develop selection criteria that can reject them to yield a clean sample. In addition, the simulations are used to determine the selection efficiency needed to extract the branching fraction and to validate the procedure for estimating the asymmetry in the $\sin 2\varphi$ distribution. The following MC samples are used in this work:

- $\boldsymbol{\eta' \to \pi^+\pi^- e^+ e^-}$: 2×10^6 events modeled with a generator [194] developed at BESIII based on VMD amplitudes from Ref. [92]. This sample will be referred to as the *signal MC* sample throughout this work.
- $\boldsymbol{\eta' \to \pi^+\pi^-\gamma}$: 20×10^6 events modeled with a generator based on experimentally measured decay distributions including ρ^0-ω interference and a box anomaly contribution [102].
- $\boldsymbol{J/\psi \to X}$: 1.3×10^9 events. This sample, hereafter referred to as the inclusive MC sample, includes all known decays of J/ψ with branching fractions set to the world averages from Ref. [6]. This sample is only intended to be used for qualitative investigations of background contributions to the analysis. Therefore the decays are generated using a phase space model with flat angular distributions. The remaining unknown decay modes are generated with `lundcharm` [180].

Both the exclusive models are implemented in `BesEvtGen` [175, 176]. In all samples, the production of J/ψ is modeled with the `KKMC` generator [173], and the decay $J/\psi \to \gamma\eta'$ is generated using the helicity amplitude method of `BesEvtGen` [177]. Final state radiation is implemented via the `PHOTOS` generator [174].

10. Analysis Description

In this chapter I will describe the procedure used to extract a clean sample of $\eta' \to \pi^+\pi^- e^+ e^-$ events from the data. Furthermore, I will discuss how the background contamination in the sample is estimated and mitigated, and describe the calculation of the corrections needed for an accurate determination of the branching fraction and asymmetry.

10.1 Event Selection

The signal process is studied through the decay chain $J/\psi \to \gamma\eta'$ followed by $\eta' \to \pi^+\pi^- e^+ e^-$. To be considered for analysis, an event must contain exactly four charged tracks with zero net charge. These tracks are required to originate from a cylindrical volume around the IP with radius $R_{xy} = 1$ cm and length $\Delta z = 10$ cm. Furthermore, the polar angle θ of each track must fulfill the condition $|\cos\theta| < 0.93$. That is, the track must lie within the detector acceptance. Each event must also include at least one photon. The energy of this photon must be at least 25 MeV if it was reconstructed using a cluster in the EMC barrel, or 50 MeV if in the endcaps. The time of arrival must be no more than 700 ns after the event start time to ensure it belongs to the same event as the charged tracks. Finally, the angle between the reconstructed photon trajectory and the nearest charged track extrapolated to the EMC shower position must be at least 15° to avoid cross-contamination.

For each charged track, the PID algorithm described in Section 8.4.1 is used to calculate the goodness-of-fit variable (χ^2_{PID}) for the hypotheses that the track originates from a pion, electron or muon. The algorithm is based on the time-of-flight and energy loss per unit length in the MDC. Moreover, a fit to all four tracks is performed under the assumption that they originate from a common vertex, as they should for a signal event. This fit is required to give a goodness-of-fit variable $\chi^2_{vtx.} < 200$. The updated track parameters from this vertex fit and the four-momentum of one photon are subsequently used as input to a fit using energy-momentum (four-constraint, 4C) conservation constrained to the energy and momentum of the initial e^+e^--system. The reaction hypotheses $\gamma\pi^+\pi^- e^+ e^-$, $\gamma\pi^+\pi^+\mu^+\mu^-$, $\gamma\pi^+\pi^-\pi^+\pi^-$ are tested. The goodness-of-fit variable χ^2_{4C} from the kinematic fit for each hypothesis is combined with the goodness-of-fit variables from PID $\chi^2_{4C+PID} = \chi^2_{4C} + \sum_{j=1}^{4} \chi^2_{PID}(j)$, where $\chi^2_{PID}(j)$ is related to the probability that track j corresponds to a particle of a given species. The events where the $\gamma\pi^+\pi^- e^+ e^-$ hypothesis gives the least

χ^2_{4C+PID} are kept for further analysis. If there is more than one photon in the event, the one that gives the least χ^2_{4C} is selected.

Furthermore, a cutoff on the χ^2_{4C+PID} variable is imposed to improve the signal-to-background ratio in the final sample. The cutoff value is optimized using a figure-of-merit (FOM) defined as $N_S/\sqrt{N_D}$, where N_S is the number of events present in the signal MC sample after the cut and N_D is the corresponding number of events in data. Since N_D includes both signal and background events, this definition gives an estimate of the expected signal significance. If increasing the cutoff value leads to more signal events than background events selected, the value of the FOM should grow. If more background events than signal events are selected, on the other hand, N_D grows faster than N_S and the value of the FOM should decrease. As is shown in Fig. 10.1, the FOM has a maximum for a cutoff at $\chi^2_{4C+PID} \simeq 62$, which is therefore selected as the upper limit for the accepted events.

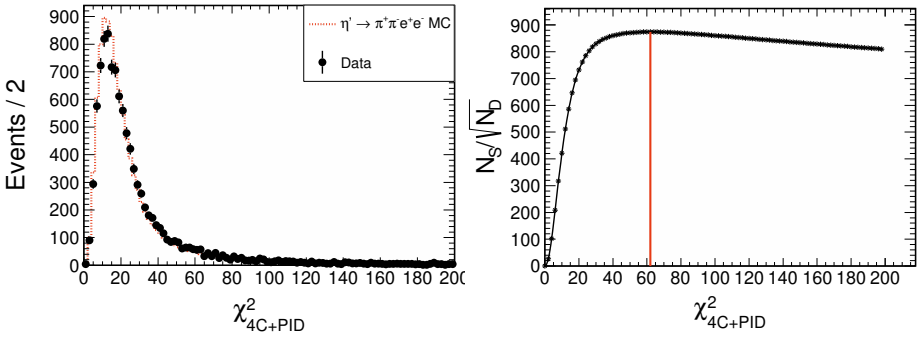

Figure 10.1. Comparison of χ^2_{4C+PID} from data and signal MC (left) and FOM as a function of χ^2_{4C+PID} (right). The solid red line indicates the maximum and the chosen cutoff.

10.2 Background Determination

The background–signal composition of the selected events is investigated using the inclusive MC sample. The numbers of signal and background events that pass the selection criteria are listed in Table 10.1. This sample was generated using the phase space model, without taking into account the specific dynamics of different processes. These results should therefore not be taken as a precise estimate of the yields. However, the important conclusion is that the main source of background is the decay $\eta' \to \pi^+\pi^-\gamma$ where the photon converts to an e^+e^--pair in the detector material.

A clear and clean η' signal is visible in the $\pi^+\pi^-e^+e^-$ invariant mass spectrum, see Fig. 10.2, but a closer inspection of other distributions corroborates

Table 10.1. *Number of background events compared to the number of $\eta' \to \pi^+\pi^- e^+e^-$ events remaining from the inclusive MC sample after the initial event selection criteria.*

Decay chain	Final state	Number of events
$J/\psi \to \gamma\eta',\ \eta' \to \rho^0\gamma,\ \rho^0 \to \pi^+\pi^-$	$\pi^+\pi^-\gamma$	3105
$J/\psi \to \gamma\eta',\ \eta' \to \pi^+\pi^-\eta,\ \eta \to \gamma e^+e^-$	$\pi^+\pi^- e^+e^-\gamma\gamma$	14
$J/\psi \to \gamma\eta',\ \eta' \to \omega\gamma,\ \omega \to \pi^+\pi^-$	$\pi^+\pi\gamma\gamma$	4
$J/\psi \to \gamma\eta',\ \eta' \to \pi^+\pi^-\pi^0,\ \pi^0 \to \gamma\gamma$	$\pi^+\pi^- 3\gamma$	2
$J/\psi \to \rho^0\pi^0,\ \rho^0 \to \pi^+\pi^-,\ \pi^0 \to \gamma\gamma$	$\pi^+\pi^-\gamma\gamma$	2
Other decays with 1 event each	-	13
$J/\psi \to \gamma\eta',\ \eta' \to \pi^+\pi^- e^+e^-$	$\pi^+\pi^- e^+e^-$	3464

the conclusion from the study of the inclusive MC sample. The contribution from $\eta' \to \pi^+\pi^-\gamma$ events with a converting photon is clearly visible as the rightmost peak in the e^+e^- invariant mass distribution. One would expect that the e^+e^--pairs from conversion events have small invariant masses, but since the BESIII track reconstruction algorithm assumes that tracks originate from the IP, the direction of tracks produced elsewhere will be misreconstructed. Therefore, the e^+e^--pairs from conversion events are reconstructed with an artificial opening angle leading to artificially large invariant masses.

The vertex fit assumes that all four tracks originate from a common vertex and provides a solution even though this assumption is clearly not correct. By studying the projection of the e^+ and e^- track helices on the xy-plane and their point of closest approach one can estimate the position of the e^+e^- vertex, and the radial distance from the IP, R_{xy}. The distribution of this variable shows that e^+e^--pairs originate from three distinct regions. The pairs from the signal events are produced at the IP, while the conversion pairs are created at $R_{xy} \sim 3$ cm, corresponding to the beam pipe, and ~ 6 cm, corresponding to the inner wall of the drift chamber. To illustrate the locations where these pairs are produced the distribution of e^+e^--vertices in the xy-plane is overlaid on the axial cross section view of the beam pipe in Fig. 10.3.

The strategy adopted to deal with the dominating background is to develop a set of criteria, hereafter referred to as the photon conversion veto, through which the vast majority of conversion events is rejected and as many of the $\eta' \to \pi^+\pi^- e^+e^-$ events as possible are retained. After any residual background has been subtracted the yields in the full angular range, as well as in the regions $\sin 2\varphi < 0$ and $\sin 2\varphi > 0$, can be used to determine the branching fraction and the CP-asymmetry.

One powerful method used for distinguishing between conversion events and signal events is to study the direction of the $e^\pm$ momentum vectors at the beam pipe. This is accomplished by changing the reference point of the $e^\pm$-helices to their respective points of intersection with the beam pipe and re-

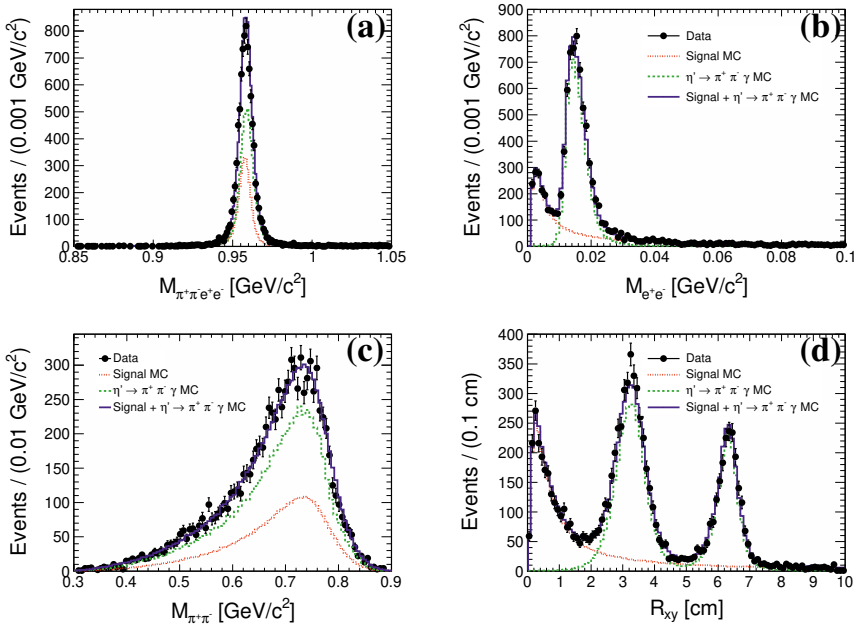

Figure 10.2. Invariant mass distributions of the $\pi^+\pi^-e^+e^-$- (a), e^+e^-- (b), and $\pi^+\pi^-$- (c) systems and the radial distance from the IP to the e^+e^- vertex in the (d) after the preselection.

calculating the momentum vectors. This changes the directions of the vectors, but not their magnitudes. For the e^+e^--pairs originating from the IP, the opening angle is increased, meaning that their invariant masses have larger values than the true ones. This is illustrated in Fig. 10.4. The e^+e^--pairs from the conversion in the beam pipe should instead be parallel, and the invariant mass close to the true value, *i.e.* $2m_e$.

These recalculations are implemented by building on functionality from the Gamma Conversion Finder [195] of BOSS. By selecting an appropriate region of the two-dimensional distribution of e^+e^--pair invariant mass at the beam pipe, M_{ee}^{BP}, versus the distance between the e^+e^--vertex and the IP, one can efficiently separate signal events from conversion events. In Fig. 10.5, this distribution is shown for signal MC, conversion MC and experimental data. All events on the low mass side of the red line in Fig. 10.5 are rejected. It is defined by straight line segments between the points (0.004 GeV/c^2, 0 cm), (0.004 GeV/c^2, 2 cm), (0.03 GeV/c^2, 3 cm), and (0.07 GeV/c^2, 10 cm). The rejection efficiency for the conversion events is 96.1%.

The rejection efficiency can be further improved by taking advantage of the fact that the e^+e^--pairs from the signal and conversion have different angular distributions. In particular, the electrons in the pairs that originate from conversion will be produced with momenta parallel to each other and to that of

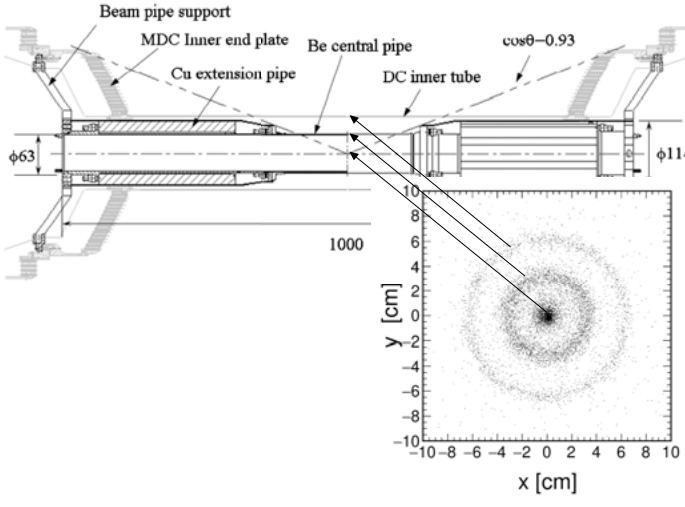

Figure 10.3. Electron–positron vertex positions from data and a cross section view of the BESIII beam pipe. The innermost circle corresponds to signal events from the interaction point, the middle circular band to conversion events from the beam pipe, and the outermost band to conversion events from the inner wall of the drift chamber.

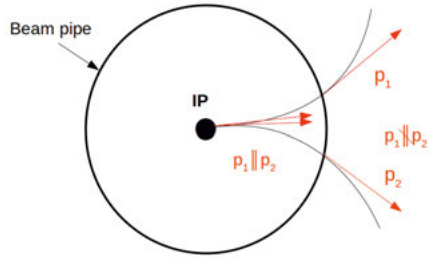

Figure 10.4. Example of how the momentum directions of tracks from the IP change with the choice of a reference point. When using the IP as the reference point the momentum vectors are parallel. If the intersection with the beam pipe is used there is an opening angle between the tracks and the invariant mass becomes artificially large.

the converting photon. The magnetic field leads to a non-zero opening angle in the $xy-$plane, but the $z-$components remain unaffected since they are parallel to the magnetic field. Pairs from the decay $\eta' \to \pi^+\pi^- e^+ e^-$ on the other hand can be produced with an opening in any direction, including the $z-$direction. Therefore, the conversion events can be separated from the signal events by measuring the opening angle in the z-direction, Φ_{ee}, defined as

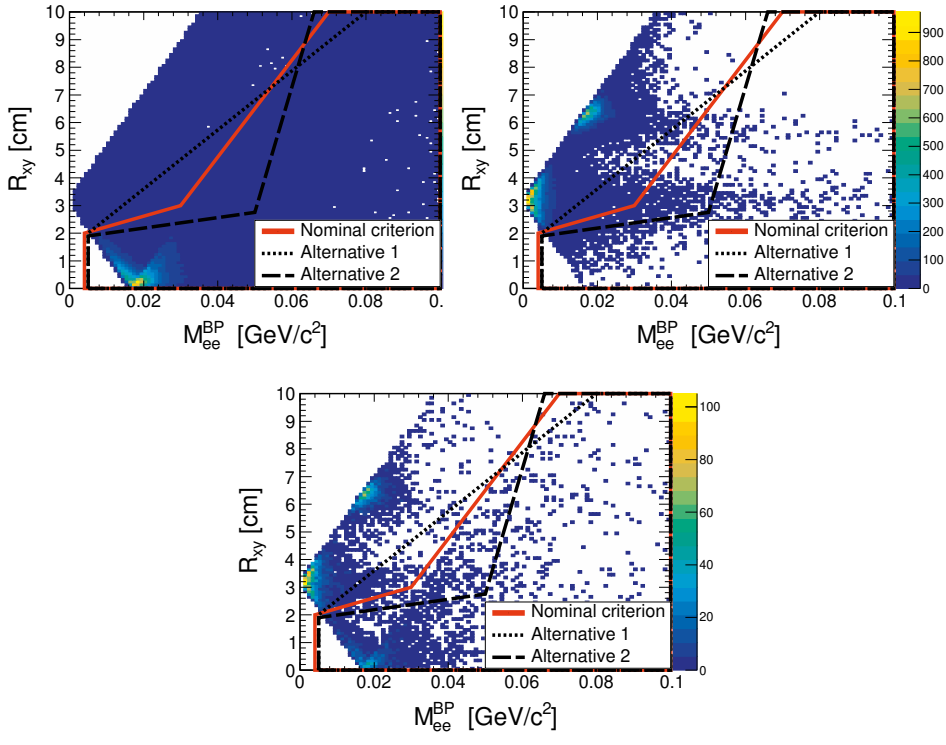

Figure 10.5. Invariant mass at the beam pipe versus radial position of the e^+e^--vertex in the $\eta' \to \pi^+\pi^- e^+e^-$ MC (top left), $\eta' \to \pi^+\pi^-\gamma$ MC (top right), and experimental data (bottom). All events enclosed by the polygon are accepted. The red solid line represents the nominal selection region while the dashed and dotted lines give alternative regions used to estimate the systematic uncertainty.

$$\vec{u} = \frac{\vec{p}_{e^+} + \vec{p}_{e^-}}{|\vec{p}_{e^+} + \vec{p}_{e^-}|} = \hat{p}_\gamma \tag{10.1}$$

$$\vec{v} = \vec{p}_{e^+} \times \vec{p}_{e^-} \tag{10.2}$$

$$\vec{w} = \vec{u} \times \vec{v} \tag{10.3}$$

$$\vec{u_a} = \frac{\vec{u} \times \hat{z}}{|\vec{u} \times \hat{z}|} \tag{10.4}$$

$$\Phi_{ee} = \cos^{-1}\left(\frac{\vec{w} \cdot \vec{u_a}}{|\vec{w}||\vec{u_a}|}\right), \tag{10.5}$$

where $\vec{p}_{e^\pm}$ are the 3-momenta of electron and positron and $\hat{z}$ is the direction of the magnetic field. The angle Φ_{ee} is expected to be close to zero for conversion events, and to have a flat distribution between 0° and 180° for the $\eta' \to \pi^+\pi^- e^+e^-$ events. The Φ_{ee} variable is combined with the distance from

the IP to the e^+e^--vertex to give a powerful veto for conversion events. In Fig. 10.6 the events inside the red polygon, defined by requiring $\Phi_{ee} > 75^\circ$ when 1.8 cm $< R_{xy} <$ 7.5 cm, are accepted. This criterion rejects 97.5% of the conversion events on its own. This corresponds to 74.7% of the background events remaining after the $M^{\mathrm{BP}}_{e^+e^-}$ criterion.

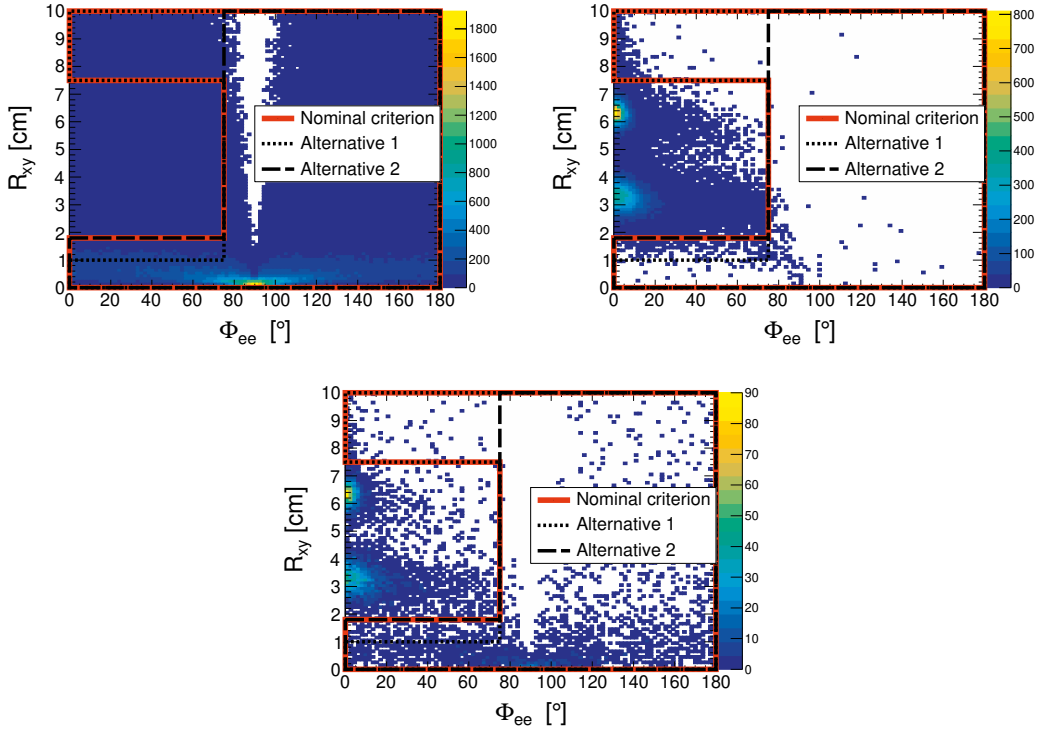

Figure 10.6. Opening angle Φ_{ee} versus radial position of the e^+e^--vertex in the $\eta' \to \pi^+\pi^- e^+e^-$ MC (top left), $\eta' \to \pi^+\pi^-\gamma$ MC (top right), and experimental data (bottom). All events enclosed by the polygon are accepted. The red solid line represents the nominal selection region while the dashed and dotted lines give alternative regions used to estimate the systematic uncertainty.

The rejection efficiency for the $\eta' \to \pi^+\pi^-\gamma$ events, whether the photon converts or not, is found to be 99.998%. Taking into account the total number of J/ψ events in the sample, $N_{J/\psi} = (1310.5 \pm 7.0) \times 10^6$ [196], and the world averages for the branching fractions $\mathscr{B}(J/\psi \to \gamma\eta') = (5.25 \pm 0.07) \times 10^{-3}$ and $\mathscr{B}(\eta' \to \pi^+\pi^-\gamma) = 29.5 \pm 0.4\%$ [6], the number of conversion events remaining in the signal region after the photon conversion veto is estimated to be 48±2. Of these, 23±1 fall in the region $\sin 2\varphi < 0$ and 25±1 in the region $\sin 2\varphi > 0$.

Background from non-η' sources is estimated from the η' sidebands, shown in Fig. 10.7, defined as 0.06 GeV/c^2 $< |M_{\eta'} - M_{\pi\pi ee}| <$ 0.08 GeV/c^2. The

number of events from the sidebands is used to estimate the background in the signal region in the following way:

$$N_{non-\eta'} = N_{sideband} \times \frac{\text{width of signal region}}{2 \times \text{width of sideband region}} = \frac{N_{sideband}}{2} \qquad (10.6)$$

After the photon conversion veto, a clean sample of $\eta' \to \pi^+\pi^- e^+ e^-$ events with $\sim 2\%$ background is selected. The invariant mass distributions of $\pi^+\pi^-$, e^+e^-, and $\pi^+\pi^- e^+ e^-$ as well as $\sin 2\varphi$ from data, shown in Fig. 10.7, are in excellent agreement with the signal MC simulations. The cumulative efficiency for the criteria of the analysis algorithm is estimated using the signal MC sample. The results are presented in table 10.2.

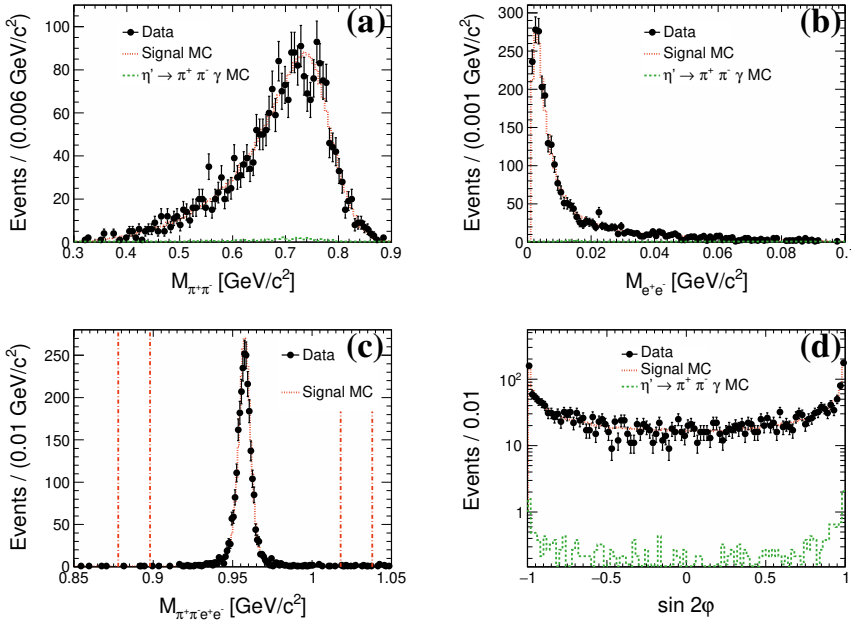

Figure 10.7. Invariant mass distributions of the $\pi^+\pi^-$- (a), e^+e^-- (b), and $\pi^+\pi^- e^+e^-$- (c) systems and the $\sin 2\varphi$ distribution (d) in the final event sample. Black points with error bars represent data, the dotted red histogram represents signal MC, and the dashed green histogram the remaining $\eta' \to \pi^+\pi^-\gamma$ background. The vertical lines in (c) indicate the sidebands.

For the purpose of the *CP*-asymmetry measurement, the efficiency is determined separately for $\sin 2\varphi > 0$ and $\sin 2\varphi < 0$. The efficiencies in the two regions are found to be identical and equal to $15.3 \pm 0.1\%$, which justifies the assumption used to derive the bin migration correction procedure in Section 9.1.

Table 10.2. *Cut flow for the analysis of $\eta' \to \pi^+\pi^- e^+ e^-$ determined from the signal MC sample.*

Cut	Cumulative efficiency ε (%)
Preselection	$26.0 \pm 0.1\%$
$\chi^2_{4C+PID} < 62$	$21.7 \pm 0.1\%$
$\lvert M_{\eta'} - M_{\pi\pi ee}\rvert < 0.02$ GeV/c^2	$21.1 \pm 0.1\%$
M_{ee}^{BP}	$16.2 \pm 0.1\%$
Φ_{ee}	$15.3 \pm 0.1\%$

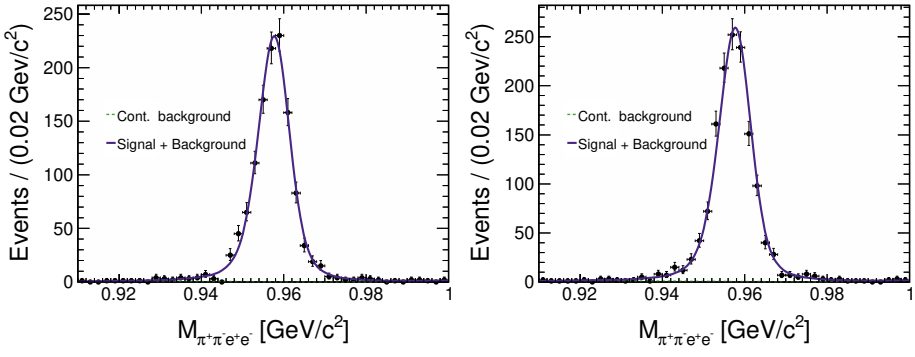

Figure 10.8. Fits to $M_{\pi^+\pi^- e^+ e^-}$ in the regions $\sin 2\varphi < 0$ (left) and $\sin 2\varphi > 0$ (right) after the photon conversion veto and subtraction of remaining $\pi^+\pi^-\gamma$ background. The dashed green histogram represents continuous background. The solid blue line is the sum of the signal and background contributions.

The event yields in the regions $\sin 2\varphi > 0$ and $\sin 2\varphi < 0$ are determined by fits to the corresponding $\pi^+\pi^- e^+ e^-$ invariant mass distributions in the range $0.91\ \mathrm{GeV}/c^2 < M_{\pi^+\pi^- e^+ e^-} < 1.00\ \mathrm{GeV}/c^2$. In these fits, shown in Fig. 10.8, the signal is represented by the MC lineshape convolved with a Gaussian function with a standard deviation of $1.5\ \mathrm{MeV}/c^2$ to account for differences in resolution between data and MC simulations, and background is represented by a second order Chebychev polynomial. Before the fit is performed, the background from $\eta' \to \pi^+\pi^-\gamma$ is subtracted based on the yields in the MC simulations.

10.3 Normalization of the Branching Fraction

In order to determine the branching fraction, the acceptance corrected number of signal events must be related to the total number of η' mesons produced in the experiment. The most straightforward way of doing this would be to use the number of J/ψ mesons in the sample [196] and the branching fraction for the decay $J/\psi \to \gamma\eta'$, which are both known, to obtain an estimate of the number of η' mesons in the sample. A second approach is to study a similar decay of η' with a well-known branching fraction in parallel with the signal channel. An appropriate choice here is $\eta' \to \pi^+\pi^-\gamma$ which is the second most common decay of η' with a precisely measured branching fraction of $29.5 \pm 0.4\%$ [6]. Furthermore, its dynamics is well known and as discussed in Section 4.2, it shares many characteristics with the signal channel. Systematic effects related to the reconstruction should thus have a similar impact on both channels. The normalization will serve to cancel out these effects and reduce the overall systematic uncertainty of the result. This is the strategy chosen for this work. The branching fraction is then given by

$$\mathscr{B}(\eta' \to \pi^+\pi^- e^+e^-) = \frac{N_{\eta'\to\pi^+\pi^- e^+e^-} \times \varepsilon_{\eta'\to\pi^+\pi^-\gamma} \times \mathscr{B}(\eta' \to \pi^+\pi^-\gamma)}{N_{\eta'\to\pi^+\pi^-\gamma} \times \varepsilon_{\eta'\to\pi^+\pi^- e^+e^-}}, \tag{10.7}$$

where N is the observed number of events for the two channels (represented by the subscript), ε is the efficiency, and $\mathscr{B}(\eta' \to \pi^+\pi^-\gamma)$ is the branching fraction for the normalization channel.

The full decay chain for the normalization channel is $J/\psi \to \gamma\eta'$ followed by $\eta' \to \pi^+\pi^-\gamma$ and the analysis aims to select events that contain exactly two charged tracks with zero net charge and at least two photons. These must fulfill the same quality criteria as in the analysis of $\eta' \to \pi^+\pi^- e^+e^-$, see Section 10.1. The parameters of the track helices of the two charged particles are used as input to a vertex fit under the assumption that they originate from the same vertex. As before, the fit is required to give a goodness-of-fit $\chi^2_{vtx.} < 200$. The updated charged track parameters from the vertex fit, the four-momenta of the two photons and the initial e^+e^--system four-momentum are used as input to an energy-momentum constrained fit procedure. The hypotheses $\pi^+\pi^-\gamma\gamma$, $\mu^+\mu^-\gamma\gamma$, and $e^+e^-\gamma\gamma$ are considered. As before, the kinematic fit is combined with the goodness-of-fit variable from PID, χ^2_{PID}, to yield the quantity $\chi^2_{PID+4C} = \chi^2_{4C} + \sum_{j=1}^{2} \chi^2_{PID}(j)$. Events for which the hypothesis $\pi^+\pi^-\gamma\gamma$ yields the least χ^2_{PID+4C} are chosen, and if an event includes more than two candidate photons, the combination that yields the least χ^2_{4C} is selected. The FOM $N_S/\sqrt{N_D}$ is used to find the cutoff for the value of χ^2_{4C+PID} that yields the best signal to background ratio. As before N_S is the number of events present in the signal MC sample after the cut and N_D is the corresponding number of events in data. As can be seen in Fig. 10.9, the FOM reaches a maximum value $\chi^2_{4C+PID} < 140$, which is therefore chosen as the selection criterion.

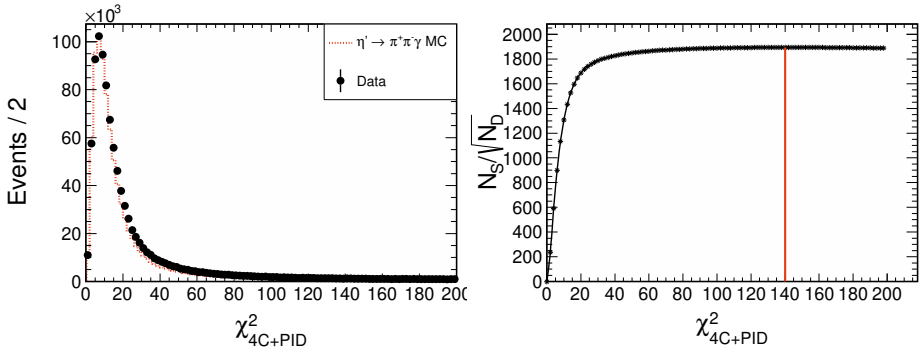

Figure 10.9. Comparison of χ^2_{4C+PID} in $\eta' \to \pi^+\pi^-\gamma$ MC and data (left) and FOM as a function χ^2_{4C+PID} (right). The red line indicates the maximum.

The final step is to differentiate between the two selected photons. The one from the two-body radiative decay $J/\psi \to \gamma\eta'$ has a well defined energy of 1.4 GeV. After reconstruction, the energy distribution for these photons has a full width at half maximum of about 20 MeV. They are therefore easily distinguished from the $\eta' \to \pi^+\pi^-\gamma$ decay photons that have a continuous distribution of with energies ranging from zero to about 1.2 GeV. Therefore, the photon with the largest energy is considered to originate from the decay of J/ψ and the other one from η'.

The background remaining after the preselection is evaluated using the inclusive MC sample. The number of selected events for the most important reactions is presented in Table 10.3. As can be seen, one should expect a significant background from processes with $\pi^+\pi^-\pi^0$, and $\pi^+\pi^-\eta$ final states where the π^0 or η decays into two photons.

Table 10.3. *Number of background events compared to the number of* $\eta' \to \pi^+\pi^-\gamma$ *events remaining in the inclusive MC sample after the initial event selection criteria.*

Decay chain	Final state	Number of events
$J/\psi \to \rho^0\pi^0,\ \rho^0 \to \pi^+\pi^-,\ \pi^0 \to \gamma\gamma$	$\pi^+\pi^-\gamma\gamma$	134743
$J/\psi \to \pi^+\pi^-\pi^0, \pi^0 \to \gamma\gamma$	$\pi^+\pi^-\gamma\gamma$	5205
$J/\psi \to \gamma\eta',\ \eta' \to \pi^+\pi^-\pi^0,\ \pi^0 \to \gamma\gamma$	$\pi^+\pi^-\gamma\gamma$	2356
$J/\psi \to \omega\pi^+\pi^-,\ \omega \to \pi^0\gamma,\ \pi^0 \to \gamma\gamma$	$\pi^+\pi^-\gamma\gamma$	2180
$J/\psi \to \rho^0\eta,\ \rho^0 \to \pi^+\pi^-,\ \eta \to \gamma\gamma$	$\pi^+\pi^-\gamma\gamma$	1958
$J/\psi \to \rho^+\pi^-,\ \rho^+ \to \pi^+\pi^0,\ \pi^0 \to \gamma\gamma$	$\pi^+\pi^-\gamma\gamma$	1702
$J/\psi \to \rho^-\pi^+,\ \rho^- \to \pi^-\pi^0,\ \pi^0 \to \gamma\gamma$	$\pi^+\pi^-\gamma\gamma$	1683
$J/\psi \to \gamma\eta',\ \eta' \to \gamma\rho^0,\ \rho^0 \to \pi^+\pi^-$	$\pi^+\pi^-\gamma\gamma$	652147

Indeed, as can be seen in Fig. 10.10, a peak at the π^0 mass and a small bump at the η mass are visible in the two-photon invariant mass spectrum. By studying the energy distribution of the photon from the η' decay, $E_{\gamma_{\eta'}}$, it is

clear that the background events are concentrated in the low $E_{\gamma_{\eta'}}$ range, see Fig. 10.10. To clean up the sample, a condition $E_{\gamma_{\eta'}} > 0.15$ GeV is required.

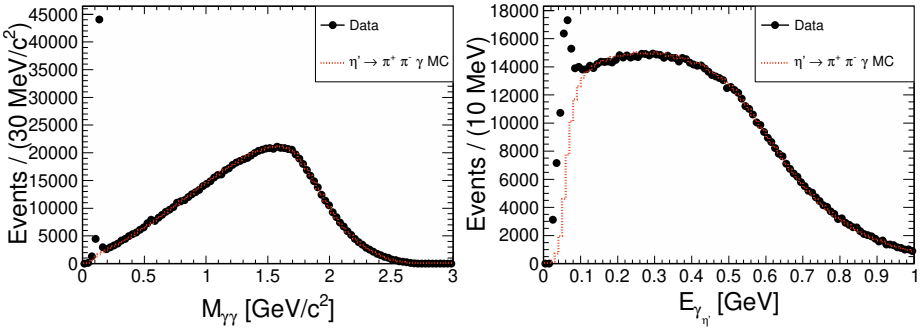

Figure 10.10. Invariant mass spectrum of the $\gamma\gamma$-pair (left) and energy of the photon from $\eta' \to \pi^+\pi^-\gamma$ (right). The black points with error bars represent data and the red dashed histogram represents the $\eta' \to \pi^+\pi^-\gamma$ MC.

After the above described selection criteria the data are in good agreement with the MC simulations of $\eta' \to \pi^+\pi^-\gamma$. A comparison of the momentum, invariant mass and angular distributions for data and MC is shown in Fig. 10.11. There is good agreement in all considered distributions. The cumulative efficiency is estimated with the $\eta' \to \pi^+\pi^-\gamma$ MC sample and is found to be $50.9 \pm 0.1\%$ after the preselection and $38.1 \pm 0.1\%$ after the requirement $E_{\gamma_{\eta'}} > 0.15$ GeV.

The number of $\eta' \to \pi^+\pi^-\gamma$ events is 786200 ± 900 extracted through a fit to the $\pi\pi\gamma$ invariant mass spectrum, see Fig. 10.12. The $\eta' \to \pi^+\pi^-\gamma$ signal is represented by the MC shape convolved with a Gaussian function with a standard deviation of 1.5 MeV/c^2 to account for differences in the resolution between data and MC. Continuous background is represented by a second order Chebychev polynomial.

As a consistency check the number of $\eta' \to \pi^+\pi^-\gamma$ events is used to calculate the branching fraction of the decay $J/\psi \to \gamma\eta'$ to compare with results from previous analyses. One finds

$$\begin{aligned}\mathscr{B}(J/\psi \to \gamma\eta') &= \frac{N_{\eta'\to\pi\pi\gamma}}{N_{J/\psi} \times \mathscr{B}(\eta' \to \pi\pi\gamma) \times \varepsilon_{\eta'\to\pi\pi\gamma}} \\ &= (5.34 \pm 0.09) \times 10^{-3},\end{aligned}$$

where the number of produced J/ψ is $N_{J/\psi} = (1310.5 \pm 7.0) \times 10^6$ [196]. This is consistent with the current PDG average $\mathscr{B}(J/\psi \to \gamma\eta') = (5.25 \pm 0.07) \times 10^{-3}$ [6] and this shows that the yield-efficiency estimate is consistent with the known value of the branching fraction for the decay $\eta' \to \pi^+\pi^-\gamma$.

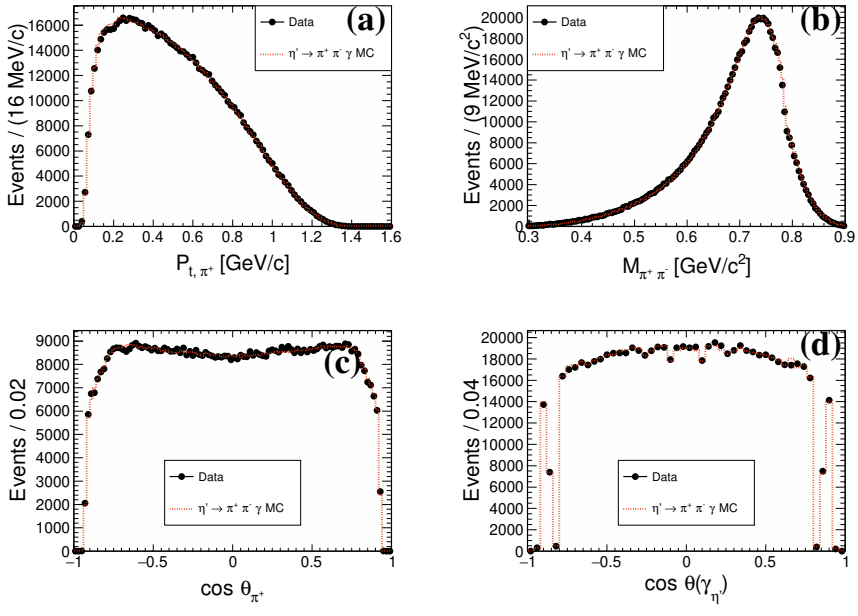

Figure 10.11. Momentum distribution of π^+ (a), invariant mass distribution of the $\pi^+\pi^-$-system (b), and polar angle in the lab frame of the π^+ (c) and of the photon from the decay $\eta' \to \pi^+\pi^-\gamma$ (d). The black points with error bars represent data, and the red dashed histogram represents the $\eta' \to \pi^+\pi^-\gamma$ MC. The sharp dip around $|\cos\theta(\gamma_{\eta'})| \approx 0.8$ seen in data and MC in (d) is due to the gap between the barrel and endcap parts of the EMC.

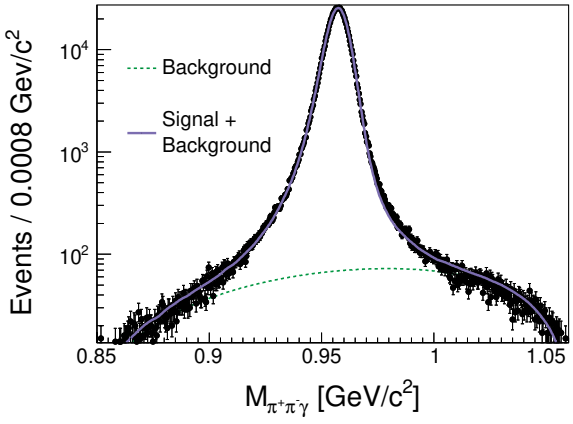

Figure 10.12. Fit to the $\pi^+\pi^-\gamma$ invariant mass distribution. The black points with error bars represent experimental data, the green dashed line represents the continuous background, and the solid blue line is the sum of the signal and background contributions.

10.4 Corrections to the *CP*-Asymmetry

The bin migration effect in $\sin 2\varphi$ is studied by comparing the true and reconstructed values of $\sin 2\varphi$. The fractions α_1 and α_2 defined in Section 9.1 are estimated as

$$\alpha_1 = \frac{N_{+/-}}{N_+} \text{ and } \alpha_2 = \frac{N_{-/+}}{N_-}, \tag{10.8}$$

where $N_{+/-}$ and $N_{-/+}$ are the numbers of events that migrated from $\sin 2\varphi > 0$ to $\sin 2\varphi_R < 0$ and from $\sin 2\varphi < 0$ to $\sin 2\varphi_R > 0$, respectively, while N_+ and N_- are the numbers of events with true value of $\sin 2\varphi > 0$ and $\sin 2\varphi < 0$, respectively. Inserting the numbers of events from the signal MC sample, $N_{+/-} = 53034$, $N_{-/+} = 52665$, $N_+ = 248791$, and $N_- = 247237$ yields $\alpha_1 = \alpha_2 = 21.3 \pm 0.1\%$.

Since the bin migration correction inflates the uncertainty, it is interesting to investigate if there are kinematic regions where the resolution is particularly poor, and if excluding these can lead to an overall improvement in the uncertainty. As can be seen in Fig. 10.13, the resolution in $\sin 2\varphi$ is strongly correlated with the invariant mass of the e^+e^--pair. The pairs with smaller invariant masses have smaller opening angles, and therefore the determination of the orientation of their decay planes is more sensitive to small perturbations in the momenta. By excluding events with low $M_{e^+e^-}$, the size of the bin migration factor can be decreased, and if the effect is large enough this can compensate for the loss of statistics, resulting in a smaller overall uncertainty. To investigate this, a region of $M_{e^+e^-}$ of varying size is excluded from the analysis of the signal MC sample and for each step the bin migration correction factor and statistical uncertainty are calculated. The results are shown in Fig. 10.13. The conclusion is that there is no cutoff for which the improvement in the resolution outweighs the loss of statistics, and consequently the full $M_{e^+e^-}$ distribution is included in the analysis.

The next step is to investigate if the asymmetry measurement procedure, with the correction factor estimated above, is a reliable estimate of the true value. To check this, a series of pseudoexperiments are performed on MC samples generated with a known asymmetry. From each sample, an estimate of the asymmetry $\mathcal{A}_{\varphi,i}$ can be extracted. The true value of the asymmetry is $\hat{\mathcal{A}}_\varphi$. If the number of events in each sample is N, the estimated uncertainty can be expressed in a general way as $\sigma_N = \frac{\Sigma}{\sqrt{N}}$, where Σ is a constant that describes how the uncertainty changes with the size of the data set. By constructing the pull distribution for the estimates, *i.e.* $\frac{\mathcal{A}_{\varphi,i} - \hat{\mathcal{A}}_\varphi}{\sigma_N}$, several different aspects of the chosen estimator can be investigated. If the number of pseudoexperiments is large the distribution is expected to be Gaussian according to the central limit theorem. If it is not, this indicates issues that must be studied in detail. If the distribution is Gaussian, it should have mean zero and standard deviation equal to one if the method is unbiased and the uncertainty is estimated correctly.

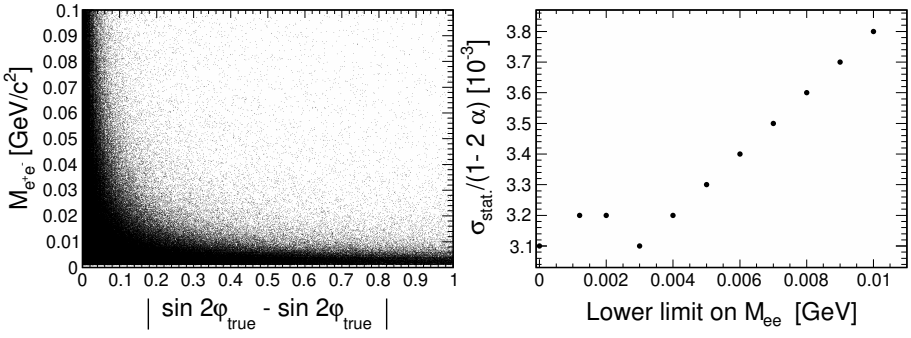

Figure 10.13. Difference between the true and reconstructed value of $\sin 2\varphi$ versus the invariant mass of the e^+e^--system in the signal MC sample (left) and corrected statistical uncertainty as a function of the lower limit imposed on M_{ee}.

These two parameters can be studied by assuming that there is a bias and that the uncertainty is not estimated correctly. The distribution in this case is given by $\mathcal{N}(\frac{\Delta}{\sigma_N}, \frac{\sigma}{\sigma_N})$. The values of Δ and σ can be determined by fitting a Gaussian distribution to $\frac{\mathcal{A}_{\varphi,i} - \hat{\mathcal{A}}_\varphi}{\sigma_N}$. If the mean of the fitted function is denoted as a and its standard deviation as b, they are related to the bias and estimated uncertainty via

$$\frac{\Delta}{\sigma_N} = a \text{ and } \frac{\sigma}{\sigma_N} = b. \tag{10.9}$$

To summarize, three separate checks can be performed: Is the pull distribution Gaussian? Is a consistent with zero? Is b consistent with one? For this purpose, eight MC ensembles with asymmetries ranging from -20% to $+20\%$ in steps of 5% are generated. Each ensemble consists of 125 samples that match the final data sample in size. The uncertainty for a single sample is $\sigma_N = 0.034$ calculated according to Eq. 9.16 with $N = 2618$. The pull distribution is shown in Fig. 10.14. The distribution is approximately Gaussian and a fit yields $a = 0.03 \pm 0.03$ and $b = 0.99 \pm 0.02$. The value of a is consistent with zero, and the value of b is consistent with one, showing that the estimator is unbiased and that the uncertainty is estimated correctly.

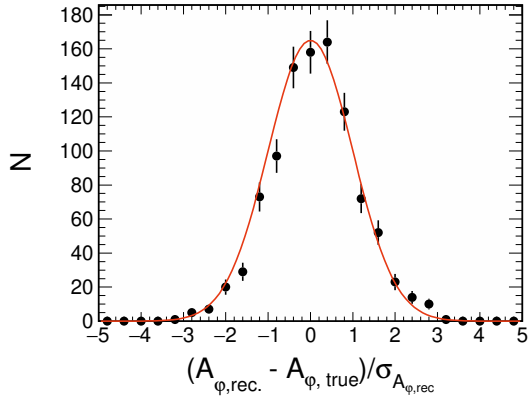

Figure 10.14. Distribution of the pull function, defined as the difference between the true and reconstructed asymmetry $\mathscr{A}_\varphi$ divided by the uncertainty, in the MC ensembles. The line shows a Gaussian function with mean 0 and standard deviation 1.

11. Systematic Uncertainties

This analysis profits from the work done within the BESIII collaboration to investigate the systematic uncertainties related to reconstruction procedures, and in particular differences in efficiency between data and MC. The size of the resulting systematic effects on the branching fraction and asymmetry measured in this work are evaluated by re-weighting the MC sample event-by-event and studying how the results change. For each event, the ratio of the efficiency in data to the efficiency in MC, $\varepsilon_{Data}/\varepsilon_{MC}$, is retrieved from a table indexed by the momenta and/or scattering angles of the tracks and photons. The event is assigned this number as a weight to improve the similarity between the MC sample and data. After all events have been weighted, the branching fraction and asymmetry are computed. The difference compared to the original result is taken as the systematic uncertainty. The corrections are applied to both the signal and normalization channel before calculating the final result, such that possible cancellations are taken into account. For photons, systematic differences in the reconstruction efficiency have been studied extensively in processes such as $J/\psi \to \rho^0\pi^0$ [197, 198], $e^+e^- \to \gamma\gamma$ [198], and $e^+e^- \to \gamma\mu^+\mu^-$ [199]. In the following, a systematic uncertainty of 0.5% in the EMC barrel ($|\cos\theta_\gamma| < 0.8$), and 1.5% in the endcaps ($0.86 \leq |\cos\theta_\gamma| \leq 0.92$) is used. The systematic uncertainty from tracking of pions has been investigated in Ref. [200] which provides a 2D distribution of the systematic uncertainty in bins of p_T versus $\cos\theta$. The systematic uncertainty of the electron tracking procedure in MC has been studied through the process $e^+e^- \to \gamma J/\psi \to \gamma e^+e^-(\gamma_{FSR})$ [201]. The study likewise provides a 2D distribution of the systematic uncertainty in bins of p_e versus $\cos\theta_e$ that is used here. Finally, the systematic uncertainty due to pion and electron identification has been studied in the processes $J/\psi \to \pi^+\pi^-\pi^0$ [202], and $J/\psi \to \gamma e^+e^-$ [201]. Both provide systematic uncertainties as a function of the momentum and scattering angle.

The χ^2_{4C} distribution is known to differ between data and MC, and to correct for this fact, a set of correction factors for the track helix parameters of pions has been prepared [203]. These corrections are applied to the MC samples of both $\eta' \to \pi^+\pi^-e^+e^-$ and $\eta' \to \pi^+\pi^-\gamma$, but are found to yield only a slight improvement in the agreement between data and MC. Therefore, the effect of these corrections on the branching fraction and asymmetry, 0.3% and 0.5% respectively, are taken as an estimate of the systematic uncertainty due to the kinematic fit.

The systematic uncertainty from the selection window on the η' invariant mass is evaluated by smearing the η' invariant mass distribution in signal and

$\eta' \to \pi^+\pi^-\gamma$ MC with a Gaussian function with mean zero and width according to the fit to $M_{\pi\pi\gamma}$ in Fig. 10.12. The resulting change in the efficiency and the branching fraction (0.4%) is taken as the systematic uncertainty.

Furthermore, the systematic uncertainty due to the fit used to extract the $\eta' \to \pi^+\pi^-\gamma$ yield is estimated by changing the background parametrization from a 2nd to a 3rd, and 4th order polynomial, and the fit range limits within 5% of their original values. The systematic uncertainty, 1.2%, is estimated as the largest fractional difference between the variations and the original result.

The world average branching fraction $\mathscr{B}(\eta' \to \pi^+\pi^-\gamma)$ is dominated by a BESIII measurement [204] using the same data set as this work. In order to properly determine the systematic uncertainty, it is therefore important to take into account the correlations between the two measurements. Differences in the event selection procedure mean that the final data sample used here is slightly smaller than that of Ref. [204], and the statistical correlation coefficient between the two is 0.93. Systematic uncertainties are assumed to be fully correlated if the sources of uncertainty appear in both analyses, and uncorrelated if they appear in only one. The sources shared by both analyses include tracking, photon reconstruction, kinematic fitting, as well as the range and background shape in the fit used to extract the signal yield.

In order to evaluate the systematic effects introduced by the photon conversion veto, the selection regions are varied as shown in Figs. 10.5 and 10.6 and the asymmetry and branching fraction computed for all combinations. The systematic error for the asymmetry is taken to be half the largest difference with respect to the original result, 0.9% for the asymmetry and 0.8% for the branching fraction.

The systematic uncertainties from all sources considered above are summarized in Table 11.1. The systematic effects of MDC tracking, PID and photon reconstruction for $\mathscr{A}_\varphi$ are considered negligible.

Table 11.1. *Systematic uncertainties contributing to the values of $\mathscr{B}(\eta' \to \pi^+\pi^-e^+e^-)$ and $\mathscr{A}_\varphi$. The contributions from all sources are summed in quadrature.*

Source	$\mathscr{B}(\eta' \to \pi^+\pi^-e^+e^-)$ [%]	$\mathscr{A}_\varphi$ $(\times 10^{-2})$
MDC tracking	0.7	-
PID	3.0	-
Photon Reconstruction	0.6	-
4C Kinematic Fit	0.3	0.5
η' mass window	0.4	-
Photon Conversion Veto	0.8	0.9
Normalization	1.3	-
Total	3.5	1.1

12. Results

The efficiencies and event yields for the signal and normalization channels are presented in Table. 12.1. Using these numbers, the ratio of branching fractions is found to be

$$\begin{aligned}\frac{\mathscr{B}(\eta' \to \pi^+\pi^- e^+e^-)}{\mathscr{B}(\eta' \to \pi^+\pi^-\gamma)} &= \frac{N_{\eta'\to\pi^+\pi^- e^+e^-} \times \varepsilon_{\eta'\to\pi^+\pi^-\gamma}}{N_{\eta'\to\pi^+\pi^-\gamma} \times \varepsilon_{\eta'\to\pi^+\pi^- e^+e^-}} \\ &= (8.20 \pm 0.16_{stat.} \pm 0.27_{syst.}) \times 10^{-3}.\end{aligned} \tag{12.1}$$

Taking into account the current world average branching fraction $\mathscr{B}(\eta' \to \pi^+\pi^-\gamma) = 29.5 \pm 0.4\%$ [6], the branching fraction of $\eta' \to \pi^+\pi^- e^+e^-$ is determined to be

$$\begin{aligned}\mathscr{B}(\eta' \to \pi^+\pi^- e^+e^-) &= \frac{N_{\eta'\to\pi^+\pi^- e^+e^-} \times \varepsilon_{\eta'\to\pi^+\pi^-\gamma} \times \mathscr{B}(\eta' \to \pi^+\pi^-\gamma)}{N_{\eta'\to\pi^+\pi^-\gamma} \times \varepsilon_{\eta'\to\pi^+\pi^- e^+e^-}} \\ &= (2.42 \pm 0.05_{stat.} \pm 0.08_{syst.}) \times 10^{-3}.\end{aligned} \tag{12.2}$$

Due to the inclusion of additional data collected in 2012, the statistical uncertainty has been improved by a factor of two compared to the previous BESIII result, which is therefore superseded by this work. As is shown in Fig. 12.1, the result of this work is consistent with the predictions presented in Table 4.1.

Table 12.1. *Efficiencies and event yields for the signal and normalization channels.*

Channel	$\varepsilon[\%]$	Yield
$\eta' \to \pi^+\pi^- e^+e^-$	15.3 ± 0.1	2584 ± 52
$\eta' \to \pi^+\pi^-\gamma$	38.1 ± 0.1	786200 ± 900

To determine the asymmetry, the event yields from the fits in Fig. 10.8, $N_{\sin 2\varphi>0} = 1331 \pm 40$ and $N_{\sin 2\varphi<0} = 1287 \pm 37$ are inserted into Eq. 9.12 together with the migration fraction $\alpha = 21.3\%$. The result is

$$\mathscr{A}_\varphi = (2.9 \pm 3.7_{stat.} \pm 1.1_{syst.}) \times 10^{-2}, \tag{12.3}$$

which is consistent with zero, and the absence of CP-violation in this process.

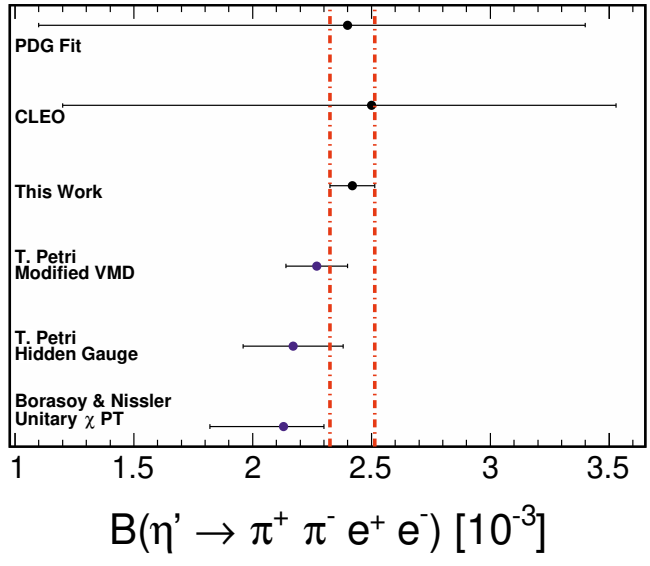

Figure 12.1. Theoretical predictions and experimental results for the branching fraction $\mathscr{B}(\eta' \to \pi^+\pi^- e^+ e^-)$ compared to the value of this measurement.

Part III:
Measurement of Λ Timelike Electromagnetic Form Factors

13. Analysis Strategy

The purpose of this this work is to study the process $e^+e^- \to \Lambda\bar{\Lambda}$ over a range of energies from 2.3864 to 3.0800 GeV and measure the Born cross section, the ratio of electromagnetic form factors R, and the relative phase $\Delta\Phi$. To make this possible the $\Lambda\bar{\Lambda}$ final state is reconstructed in two different ways. The most straightforward method, hereafter referred to as "double-tag" reconstruction, is when the full final state, *i.e.* both the Λ hyperon and $\bar{\Lambda}$ antihyperon are reconstructed. This gives us the complete information about the event but excludes a large number of events which could provide relevant information. Additional events can be obtained by reconstructing either the hyperon or the antihyperon and inferring from kinematic constraints that it comes from an $e^+e^- \to \Lambda\bar{\Lambda}$ event. This method will be referred to as "single-tag" reconstruction throughout this work.

By following the double-tag reconstruction whenever possible and using the single-tag approach for events where only Λ or $\bar{\Lambda}$ could be reconstructed, three statistically independent data samples (double-tag, single-tag $\bar{\Lambda}$, single-tag Λ) are obtained that can subsequently be combined in order to improve the precision of the measurements.

The Λ hyperon has two dominating decay modes $\Lambda \to p\pi^-$ and $\Lambda \to n\pi^0$ with branching fractions 64% and 36%, respectively. Since they constitute close to 100% of all decays, only these two modes are considered. The double-tag analysis will only select events where both Λ and $\bar{\Lambda}$ decay into charged particles, but in the single-tag analyses the undetected hyperon can decay in either of the two modes. This means that two classes of events are involved. When performing the single-tag reconstruction of Λ, these are:

$$\begin{aligned} &\text{Class 1: } \Lambda \to p\pi^-, \bar{\Lambda} \to \bar{p}\pi^+ \\ &\text{Class 2: } \Lambda \to p\pi^-, \bar{\Lambda} \to \bar{n}\pi^0 \end{aligned} \tag{13.1}$$

Since it is explicitly required that the $\bar{\Lambda}$ is not reconstructed, the efficiencies for selecting these two classes are not equal and this has to be accounted for in the analysis. When performing the single-tag reconstruction of $\bar{\Lambda}$, the two classes correspond to the charge-conjugates of the processes mentioned above.

13.1 Data Samples

To accomplish a measurement of the energy dependence of the timelike electromagnetic form factors of the Λ hyperon, the scan method is used as outlined

in section 5.4, and data in the energy range from 2.3864 GeV to 3.0800 GeV are analyzed. The center-of-mass energies and luminosities for the considered samples [205] are listed in Table 13.1. The two closely lying data points at 2.6444 GeV and 2.6464 GeV are analyzed together throughout this work.

Table 13.1. *Center-of-mass energies and integrated luminosities for the energy scan data samples used in this analysis.*

E_{cm} [GeV]	Integrated Luminosity [pb^{-1}]
2.3864	$22.59 \pm 0.01 \pm 0.17$
2.3960	$66.89 \pm 0.02 \pm 0.46$
2.6444	$33.65 \pm 0.01 \pm 0.21$
2.6464	$34.06 \pm 0.01 \pm 0.28$
2.9000	$105.53 \pm 0.03 \pm 0.90$
3.0800	$126.21 \pm 0.03 \pm 0.90$

Detection efficiencies as well as the ISR and VP corrections factors discussed in Section 13.2, are determined using the `ConExc` MC generator [178]. The form factor ratio, R, determines the scattering angle distribution of the hyperon in these simulations, according to Eq. 5.13 and is set for each energy point to the value determined in this analysis. The following MC samples are used:

- $e^+e^- \to \Lambda\bar{\Lambda}$, $\Lambda \to p\pi^-$, $\bar{\Lambda} \to \bar{p}\pi^+$: 10^5events at each energy point.
- $e^+e^- \to \Lambda\bar{\Lambda}$, $\Lambda \to p\pi^-$, $\bar{\Lambda} \to \bar{n}\pi^0$: 10^5 events at each energy point.
- $e^+e^- \to \Lambda\bar{\Lambda}$, $\Lambda \to n\pi^0$, $\bar{\Lambda} \to \bar{p}\pi^+$: 10^5 events at each energy point.

Furthermore, the following samples generated with a phase space model (`PHSP`) are used to calculate the normalization factors for the maximum log-likelihood fit (see Section 13.3):

- $e^+e^- \to \Lambda\bar{\Lambda}$, $\Lambda \to p\pi^-$, $\bar{\Lambda} \to \bar{p}\pi^+$: 5×10^6 events at each energy point.
- $e^+e^- \to \Lambda\bar{\Lambda}$, $\Lambda \to p\pi^-$, $\bar{\Lambda} \to \bar{n}\pi^0$: 5×10^6 events at each energy point.
- $e^+e^- \to \Lambda\bar{\Lambda}$, $\Lambda \to n\pi^0$, $\bar{\Lambda} \to \bar{p}\pi^+$: 5×10^6 events at each energy point.

Finally, the "do it yourself" (DIY) function of `BesEvtGen` is used to implement a generator which describes the production and decay of $\Lambda\bar{\Lambda}$ using the full differential cross section from Ref. [137], including both R and the relative phase. These samples are used for input/output and bias checks of the parameter estimation procedure. Throughout the thesis, this generator will be referred to as "mDIY". The following mDIY samples are used:

- $e^+e^- \to \Lambda\bar{\Lambda}$, $\Lambda \to p\pi^-$, $\bar{\Lambda} \to \bar{p}\pi^+$: 5×10^6 events at 2.396 GeV.
- $e^+e^- \to \Lambda\bar{\Lambda}$, $\Lambda \to p\pi^-$, $\bar{\Lambda} \to \bar{n}\pi^0$: 5×10^6 events at 2.396 GeV.
- $e^+e^- \to \Lambda\bar{\Lambda}$, $\Lambda \to n\pi^0$, $\bar{\Lambda} \to \bar{p}\pi^+$: 5×10^6 events at 2.396 GeV.

13.2 Determination of the Born Cross Section

As already mentioned in Section 5.4,the electron or positron or both may radiate off ISR photons and lose some of their energy before colliding. Because of the loss of energy, some of the collisions in data taken at the nominal center-of-mass energy $\sqrt{s}$ instead occur at the lower effective energy m. The observed cross section for any given process is therefore a combination of the true cross section at $\sqrt{s}$ and other energies m down to the production threshold M_{thr} of the hadronic state. The size of the contamination depends on two factors. The first is the probability for emitting an ISR photon with energy $\sqrt{s}-m$, which is given by the radiator function $W(s,x)$, where $x = 1-m^2/s$. The second factor is the probability that a signal-type event will occur at the effective energy m. This is given by the bare cross section for the process at energy m, $\sigma_0(m)$.

Since the production of hyperon-antihyperon pairs in e^+e^--annihilation is a process mediated by the exchange of a photon, the effects of vacuum polarization (VP) must also be taken into account. The photon quantum state can include both virtual lepton-antilepton pairs and hadrons. These are higher order electromagnetic processes and their contribution to the observed cross section must be corrected for in order to obtain the Born cross section. The effect of VP is parametrized by the vacuum polarization function $\Pi(\sqrt{s})$. The leptonic contributions to the VP function can be calculated perturbatively in QED while the hadronic part requires dispersive approaches.

Taking into account both ISR and VP, the observed cross section can be expressed as

$$\sigma_{obs.}(s) = \int_{M_{th}}^{\sqrt{s}} dm \frac{2m}{s} W(s,x) \frac{\sigma_0(m)}{|1-\Pi(m)|^2}. \tag{13.2}$$

From this one defines a correction factor

$$(1+\delta)_{ISR} = \frac{\sigma(s)}{\sigma_0(s)}, \tag{13.3}$$

that can be used to relate the observed cross section to the Born cross section. But as is clear from both Eq. 13.2 and Eq. 13.3, computing the correction factor requires prior knowledge of the cross section. This complicates matters since the cross section is precisely the quantity that is to be measured. In practice, the cross section and correction factor must therefore be determined together in an iterative procedure that will be described in Chapter 15. In this work, the `ConExc` MC generator [178] is used to determine the correction factors. `ConExc` takes an estimate of the energy dependence of the cross section as input and uses a radiator function calculated up to second order in QED to calculate the observed cross section. Details on how the vacuum polarization correction factor is calculated can be found in Ref. [206] and references therein. `ConExc` then uses the observed and true cross sections to generate a sample that consists of both ISR and non-ISR events. In an analysis that

demands that the nominal beam energy is conserved, the ISR events will be rejected. This means that the efficiency ε estimated with `ConExc` will change depending on the difference between the observed and true cross sections. The larger the difference, the smaller the efficiency. The product $\varepsilon(1+\delta)$ will however remain roughly constant provided that there are no other energy dependent selection criteria in the analysis.

Having selected clean samples of $e^+e^- \to \Lambda\bar{\Lambda}$ events and determined the correction factors, the cross section measurement is done as follows. Given a number of observed double-tag events N_{DT}, the Born cross section is obtained as

$$\sigma_{Born} = \frac{N_{DT}}{\mathscr{L}\varepsilon(1+\delta)\mathscr{B}(\Lambda \to p\pi^-)^2}, \tag{13.4}$$

where $\mathscr{L}$ is the luminosity, ε is the efficiency, and $\mathscr{B}(\Lambda \to p\pi^-)$ is the branching fraction for that decay. For a number of observed single-tag events N_{ST}, the Born cross section is given by

$$\sigma_{Born} = \frac{N_{ST}}{\mathscr{L}(1+\delta)\mathscr{B}(\Lambda \to p\pi^-)\left[\varepsilon_1\mathscr{B}(\Lambda \to p\pi^-) + \varepsilon_2\mathscr{B}(\Lambda \to n\pi^0)\right]}, \tag{13.5}$$

where ε_1 and ε_2 are the efficiencies for the two classes of events defined in Eq. 13.1.

The three samples: double-tag, single-tag $\bar{\Lambda}$, and single-tag Λ are statistically independent. The combined result for the cross section can thus be obtained by taking the inverse variance weighted mean of the results from the individual samples,

$$\hat{x} = \frac{\sum_i x_i/\sigma_i^2}{\sum_i 1/\sigma_i^2} \tag{13.6}$$

where σ is the standard deviation, and the index i represents the three samples. The standard deviation of the mean is given by

$$\sigma_{\hat{x}} = \sqrt{\frac{1}{\sum_i 1/\sigma_i^2}}. \tag{13.7}$$

13.3 Maximum Log-Likelihood Fit

The form factor parameters R and $\Delta\Phi$ will be extracted using an unbinned maximum log-likelihood fit. The likelihood for a measurement based on N events is defined using the decay distributions from Section 5.3.1 as

$$\mathscr{L}(\xi_1, \xi_2, ..., \xi_N; \eta, \Delta\Phi) = \prod_{i=1}^{N} \mathscr{P}(\xi_i; \eta, \Delta\Phi) = \prod_{i=1}^{N} \frac{\mathscr{W}(\xi_i; \eta, \Delta\Phi)\varepsilon(\xi_i)}{\mathscr{N}(\eta, \Delta\Phi)}, \tag{13.8}$$

where $\varepsilon(\xi_i)$ is the efficiency. By taking the logarithm, the efficiency can be separated out

$$\ln \mathscr{L}(\xi_1, \xi_2, ..., \xi_N; \eta \Delta\Phi) = \sum_{i=1}^{N} \ln \frac{\mathscr{W}(\xi_i; \eta, \Delta\Phi)}{\mathscr{N}(\eta, \Delta\Phi)} + \sum_{i=1}^{N} \ln \varepsilon(\xi_i). \tag{13.9}$$

This can be turned into a minimization problem instead by taking the negative log-likelihood

$$-\ln \mathscr{L} = -\sum_{i=1}^{N} \ln \frac{\mathscr{W}(\xi_i; \eta, \Delta\Phi)}{\mathscr{N}(\eta, \Delta\Phi)} - \sum_{i=1}^{N} \ln \varepsilon(\xi_i). \tag{13.10}$$

It is clear that the efficiency term does not depend on the parameters R and $\Delta\Phi$, and does not affect the estimation of the parameters. The efficiency does, however, enter the normalization factor $\mathscr{N}$ which is given by

$$\mathscr{N}(\eta, \Delta\Phi) = \int \mathscr{W}(\xi; \eta, \Delta\Phi) \varepsilon(\xi) d\cos\theta d\Omega_1 d\Omega_2. \tag{13.11}$$

In practice, the integral is calculated using MC integration with weights representing the angular distribution $\mathscr{W}$ and detector reconstructed `PHSP` events representing the efficiency term. When fitting to all three event classes simultaneously, the combined negative-log-likelihood function to be minimized is

$$-\ln \mathscr{L}_{tot.} = -\ln \mathscr{L}_{\Lambda\bar{\Lambda}} - \ln \mathscr{L}_{\bar{\Lambda}} - \ln \mathscr{L}_{\Lambda},$$

where each contribution is normalized separately.

14. Analysis Description

The reaction $e^+e^- \to \Lambda\bar{\Lambda}$ has been studied in several recent BESIII analyses [142, 144]. These were double-tag analyses where all final state particles are reconstructed, sharing the same basic event selection criteria. The event selection used in this work largely follows the same standard. The main difference is that this analysis includes both a double-tag and a single-tag selection and combines the results from both. To make this possible the PID algorithm, described in Section 8.4.1, is used to identify protons and pions, whereas the previous analyses only used a selection based on particle momentum ranges. The PID algorithm is chosen here because it is able to provide much cleaner single-tag samples while maintaining comparable double-tag efficiency.

The event selection criteria used in this work can be divided into two stages. The first is a "preselection" stage providing a first filter. The second stage is more specific using criteria that apply only to either the double-tag, single-tag $\bar{\Lambda}$, or single-tag Λ samples. All criteria are explained in detail in the following sections. A common event selection procedure is used for all five data points, but for the sake of legibility, only the one at 2.396 GeV, will be used to illustrate and motivate the event selection criteria. The event selection is performed using software tools developed in Uppsala by Jacek Biernat.

14.1 Preselection

The first step of the event selection is the identification of charged tracks. The tracks are required to originate from a cylindrical volume around the IP with radius $R_{xy} = 10$ cm and length $\Delta z = 30$ cm. The allowed interaction volume is larger than in the analysis of $\eta' \to \pi^+\pi^-e^+e^-$ described in Chapter 9 to account for the long Λ lifetime. The polar angle θ of the charged tracks is required to satisfy $|\cos\theta| < 0.93$. The PID algorithm is used to identify protons/antiprotons and pions. For each track the particle-hypotheses p, π, and K are evaluated and the track is assigned the identity that is found to be most probable. There is no explicit requirement on the number of tracks, but in order for the event to be considered for further analysis the event needs to contain at least one $p\pi^-$ or $\bar{p}\pi^+$ combination. A vertex fit and subsequent secondary vertex fit is performed for all such combinations. The primary vertex fit, see Section 8.4.2, uses the track parameters of the final state particles to find the decay vertex and momentum of the corresponding $\Lambda/\bar{\Lambda}$. The secondary vertex fit, likewise described in Section 8.4.2, determines the decay length given

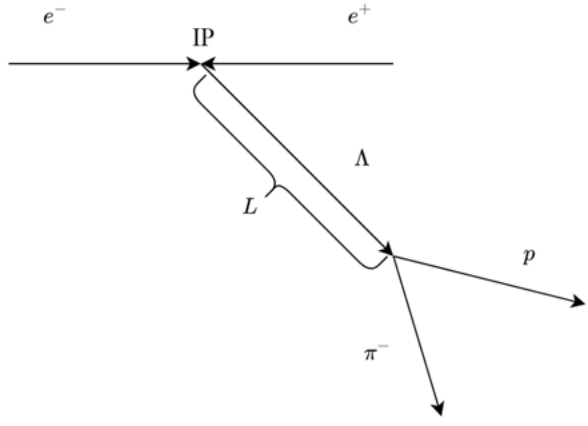

Figure 14.1. Sketch of the process $e^+e^- \to \Lambda\bar{\Lambda}, \Lambda \to p\pi^-$. There are two types of vertices that need to be considered: the production vertex, IP, where the e^+ and e^- collide to produce the $\Lambda\bar{\Lambda}$-pair and the decay vertex, where the Λ hyperon decays to produce the final state particles. The distance between the two is the decay length L.

the decay vertex from the primary vertex fit and the experimentally measured position of the IP. An illustration of the two vertices is shown in Fig. 14.1. If there is more than one combination of proton and pion tracks, the one with the largest decay length is kept as a $\Lambda/\bar{\Lambda}$ candidate. This procedure is repeated until there are no more tracks left to form a Λ or $\bar{\Lambda}$.

If there is exactly either one Λ or one $\bar{\Lambda}$ candidate, the event will be analyzed as a single-tag type event. If there is exactly one Λ- and one $\bar{\Lambda}$-candidate, the event will be analyzed as a double-tag event. By definition, these criteria ensure that there is no overlap between the double- and single-tag analyses.

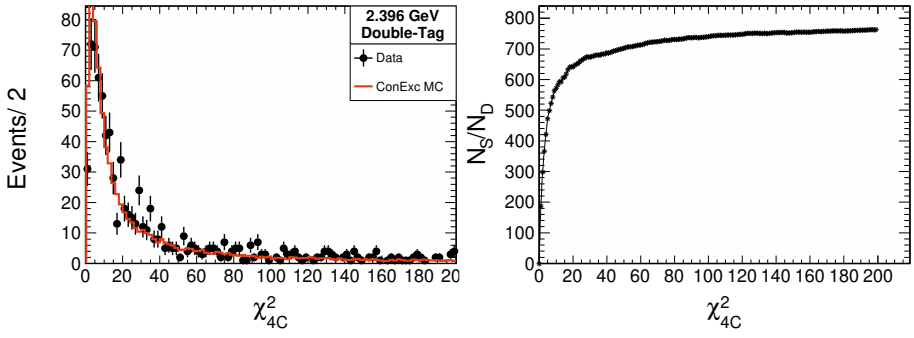

Figure 14.2. Distribution of the χ^2-variable from the 4C kinematic fit (left) and the FOM as a function of the χ^2 cutoff (right).

14.2 Double-Tag Selection

In the first step of the double-tag analysis chain, the four-momenta of the Λ and $\bar{\Lambda}$ candidates are used as input to a four constraint (4C) kinematic fit where the energy and momentum of the initial e^+e^--system are known. The fit is required to succeed and a cutoff is imposed on the goodness-of-fit. A comparison of the χ^2_{4C} distribution from data and MC is shown in Fig. 14.2. In order to find the optimal selection on χ^2_{4C}, the FOM N_S/N_D, where N_S is the number of events in the signal MC sample and N_D is the number of events in data, is calculated as a function of the upper limit. However, as can be seen in see Fig. 14.2, the resulting distribution has no maximum and hence the FOM does not help to decide on a cut. Therefore, an upper limit of $\chi^2_{4C} < 130$, which includes 95% of the data is chosen.

Subsequently, the invariant mass of the $p\pi^-$- and $\bar{p}\pi^+$-systems is required to be within a window around the mass of Λ [6]: $1.110\ \text{GeV}/c^2 < M_{p\pi^-/\bar{p}\pi^+} < 1.122\ \text{GeV}/c^2$. The width of the window corresponds to about four standard deviations, as determined by fitting a Gaussian function to the corresponding invariant mass distributions as shown in Fig. 14.3.

The number of background events remaining in the final data sample is estimated using the sidebands of the two-dimensional invariant mass distribution $M_{p\pi^-}$ versus $M_{\bar{p}\pi^+}$, see Fig. 14.4. The dashed black boxes in Fig. 14.4 represent the $\Lambda/\bar{\Lambda}$-sidebands, defined as $11\ \text{MeV}/c^2 < |M_{p\pi^-/\bar{p}\pi^+} - m_\Lambda| < 31\ \text{MeV}/c^2$, and the solid gray boxes represent non-Λ, non-$\bar{\Lambda}$ events for the same ranges. The number of background events in the signal region is estimated as

$$N_{BG} = \frac{1}{2}N_{dashed} - \frac{1}{4}N_{gray} = 13 \pm 3. \tag{14.1}$$

The background subtracted number of signal events in the experimental data sample becomes 583 ± 25 after these selection criteria. A cut flow for the

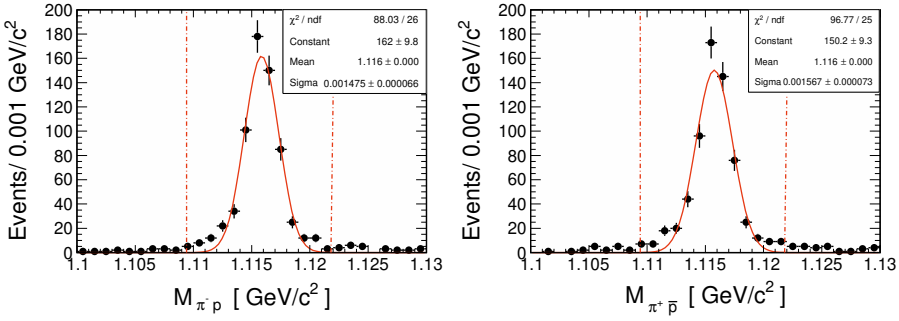

Figure 14.3. Fit of a Gaussian function to the invariant mass distributions of the $p\pi^-$- (left) and $\bar{p}\pi^+$- (right) systems used to determine the mass resolution at 2.396 GeV.

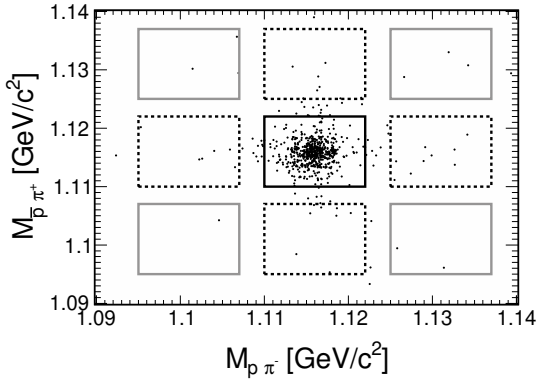

Figure 14.4. Two-dimensional $\Lambda/\bar{\Lambda}$ sidebands used to estimate the background content in the double-tag sample at 2.396 GeV.

analysis, including the cumulative efficiency, ε, estimated using the `ConExc` MC sample, is given in Table 14.1. Figures 14.5 and 14.6 show a comparison of data and MC in the momentum and angular distributions of the final double-tag event sample. The Λ and $\bar{\Lambda}$ angular distributions and final state particle momentum distributions agree well, while for the $\Lambda/\bar{\Lambda}$ invariant masses the resolution seems to differ between data and MC. This could affect the cross section result due to the invariant mass window selection and is considered below as a systematic effect. Moreover, there is a shift between data and MC in the $\Lambda/\bar{\Lambda}$ momentum distributions. The likely explanation for this effect is the known differences between data and MC in the resolution of the reconstructed track parameters for low momentum pions. Since the whole distribution is included in the analysis the shift is believed to have a negligible impact on the cross section. Another possible explanation is that the detection efficiency is

not correctly estimated by the detector simulations. This effect is considered as a source of systematic uncertainty.

Table 14.1. *Cut flow for the double-tag analysis chain estimated with 100,000* `ConExc` *MC events.*

Cut	N_{MC}	Cumulative efficiency (%)	N_{Data}
Preselection	21943	21.9 ± 0.1	817
χ^2_{4C}	20763	20.8 ± 0.1	758
Invariant mass window	18494	18.5 ± 0.1	596

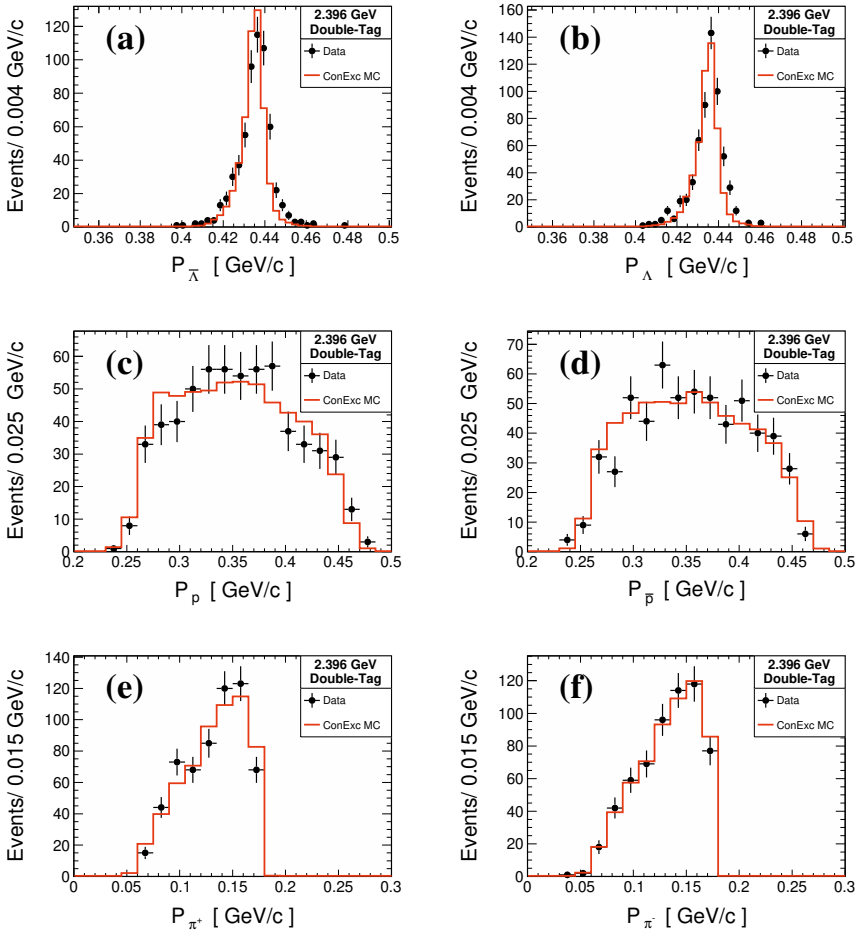

Figure 14.5. Momentum distributions for $\bar{\Lambda}$ (a), Λ (b), p (c), $\bar{p}$ (d), π^+ (e), and π^- (f) in the final double-tag event sample. The events fulfill the preselection as well as the χ^2_{4C} selection and the invariant mass window. The black points with error bars represent data, and the red histogram represents `ConExc` signal MC.

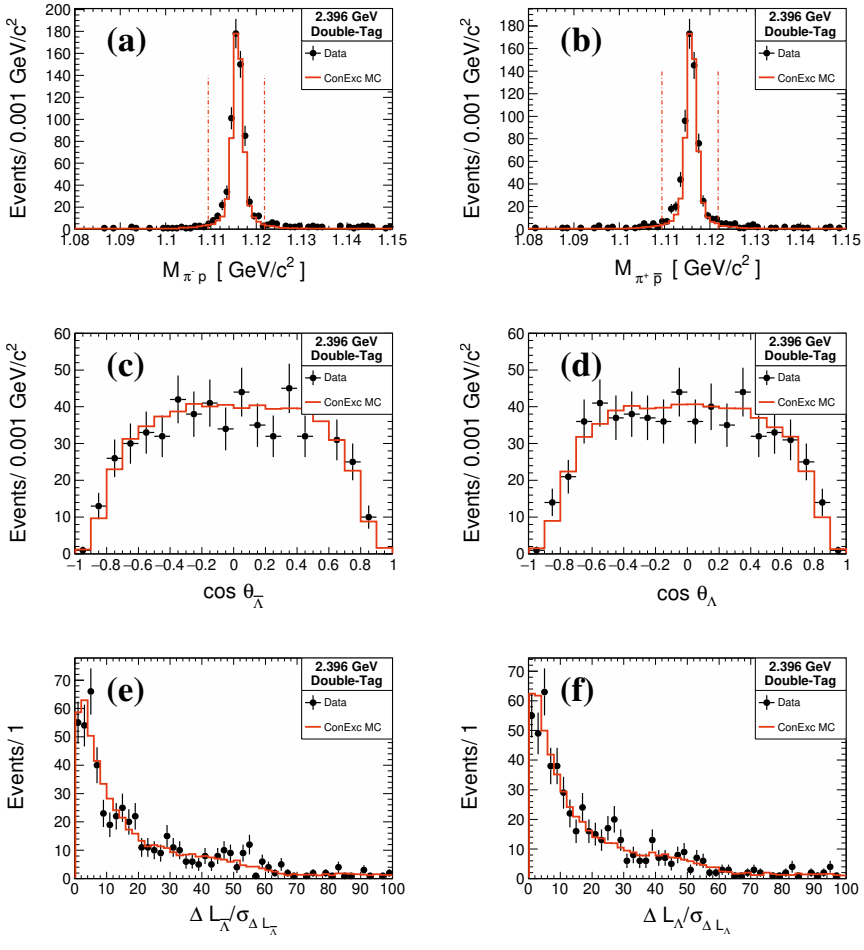

Figure 14.6. Distribution of the invariant mass of the $\pi^- p$- (a) and $\pi^+ \bar{p}$- (b) systems, the $\bar{\Lambda}$ (c) and Λ (d) scattering angles, and the decay length divided by its uncertainty for $\bar{\Lambda}$ (e) and Λ (f) in the final double-tag event sample. The invariant mass distributions (a, b) fulfill all criteria except the invariant mass window. The rest (c-f) fulfill all selection criteria. The black points with error bars represent data, and the red histogram represents `ConExc` signal MC. The dash-dotted vertical lines in the invariant mass distributions represent the selection windows.

14.3 Single-Tag $\bar{\Lambda}$ Selection

In the first step of the single-tag $\bar{\Lambda}$ analysis chain the four-momentum of the $\bar{\Lambda}$-candidate is used as input to a kinematic fit constrained to the energy and momentum of the initial e^+e^-- system. Because the corresponding Λ is undetected, a "missing particle" with unknown momentum but the mass of a Λ is assumed. Because the momentum direction of the missing particle is unknown, there is only one over-constraint and in the following this kinematic fit will be referred to as a one-constraint (1C) fit. For an event to be retained the fit is required to be successful, which means that the χ^2_{1C}-value must be lower than the default cutoff of 200.

Since $e^+e^- \to \Lambda\bar{\Lambda}$ is a two-body reaction, the Λ and $\bar{\Lambda}$ momenta are given by the center-of-mass energy and are different from that of $\bar{\Lambda}$'s produced in other processes such as $\Sigma^0\bar{\Lambda}$. The threshold for production of $\Sigma^0\bar{\Lambda}$ or $\Lambda\bar{\Sigma}^0$ is 2.308 GeV, and such background events are present in all samples. However, they are primarily expected to contaminate the signal region at higher energies, *i.e.* the samples with center-of-mass energy ≥ 2.64 GeV where the difference between the Λ and Σ^0 momenta is smaller. Furthermore, the cross section for $e^+e^- \to \Lambda\bar{\Sigma}$ is known to be lower than that for $e^+e^- \to \Lambda\bar{\Lambda}$ at the low energies, but approximately the same at the higher energies.

To guard against selecting events where the untagged particle is not a Λ, or a Λ that originates from the decay of another hyperon, a selection window is imposed on the $\bar{\Lambda}$ momentum. The momentum resolution of the $\bar{\Lambda}$ is estimated by fitting a Gaussian function to data, and is found to be approximately 4.7 MeV/c. The momentum is required to be within a window $|P_{\bar{\Lambda}} - \hat{P}_{\bar{\Lambda}}| < 14.1$ MeV/c, corresponding to about 3σ of the resolution, where $\hat{P}_{\bar{\Lambda}}$ is the expected momentum given the center-of-mass energy.

As can be seen in Fig. 14.7, the $\bar{\Lambda}$ momentum distribution in MC is shifted relative to data. This effect is primarily believed to be caused by differences in the estimation of track parameters for low momentum pions in data and MC, and its impact on the results of this work is discussed further in Section 17.5.

Furthermore, the invariant mass of the $\bar{p}\pi^+$-system is required to be within a window $|M_{\bar{p}\pi^+} - m_{\bar{\Lambda}}| < 4.7$ MeV/c^2, where $m_{\bar{\Lambda}}$ is the $\bar{\Lambda}$ mass. This corresponds to about four standard deviations, where the resolution is determined by fitting a Gaussian function to the $\bar{p}\pi^+$ invariant mass distribution, and is found to be about 1.2 MeV/c^2, see Fig. 14.8.

The number of background events remaining in the final data sample is estimated using the $\bar{\Lambda}$ sidebands, defined as 1.097 GeV/$c^2 < M_{\bar{p}\pi^+} <$ 1.106 GeV/c^2 and 1.125 GeV/$c^2 < M_{\bar{p}\pi^+} <$ 1.134 GeV/c^2. Figure 14.8 shows the $\bar{p}\pi^+$ invariant mass distribution from data with the sideband regions indicated. From the number of events in the sidebands, the number of background events in the signal region is given by

$$N_{BG} = \frac{N_{sidebands}}{2} = \frac{22}{2} = 11 \pm 2. \tag{14.2}$$

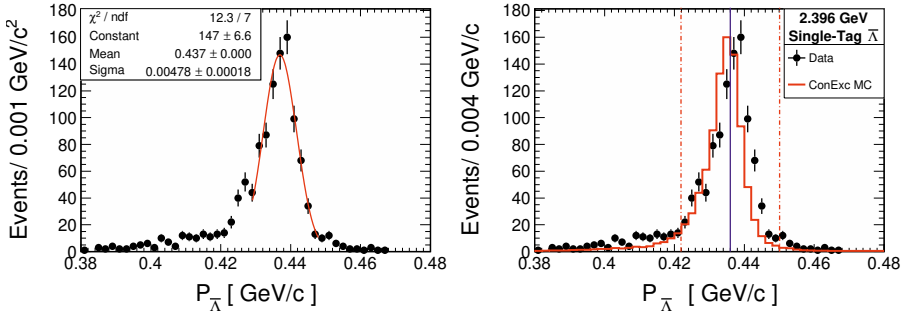

Figure 14.7. Fit to the $\bar{\Lambda}$ momentum distribution from data (left), and comparison of the $\bar{\Lambda}$ momentum distribution in data and `ConExc` MC (right). Black points with error bars represent data and the red histogram represents MC. The red dash-dotted vertical lines represent the selection window and the solid blue vertical line represents $\hat{P}_{\bar{\Lambda}}$.

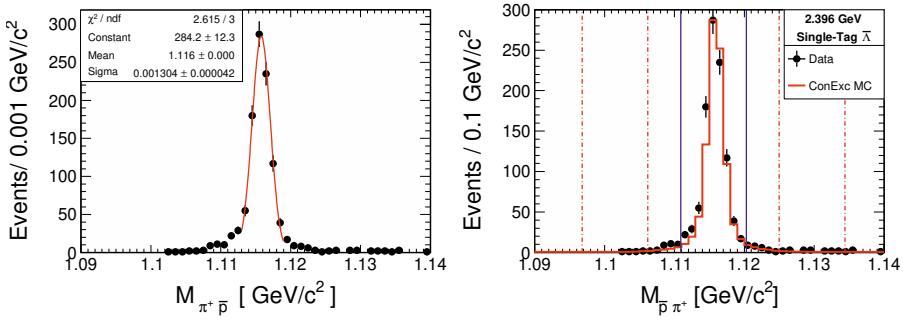

Figure 14.8. Fit to the invariant mass distribution in data (left) and comparison of the invariant mass distribution in data and `ConExc` MC (right). Data is represented by the black points and MC by the red histogram. The solid blue vertical lines represent the selection window and the red dash-dotted vertical lines represent the sideband regions.

The signal purity of the sample, defined as $N_S/(N_S+N_{BG})$, is approximately 99.5%. After all selection criteria and background subtraction, the number of signal events is determined to be 973±32. A cut flow, including the cumulative efficiency, is given in Table 14.2. Figure 14.9 shows a comparison of data and MC in the momentum and angular distributions of the final $\bar{\Lambda}$ single-tag event sample. There is generally a good agreement except for a shift in the missing mass distribution. The latter can be traced back to the aforementioned shift between data and MC in the Λ momentum distribution. Its impact on the results of this work is discussed in Section 17.5.

Table 14.2. *Cut flow for the single-tag $\bar{\Lambda}$ analysis chain estimated with 100,000 ConExc MC events.*

Cut	$N_{MC,1}$	ε_1 (%) $(\Lambda \to p\pi^-)$	$N_{MC,2}$	ε_2 (%) $(\Lambda \to \pi^0 n)$	N_{Data}
Preselection	16517	16.5 ± 0.1	41884	41.9 ± 0.1	2205
$L/\Delta L > 0$	14365	14.4 ± 0.1	37014	37.0 ± 0.1	1509
Momentum window	12611	12.6 ± 0.1	33035	33.0 ± 0.1	1079
Invariant mass window	11896	11.9 ± 0.1	31141	31.1 ± 0.1	984

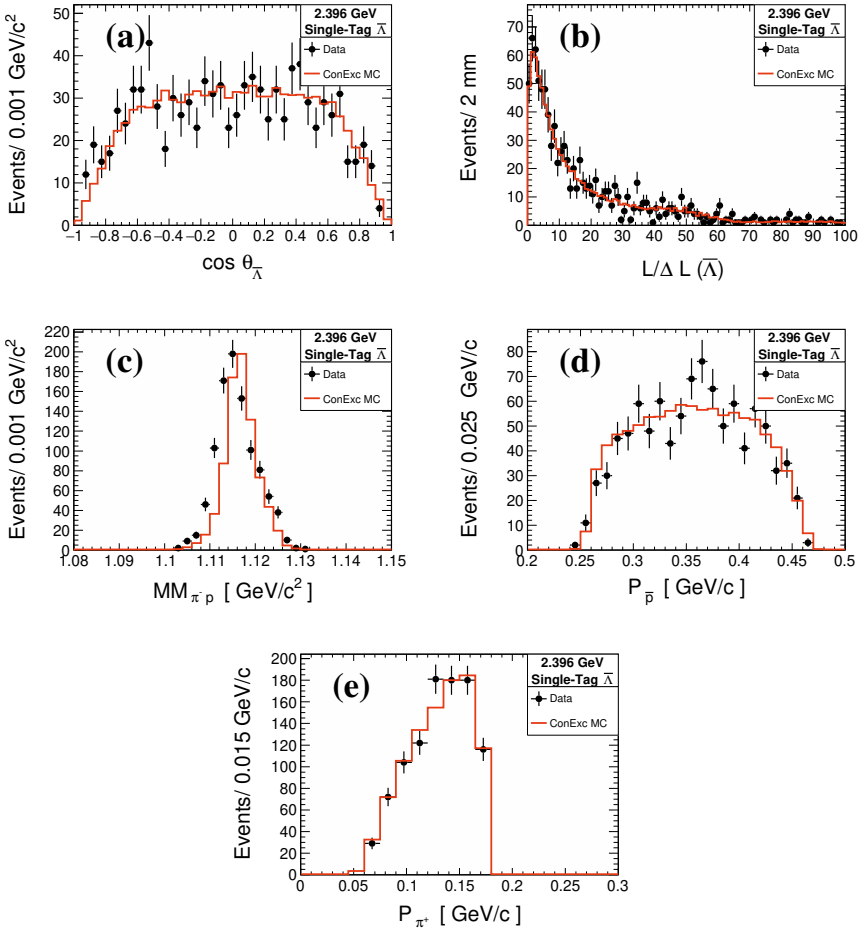

Figure 14.9. Distribution of the $\bar{\Lambda}$ scattering angle (a), decay length divided by its uncertainty (b), missing mass (c), $\bar{p}$ momentum (d), and π^+ momentum (e) in the final $\bar{\Lambda}$ single-tag event sample. The events fulfill the preselection criteria as well as the momentum and invariant mass conditions. The black points with error bars represent data, and the red histogram represents ConExc signal MC.

14.4 Single-Tag Λ Selection

As for the single-tag $\bar{\Lambda}$, the first step of the single-tag Λ selection is a 1C kinematic fit that is required to have a goodness-of-fit $\chi^2_{1C} < 200$. This initial event selection is not able to reject a large number of background events where the Λ candidate originates from the beam pipe region. This is clearly visible in the xy-projection of the Λ vertex distribution shown in Fig. 14.10. This effect is not reproduced in either the signal or inclusive MC samples and these events are concluded to be due to secondary material interactions that are not included in the GEANT4 simulation of the BESIII detector. Since the contribution from the side of the beam pipe which faces the outside of the storage rings dominates, these events are likely caused by lost or scattered beam particles. Their interactions with the beam pipe seem to produce a secondary proton as there is no corresponding source of background for the analysis of $\bar{\Lambda}$.

The strategy for dealing with these background events, as in the analysis of $\eta' \to \pi^+\pi^- e^+ e^-$, is to define a veto that can yield a clean sample of signal events. This is especially important for the unbinned maximum-log-likelihood fit. However, unlike the photon conversion background, which is well-known and included in the detector simulations, the behavior of these background events cannot be studied in an isolated setting. They can however still be rejected by identifying distributions where data and MC differ. From the experience with the study of $\eta' \to \pi^+\pi^- e^+ e^-$, criteria related to the location of the production vertex are expected to be powerful.

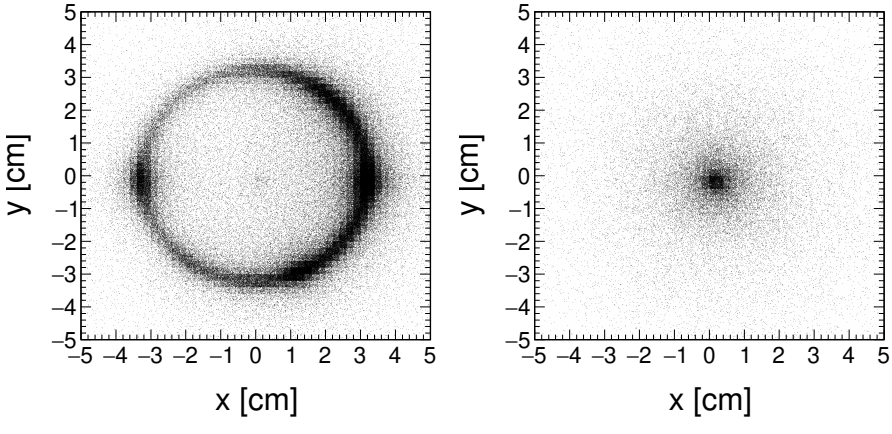

Figure 14.10. Distribution of Λ vertices in the xy-plane in data (left) and ConExc signal MC (right) after the selection based on the momentum and invariant mass criteria has been applied.

In the following, selection criteria using two variables to improve the sample purity are introduced. The first is the sum of χ^2-values from the primary and secondary vertex fits. All events with $\chi^2_{\text{vtx. 1}} + \chi^2_{\text{vtx. 2}} < 8$ are retained. This

specific value is chosen as an estimate of where the data and MC distributions deviate significantly from each other, see Fig 14.11.

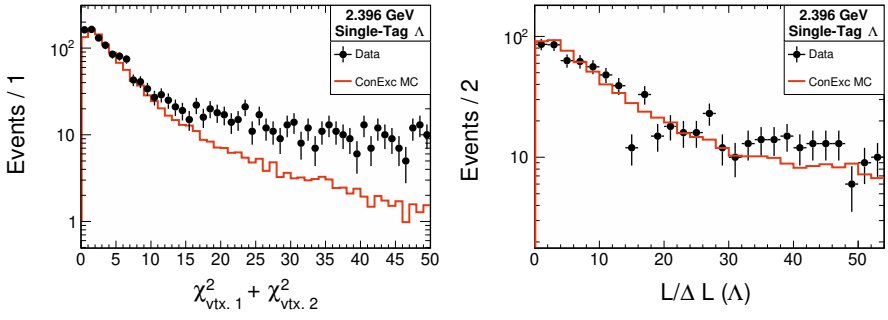

Figure 14.11. Comparison of $\chi^2_{\text{vtx. 1}} + \chi^2_{\text{vtx. 2}}$ (left) and $L/\Delta L$ (right) from data and MC. Black points with errors bars represent data and the red histogram represents `ConExc` MC.

The second variable is the decay length divided by its uncertainty. Its distribution is shown in Fig. 14.11. The distribution exhibits a discrepancy between data and MC above a value of 30. Hence, a selection criterion $L/\Delta L < 30$ is applied to improve the agreement and discard potential background events.

As in the single-tag analysis chain for $\bar{\Lambda}$, the momentum resolution of the Λ is estimated by fitting a Gaussian function to data as shown in Fig. 14.12. It is found to be 4.7 MeV/c. The Λ momentum is required to be within a range $|P_\Lambda - \hat{P}_\Lambda| < 14.1$ MeV/c, corresponding to about 3σ of the resolution, where $\hat{P}_\Lambda$ is the expected momentum given the center-of-mass energy.

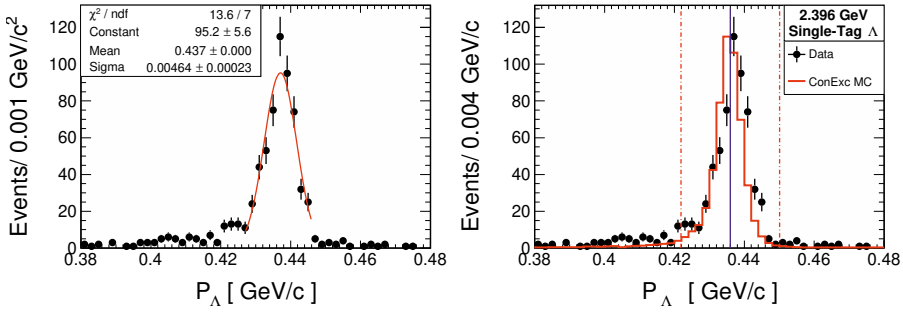

Figure 14.12. Fit to the Λ momentum distribution in data (left), and comparison of Λ momentum distribution in data and `ConExc` MC (right). Black points with errors bars represent data and the red histogram represents MC. The red dash-dotted vertical lines represent the selection window and the solid blue vertical line represents $\hat{P}_\Lambda$.

The resolution of the $p\pi$ invariant mass is determined by fitting a Gaussian function to the $p\pi^-$ invariant mass distribution. It is found to be about 1.2

MeV/c^2, see Fig. 14.13. The invariant mass of the $p\pi^-$-system is required to be within a window $|M_{p\pi^-} - m_\Lambda| < 4.7$ MeV/c^2, where m_Λ is the Λ PDG mass, corresponding to about 4σ of the peak.

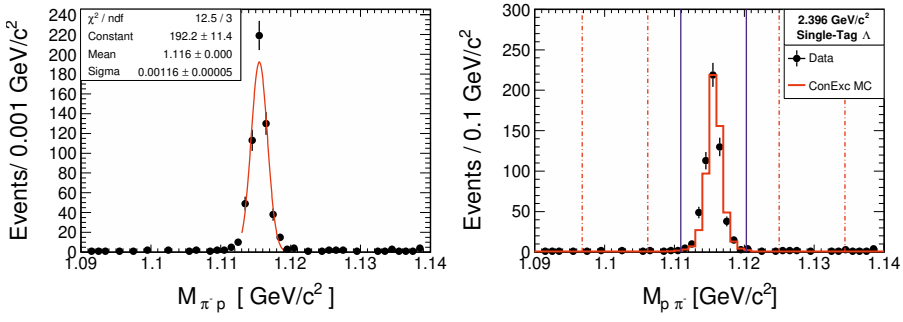

Figure 14.13. Fit to the invariant mass distribution in data (left) and comparison of the invariant mass distribution in data and `ConExc` MC (right). Data is represented by the black points and MC by the red histogram. The solid blue vertical lines represent the selection window and the red dash-dotted vertical lines represent the sidebands.

The number of background events remaining in the sample is estimated using the Λ sidebands, defined as $1.097\ \text{GeV}/c^2 < M_{p\pi^-} < 1.106\ \text{GeV}/c^2$ and $1.125\ \text{GeV}/c^2 < M_{p\pi^-} < 1.134\ \text{GeV}/c^2$. Figure 14.13 shows the $p\pi^-$ invariant mass distribution from data with the sideband regions indicated. From the number of events in the sidebands, the number of background events in the signal region is given by

$$N_{BG} = \frac{N_{sidebands}}{2} = \frac{18}{2} = 9 \pm 2. \tag{14.3}$$

The signal purity of the sample is approximately 98.5%. After all cuts and background subtraction 575 ± 25 events remain. A cut flow, including the cumulative efficiency, is given in Table 14.3.

Table 14.3. *Cut flow for the single-tag Λ analysis chain estimated with 100,000 `ConExc` MC events.*

Cut	$N_{MC,1}$	ε_2 (%) ($\bar{\Lambda} \to \bar{p}\pi^+$)	$N_{MC,2}$	ε_2 (%) ($\bar{\Lambda} \to \bar{n}\pi^0$)	N_{Data}
Preselection	18752	18.8 ± 0.1	44261	44.3 ± 0.1	620892
$\chi^2_{\text{vtx. 1}} + \chi^2_{\text{vtx. 2}}$	10990	11.0 ± 0.1	26701	26.7 ± 0.1	6222
$L/\Delta L$	8243	8.2 ± 0.1	19636	19.6 ± 0.1	1896
Momentum window	7742	7.7 ± 0.1	18543	18.5 ± 0.1	646
Invariant mass window	7612	7.6 ± 0.1	18215	18.2 ± 0.1	584

Figure 14.14 shows a comparison of data and MC for the momentum and angular distributions of the final Λ single-tag event sample. As for the $\bar{\Lambda}$ sample, there is generally a good agreement except for the shift in the missing

mass distribution. Figure 14.15 shows a comparison of the Λ vertex distribution in data and MC for the final data sample. The reduction of background events from the beam pipe compared to Fig. 14.10 can be clearly seen.

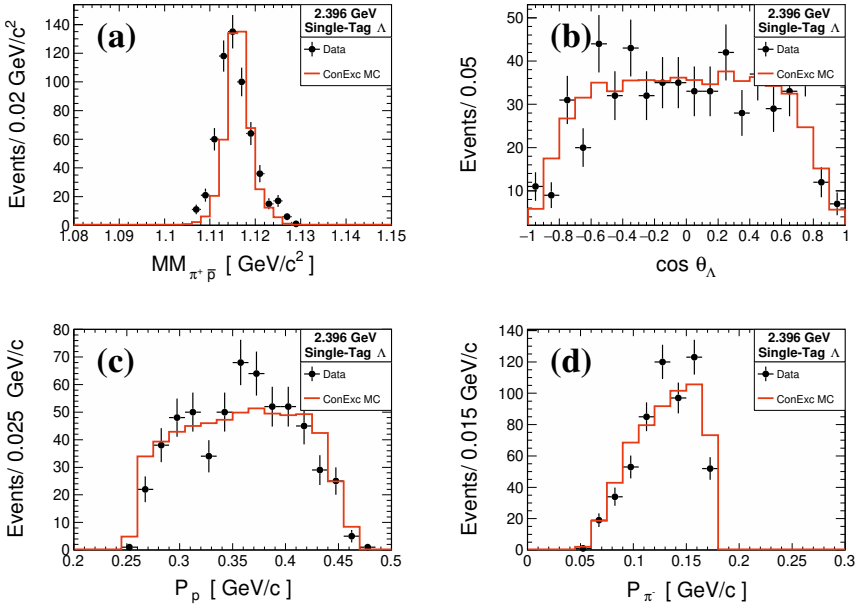

Figure 14.14. Distribution of the missing mass (a), Λ scattering angle (b), momentum of p (c), and momentum of π^- (d) in the final Λ single-tag sample. The events fulfill the preselection criteria as well as the momentum and invariant mass windows together with the cuts on $\chi^2_{\text{vtx. 1}} + \chi^2_{\text{vtx. 2}}$ and $L/\Delta L$. The black points with error bars represent data, and the red histogram represents signal MC.

14.5 Background Determination

While the momentum selection used in the single-tag analyses should reject most events where the undetected particle is not a Λ or $\bar{\Lambda}$, the processes $e^+e^- \to \Lambda\bar{\Sigma}^0$ or $e^+e^- \to \bar{\Lambda}\Sigma^0$ are particularly difficult to reject since the mass of Σ^0, 1192 MeV/c^2, is close to that of Λ. The momentum distribution of $\Lambda/\bar{\Lambda}$ produced together with $\bar{\Sigma}^0/\Sigma^0$ has a different mean value from those originating from $e^+e^- \to \Lambda\bar{\Lambda}$, but because of finite resolution some events in the tails may fall inside the chosen signal region. This effect is expected to be more significant at higher energies. In order to evaluate the contribution from such background, MC samples of 100,000 $e^+e^- \to \Lambda\bar{\Sigma}^0$ and 100,000 $e^+e^- \to \bar{\Lambda}\Sigma^0$ events are generated at all considered center-of-mass energies using the `ConExc` generator. The yields determined from these samples are subsequently normalized to the corresponding $e^+e^- \to \Lambda\bar{\Sigma}^0$ cross sections reported in Ref. [207]. The results are shown in Table 14.4. These background

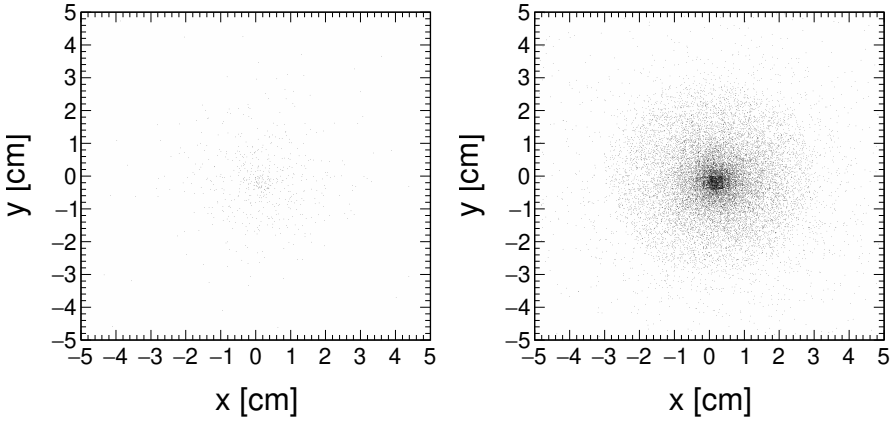

Figure 14.15. Distribution of Λ vertices in the xy-plane in data (left) and `ConExc` signal MC (right) after all selection criteria have been applied.

yields are subtracted from the signal yields presented above for the final result. The uncertainty of the background estimation is included in the cross section measurement as a systematic uncertainty. This contribution to the systematic uncertainty on σ_{Born} is non-negligible only at 2.9000 and 3.0800 GeV.

Table 14.4. *Normalized background yields from $e^+e^- \to \Lambda\bar{\Sigma}$ and $e^+e^- \to \bar{\Lambda}\Sigma^0$ events in the single-tag Λ and $\bar{\Lambda}$ samples and the corresponding contribution to the systematic uncertainty of the cross section measurement.*

E_{cms} (GeV)	Single-Tag Λ Yield	Single-Tag $\bar{\Lambda}$ Yield	$\sigma_{syst.}$ (%)
2.3864	0.1 ± 0.1	0.1 ± 0.1	-
2.3960	0.1 ± 0.1	0.7 ± 0.3	-
2.6450	0.5 ± 0.2	1.1 ± 0.3	-
2.9000	3.4 ± 1.1	4.0 ± 1.2	1.0
3.0800	2.0 ± 0.7	3.2 ± 1.1	0.9

15. Cross Section Measurement

The cross section is determined following the procedure described in Section 13.2. The background subtracted signal yields and efficiencies for all energy points are given in Table 15.1.

Table 15.1. *Background subtracted yields and efficiencies in units of percent for all data points.*

Energy (GeV)	$N_{\Lambda\bar{\Lambda}}$	$N_{\bar{\Lambda}}$	N_{Λ}	$\varepsilon_{\Lambda\bar{\Lambda}}$	$\varepsilon_{1,\bar{\Lambda}}$	$\varepsilon_{2,\bar{\Lambda}}$	$\varepsilon_{1,\Lambda}$	$\varepsilon_{2,\Lambda}$
2.3864	215 ± 16	373 ± 19	315 ± 20	18.5	12.3	31.5	11.6	28.0
2.3960	583 ± 25	973 ± 32	575 ± 25	18.5	11.9	31.1	7.6	18.2
2.6450	214 ± 16	294 ± 18	244 ± 17	21.7	9.5	30.7	8.7	27.5
2.9000	113 ± 11	118 ± 11	108 ± 11	19.11	6.6	24.4	6.3	22.5
3.0800	57 ± 8	60 ± 8	62 ± 8	14.8	4.5	17.4	4.1	16.0

Before the cross section can be calculated, the ISR and vacuum polarization correction factor $(1+\delta)$ must be determined for each energy point. This is done using the `ConExc` generator that requires an estimate of the energy dependence of the Born cross section as input. The cross section can be expressed in terms of the effective form factor $G_{eff}(q^2)$ defined in Eq. 5.17 as

$$\sigma_{Born}(q^2) = \left(1 + \frac{1}{2\tau}\right) \frac{4\pi\alpha^2\beta}{3q^2} |G_{eff}(q^2)|^2. \tag{15.1}$$

It has been established empirically that up to $|q^2|$ of a few $(\mathrm{GeV}/c^2)^2$, the form factors of the nucleons approximately follow a dipole behavior [69] of the form

$$G_D(q^2) \propto \frac{1}{(q^2 - c_1^2)^2}, \tag{15.2}$$

where the constant c_1 can be interpreted as the effective mass of the vector mesons that mediate the interaction with the photon. In the case of the proton, it has been found that $c_1 \approx 0.71$ GeV/c indicating that ρ^0 and/or ω mesons contribute the most. Making the ansatz that the same dipole behavior holds for the form factors of the Λ-hyperon at the momentum transfer scale considered here, the effective form factor is given by G_D multiplied by a scale parameter. The Born cross section can be expressed as

$$\sigma_{Born}(q^2) = \frac{1}{q^2} \frac{c_0 \cdot \beta}{\left(q^2 - c_1^2\right)^4}, \tag{15.3}$$

where the parameters c_0, c_1 are determined by fitting to data. This formula is fitted to previous cross section results from BaBar [140] and BESIII [143] along with the results from this work. The BESIII data point close to the production threshold is excluded from the fit as the dipole form factor cannot be expected to describe the cross section enhancement observed there. The width of the energy bins from BaBar is taken into account as uncertainty in the fit. The fitted function is used to re-evaluate the efficiencies and correction factors, whereafter the cross sections are calculated again. This procedure is repeated until the difference in the cross section results between the last two iterations is smaller than 0.1 pb. This tolerance is chosen to be significantly smaller than the statistical precision of the measurement. The condition is met after three iterations, and the final fit is shown in Fig. 15.1. The goodness-of-fit per degree of freedom is $\chi^2/(17-2) = 0.5$. The values of the fitted parameters are $c_0 = (8.9 \pm 0.7) \times 10^4$ pb $\cdot$ (GeV)^{10} and $c_1 = 1.77 \pm 0.01$ GeV. The value of c_1 indicates a mixture of contributions from the $\phi(1680)$ and $\phi(2170)$ mesons. This is discussed further in Section 20.2. The cross section values determined for each subsample at all energies are given in Table 15.2. The final correction factors and the weighted mean value for the cross section at all energies are given in Table 16.1.

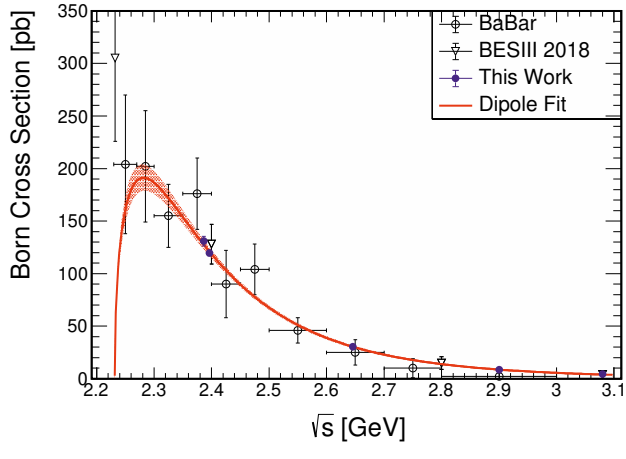

Figure 15.1. Fit of the cross section lineshape assuming the dipole form for the effective form factor (Eq. (15.3)) to the previous results from BaBar [140] (black points) and BESIII [143] (white triangles), together with data from this work (blue points). The solid red line represents the fit result, and the pink bands represent a 1σ deviation.

Table 15.2. *Born cross section determined for each subsample at all energies.*

Energy [GeV]	σ_{Born} [pb] (Single-Tag Λ)	σ_{Born} [pb] (Single-Tag $\bar{\Lambda}$)	σ_{Born} [pb] (Double-Tag)
2.3864	127.0 ± 7.6	137.0 ± 7.1	127.5 ± 9.2
2.3960	118.9 ± 5.0	122.1 ± 4.0	116.4 ± 5.0
2.6450	29.6 ± 2.0	32.0 ± 1.9	29.1 ± 2.1
2.9000	8.2 ± 0.8	8.5 ± 0.8	8.7 ± 0.8
3.0800	4.8 ± 0.7	4.1 ± 0.7	4.4 ± 0.6

16. Form Factor Measurement

In order to measure the form factors of Λ, the angles defined in section 5.3.1 are determined for all events. These are subsequently used as input to the MLL fit procedure described in Section 13.3. Before applying the MLL fitting procedure to data, it must be ensured that it can correctly estimate the parameters of the angular distribution. This is tested using the `mDIY` generator based on the full angular distribution given in Eq. 5.33 with parameters set to $\Delta\Phi = 42.2^\circ$, $R = 0.959$ ($\eta = 0.112$), and $\alpha_\Lambda = -\alpha_{\bar{\Lambda}} = 0.754$ (values based on Ref. [121]). An ensemble of samples that match the data sample at 2.396 GeV in size is generated. Each sample contains 583 double-tag events, 973 single-tag $\bar{\Lambda}$ events, and 575 single-tag Λ events. Furthermore a number of extra events corresponding to background are added to each of the samples to check if the background contamination in the samples has any effect on the fit result. The background events are drawn from a phase space MC sample. The MLL fit is performed for each sample and the values of the parameters R_i and $\Delta\Phi_i$ are estimated. The corresponding true values can be labelled $\hat{R}$ and $\Delta\hat{\Phi}$. Following the reasoning presented in Section 10.4, the distributions of the R_i and $\Delta\Phi_i$ variables are subsequently studied. The shapes of these distributions allow several different aspects of the estimator to be investigated. If the conditions of the central limit theorem are fulfilled, the distribution should be Gaussian. If it is not, this indicates issues that need to be investigated further. If the distribution is Gaussian, its mean value a can be studied to estimate the bias of the method. Note that unlike in Section 10.4, it is not divided by the fit uncertainty to get the pull distribution. The reason for this is that there is no a priori estimate of the uncertainty. Rather, the distribution of fit results should be used to establish a relationship between the number of events and the expected precision. The standard deviation of the Gaussian distribution of the fit results can be expressed as

$$\sigma = \Sigma/\sqrt{N}, \tag{16.1}$$

where N is the number of events in one sample and Σ is a scaling parameter that can be used to estimate the amount of data needed for a given level of precision. Figure 16.1 shows the distributions for R_i and $\Delta\Phi_i$. The distribution for R is approximately Gaussian and a fit yields the mean value $\mu_R = 0.959 \pm 0.003$ and standard deviation $\sigma_R = 0.086 \pm 0.002$. That is, the bias is $\Delta_R = \mu_R - \hat{R} = 0.000 \pm 0.003$ which is consistent with zero. The scaling parameter is determined to be $\Sigma_R = \sigma_R \cdot \sqrt{N} = 126 \pm 3$. The corresponding distribution

for $\Delta\Phi$ is approximately Gaussian, but with a tail toward higher values. A fit to the Gaussian component yields $a = 42.0 \pm 0.3$ and $b = 8.0 \pm 0.2$. The bias is found to be $\Delta_{\Delta\Phi} = 0.2 \pm 0.3$, consistent with zero, and the uncertainty parameter $\Sigma_{\Delta\Phi} = \sqrt{N} \cdot b_{\Delta\Phi} = 369 \pm 9$.

The tail can be understood as a consequence of the ambiguity between the solutions $\Delta\Phi$ and $180^\circ - \Delta\Phi$. In principle, the $\cos(\Delta\Phi)$ terms of the angular distribution should make it possible to choose the correct solution. However, it is suppressed by an additional factor of α_Λ compared to the $\sin(\Delta\Phi)$ term and is consequently a weaker constraint. For small sample sizes a drift toward higher values of $\Delta\Phi$ is therefore visible. But since this effect is rare and less than 10% of all fits lie in this tail, it is not corrected for. However, it is still worthwhile to investigate if there are other reasons for the asymmetry. Therefore the same type of consistency check is performed for the individual subsamples.

In particular, studies of the single-tag Λ sample reveal a hidden effect. As can be seen in Fig. 16.2, the distribution of $\Delta\Phi_i$ for the single-tag Λ sample shows a strong bias. About 10% of all fits yield a result of 90°. Since this does not occur for the double-tag or single-tag $\bar{\Lambda}$ samples, the conclusion is that this is an artifact of the small sample size. To learn more, a scan of the likelihood function as a function of the value of $\Delta\Phi$ can be performed. This is done for one of the samples that yields the correct solution and four randomly chosen samples that yield the result $\Delta\Phi = 90^\circ$. The result is shown in Fig. 16.3. In all cases where $\Delta\Phi = 90^\circ$, the distribution has a single minimum. This is different from what is expected in the single-tag fit. The angular distribution in this case only depends on $\sin\Delta\Phi$, and there are therefore always two equivalent solutions $\Delta\Phi$ and $180^\circ - \Delta\Phi$. This is indeed what is seen for the samples that yield results $\Delta\Phi \neq 90^\circ$. Whether or not this is a problem depends on the depth of the minimum, which is directly related to the fit uncertainty. If the uncertainty is much larger than the difference between the true and estimated value, the corresponding sample can safely be included in the overall fit since its impact on the result will be small. If the uncertainty is small, on the other hand, including such a sample in the overall fit will shift the $\Delta\Phi$ away from the true value. In such cases it should clearly not be included. By studying the pull distribution $(\Delta\Phi_i - \hat{\Delta\Phi})/\sigma_{\Delta\Phi_i}$ the typical significance of the discrepancy can be estimated. In Fig. 16.4, the pull distribution for the samples that yield $\Delta\Phi = 90^\circ$ is shown, and the deviation from the nominal result is always larger than 1σ. The conclusion is that in order to avoid a systematic shift of the overall fit result, such samples must be excluded from the overall fit. Fortunately, the likelihood-scan can be done for any individual sample and this ensures that the wrongly fitted cases can always be identified even in the experimental data.

When fitting to the experimental Λ single-tag sample at 2.396 GeV, one finds $\Delta\Phi = 90^\circ$ and a likelihood scan, see Fig. 16.5, shows a single, narrow minimum similar to the cases shown in Fig. 16.3. Therefore it is not included in the overall fit used to determine $\Delta\Phi$ at this particular energy. The value of

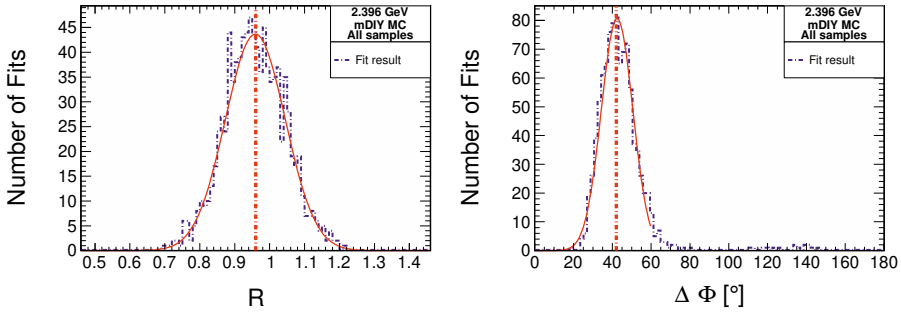

Figure 16.1. Distribution of R_i (left) and $\Delta\Phi_i$ (right) from the fits to the ensemble with background events included. The solid red line represents the fitted Gaussian function, and the dash-dotted vertical line represents the input value.

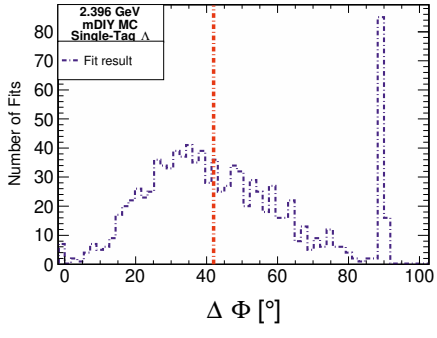

Figure 16.2. Results for the parameter $\Delta\Phi$ from the fits to the Λ single-tag ensemble with background events included. The dash-dotted vertical line represents the input value.

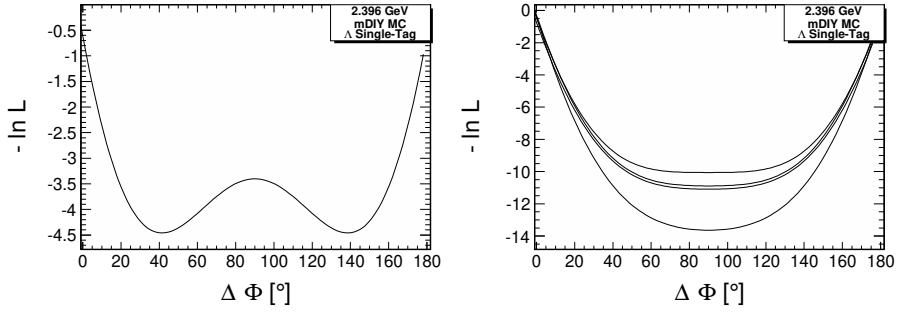

Figure 16.3. Likelihood scans for one of the samples that yields a correct result (left) and for four MC samples that yield $\Delta\Phi = 90^\circ$ (right).

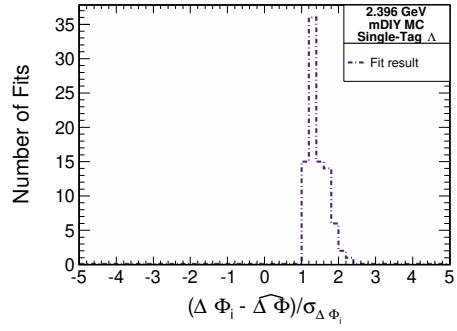

Figure 16.4. Pull distribution for $\Delta\Phi$ for the samples that yield a result $\Delta\Phi = 90^\circ$.

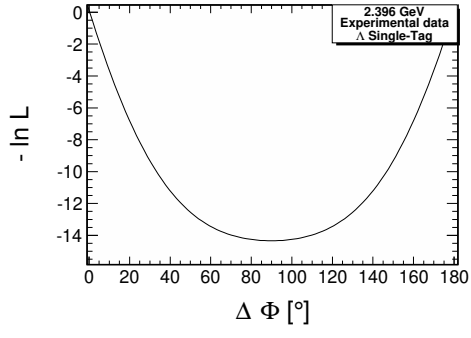

Figure 16.5. Likelihood scan for the experimental single-tag Λ data sample at 2.396 GeV.

$\Delta\Phi$ is instead fixed from the fit to the double-tag and single-tag $\bar{\Lambda}$ samples, such that the single-tag Λ sample can still be used for the determination of R. The latter is unproblematic. At the other energies studied in this work, this effect is not seen, and all three samples can be used. The results of the MLL fit at all energies are shown in Table 16.1. It is worth noting that the relative phase $\Delta\Phi$ lies in the range $[0^\circ, 90^\circ]$ at 2.3864 GeV and 2.396 GeV, while at 2.645 GeV and 2.9 GeV it lies in the range $[90^\circ, 180^\circ]$. The interpretation of this result is discussed in Section 20.2.

From Eq. 5.40 it is clear that any polarization or spin correlation matrix element $C_{\mu\nu}$ can be inspected via the moment defined as

$$M_{C_{\mu\nu}}(\cos\theta) = \frac{1}{N}\sum_{i}^{N_{\cos\theta}} \hat{n}_\mu \hat{n}_\nu, \tag{16.2}$$

where N is the total number of events and the index i runs over all events in a $\cos\theta$ bin. To evaluate, as a cross check, if the parameters determined with

Table 16.1. *Results for the Born cross section, form factor R, and relative phase* $\Delta\Phi$*. The former is calculated by taking the inverse variance weighted mean of results from the double-tag, single-tag* $\bar{\Lambda}$*, and single-tag* Λ *samples and the latter is determined through the MLL fit.*

Energy [GeV]	$(1+\delta)$	σ_{Born} [pb]	R	$\Delta\Phi$ [°]	τ
2.3864	0.97	$131.6 \pm 4.6_{stat.}$	$1.01 \pm 0.14_{stat.}$	$39 \pm 12_{stat.}$	1.14
2.3960	0.98	$120.3 \pm 2.6_{stat.}$	$0.91 \pm 0.08_{stat.}$	$42 \pm 10_{stat.}$	1.15
2.6450	1.21	$30.4 \pm 1.1_{stat.}$	$1.04 \pm 0.16_{stat.}$	$146 \pm 13_{stat.}$	1.41
2.9000	1.59	$8.8 \pm 0.5_{stat.}$	$0.98 \pm 0.24_{stat.}$	$151 \pm 19_{stat}$	1.69
3.0800	1.96	$4.6 \pm 0.4_{stat.}$	$0.51 \pm 0.29_{stat.}$	$78 \pm 59_{stat.}$	1.91

the MLL fit describe our data well, first an MC sample is generated using the `mDIY` generator where R and $\Delta\Phi$ are set to the fit results at 2.396 GeV. Then all 16 (acceptance uncorrected) moments in 10 bins of $\cos\theta_\Lambda$ for this sample. The result is compared with data and a phase space MC sample with $\eta = 0$ and $\Delta\Phi = 0$. For the single-tag samples, only the polarizations $M_{C_{\mu 0}}/M_{C_{0\nu}}$ are accessible. The combined result for the polarizations from all three samples is shown in Fig. 16.6. The fit results yield good agreement in all four distributions and, in particular, for the polarization in the y-direction. Since $\Lambda/\bar{\Lambda}$ is only polarized in the y-direction, the `mDIY` and phase space samples give the same result for the polarizations in the x- and z-directions.

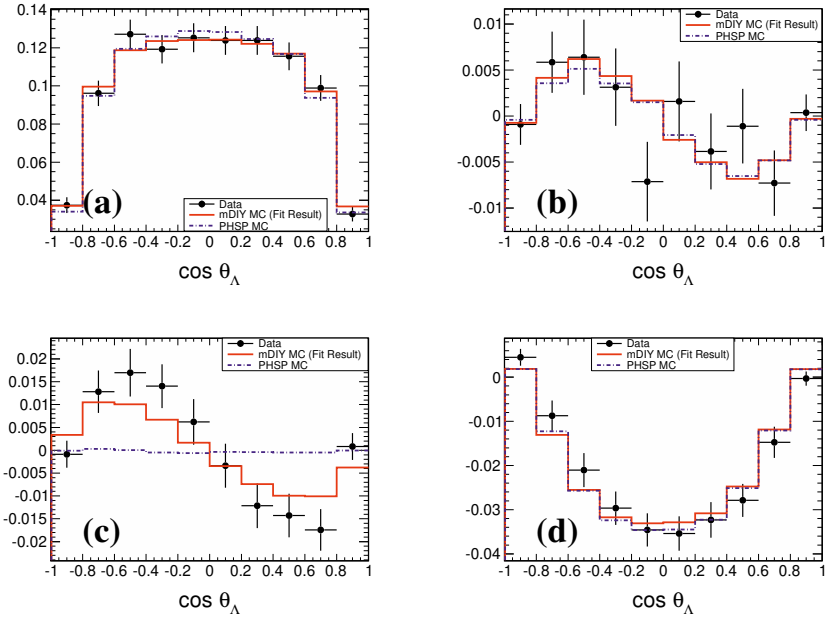

Figure 16.6. Moments of C_{00} (a), $C_{x0}+C_{0x}$ (b), $C_{y0}+C_{y0}$ (c), and $C_{z0}+C_{0z}$ (d) as a function of $\cos\theta_{\Lambda/\bar{\Lambda}}$ determined from the double-tag and single-tag samples at 2.396 GeV.

17. Systematic Uncertainties

This work is based on several data sets taken at different center-of-mass energies that, in principle, all come with different systematic uncertainties. However, performing a full evaluation of the systematic uncertainties at each point quickly becomes cumbersome. Furthermore, many of the data samples analyzed in this work are quite small, and statistical fluctuations are expected to dominate over systematic effects. When analyzing these samples, it is difficult to determine whether any of the observed deviations from the nominal results are statistical or systematic in nature and one risks double-counting statistical uncertainties as systematic ones. A more precise estimate can be achieved by evaluating systematic uncertainties using high statistics samples and extrapolating from these to the other samples.

As a compromise between using large samples and covering the whole energy range, the systematic uncertainties are evaluated for the data samples at 2.396 and 2.9 GeV and extrapolated to the other data points using a linear extrapolation of the form

$$\sigma_{E_{cms}} = \sigma_{2.396} + \frac{\sigma_{2.9} - \sigma_{2.396}}{2.9 - 2.396}\,(E_{cms} - 2.396)\,, \tag{17.1}$$

where E_{cms} is the center-of-mass energy where the systematic uncertainty is to be evaluated, and $\sigma_{2.396}$ and $\sigma_{2.9}$ are the systematic uncertainties at 2.396 GeV and 2.9 GeV.

The procedure for estimating systematic uncertainties consists of two parts. First, there are well-known systematic effects that need to be propagated to the cross section and form factor measurements. For example, the luminosity at all energy points has been measured up to 1% precision, and 1% is taken as the associated systematic uncertainty on the Born cross section. The uncertainty of the $e^+e^- \to \Lambda\bar{\Sigma}$ background yields must likewise be propagated to the cross section result. The second aspect is that the specific event selection procedure used in this work may have introduced new systematic effects. In order to investigate if this is the case, the criteria are varied and σ_{Born}, R, and $\Delta\Phi$ are determined for each variation. Then, one must determine whether the associated change in results is significant or not, *i.e.* whether it indicates a systematic effect or is merely a statistical fluctuation. However, data sets selected from the same sample with varying selection criteria are highly correlated, and comparing the differences directly to the full statistical uncertainty is not appropriate. Instead, the uncorrelated uncertainty is computed following

Barlow [208]

$$\sigma_{uncorr} = \sqrt{\left|\sigma^2_{nominal} - \sigma^2_{variation}\right|}. \tag{17.2}$$

The significance of the deviation from the nominal result is then given by

$$\zeta = \frac{a_{nominal} - a_{variation}}{\sigma_{a,uncorr.}}, \tag{17.3}$$

where a represents either σ_{Born}, R, or $\Delta\Phi$. Deviations with a significance corresponding to two or more $\sigma_{uncorr.}$, *i.e.* with $\zeta > 2$, are considered to be significant and the origin of these deviations is investigated further. The convention of considering deviations larger than two standard deviations significant is based on the argument that the probability that the two results come from the same underlying distribution is less than about 5%. There may also be cases where the results show a clear trend as a function of the selection criterion. Such trends are signs of systematic effects and must be investigated more closely even if the individual results do not deviate significantly from the nominal value.

As selection criteria are made either more inclusive or more exclusive, one will eventually reach a critical point where relatively small differences between data and MC have a significant impact on the result. One must aim to choose selection criteria with a certain safety margin away from such points. If one finds that the results deviate significantly from the nominal value at extreme values of the selection criteria, this does not necessarily indicate a systematic effect that must be accounted for, but can mean that a critical value has been reached. In such a case, there is no need to assign a systematic uncertainty or apply corrections as long as the nominal selection criterion can be chosen well away from the critical value.

In some cases, a systematic uncertainty may apply to the results from just one or two, but not all three subsamples. These uncertainties are propagated to the combined result from all three subsamples by taking the mean across the three samples weighted by the statistical uncertainty

$$\hat{\sigma}_{syst.} = \frac{\sum_i \sigma_{syst.,i}/\sigma^2_{stat.,i}}{\sum_i 1/\sigma^2_{stat.,i}}, \tag{17.4}$$

where $\sigma_{syst.}$ and $\sigma_{stat.}$ are the systematic and statistical uncertainties of a particular quantity. When a systematic uncertainty is not applicable for a given sample, it is taken to be zero. The statistical uncertainty is used here as a measure of the importance of a subsample for the combined result.

The structure of this chapter is as follows. In the first three sections I will discuss the known systematic effects and evaluate their impact on the measurement of the Born cross section, R and $\Delta\Phi$. The final two sections are devoted to searches for systematic effects caused by the event selection criteria in the

double-tag and single-tag analyses respectively. Throughout the chapter, the data set taken at 2.396 GeV will be used to demonstrate the procedure. For brevity, only the checks where significant systematic effects are found are described. Summaries of all systematic uncertainties, including the results of the extrapolation, can be found in Tables 18.1, 18.2, and 18.3.

17.1 Efficiency Model Dependence

The reaction $e^+e^- \to \Lambda\bar{\Lambda}$ is described by two global parameters η (related to R, see Eq. 5.14), and $\Delta\Phi$ and their influence on the angular distribution of the hyperons and their daughter baryons is given by Eq. 5.33. In general, this means that the detection efficiency depends on the value of both parameters. However, studies of the `mDIY` MC sample have shown that the efficiency dominantly depends on the distribution of the Λ scattering angle θ. Integrating Eq. 5.33 over all angles except θ, we find

$$\frac{d\sigma}{d\cos\theta} \propto 1 + \eta\cos^2\theta, \tag{17.5}$$

and we see that if only the angle θ is important, the efficiency only depends on the parameter η. So far, we have used the central value of η determined with the MLL fit as input to the `ConExc` MC generator to estimate the efficiency. It is however also important to propagate the uncertainty of η to the efficiency. This is done through a series of pseudo-experiments where a large MC sample with flat angular distribution that has been subjected to the detector simulation is re-weighted according to the expected Λ scattering angle distribution. Each event is assigned a weight $1+\eta\cos^2\theta$, where η is sampled from a Gaussian distribution given by the central value and standard deviation from the MLL fit. Subsequently, the sum of weights is divided by the total number of generated events and the analytical integral of the probability distribution, $\frac{1}{3}(3+\eta)$. This yields the efficiency corresponding to the given angular distribution. This number can then be used to calculate the cross section. The pseudo-experiments yield an approximately Gaussian distribution for the cross section as shown in Fig. 17.1. The standard deviation of this Gaussian, 0.75 pb or 0.5%, is taken as the systematic uncertainty due to the model dependence of the efficiency at 2.396 GeV.

17.2 Cross Section Energy Dependence

The ISR and VP correction factors depend on the model used to describe the energy dependence of the cross section. The nominal results were produced assuming a dipole approximation. To investigate how much the correction factors can vary between different models, we determine the correction factors

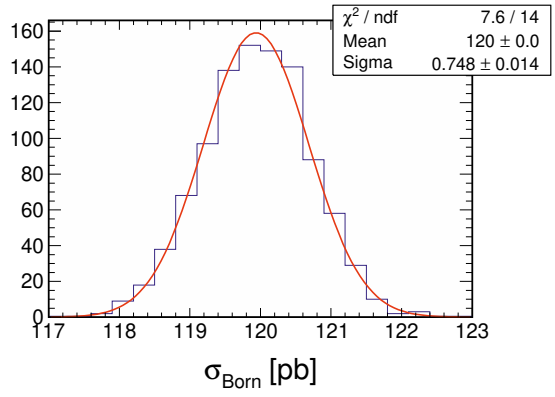

Figure 17.1. Distribution of the Born cross section in the ensemble of pseudo-experiments where the angular distribution parameter η was sampled from a Gaussian distribution with mean 0.164 and standard deviation 0.086. The red curve represents a Gaussian function fitted to the data.

using a pQCD description of the cross section instead. It has been shown [131, 132] that at high $q^2 \gg (\Lambda_{QCD})^2 \approx 0.3$ GeV$^2/c^4$ the effective form factor for baryon-antibaryon production in e^+e^--annihilation is described by the power law

$$G_{eff}(q^2) \propto \frac{1}{(q^2)^2}, \tag{17.6}$$

where the constant of proportionality cannot be predicted from QCD but must be determined empirically. The Born cross section is sometimes expressed by representing the denominator as [209]

$$\sigma_{Born}(q^2) = \frac{c_0 \cdot \beta}{\left(\sqrt{q^2} - c_1\right)^{10}}, \tag{17.7}$$

where the parameters c_0, c_1 are determined by fitting to data. With this function, the iterative procedure described in Chapter 15 is repeated. Once again, the stopping condition is met after three iterations, and the final fit is shown in Fig. 17.2. The goodness-of-fit per degree of freedom is $\chi^2/(17-2) = 1.0$. The cross section is estimated using the new correction factors, and the difference compared to the nominal result, shown in Table 17.1, is taken as the systematic uncertainty due to the model dependence of the correction factors.

17.3 Reconstruction Efficiency for $\Lambda/\bar{\Lambda}$

The efficiencies of the track reconstruction and particle identification algorithms are different in data and MC and as a result there are also differences

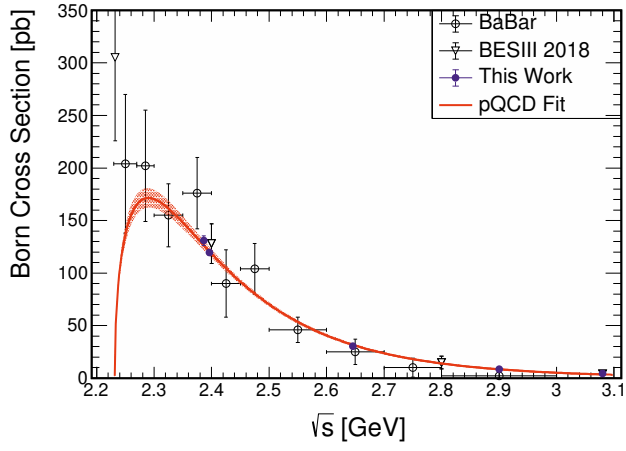

Figure 17.2. Fit of the pQCD power law of Eq. (17.7) to the previous cross section results from BaBar [140] (black points) and BESIII [143] (white triangles), together with data from this work (blue points). The solid red line represents the fit result, and the pink bands represent a 1σ deviation.

Table 17.1. *Difference between the cross sections calculated using correction factors determined with the nominal dipole fit and pQCD fit at each energy point.*

Energy [GeV]	$\Delta\sigma_{Born}[\%]$
2.3864	0.6
2.3960	0.6
2.6450	0.3
2.9000	0.2
3.0800	0.1

in the reconstruction efficiency for Λ hyperons. This affects both the cross section and form factor measurement. To evaluate how large the effect is, one needs to first analyze a control sample and estimate the size of the efficiency difference. However, the possibilities for doing this with the samples used in this work are severely limited by the sample size. Instead, the best option available is to use the much larger J/ψ sample where the amount of data is not an issue. Since this data set was taken with the same detector setup and reconstruction software, one expects to find the same systematic differences between data and MC. The final question to be addressed is what process to use for studying the Λ hyperons. Within the BESIII collaboration, two studies have been performed: one using $J/\psi \to \Lambda\bar{\Lambda}$ [210] and one using $J/\psi \to pK^-\Lambda$ [211]. The latter has the advantage of producing Λ hyperons with a continuous momentum distribution, but the study only provides the

efficiency difference between data and MC for the final state particles. The former gives Λ hyperons with one single momentum, which is much larger than the average Λ momentum in this work, but on the other hand the study investigated the difference between data and MC in the combined efficiency of tracking, PID, and vertex fit for reconstructing Λ hyperons. For the purpose of this work, it was considered most important to study systematic effects in the combined efficiency. To do this using $J/\psi \to pK^-\Lambda$ would require a new analysis that includes the vertex fit, and this was considered beyond the scope of this work. Therefore, the results from Ref. [210] based on the $J/\psi \to \Lambda\bar{\Lambda}$ control sample are used. While the $\Lambda/\bar{\Lambda}$ momenta differ significantly in the control sample and this work, the scattering angle distributions are similar. For the final state particle momentum ranges, the situation is somewhat better. The pion momenta overlap almost completely, while for (anti)protons, there is an overlap with the tail of the distributions from $J/\psi \to \Lambda\bar{\Lambda}$ with comparatively few events. However, it has been shown that the largest differences between data and MC arise for pions. Therefore this method can provide at least a rough estimate of the systematic uncertainties at the energies studied in this work.

Reference [210] provides correction factors for the efficiency difference between data and MC as a function of the $\Lambda(\bar{\Lambda})$ scattering angle. To evaluate the effect on the cross section, the ConExc MC samples are generated and reweighted using these correction factors. For each event, the following procedure is applied:

1. Find the central value and uncertainty of the correction factor based on $\cos\theta$. For double-tag events, this is done for both Λ and $\bar{\Lambda}$.
2. Sample the correction factor from a Gaussian distribution with mean and standard deviation according to the previous step. For double-tag events, sample one factor for Λ and one for $\bar{\Lambda}$.
3. Assign the correction factors as the event weight. For double-tag events, the weight is the product of the Λ and $\bar{\Lambda}$ correction factors.

Once all events in a sample have been assigned weights, the efficiency is calculated. This procedure is repeated to create an ensemble of samples and for each of these, the cross section is calculated. The average difference with respect to the nominal result is taken as the systematic uncertainty. The results are presented in Table 17.2.

The effect on the fit parameters is evaluated using the same reweighting procedure as above, but applied to the `PHSP` sample used for normalization in the fit instead. The average difference between the nominal and reweighted result is 1.6% for R and 0.6% for $\Delta\Phi$.

Table 17.2. *Difference between the nominal cross section result and the result obtained using ConExc MC samples reweighted according to the difference between data and MC in Λ reconstruction efficiency. The results at 2.396 GeV are given as an example.*

Sample	Absolute difference (pb)	Relative difference (%)
Double-Tag	1.0	0.9
Single-Tag $\bar{\Lambda}$	0.99	0.8
Single-Tag Λ	0.92	0.8

17.4 Tests of Systematic Effects for the Double-Tag Selection

In this section I will investigate systematic effects caused by the two criteria used in the double-tag selection. The first is the selection on the χ^2_{4C} variable and the second is the invariant mass window.

The selection criterion on χ^2_{4C} is varied between 20 and 200 with a step size of 10. Fig. 17.3 shows how the values of the cross section changes as a result. The main interest here is the region below the nominal cut value. However, using a cut that is too narrow may also not be reasonable as data and MC do not agree perfectly. In Fig. 17.3 one can see a clear change in behavior for cut values < 60. This is most likely due to imperfect agreement between data and MC in the peak region, and cuts in the region between 60 and the nominal cut value are chosen in the following.

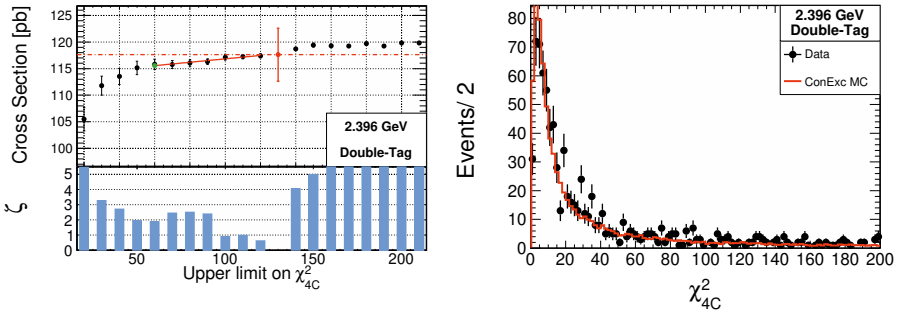

Figure 17.3. Cross section determined from the double-tag sample (left) as a function of the selection on χ^2_{4C}. The red point represents the nominal result, and its error bar shows the full statistical uncertainty. The error bars for the black points represent the uncorrelated uncertainty. A line is fitted to the cross section as a function of χ^2_{4C}. The green point represents the value of the fitted function at the point chosen for the estimation of the systematic uncertainty. The χ^2_{4C} distribution in data and signal MC is shown for reference (right).

Figure 17.3 shows that the cross section varies significantly with the selection criterion on χ^2_{4C}. This effect is believed to originate from low momentum pions, for which the resolution of the estimated track parameters is not the same in data and MC. These differences lead to differing efficiencies via the kinematic fit and χ^2_{4C} selection. Note that this is distinct from the effect considered in Section 17.3 which is only due to differences in efficiency and not the values of the reconstructed track parameters.

Because adressing the underlying issue by improving the MC/Data agreement in tracking of low momentum pions is well beyond the scope of this work, the effect on the cross section is accounted for by assigning a systematic uncertainty. This is done by fitting a line to the trending part of the cross section distribution in Fig 17.3. The fitted function is evaluated at $\chi^2_{4C} \leq 60$, the point farthest away from the nominal cut. This result and the nominal result should be considered to represent the extreme cases that are equally likely to be true and, following the advice of the BaBar statistics working group [212], half the difference between them, 1%, is taken as the systematic uncertainty.

The second check concerns the selection window that is applied to the invariant masses of the $p\pi^-$ and $\bar{p}\pi^+$ systems. The width of the window is varied between 1.55 MeV/c^2 and 13.95 MeV/c^2. In $\Delta\Phi$, there is a clear trend to either side of the nominal criterion, as can be seen in Fig. 17.4, and this is treated as a systematic effect even though the individual points do not deviate significally from the nominal value. The most likely origin for this behavior is the difference between data and MC in the track parameters of low momentum pions. To determine the associated systematic uncertainty, a straight line is fitted to the region between 3 MeVc^2 and 9 MeV/c^2, see Fig. 17.4. The line is evaluated at 1σ below the nominal selection, which occurs at 4.5 MeV/c^2, and the deviation from the nominal result, 5.3 %, is taken as the systematic uncertainty.

17.5 Tests of Systematic Effects for the Single-Tag Selection

In this section, I will discuss three of the selection criteria used in the single-tag analyses. The first is the momentum window that is applied to the analysis of both Λ and $\bar{\Lambda}$. The second and third are the selection on $L/\Delta L$ and $\chi^2_{\text{vtx. 1}} + \chi^2_{\text{vtx. 2}}$ that are only used in the single-tag Λ analysis.

We have already seen in Figs. 14.7 and 14.12 that there is a shift between the Λ and $\bar{\Lambda}$ momentum distributions in data and MC. In order to check if this means that the results of this work are sensitive the cut on the $\Lambda/\bar{\Lambda}$ momentum, the size of the momentum selection window is varied between 4.7 MeV/c and 37.6 MeV/c with a step of 2.35 MeV/c. Figure 17.5 shows how the cross section varies as the selection window on the $\bar{\Lambda}$ and Λ momentum is changed. Significant deviations from the nominal result can be attributed

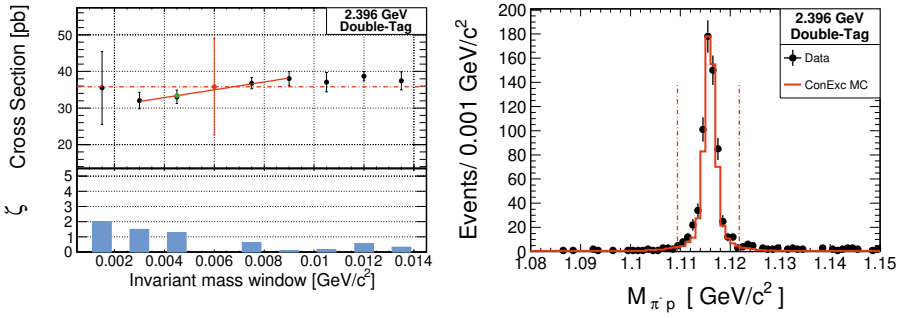

Figure 17.4. Value of $\Delta\Phi$ determined from the double-tag sample (left) as a function of the width of the invariant mass selection window. The red point represents the nominal result, and its error bar shows the full statistical uncertainty. The error bars for the black points represent the uncorrelated uncertainty. A line is fitted to the distribution and the green point represents the value of the fitted function at the point chosen for the estimation of the systematic uncertainty. The invariant mass distribution of the $p\pi^-$-system in in data and signal MC is shown for reference (right).

both to increasing background content in the final sample, and to increasing differences between data and MC. The former is typically probable as the cut value increases, while the latter becomes more prominent as it decreases. The background content is an artifact of the event selection procedure, and its effects can be minimized by appropriate selection criteria. Differences between data and MC, on the other hand, may adversely affect the result. The most interesting region in Fig. 17.5 is therefore the one below the nominal cut value. In this region, there are significant deviations in the cross section, and a clear trend toward lower values as the size of the selection window is decreased. This indicates a systematic effect that must be accounted for.

The source of this systematic effect is believed to be the clear difference between data and MC in the $P_{\Lambda/\bar{\Lambda}}$ distribution that can be seen in Figs. 14.7 and 14.12. The peak in MC is narrower than, and shifted relative to its counterpart in data. This in turn originates from the Data/MC difference in estimating the track parameters of low momentum pions. Because this effect is due to the reconstructed track parameters, and not reconstruction efficiency, it is distinct from the effect studied in Section 17.3.

The difference between the momentum distributions from data and MC may be corrected for by first fitting the MC distribution to data with a shift along the x-axis and a Gaussian smearing, and subsequently using the fitted parameters (shown in Table 17.3) to smear the MC sample in the analysis procedure. The average difference between the cross section obtained using smeared MC samples and the nominal result is 0.5% for the $\bar{\Lambda}$ sample and 0.3% for the Λ sample. These numbers are taken as the systematic uncertainties. The original

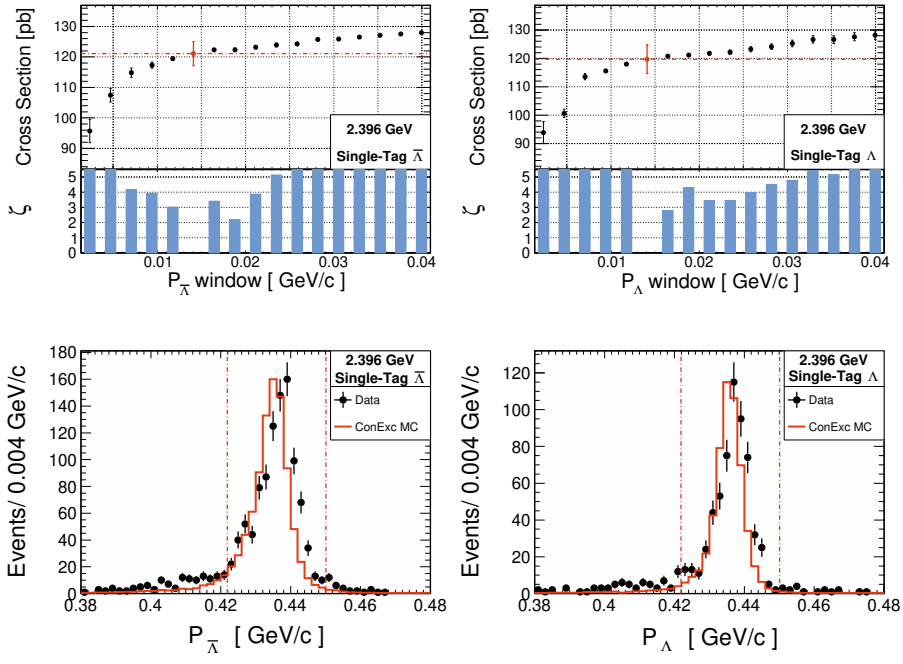

Figure 17.5. Cross section determined from the $\bar{\Lambda}$ (top left) and Λ (top right) single-tag samples as a function of the size of the momentum window. The red point represents the nominal result, and its error bars show the full statistical uncertainty. The error bars on the black points represent the uncorrelated uncertainty. The $P_{\bar{\Lambda}/\Lambda}$ distribution in data and signal MC is shown for reference (bottom left/right). The dash-dotted vertical lines represent the nominal momentum window.

distributions are shown in Fig. 17.5 and the smeared and shifted distributions are shown in Fig. 17.6.

Table 17.3. *Shift and smearing parameters for the Λ and $\bar{\Lambda}$ momenta determined by fitting the corresponding signal MC distributions to data.*

Sample	Shift (MeV/c)	Smearing (MeV/c)
Single-tag Λ	2.6 ± 0.2	2.3 ± 0.4
Single-tag $\bar{\Lambda}$	2.3 ± 0.2	1.6 ± 0.6

For the second check, the selection on $L/\Delta L$ that is used for the single-tag Λ sample is varied between 5 and 50 in steps of 5. Figure 17.7 shows how the cross section and R change as the cutoff changes. No significant deviations from the nominal results are found, but for R there is a clear trend for cutoffs below 20 that needs to be investigated further. From Fig. 17.8 it is clear that events on the edges of the $\cos\theta_p$ distribution, where θ_p is the proton angle used in the fit, tend to get larger values of $L/\Delta L$. Lowering the

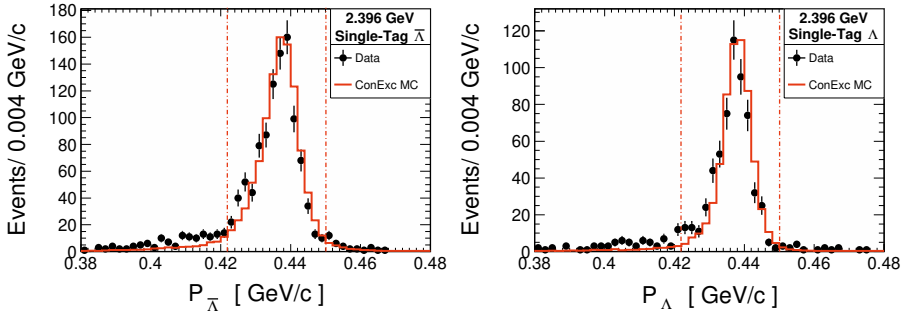

Figure 17.6. Smeared and shifted distribution of Λ (left) and $\bar{\Lambda}$ (right) momentum. The vertical lines represent the nominal momentum window.

selection value therefore affects the edges of the distribution more strongly than the central bins, and there is most likely a critical region for selection values below $L/\Delta L \leq 20$ where the efficiency correction applied in the fit does not accurately account for this effect. Since the nominal selection has a flat efficiency in $\cos\theta_p$, there is no need to assign a systematic uncertainty.

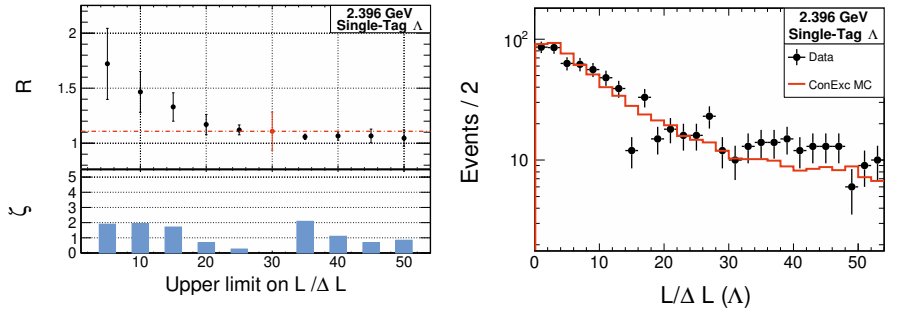

Figure 17.7. The R-value determined from the single-tag Λ sample (left) as a function of the selection on $L/\Delta L$. The $L/\Delta L$ distribution is shown for reference (right). The red point represents the nominal result, and its error bars are the full statistical uncertainty. The error bars for the black points represent the uncorrelated uncertainty.

Finally, the cut on $\chi^2_{\text{vtx.}} + \chi^2_{\text{second vtx.}}$ that is used in the single-tag Λ analysis is varied between 1 and 30 in steps of 1. Figure 17.9 shows how R changes as a result of these variations. Below the nominal value of the cut, there are no significant deviations or trends in R. However, there are significant deviations above the nominal value of the cut, and up to a value of about 16 it does not seem that these can be attributed entirely to increasing background content in the sample. Indeed, Fig. 17.9 shows fairly good agreement between data and

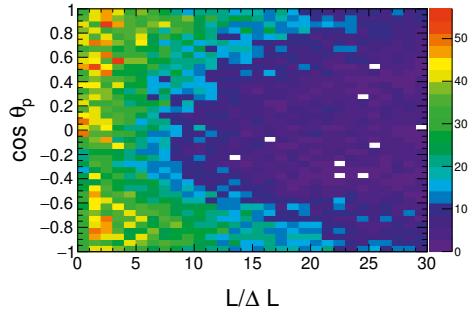

Figure 17.8. Distribution of $L/\Delta L$ versus $\cos\theta_p$ in the signal MC sample.

MC up to this point. This indicates a systematic effect that must be accounted for.

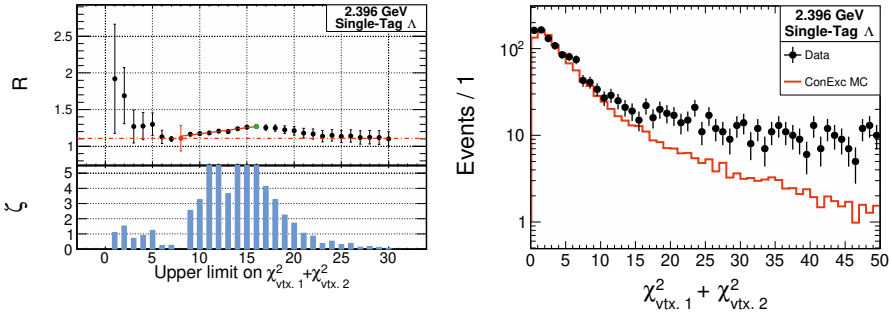

Figure 17.9. The R-value determined from the single-tag Λ sample as a function of the cut on $\chi^2_{\text{vtx.}} + \chi^2_{\text{second vtx.}}$ (left). The red point represents the nominal result, and its error bar is the full statistical uncertainty. The error bars for the black points represent the uncorrelated uncertainty. The solid red line is fitted to the region between 8 and 16 for estimating the systematic uncertainty. The green point represents the value where the systematic uncertainty is evaluated. The $\chi^2_{\text{vtx. 1}} + \chi^2_{\text{vtx. 2}}$ distribution in data and signal MC is shown for reference (right).

There are no clear correlations between the value of $\chi^2_{\text{vtx. 1}} + \chi^2_{\text{vtx. 2}}$ and the distribution of $\cos\theta$ or $\cos\theta_p$ that could explain the trend of R with respect to the cut value on $\chi^2_{\text{vtx. 1}} + \chi^2_{\text{vtx. 2}}$ and therefore a systematic uncertainty due to this selection criterion is assigned. As before, a line is fitted to the trending part of the R distribution in Fig. 17.9, and evaluated at $\chi^2_{\text{vtx. 1}} + \chi^2_{\text{vtx. 2}} < 16$. Any cut values in the fitted range are considered to be valid, and the nominal result and the result for $\chi^2_{\text{vtx. 1}} + \chi^2_{\text{vtx. 2}} < 16$ therefore represent extreme cases that are equally likely to be true. The systematic uncertainty is consequently taken as half the difference between them, 7.4%.

18. Results

The reaction $e^+e^- \to \Lambda\bar{\Lambda}$ has been studied at five center-of-mass energies between 2.3864 and 3.0800 GeV. All non-negligible systematic uncertainties are listed in Tables 18.1, 18.2, and 18.3. The results for the Born cross section, the ratio of electromagnetic form factors R, and the relative phase $\Delta\Phi$ are given in Table 18.4, and plotted as a function of the center-of-mass energy in Figures 18.1 and 18.2.

Table 18.1. *Systematic uncertainties on σ_{Born} given in percent for all data points. The center-of-mass energies are given in GeV. The contributions from all sources are summed in quadrature.*

Source	2.3864	2.396	2.64	2.9	3.08
Luminosity	1	1	1	1	1
Efficiency model dependence	0.6	0.6	1.4	2.2	2.8
ISR corrections	0.6	0.6	0.3	0.2	0.1
χ^2_{4C}	0.3	0.3	0.4	0.5	0.6
Single-tag momentum cut	0.3	0.3	0.2	0	0
Λ reconstruction	0.8	0.8	0.6	0.3	0.1
$\Lambda\Sigma$ background	0.	0.	0.	1.0	1.2
Sum	1.5	1.5	1.9	2.7	3.3

Table 18.2. *Systematic uncertainties on R given in percent for all data points. The center-of-mass energies are given in GeV. The contributions from all sources are summed in quadrature.*

Source	2.3864	2.396	2.64	2.9	3.08
$\chi^2_{\text{vtx. + 2nd vtx.}}$ cut	1.6	1.6	0.8	0.0	0.0
Λ reconstruction	1.6	1.6	1.8	2.0	2.1
Sum	2.3	2.3	2.0	2.0	2.1

Table 18.3. *Systematic uncertainties on $\Delta\Phi$ given in percent for all data points. The center-of-mass energies are given in GeV. The contributions from all sources are summed in quadrature.*

Source	2.3864	2.396	2.64	2.9	3.08
Invariant mass window	3.7	3.6	1.9	0	0
Λ reconstruction	0.6	0.6	1.0	1.5	1.8
Sum	3.7	3.6	2.1	1.5	1.8

Table 18.4. *Born cross section for $e^+e^- \to \Lambda\bar{\Lambda}$, ratio of electromagnetic form factors R, and relative phase $\Delta\Phi$ measured in this work.*

Energy [GeV]	σ_{Born} [pb]	R	$\Delta\Phi$ [°]
2.3864	$131.2 \pm 4.6_{stat.} \pm 2.0_{syst.}$	$1.01 \pm 0.14_{stat.} \pm 0.02_{syst.}$	$39 \pm 12_{stat.} \pm 1_{syst.}$
2.3960	$119.6 \pm 2.6_{stat.} \pm 1.8_{syst.}$	$0.91 \pm 0.08_{stat.} \pm 0.02_{syst.}$	$42 \pm 10_{stat.} \pm 2_{syst.}$
2.6450	$30.3 \pm 1.1_{stat.} \pm 0.6_{syst.}$	$1.00 \pm 0.16_{stat.} \pm 0.02_{syst.}$	$146 \pm 13_{stat.} \pm 1_{syst.}$
2.9000	$8.5 \pm 0.5_{stat.} \pm 0.2_{syst.}$	$0.88 \pm 0.27_{stat.} \pm 0.02_{syst.}$	$151 \pm 19_{stat.} \pm 1_{syst.}$
3.0800	$4.4 \pm 0.4_{stat.} \pm 0.1_{syst.}$	$0.51 \pm 0.29_{stat.} \pm 0.02_{syst.}$	$78 \pm 60_{stat.} \pm 1_{syst.}$

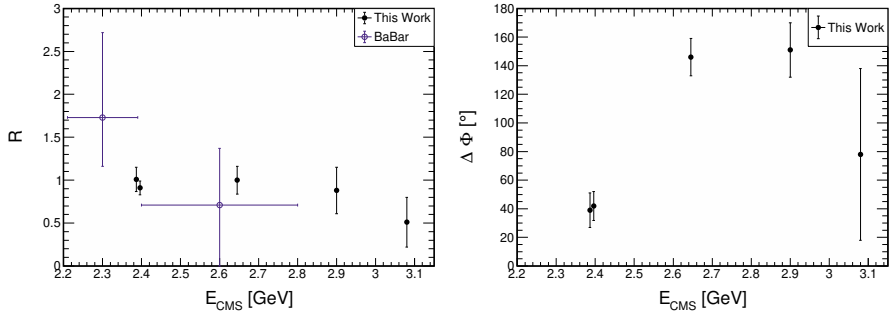

Figure 18.1. R (left) and $\Delta\Phi$ (right) determined in this analysis as a function of the center-of-mass energy. Previous results from BaBar are taken from Ref. [140].

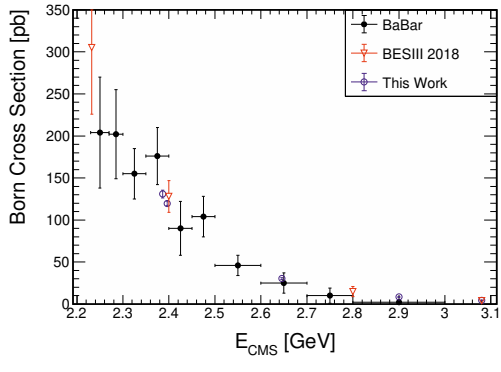

Figure 18.2. $\sigma_{Born}(e^+e^- \to \Lambda\bar{\Lambda})$ as a function of center-of-mass energy. The blue circles indicate the results from this work. Red triangles represent results from the previous BESIII measurement [143] and the black points represent results from BaBar [140].

19. Benchmark Tests of the CGEM Track Reconstruction Algorithm

The development of the new CGEM inner tracker for the BESIII experiment, see Section 7.4 and Ref. [167] for details, involves both hardware and software components. In order to make use of data collected with the new subdetector, a new track reconstruction software must be developed and integrated with existing algorithms for tracking in the outer MDC. As a part of this process, it is important to evaluate the performance of the new algorithms and ensure that they are at least on par with the current methods before the new detector is installed. One important benchmark is the performance for well-known and frequently studied physics channels with respect to reconstruction efficiencies and resolution in important observables. In this work, the ability of the CGEM software to reconstruct the reaction $e^+e^- \to \Lambda\bar{\Lambda}$ is evaluated and compared to the software used for the current detector configuration using MC simulations. The main motivation for the use of this particular channel is that it tests the reconstruction of displaced vertices. These are central to the study of hyperons, which are the focus of many important measurements at BESIII that may be interesting to continue with new data in the future. Previous studies of the CGEM track reconstruction have primarily used particles that originate from the interaction point, see *e.g.* Ref. [213], and therefore this work provides a new angle that gives complementary information.

When this work was carried out, two comparable versions of the software for the CGEM inner tracker were available: `CGEMBOSS 6.6.5b` and `CGEMBOSS 6.6.5c`. The main difference between them, is that the latter combines hits from CGEM and the outer drift chamber (MDC) to perform a global track finding, while the former finds track segments separately in the CGEM-IT and the outer MDC matching these to each other. Furthermore, the versions differ in their approach to track finding. Version `6.6.5.c` uses the Hough transform approach for finding tracks, while `6.6.5b` uses only the TSF algorithm. The two versions of `CGEMBOSS` will be compared to the latest version of the track reconstruction software for the MDC, `BOSS 7.0.3-1`. Like `CGEMBOSS 6.6.5c`, it performs global tracking using all available tracking algorithms: pattern recognition, TSF, and Hough transform. For more details about the different track finding algorithms, see Section 8.3.1.

19.1 Questions for the study

The purpose of this study is to evaluate how well the CGEM track reconstruction algorithm performs in reconstructing the reaction $e^+e^- \to \Lambda\bar{\Lambda}$. To that end, it aims to answer the following questions: What are the efficiencies for reconstructing tracks that originate from a displaced vertex? Given that the CGEM-IT has slightly more material than the current MDC, slightly lower efficiencies are expected with the CGEM. How large is the reduction in efficiency? How do the momentum, invariant mass, and position resolutions in CGEM compare to those of the MDC? In particular, it is interesting to see if the CGEM track reconstruction algorithm can meet the goal of improving the resolution in the z-coordinate compared to the current MDC. Finally, is there any improvement in efficiency and resolution between the two latest version of the CGEM software, `6.6.5b` and `6.6.5c`?

19.2 Strategy

To answer the questions concerning the performance of the CGEM software I will discuss three quantities of interest. The first is the single-track efficiency, defined as

$$\varepsilon_i = \frac{N_{i,rec.}}{N_{i,gen.}}, \tag{19.1}$$

where the subscript i represents the particle species (p or π). $N_{rec.i}$ and $N_{gen.i}$ represent the number of reconstructed and generated tracks, respectively. A measurement of the single-track efficiency provides a test of the track finding algorithm, and will show how the slightly larger material budget for the CGEM-IT impacts the efficiency. The second quantity of interest is the efficiency for reconstructing a full $\Lambda\bar{\Lambda}$ event, defined as

$$\varepsilon_{\Lambda\bar{\Lambda}} = \frac{N_{\Lambda\bar{\Lambda},rec.}}{N_{\Lambda\bar{\Lambda},gen.}}, \tag{19.2}$$

where $N_{\Lambda\bar{\Lambda},rec.}$ and $N_{\Lambda\bar{\Lambda},gen.}$ are the numbers of reconstructed and generated events. The event reconstruction efficiency tests how well the CGEM track reconstruction algorithm can estimate the parameters of the reconstructed tracks, and in particular if they can be used to successfully find the decay vertices of Λ and $\bar{\Lambda}$. Finally, the momentum and position resolutions for the reconstructed events will be studied. For a given quantity with true value $\hat{q}$ and reconstructed value q_i, the resolution is defined as the standard deviation of the distribution of $q_i - \hat{q}_i$ across the sample. The value of the standard deviation can be estimated by fitting a Gaussian function to the distribution. Since other analyses have studied the single-track position resolutions before, this work will focus instead on the decay length of the $\Lambda/\bar{\Lambda}$, which was so far unexplored.

19.3 Analysis

In order to estimate the efficiencies and resolutions, an MC sample of 100,000 $e^+e^- \to \Lambda\bar{\Lambda} \to p\bar{p}\pi^+\pi^-$ events at center-of-mass energy 2.396 GeV is generated with the `ConExc` generator. The sample is propagated through the detector simulation and reconstructed with the three different software versions: `BOSS 7.0.3-1`, `CGEMBOSS 6.6.5b` and `CGEMBOSS 6.6.5c`. At the first stage of the analysis, the reconstructed tracks of different species are counted without any further selection criteria. This information is used to estimate the single-track efficiencies.

In the next step, $\Lambda\bar{\Lambda}$ events are reconstructed following the double-tag procedure described in Section 14.2, except for the requirement on the kinematic fit χ^2-value and the invariant mass window. The number of reconstructed events is used to calculate the reconstruction efficiency. Finally, the momentum, invariant mass and decay length resolutions are estimated using the reconstructed Λ and $\bar{\Lambda}$ four-vectors, and the decay length vector.

19.4 Results

The single track efficiencies for each particle species as well as the full reconstruction efficiency are given in Table 19.1. The resolution of the invariant masses of the $p\pi^-$ and $\bar{p}\pi^+$ systems as well as the *xy*- and *z*-components of the decay length are shown in Table. 19.2.

Table 19.1. *Single track efficiencies and full reconstruction efficiency for the reaction $e^+e^- \to \Lambda\bar{\Lambda} \to p\bar{p}\pi^+\pi^-$ in the three versions of the BESIII track reconstruction software.*

	6.6.5b (CGEM)	6.6.5c (CGEM)	7.0.3-1 (MDC)
ε_p (%)	50	49	60
$\varepsilon_{\bar{p}}$ (%)	48	47	58
ε_{π^+} (%)	22	18	35
ε_{π^-} (%)	23	19	35
$\varepsilon_{\Lambda\bar{\Lambda}}$ (%)	7	4	20

Table 19.2. *Resolution of the decay length and invariant masses of Λ and $\bar{\Lambda}$ in the three versions of the track reconstruction software. The decay length resolutions are given in centimeters and the mass resolutions in MeV/c^2.*

Version	$\sigma_{L_{z,\Lambda}}$	$\sigma_{L_{z,\bar{\Lambda}}}$	$\sigma_{L_{xy,\Lambda}}$	$\sigma_{L_{xy,\bar{\Lambda}}}$	σ_{M_Λ}	$\sigma_{M_{\bar{\Lambda}}}$
6.6.5b (CGEM)	0.10	0.10	0.17	0.17	1.3	1.3
6.6.5c (CGEM)	0.10	0.10	0.16	0.17	1.3	1.4
7.0.3-1 (MDC)	0.24	0.25	0.18	0.18	1.4	1.4

19.5 Conclusions

The CGEMBOSS reconstruction software evaluated here shows, as expected, improvements in the z-resolution compared to the reconstruction based on the current MDC already achieving a vertex position resolution better than 1 mm. At the same time, it yields significantly lower efficiency both for individual tracks and for reconstructing full $\Lambda\bar{\Lambda}$ events. There are several factors that explain this result. The effect mainly comes from the fact that both the TSF and Hough track reconstruction algorithms use conformal mapping procedures where tracks are assumed to originate at the IP. This lowers the efficiency for reconstructing tracks that are produced at displaced vertices. For the tracks that can be reconstructed, the assumption is propagated to the track parameters, which can lead to problems with reconstructing the decaying Λ or $\bar{\Lambda}$. The MDC tracking software uses the pattern recognition algorithm that is free of assumptions on the point of origin, and therefore performs better. A second factor is that the larger amount of material in the CGEM inner tracker compared to the MDC lowers the efficiency. However, the exact size of this effect is difficult to deduce from these studies. What may appear particularly worrying is that the efficiency is lower in the newer CGEMBOSS version 6.6.5c than in 6.6.5b. It has been found that the current implementation of the Hough transform performs poorly for low momentum tracks that only leave a few hits or move along a circular trajectory without exiting the detector. This is consistent with the observation, see Table 19.1, that the efficiency loss for pions is larger than for protons. It is expected that these issues can be effectively resolved with further optimization of the peak finding algorithm used to find the best track parameter combination, see Section 8.3.1. Therefore, improvements to the single-track efficiencies are foreseen in the near future.

The results presented here show clearly that the current CGEM track finding algorithms that rely on the assumption that all tracks originate from the IP lead to poor performance for reactions with displaced vertices. Therefore, the benchmark tests with the channel $e^+e^- \to \Lambda\bar{\Lambda}$ are postponed until new and more suitable methods have been introduced. Before then, other more pressing issues related to the reconstruction of single low momentum tracks must be resolved.

20. Summary & Outlook

In this thesis I have presented two analyses of data from the BESIII experiment where electromagnetic interactions of hadrons are investigated to learn about the strong interactions at low energies and *CP*-violation. Here I discuss the implications of the results and outline possible next steps and potential uses of the developed methods.

20.1 Meson Decays

A method for selecting clean samples of $\eta' \to \pi^+\pi^- e^+ e^-$ events was established to measure the branching fraction for the decay with world leading precision and to determine the *CP*-violating asymmetry $\mathcal{A}_\varphi$ for the first time. The BESIII experiment has already collected an additional data sample of 8.7×10^9 J/ψ events that is yet to be analyzed, where methods developed in this thesis will be used. The statistical precision for the branching fraction and asymmetry will be improved by almost a factor three. For the asymmetry, this would put the precision on the same level as the theoretical upper bound. The larger data sample also opens up the possibility for more detailed investigations. For example, it may be possible to measure the transition form factors by studying the invariant mass distributions of the $\pi^+\pi^-$- and e^+e^--systems. These are in turn important for the calculation of the hadronic light-by-light contribution to the anomalous muon magnetic moment. One could furthermore test lepton flavor universality by comparison with the related process $\eta' \to \pi^+\pi^-\mu^+\mu^-$ which was recently observed for the first time by BESIII [214]. It has also been suggested that $\eta' \to \pi^+\pi^- e^+ e^-$ may be a suitable candidate for searches for the QCD axion [109, 215] or a dark photon [109] that would couple to the e^+e^--pair.

Another possibility is to develop new methods to probe the *CP*-violating contribution to the decay. As was discussed in Section 4.2, the interference between *CP*-even and *CP*-odd amplitudes leads to polarization of the real photon in the more commonly occurring process $\eta' \to \pi^+\pi^-\gamma$. It would be interesting to investigate how the conversion into an e^+e^--pair in the detector material, which was treated as background in this work, could be used as a polarimeter. If this is possible, the photon conversion veto used in this work could be inverted in order to select the conversion events instead. And since there are more such events than from the process $\eta' \to \pi^+\pi^- e^+ e^-$, one could improve

the measurement of the *CP*-violating interference. A precise measurement of the polarization could also be used to probe the transition form factors.

To summarize, the methods developed in this work to isolate those e^+e^--pairs that originate from the conversion of real photons lay the groundwork for many future studies of the decay $\eta' \to \pi^+\pi^- e^+e^-$ and similar rare decays of other mesons. These studies serve as important tests of various descriptions of the strong interaction at low energies and probe a wide range of topics in contemporary particle physics. The results presented in this part of the thesis were published in a peer reviewed journal, see Ref. [84].

20.2 Hyperon Form Factors

The reaction $e^+e^- \to \Lambda\bar{\Lambda}$ was studied at five center-of-mass energies between 2.3864 and 3.08 GeV by combining double- and single-tag analysis methods and thereby maximizing the size of the data sample. At each energy, the Born cross section, the ratio of electromagnetic form factors R, and their relative phase $\Delta\Phi$ were determined. This work improves the precision and supersedes the previous BESIII measurement at 2.396 GeV, and extends the analysis to both higher and lower energies. In particular for $\Delta\Phi$, the results presented here cover a hitherto unexplored energy range and it will be exciting to see them confronted with the predictions from meson exchange models and dispersive approaches [76, 130]. The relative phase $\Delta\Phi$ exhibits an unexpected q^2-dependence, going from the first to the second quadrant between the lower and higher energies. This may be an artifact of the method or the limited size of the data samples. In principle, the double-tag analysis allows for an unambiguous determination of the phase. It has, however, been shown in previous studies within BESIII that it is possible for the exclusive analysis of small data samples to yield a result $180 - \Delta\hat{\Phi}$ where $\Delta\hat{\Phi}$ is the true value. The spin correlation terms that depend on $\cos(\Delta\Phi)$ are a weaker constraint than the polarization terms that depend on $\sin(\Delta\Phi)$. From Eq. 5.33, it can be understood that this occurs because since the spin correlation terms are multiplied by an additional factor of α_Λ. A natural next step is to investigate the likelihood of finding the solution $180^\circ - \Delta\Phi$ given the samples sizes used in this work. Figure 20.1 shows scans of the negative log-likelihood values as functions of $\Delta\Phi$ for the experimental data samples at all five energies. At 3.08 GeV there is only one broad minimum, and the uncertainty is consistent with solutions both below and above 90°. At the other energies the likelihood values for the two solutions can be compared. The difference between them gives an estimate of the statistical significance of the preferred solution compared to the alternative one. In terms of standard deviations the difference is 0.8σ at 2.3864 GeV, 7.6σ at 2.396 GeV, 3.5σ at 2.64 GeV and 3.4σ at 2.9 GeV. Since the statistical significance of the preferred solution does not reach the 5σ level it is not considered conclusive according to high energy physics standards, ex-

cept at 2.396 GeV. It would therefore be interesting to use bootstrap methods, see *e.g.* [216], to investigate the variability of the experimental data sets and see to what extent the same data set could yield differing results. Furthermore one should include the impact of the systematic uncertainties when comparing the two solutions. If the limitations of the method can be identified and a corrected method developed, this would hold great value for the research field as a whole. Many studies of hyperon form factors are ongoing at BESIII and are being planned elsewhere. A thorough understanding of the methods improves the prospects for precise results and facilitates their interpretation.

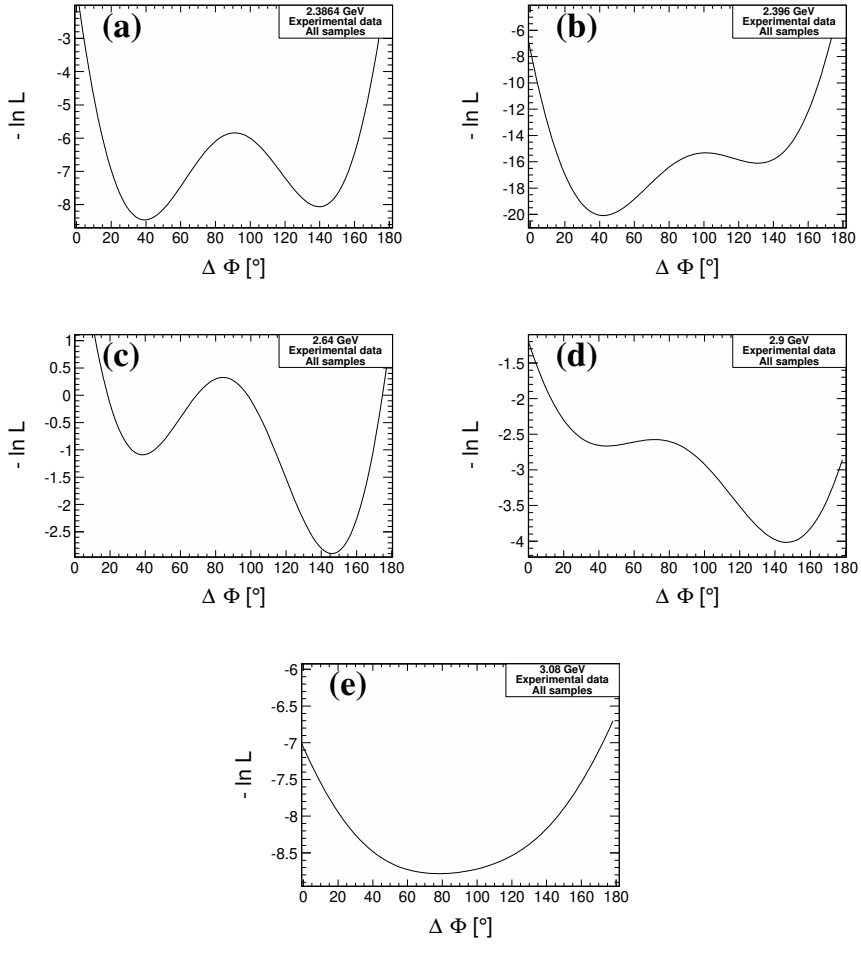

Figure 20.1. Negative log-likelihood as a function of the parameter $\Delta\Phi$ for the experimental data samples at 2.3864 GeV (a), 2.396 GeV (b), 2.64 GeV (c), 2.9 GeV (d) and 3.08 GeV (e).

If we instead consider the possibility that the results are correct, the implications would be very interesting. Since the form factors are continuous functions, this means that $\Delta\Phi$ must cross 90° somewhere between 2.3960 GeV and 2.6450 GeV and at this particular energy the hyperons are maximally polarized, *cf.* Eq. 5.15. It would be interesting to collect more data in this range to investigate this prediction. It has also been shown in Ref. [130] that the number of oscillations of $\sin(\Delta\Phi)$ are a key piece of information needed to pin down the form factors of the hyperons in the whole complex plane. The results shown in this thesis are a promising step in that direction. One can speculate that this behavior of the phase might be *e.g.* due to some hitherto unknown resonance with a mass larger than 2.396 GeV/c^2 or that heavier hyperon-antihyperon channels like $\Sigma\bar{\Sigma}$ or $\Xi\bar{\Xi}$, that are opened up in the vicinity of the energies studied here, contribute via rescattering processes.

Whether the observed behavior of $\Delta\Phi$ is a an artifact of the method or not, I have provided the first measurement of the q^2 dependence of $\sin(\Delta\Phi)$. This serves as an important input for dispersive calculations that can estimate the unmeasurable, at least for now, spacelike structure of the Λ. It is possible that they can already lead to the first determination of the Λ charge radius, or at least be used to determine whether it is negative like that of the neutron, or positive like that of the Σ^-. The charge radius for a baryon is defined in terms of the first derivative of either the electric form factor G_E or the form factor ratio R at $q^2 = 0$:

$$< r_E^2 >= 6\frac{dG_E(q^2)}{dq^2}\bigg|_{q^2=0} = 6\mu\frac{dR}{dq^2}\bigg|_{q^2=0}, \tag{20.1}$$

where μ is the magnetic moment. The value of the magnetic moment of Λ its known $\mu_\Lambda = -0.613 \pm 0.004\mu_N$ [6].

The observed values of $\Delta\Phi$ are not an integer multiple of π, indicating that the momentum transfer scale where the behavior predicted by perturbative QCD sets in is higher and that further measurements are needed to find it. Measurements of $\Delta\Phi$ around and above the $\psi(2S)$ resonance are underway at BESIII, and other experiments like BelleII could probe even higher energies. BESIII has also collected data at the production threshold, but a measurement of the form factors at this energy is challenging both due to the low efficiency and difficulties in modeling the detector response. Therefore a measurement with the methods used in this work is not feasible. In the past, dedicated methods for a cross section measurement at threshold were developed, and it is possible that they could be extended to be used determine the form factors. Such an analysis would most likely need to use the single-tag approach because of the low efficiency and therefore only $\sin(\Delta\Phi)$ can be measured. Improvements at threshold, and for that matter the whole energy range considered by BESIII, may be possible with the planned Super-Charm

Tau Factory [217, 218] that will have both higher luminosity and a polarized electron beam.

The analysis presented in this study has furthermore provided the most precise measurement of the Born cross section of $e^+e^- \to \Lambda\bar{\Lambda}$ at five center-of-mass energies between 2.3864 GeV and 3.0800 GeV. This work will soon be extended to five additional energies between 2.95 GeV and 3.02 GeV with data samples that have already been collected at BESIII. The value of the effective vector meson mass determined from the dipole fit in Chapter 15, $c_1 = 1.77 \pm 0.01$ GeV, seems to suggest a mixture of contributions from the $\phi(1680)$ and $\phi(2170)$ mesons. It was recently shown in Ref. [219] that including the $\phi(2170)$ in a multipole description of the effective form factor could explain the near threshold enhancement in the cross section previously observed by BESIII. It would be interesting to fit our new measurements with the form factor from Ref. [219] to see if they support this idea.

To summarize, this work has provided both methodological improvements and new precise measurements that, with some further development, can have a great impact on our understanding of the electromagnetic form factors of the Λ-hyperon.

Sammanfattning på svenska

En av fysikens mest grundläggande målsättningar är att förstå hur den värld vi lever i fungerar och är uppbygd. Å ena sidan leder denna strävan till nya uppfinningar som kan förenkla våra liv, och å andra sidan hjälper den oss att sätta in vår existens i ett större sammanhang och besvara våra frågor om varför vi finns här. I den här avhandlingen har jag bidragit till detta arbete genom att undersöka universums allra minsta beståndsdelar och hur de interagerar med varandra.

All materia som har någon betydlse för vårt vardagliga liv, och för den delen all materia som vi överhuvudtaget kan observera, består av protoner och neutroner. Dessa består i sin tur av *kvarkar* som hålls samman av den *starka* kraften. Interaktionerna mellan kvarkarna ger protonerna och neutronerna de egenskaper som vi kan observera och bär ansvaret för de mest grundläggande förutsättningarna för vår existens, men vi vet förvånansvärt lite om dem. Till exempel genereras nästan all massa som vi kan observera av dessa interaktioner, men exakt hur det går till är okänt.

Den starka kraften är en av tre fundamentala växelverkningar som beskrivs av partikelfysikens standardmodell (SM). Enligt den består all materia i grund och botten av en uppsättning av tolv partiklar med halvtalsspinn som kallas *fermioner*. De svaga, elektromagnetiska, och starka krafterna mellan dem förmedlas av *bosoner*. Den mest välkända av dessa är förmodligen fotonen som förmedlar den eletktromangetiska kraften. Fermionerna kan i sin tur delas in i *leptoner* och kvarkar. Bland leptonerna hittar vi de välbekanta elektronerna (e) tillsammans med myoner (μ) och tauoner (τ), samt elektron- (ν_e), myon- (ν_μ), och tauneutriner (ν_τ). De första tre är elektriskt laddade medan de tre sista är neutrala. Kvarkarna å sin sida har både en elektrisk laddning och en *färgladdning*. Den senare betyder att de påverkas av den starka kraften som förmedlas av *gluoner* (dessa får sitt namn av engelskans "glue"). Totalt finns det sex olika typer av kvarkar: *ner* (d), *upp* (u), *sär* (s), *charm* (c), *botten* (b), och *topp* (t) . Upp- och nerkvarkar är de lättaste och vanligast förekommande av dessa. För var och en av dessa partiklar finns en motsvarande antipartikel med motsatt laddning men samma massa.

Som namnet antyder är den starka kraften just väldigt stark, och vid de energiskalor som vi är intresserade av existerar kvarkarna i praktiken aldrig som fria partiklar utan binds samman till objekt som kallas *hadroner*. Hadronerna kan antingen vara *mesoner*, som består av en kvark och en antikvark, eller *baryoner*, som består av tre kvarkar. Protonerna och neutronerna är baryoner. Ytterligare en konsekvens av den starka kraftens styrka är att det är mycket

svårt att göra förutsägelser för hur den fungerar vid låga energier. Detta är orsaken till vår okunskap om hadronernas inre.

Den starka kraften är alltså svår att förstå trots att den är en del av SM, men det finns också ett antal fenomen som SM inte kan förklara. Ett sådant är varför vårt universum består av materia och inte antimateria. I big bang tror vi att lika mycket materia som antimateria måste ha bildats, och så småningom borde alla partiklar och antipartiklar ha stött ihop och annihilerats. Inget annat än en tom intighet borde ha blivit kvar. Trots det existerar vi, och det universum vi kan observera består nästan uteslutande av materia. En bråkdel av den ursprungliga materien måste alltså ha klarat sig, och hur det gick till kan SM inte förklara. En nödvändig ingrediens i förklaringen är att partiklar och antipartiklar inte beter sig precis likadant, och inte lyder under exakt samma naturlagar. Mer specifikt måste *CP-symmetrin*, som säger att fysikens lagar måste vara desamma om man samtidigt byter tecken på en partikels laddning och rumskoordinater, vara bruten. Detta förekommer i SM, och har observerats i experiment, men inte i tillräckligt stor utsträckning för att kunna förklara varför materia är så mycket vanligare än antimateria. En möjlighet är att denna ojämvikt orsakas av nya typer av processer bortom SM som vi ännu inte känner till.

Hadronernas elektromagnetiska interaktioner utgör ett viktigt laboratorium som samtidigt kan användas för att förbättra vår förståelse av vad som egentligen händer i hadronernas inre och leta efter nya mekanismer som bryter *CP*-symmetrin. Hur dessa interaktioner ser ut varierar beroende på hadronernas inre struktur, d.v.s. på vilket sätt kvarkarna är ordnade. Matematiskt beskrivs strukturen av *formfaktorer* som kvantifierar hur mycket hadronerna avviker från att vara punktformiga. I Fig. I illustreras diagrammatiskt hur formfaktorerna används för att beskriva hadronernas elektromagnetiska interaktioner. Formfaktorer kan vara antingen *rumslika* eller *tidslika*. De rumslika formfaktorerna beskriver hur elektriska laddningar och magnetmoment är fördelade. Vi kan betrakta dem som ett slags karta över var kvarkarna befinner sig. Dessa kan studeras i experiment där en måltavla av hadroner bombarderas med en stråle av elektroner eller vice versa. Denna metod har länge använts för att studera protoner och neutroner. De tidslika formfaktorerna ger istället ögonblicksbilder av processerna där hadronerna bildas. Vi kan studera dem i experiment där en elektron kolliderar med sin antipartikel, positronen, och ett hadron-antihadronpar bildas. Om vi tänker oss processen som en fabrik där en elektron och positron stoppas in och hadron-antihadronparet kommer ut på andra sidan beskriver de tidslika formfaktorerna det löpande bandet där de sätts samman. Till skillnad från de rumslika formfaktorerna tar de tidslika formfaktorerna komplexa värden och man kan definiera en fasvinkel $\Delta\Phi$ mellan dem. Om denna vinkel är nollskild blir de hadroner som bildas i elektron-positronkollisionerna *polariserade* trots att det ursprungliga e^+e^--systemet inte är det. Det vill säga att hadronerna föredrar att rikta sitt spinn åt ett särskilt håll. Om man kan mäta polarisationen kan man bestämma fasvinkeln som är

en nyckelingrediens för att till fullo förstå formfaktorerna. Polarisationen är också ett kraftfullt verktyg för att särskilja olika typer av interaktioner som bidrar till en given process, och kan därför användas för att identifera tidigare okända brott av *CP*-symmetrin som annars inte skulle gå att urskilja. I den har avhandlingen använder jag polarisationen hos både fotoner och baryoner för att utforska *CP*-symmetrin och undersöka hadronernas inre.

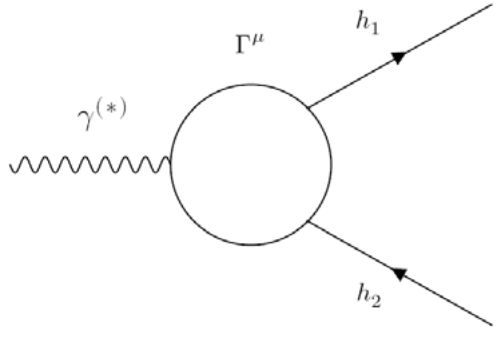

Figur I. Diagram över interaktionen mellan en foton $\gamma^{(*)}$ och två hadroner h_1 och h_2. Den vita cirkeln representerar formfaktorerna för interaktionen.

För att testa förutsägelser från olika modeller och utveckla vår förståelse av den starka kraften behövs stora mängder experimentella data. Därför har jag samarbetat med cirka 500 forskare från 17 olika länder i Asien, Europa, Syd-, och Nordamerika inom Beijing Spectrometer-experimentet (BESIII) vid elektron-positronkollideraren Beijing Electron Positron Collider (BEPCII) i Peking, Kina. Där kolliderar hundratals elektroner och positroner varje sekund, och ur kollisionerna bildas en uppsjö av hadroner. BESIII-detektorn registrerar hur hadronerna rör sig och från denna information kan vi dra slutsatser om hadronernas egenskaper. Bland de data som hittills har samlats in av BESIII-experimentet finns en världsledande datamängd med 10 miljarder J/ψ-mesoner och ett antal datamängder mellan 2 och 3 GeV för studier av energiberoende fenomen.

Mesonsönderfall

Ett antal experiment från 1960-talet och framåt har visat att det finns processer där *CP*-symmetrin bryts, men dessa effekter är för små för att ensamma förklara varför det finns en sådan övervikt av materia i universum. Det måste alltså finnas fler sådana processer och eventuellt helt okända mekanismer för hur det kan gå till. I sönderfallet $\eta' \to \pi^+\pi^-\gamma$ har man visat att en typ av mekanism som bryter *CP*-symmetrin men som inte beskrivs av SM kan bidra. Om det är korrekt leder det till att fotonerna som produceras i processen är polariserade. Om man kan mäta polarisationen kan man påvisa att

denna mekanism förekommer och mäta hur stort dess bidrag är. Dessvärre är de experimentuppställningar som bäst används för att studera mesoner inte utrustade för mäta fotoners polarisation, och vice versa. En sådan mätning är därför svår att genomföra i dagsläget. Istället kan vi studera den besläktade processen $\eta' \to \pi^+\pi^-\gamma^{(*)} \to \pi^+\pi^- e^+e^-$. Här omvandlas fotonen till ett elektron-positronpar och eventuella brott av *CP*-symmetrin går att mäta genom att studera hur paret rör sig. Specifikt förväntar man sig att den nya mekanismen ska leda till att vinkeln φ mellan planen som e^+e^-- och $\pi^+\pi^-$-paren färdas i, se Fig. II, har en asymmetrisk fördelning. Detta specifika sönderfall är också intressant för att testa de teoretiska beskrivningarna av den starka kraften vid låga energier. Det är nämligen mycket sällsynt, och att studera sådana extremfall är viktigt för att testa vår förståelse för den bakomliggande fysiken till det yttersta och identifiera eventuella luckor. Genom att mäta *fördelningskvoten*, d.v.s. hur ofta just detta sönderfall inträffar jämfört med andra möjligheter, testar vi förutsägelserna från olika modeller som används för att beskriva den starka kraften vid låga energier.

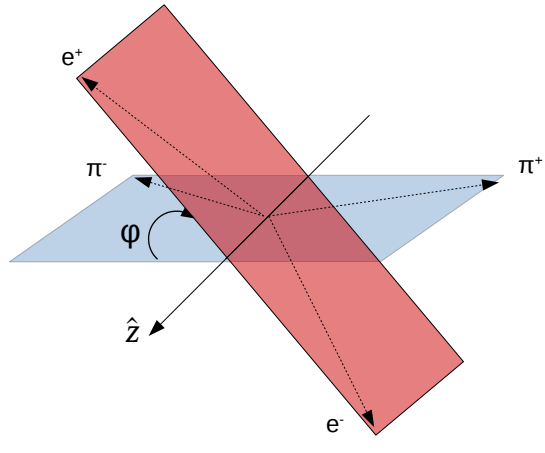

Figur II. Illustration av vinkeln φ mellan $\pi^+\pi^-$- och e^+e^--parens sönderfallsplan. Figur från Ref. [84].

I den första av två analyser som presenteras i den här avhandlingen har jag använt data från BESIII för att studera sönderfallet $\eta' \to \pi^+\pi^- e^+e^-$. Jag har mätt fördelningskvoten med två gånger bätrre precision än den tidigare bästa mätningen och studerat vinkeln mellan $\pi^+\pi^-$- och e^+e^--paren för första gången någonsin. Vinkelfördelningen uppvisar ingen asymmetri. Slutsatsen är därför att inget brott av *CP*-symmetrin kan påvisas och att förutsägelsen från SM är korrekt.

Hyperoners formfaktorer

Ett enormt arbete pågår världen över med att förfina de experimentella metoder som används för att studera protoner och neutroner, men det är värdefullt att attackera frågorna om hadronernas inre struktur längs flera parallella fronter samtidigt. Ett komplementärt angreppssätt är att studera andra baryoner än just de två vanligaste för att på så sätt försöka skapa en mer komplett och övergripande förståelse för hur det går till när den starka kraften binder samman kvarkarna. I den andra delen av den här avhandlingen fokuserar jag på *hyperoner*, d.v.s. baryoner som innehåller minst en särkvark. Hur ser den elektromagnetiska strukturen hos en hyperon ut? Har särkvarkens tyngre massa någon inverkan på hur kvarkarna ordnar sig? Och vad säger det i sådant fall om den starka kraften? Svaren på dessa frågor kompletterar vår kunskap om protonerna och neutronerna och bidrar med ny information som kan hjälpa oss att forma en mer komplett och övergripande förståelse för hur den starka kraften binder samman kvarkar och bildar all den materia som omger oss.

Till skillnad från protoner och neutroner är hyperoner instabila. De mest långlivade hyperonerna lever i blott 10^{-10} sekunder innan de sönderfaller. Detta gör att det dessvärre är mycket svårt att mäta deras rumslika formfaktorer. Vi kan däremot mäta deras tidslika formfaktorer i elektron-positron-kollisioner. I dessa studier är det till stor hjälp att hyperonernas sönderfall är *självanalyserande*. Det betyder att sönderfallsprodukternas rörelseriktningar avslöjar i vilken riktning den sönderfallande hyperonens spinn pekade. Genom att mäta detta i en ensemble av hyperoner får vi ett mått på polarisationen och det gör i sin tur att vi kan bestämma fasvinkeln mellan formfaktorerna. För protonerna och neutronerna är det omöjligt att mäta polarisationen utan specialdesignade experimentuppställningar som ännu inte existerar. Om man kan mäta både hyperonernas tidslika formfaktorer inklusive fasvinkeln, samt hur dessa varierar vid olika energier, kan denna information användas för att beräkna de rumslika formfaktorerna. Med hyperoner kan vi alltså lära oss både om var kvarkarna befinner sig och hur det går till när de sätts samman med en och samma mätning. Denna information kan i sin tur jämföras med det vi vet om nukleonerna för att skapa oss en bredare förståelse för materiens inre.

I den andra analysen som presenteras i den här avhandlingen har jag studerat processen $e^+e^- \to \Lambda\bar{\Lambda}$ med data från BESIII-experimentet för att mäta Λ-hyperonens tidslika formfaktorer. Genom en ny metod där både helt och delvis rekonstruerade $\Lambda\bar{\Lambda}$-händelser kombineras har jag mätt formfaktorerna, inklusive fasvinkeln, vid totalt fem olika energier. Vid fyra av dessa är det den första mätningen någonsin, och i samtliga fall är precisionen den bästa som har uppnåtts. Resultaten visar att fasvinkeln varierar mycket mellan de högre och lägre energierna, och detta är oväntat. Det är möjligt att detta är artefakt av metoden eller en statistisk effekt som uppstår på grund av att datamängderna som används är små och därför krävs vidare undersökningar. Oavsett vilket är resultaten som presenteras i avhandlingen en viktig pusselbit

i arbetet med att förstå Λ-hyperonens inre, och skulle kunna användas för att bestämma de rumslika formfaktorerna som för närvarande inte går att mäta. Denna information skulle i sin tur kunna användas för att för första gången kunna beräkna Λ-hyperonens laddningsradie. Jag presenterar även en precis mätning av *tvärsnittet* för processen $e^+e^- \to \Lambda\bar{\Lambda}$, d.v.s. sannolikheten att processen inträffar, vid samtliga fem energier. Denna information kan användas för att utvidga vår förståelse för hur det går till när $\Lambda\bar{\Lambda}$-paret produceras.

Slutligen har jag undersökt hur väl en planerad uppgradering av BESIII-detektorn kan förväntas fungera för att rekonstruera hyperonerna i processen $e^+e^- \to \Lambda\bar{\Lambda}$. Detta är utmanande eftersom hyperonerna, till skillnad från många andra partiklar, inte sönderfaller vid interaktionspunkten utan först färdas en mätbar sträcka i detektorn. Studien inriktades specfikt på den mjukvara som ska användas för att spåra laddade partiklar och beräkna deras egenskaper. Ett minimikrav för att den nya detektorn ska kunna användas är att den och dess mjukvara kan registrera ungefär en lika stor andel av alla laddade spår som den nuvarande detektorn, samt att upplösningen i mätningen av spårens position ska vara bättre än för den nuvarande detektorn. Mina studier visar att mjukvaran redan i detta tidiga skede uppfyller kraven på upplösningen, men däremot är effektivteten låg eftersom de algoritmer som används inte lämpar sig för att för att rekonstruera hyperoner. Mjukvaran är alltså på väg mot att nå målen, men måste vidareutvecklas för att fungera väl för studier av hyperoner eller andra partiklar inte sönderfaller vid interaktionspunkten.

Acknowledgements

Much of the work that went into this thesis happened during a global pandemic. It was a strange time in many ways but also, I think, a productive one. There were many people that contributed in one way or another to making this thesis a reality, and in the following I will try to express my gratitude.

First of all I want to thank my supervisors. Andrzej for getting me hooked on hadron physics in the first place and for always being a fountain of ideas that I have had the pleasure to try and translate into action. Karin for your tireless enthusiasm and great feedback. Magnus for your thoroughness, support, and the many teaching opportunities (and cookies of course).

I also want to thank Lars, Stefan, and Tord for your advice and for proofreading the thesis.

A big thanks to the post-doctoral members of our BESIII group throughout the years. Jacek for all the intense programming sessions and many late nights! Patrik for your conscientiousness and for always staying positive, upbeat and a friendly face. Cui for sharing your knowledge of the BESIII experiment. I would also like to thank Shuangshi for welcoming me to IHEP many times, and all the people, far too many to mention everyone by name, that I met while I was there.

Thanks also to all my Ph.D. student colleagues in Uppsala over the years; Joachim, Walter, and Liu Liang for sharing an office with me, and to Elisabetta, Bo, Aila, Jenny, Adeel, An Di, Jana, and Ebba for the fun times.

I also had the pleasure of collaborating with many different people in teaching and outreach activites and I thank all of you for great learning experiences. Special thanks to Hans and Johan for help with the Nuclear physics lab. Thanks also to Michael for interesting coding discussions.

Thanks to my parents for all that you have done for me over the years and for teaching me to work hard and do what I want in life. And to Maja, my sister, for being incredibly cool in everything you do, and inspiring me by being good at completely different things than I am.

Finally, I want to thank Olga for being the spontaneity to my routine and, of course, for being funnier than me. You bring purpose and happiness to every day of my life.

References

[1] E. Noether, *Invariant Variation Problems*, *Gott. Nachr.* **1918** (1918) 235.

[2] S. Weinberg, *A model of leptons*, *Phys. Rev. Lett.* **19** (1967) 1264.

[3] A. Salam and J.C. Ward, *Weak and electromagnetic interactions*, *Nuovo Cim.* **11** (1959) 568.

[4] S.L. Glashow, *Partial-symmetries of weak interactions*, *Nuclear Physics* **22** (1961) 579.

[5] MissMJ and Cush, *Standard Model of Elementary Particles* , `https://en.wikipedia.org/wiki/File:Standard_Model_of_Elementary_Particles.svg` Accessed: 2022-01-31.

[6] P. Zyla et al., *Review of Particle Physics*, *Prog. Theor. Exp. Phys.* **2020** (2020) 083C01.

[7] D.J. Gross and F. Wilczek, *Ultraviolet Behavior of Non-Abelian Gauge Theories*, *Phys. Rev. Lett.* **30** (1973) 1343.

[8] H.D. Politzer, *Reliable Perturbative Results for Strong Interactions?*, *Phys. Rev. Lett.* **30** (1973) 1346.

[9] S. Bethke and J.E. Pilcher, *Tests of perturbative QCD at LEP*, *Ann. Rev. Nucl. Part. Sci.* **42** (1992) 251.

[10] C. Mesropian and D. Bandurin, *Review of physics results from the Tevatron: QCD physics*, *Int. J. Mod. Phys. A* **30** (2015) 1541002.

[11] H1, ZEUS collaboration, *New HERA Results on Perturbative QCD*, *Acta Phys. Polon. Supp.* **11** (2018) 429.

[12] C.S. Wu, E. Ambler, R.W. Hayward, D.D. Hoppes and R.P. Hudson, *Experimental Test of Parity Conservation in Beta Decay*, *Phys. Rev.* **105** (1957) 1413.

[13] T.D. Lee and C.N. Yang, *Question of Parity Conservation in Weak Interactions*, *Phys. Rev.* **104** (1956) 254.

[14] T.D. Lee, R. Oehme and C.N. Yang, *Remarks on Possible Noninvariance under Time Reversal and Charge Conjugation*, *Phys. Rev.* **106** (1957) 340.

[15] J.H. Christenson, J.W. Cronin, V.L. Fitch and R. Turlay, *Evidence for the* 2π *Decay of the* K_2^0 *Meson*, *Phys. Rev. Lett.* **13** (1964) 138.

[16] C. Abel, S. Afach, N.J. Ayres, C.A. Baker, G. Ban, G. Bison et al., *Measurement of the Permanent Electric Dipole Moment of the Neutron*, *Phys. Rev. Lett.* **124** (2020) 081803.

[17] L. Di Luzio, M. Giannotti, E. Nardi and L. Visinelli, *The landscape of QCD axion models*, *Physics Reports* **870** (2020) 1.

[18] A.D. Sakharov, *Violation of CP invariance, C asymmetry, and baryon asymmetry of the universe*, *Sov. Phys. Usp.* **34** (1991) 392.

[19] NA31 collaboration, *First Evidence for Direct CP Violation*, *Phys. Lett. B* **206** (1988) 169.

[20] NA48 collaboration, *A new measurement of direct CP violation in two pion decays of the neutral kaon*, *Phys. Lett. B* **465** (1999) 335.

[21] KTeV collaboration, *Observation of direct CP violation in $K_{S,L} \to \pi\pi$ decays*, *Phys. Rev. Lett.* **83** (1999) 22.
[22] KTeV collaboration, *Observation of CP violation in $K_L \to \pi^+\pi^- e^+ e^-$ decays*, *Phys. Rev. Lett.* **84** (2000) 408.
[23] NA48 collaboration, *Results on CP violation from the NA48 experiment at CERN*, *Int. J. Mod. Phys. A* **17** (2002) 3012.
[24] LHCb collaboration, *Observation of CP Violation in Charm Decays*, *Phys. Rev. Lett.* **122** (2019) 211803.
[25] BaBar collaboration, *Observation of CP Violation in the B^0 Meson System*, *Phys. Rev. Lett.* **87** (2001) 091801.
[26] Belle collaboration, *Observation of Large CP Violation in the Neutral B Meson System*, *Phys. Rev. Lett.* **87** (2001) 091802.
[27] M. Gell-Mann, *The Eightfold Way: A Theory of strong interaction symmetry*, *CTSL-20, TID-12608* (1961) .
[28] Y. Ne'eman, *Derivation of strong interactions from a gauge invariance*, *Nuclear Physics* **26** (1961) 222.
[29] M. Gell-Mann, *A schematic model of baryons and mesons*, *Physics Letters* **8** (1964) 214.
[30] G. Zweig, *An SU(3) model for strong interaction symmetry and its breaking. Version 1*, *CERN-TH-401* (1964) .
[31] E2m, *Noneto mesônico de spin 0* , `https://commons.wikimedia.org/wiki/File:Noneto_mesônico_de_spin_0.png`. Accessed 2022-01-31.
[32] E2m, *Noneto mesônico de spin 1* , `https://commons.wikimedia.org/wiki/File:Noneto_mesônico_de_spin_1.png`. Accessed 2022-01-31.
[33] BESIII collaboration, *Observation of a Charged Charmoniumlike Structure in $e^+e^- \to \pi^+\pi^- J/\psi$ at $\sqrt{s}$=4.26 GeV*, *Phys. Rev. Lett.* **110** (2013) 252001.
[34] Belle collaboration, *Study of $e^+e^- \to \pi^+\pi^- J/\psi$ and Observation of a Charged Charmoniumlike State at Belle*, *Phys. Rev. Lett.* **110** (2013) 252002.
[35] E2m, *Octeto bariônico* , `https://commons.wikimedia.org/wiki/File:Octeto_bariônico.png`. Accessed 2022-02-03.
[36] E2m, *Decupleto bariônico* , `https://commons.wikimedia.org/wiki/File:Decupleto_bariônico.png`. Accessed 2022-02-03.
[37] LHCb collaboration, *Observation of $J/\psi p$ Resonances Consistent with Pentaquark States in $\Lambda_b^0 \to J/\psi K^- p$ Decays*, *Phys. Rev. Lett.* **115** (2015) 072001.
[38] C.A. Aidala, S.D. Bass, D. Hasch and G.K. Mallot, *The spin structure of the nucleon*, *Rev. Mod. Phys.* **85** (2013) 655.
[39] M. Schumacher, *Nambu's nobel prize, the meson and the mass of visible matter*, *Annalen der Physik* **526** (2014) 215.
[40] F. Myhrer and A.W. Thomas, *Understanding the proton's spin structure*, *Journal of Physics G: Nuclear and Particle Physics* **37** (2010) 023101.
[41] R. Pohl et al., *The size of the proton*, *Nature* **466** (2010) 213.
[42] M. Niering, R. Holzwarth, J. Reichert, P. Pokasov, T. Udem, M. Weitz et al., *Measurement of the Hydrogen 1S- 2S Transition Frequency by Phase Coherent*

Comparison with a Microwave Cesium Fountain Clock, *Phys. Rev. Lett.* **84** (2000) 5496.
[43] M. Fischer, N. Kolachevsky, M. Zimmermann, R. Holzwarth, T. Udem, T.W. Hänsch et al., *New Limits on the Drift of Fundamental Constants from Laboratory Measurements*, *Phys. Rev. Lett.* **92** (2004) 230802.
[44] de Beauvoir, B., Schwob, C., Acef, O., Jozefowski, L., Hilico, L., Nez, F. et al., *Metrology of the hydrogen and deuterium atoms: Determination of the Rydberg constant and Lamb shifts*, *Eur. Phys. J. D* **12** (2000) 61.
[45] C. Schwob, L. Jozefowski, B. de Beauvoir, L. Hilico, F. Nez, L. Julien et al., *Optical frequency measurement of the* $2S-12D$ *transitions in hydrogen and deuterium: Rydberg constant and lamb shift determinations*, *Phys. Rev. Lett.* **82** (1999) 4960.
[46] P.G. Blunden and I. Sick, *Proton radii and two-photon exchange*, *Phys. Rev. C* **72** (2005) 057601.
[47] N. Bezginov, T. Valdez, M. Horbatsch, A. Marsman, A.C. Vutha and E.A. Hessels, *A measurement of the atomic hydrogen Lamb shift and the proton charge radius*, *Science* **365** (2019) 1007.
[48] W. Xiong et al., *A small proton charge radius from an electron–proton scattering experiment*, *Nature* **575** (2019) 147.
[49] R. Hofstadter, *Electron Scattering and Nuclear Structure*, *Rev. Mod. Phys.* **28** (1956) 214.
[50] Y. Nambu, *Possible Existence of a Heavy Neutral Meson*, *Phys. Rev.* **106** (1957) 1366.
[51] W.R. Frazer and J.R. Fulco, *Effect of a Pion-Pion Scattering Resonance on Nucleon Structure*, *Phys. Rev. Lett.* **2** (1959) 365.
[52] J. Sakurai, *Theory of strong interactions*, *Annals of Physics* **11** (1960) 1 .
[53] M. Bando, T. Kugo, S. Uehara, K. Yamawaki and T. Yanagida, *Is the* ρ *Meson a Dynamical Gauge Boson of Hidden Local Symmetry?*, *Phys. Rev. Lett.* **54** (1985) 1215.
[54] E.D. Bloom, D.H. Coward, H. DeStaebler, J. Drees, G. Miller, L.W. Mo et al., *High-Energy Inelastic* $e-p$ *Scattering at* 6° *and* 10°, *Phys. Rev. Lett.* **23** (1969) 930.
[55] F. Iachello, A. Jackson and A. Lande, *Semi-phenomenological fits to nucleon electromagnetic form factors*, *Physics Letters B* **43** (1973) 191.
[56] Y. Klopot, A. Oganesian and O. Teryaev, *Axial anomaly and vector meson dominance model*, *JETP Lett.* **99** (2014) 679.
[57] S.L. Adler, *Axial-Vector Vertex in Spinor Electrodynamics*, *Phys. Rev.* **177** (1969) 2426.
[58] J.S. Bell and R. Jackiw, *A PCAC puzzle:* $\pi^0 \to \gamma\gamma$ *in the* σ *model*, *Nuovo Cim. A* **60** (1969) 47.
[59] S. Weinberg, *The U(1) problem*, *Phys. Rev. D* **11** (1975) 3583.
[60] J. Wess and B. Zumino, *Consequences of anomalous Ward identities*, *Phys. Lett. B* **37** (1971) 95.
[61] E. Witten, *Global Aspects of Current Algebra*, *Nucl. Phys. B* **223** (1983) 422.
[62] K.G. Wilson, *Confinement of quarks*, *Phys. Rev. D* **10** (1974) 2445.
[63] Y. Aoki et al., *FLAG Review 2021*, 2111.09849.
[64] C. Alexandrou, M. Constantinou, K. Hadjiyiannakou, K. Jansen,

C. Kallidonis, G. Koutsou et al., *Nucleon Spin and Momentum Decomposition Using Lattice QCD Simulations*, *Phys. Rev. Lett.* **119** (2017) 142002.
[65] C. Alexandrou, A. Athenodorou, K. Hadjiyiannakou and A. Todaro, *Neutron electric dipole moment using lattice QCD simulations at the physical point*, *Phys. Rev. D* **103** (2021) 054501.
[66] L. Landsberg, *Electromagnetic decays of light mesons*, *Physics Reports* **128** (1985) 301.
[67] F.J. Ernst, R.G. Sachs and K.C. Wali, *Electromagnetic Form Factors of the Nucleon*, *Phys. Rev.* **119** (1960) 1105.
[68] R.G. Sachs, *High-Energy Behavior of Nucleon Electromagnetic Form Factors*, *Phys. Rev.* **126** (1962) 2256.
[69] R. Hofstadter, F. Bumiller and M.R. Yearian, *Electromagnetic Structure of the Proton and Neutron*, *Rev. Mod. Phys.* **30** (1958) 482.
[70] M.N. Rosenbluth, *High Energy Elastic Scattering of Electrons on Protons*, *Phys. Rev.* **79** (1950) 615.
[71] J. Arrington, K. de Jager and C.F. Perdrisat, *Nucleon Form Factors: A Jefferson Lab Perspective*, *J. Phys. Conf. Ser.* **299** (2011) 012002.
[72] C.F. Perdrisat, V. Punjabi and M. Vanderhaeghen, *Nucleon Electromagnetic Form Factors*, *Prog. Part. Nucl. Phys.* **59** (2007) 694.
[73] The Jefferson Lab Hall A collaboration, *Final analysis of proton form factor ratio data at* $Q^2 = 4.0$*, 4.8, and 5.6 gev*^{2}, *Phys. Rev. C* **85** (2012) 045203.
[74] A.Z. Dubnickova, S. Dubnicka and M.P. Rekalo, *Investigation of the nucleon electromagnetic structure by polarization effects in* e^+e^- *—> N anti-N processes*, *Nuovo Cim. A* **109** (1996) 241.
[75] E. Kuraev, A. Dbeyssi and E. Tomasi-Gustafsson, *A model for space and time-like proton (neutron) form factors*, *Physics Letters B* **712** (2012) 240.
[76] J. Haidenbauer, U.-G. Meißner and L.-Y. Dai, *Hyperon electromagnetic form factors in the timelike region*, *Phys. Rev. D* **103** (2021) 014028.
[77] BESIII collaboration, *Measurement of Proton Electromagnetic Form Factors in* $e^+e^- \to p\overline{p}$ *in the Energy Region 2.00–3.08 GeV*, *Phys. Rev. Lett.* **124** (2020) 042001.
[78] BESIII collaboration, *Oscillating features in the electromagnetic structure of the neutron*, *Nature Phys.* **17** (2021) 1200.
[79] S.M. Bilenky, C. Giunti and V. Wataghin, *The process anti-p p —> e- e+ with polarized initial particles and proton form-factors in timelike region*, *Z. Phys. C* **59** (1993) 475.
[80] Tomasi-Gustafsson, E., Lacroix, F., Duterte, C. and Gakh, G. I., *Nucleon electromagnetic form factors and polarization observables in space-like and time-like regions*, *Eur. Phys. J. A* **24** (2005) 419.
[81] PANDA collaboration, *Physics Performance Report for PANDA: Strong Interaction Studies with Antiprotons*, 0903.3905.
[82] H. Stroher, P. Lenisa and F. Rathmann, *The road towards polarized antiprotons*, *PoS* **STORI11** (2011) 030.
[83] H. Gisbert and A. Pich, *Direct CP violation in* $K^0 \to \pi\pi$ *: Standard Model Status*, *Rep. Prog. Phys.* **81** (2018) 076201.
[84] BESIII collaboration, *Measurement of the branching fraction of and search for a CP-violating asymmetry in* $\eta' \to \pi^+\pi^-e^+e^-$ *at BESIII*, *Phys. Rev. D* **103**

(2021) 092005.
[85] P. Heiliger and L.M. Sehgal, *Direct and indirect* CP *violation in the decay* $K_L \to \pi^+\pi^- e^+ e^-$, *Phys. Rev. D* **48** (1993) 4146.
[86] P. Herczeg and P. Singer, *Weak-Interaction Effects in* $\eta \to \pi^+\pi^-\gamma$, *Phys. Rev. D* **8** (1973) 4107.
[87] C. Jarlskog and E. Shabalin, *How large are the rates of the CP-violating* $\eta,\eta' \to \pi\pi$ *decays?*, *Phys. Rev. D* **52** (1995) 248.
[88] LHCb collaboration, *Search for the CP-violating strong decays* $\eta \to \pi^+\pi^-$ *and* $\eta'(958) \to \pi^+\pi^-$, *Phys. Lett. B* **764** (2017) 233.
[89] L. Ametller, *Eta decays involving photons*, *Phys. Scripta T* **99** (2002) 45.
[90] B.R. Holstein, *Allowed eta decay modes and chiral symmetry*, *Phys. Scripta T* **99** (2002) 55.
[91] B. Borasoy and R. Nissler, $\eta,\ \eta' \to \pi^+\pi^- l^+ l^-$ *in a chiral unitary approach*, *Eur. Phys. J.* **A33** (2007) 95.
[92] T. Petri, *Anomalous decays of pseudoscalar mesons*, Ph.D. thesis, Julich, Forschungszentrum, 2010. 1010.2378.
[93] T. Fujiwara, T. Kugo, H. Terao, S. Uehara and K. Yamawaki, *Nonabelian Anomaly and Vector Mesons as Dynamical Gauge Bosons of Hidden Local Symmetries*, *Prog. Theor. Phys.* **73** (1985) 926.
[94] M. Harada and K. Yamawaki, *Hidden local symmetry at loop: A New perspective of composite gauge boson and chiral phase transition*, *Phys. Rept.* **381** (2003) 1.
[95] M. Benayoun, P. David, L. DelBuono, P. Leruste and H.B. O'Connell, *Anomalous* η/η' *decays: The Triangle and box anomalies*, *Eur. Phys. J. C* **31** (2003) 525.
[96] A. Grigorian, A. Ladage, D.J. Mellema, F.D. Rudnick, D.I. Sober, D.H. Stork et al., *Charge Conjugation Invariance in* $\eta'(958) \to \pi^+\pi^-\gamma$, *Nucl. Phys. B* **91** (1975) 232.
[97] TASSO collaboration, *Measurement of the Radiative Width of the* η' *(958) in Two Photon Interactions*, *Phys. Lett. B* **147** (1984) 487.
[98] ARGUS collaboration, *Measurement of* $\eta' \to \pi^+\pi^-\gamma$ *in* $\gamma\gamma$ *Collisions*, *Phys. Lett. B* **199** (1987) 457.
[99] TPC/Two Gamma collaboration, *A study of* η' *formation in photon-photon collisions*, *Phys. Rev. D* **35** (1987) 2650.
[100] S.I. Bityukov et al., *Study of the radiative decay* $\eta' \to \pi^+\pi^-\gamma$, *Z. Phys. C* **50** (1991) 451.
[101] Crystal Barrel collaboration, *Measurement of the decay distribution of* $\eta' \to \pi^+\pi^-\pi^-\gamma$ *and evidence for the box anomaly*, *Phys. Lett. B* **402** (1997) 195.
[102] BESIII collaboration, *Precision Study of* $\eta' \to \gamma\pi^+\pi^-$ *Decay Dynamics*, *Phys. Rev. Lett.* **120** (2018) 242003.
[103] M. Benayoun, P. David, L. DelBuono and O. Leitner, *A Global Treatment Of VMD Physics Up To The* ϕ*: I.* e^+e^- *Annihilations, Anomalies And Vector Meson Partial Widths*, *Eur. Phys. J. C* **65** (2010) 211.
[104] C.Q. Geng, J.N. Ng and T.H. Wu, *CP violation in the decay* $\eta \to \pi^+\pi^-\gamma$, *Mod. Phys. Lett. A* **17** (2002) 1489.
[105] L.M. Sehgal and J. van Leusen, *Violation of Time Reversal Invariance in the*

Decays $K_L \to \pi^+\pi^-\gamma$ and $K_L \to \pi^+\pi^-e^+e^-$, *Phys. Rev. Lett.* **83** (1999) 4933.
[106] H. Olsen and L.C. Maximon, *Photon and Electron Polarization in High-Energy Bremsstrahlung and Pair Production with Screening*, *Phys. Rev.* **114** (1959) 887.
[107] Y. Grossman and D. Pirjol, *Extracting and using photon polarization information in radiative B decays*, *JHEP* **06** (2000) 029.
[108] D.-N. Gao, *The CP violating asymmetry in $\eta \to \pi^+\pi^-e^+e^-$*, *Mod. Phys. Lett.* **A17** (2002) 1583.
[109] L. Gan, B. Kubis, E. Passemar and S. Tulin, *Precision tests of fundamental physics with η and η' mesons*, 2007.00664.
[110] KLOE collaboration, *Measurement of the branching ratio and search for a CP violating asymmetry in the $\eta \to \pi^+\pi^-e^+e^-$ decay at KLOE* , *Phys. Lett. B* **675** (2009) 283 .
[111] WASA-at-COSY collaboration, *Measurements of Branching Ratios for η Decays into Charged Particles*, *Phys. Rev.* **C94** (2016) 065206.
[112] CLEO collaboration, *Observation of η' decays to $\pi^+\pi^-\pi^0$ and $\pi^+\pi^-e^+e^-$*, *Phys. Rev. Lett.* **102** (2009) 061801.
[113] BESIII collaboration, *Measurement of $\eta' \to \pi^+\pi^-e^+e^-$ and $\eta' \to \pi^+\pi^-\mu^+\mu^-$*, *Phys. Rev.* **D87** (2013) 092011.
[114] M. Gell-Mann and A. Pais, *Theoretical Views on the New Particles*, 1954.
[115] T.D. Lee and C.N. Yang, *General Partial Wave Analysis of the Decay of a Hyperon of Spin ½*, *Phys. Rev.* **108** (1957) 1645.
[116] J.W. Cronin and O.E. Overseth, *Measurement of the decay parameters of the Λ^0 particle*, *Phys. Rev.* **129** (1963) 1795.
[117] O.E. Overseth and R.F. Roth, *Time Reversal Invariance in Λ^0 Decay*, *Phys. Rev. Lett.* **19** (1967) 391.
[118] P.M. Dauber, J.P. Berge, J.R. Hubbard, D.W. Merrill and R.A. Muller, *Production and decay of cascade hyperons*, *Phys. Rev.* **179** (1969) 1262.
[119] W.E. Cleland, G. Conforto, G.H. Eaton, H.J. Gerber, M. Reinharz, A. Gautschi et al., *A measurement of the beta-parameter in the charged nonleptonic decay of the Λ^0 hyperon*, *Nucl. Phys. B* **40** (1972) 221.
[120] P. Astbury et al., *Measurement of the Differential Cross-Section and the Spin-Correlation Parameters P,A, and R in the Backward Peak of $\pi^- p \to K^0\Lambda$ at 5-GeV/c*, *Nucl. Phys. B* **99** (1975) 30.
[121] BESIII collaboration, *Polarization and Entanglement in Baryon-Antibaryon Pair Production in Electron-Positron Annihilation*, *Nature Phys.* **15** (2019) 631.
[122] D.G. Ireland, M. Döring, D.I. Glazier, J. Haidenbauer, M. Mai, R. Murray-Smith et al., *Kaon Photoproduction and the Λ Decay Parameter α_-*, *Phys. Rev. Lett.* **123** (2019) 182301.
[123] BESIII collaboration, *Weak phases and CP-symmetry tests in sequential decays of entangled double-strange baryons*, 2105.11155.
[124] LHCb collaboration, *Measurement of the $\Lambda_b^0 \to J/\psi\Lambda$ angular distribution and the Λ_b^0 polarisation in pp collisions*, *JHEP* **06** (2020) 110.
[125] B. Kubis and U.G. Meissner, *Baryon form-factors in chiral perturbation theory*, *Eur. Phys. J. C* **18** (2001) 747.
[126] H.-W. Lin and K. Orginos, *Strange Baryon Electromagnetic Form Factors and*

SU(3) Flavor Symmetry Breaking, *Phys. Rev. D* **79** (2009) 074507.
[127] SELEX collaboration, *Measurement of the Σ^- Charge Radius by Sigma-Electron Elastic Scattering*, *Phys. Lett. B* **522** (2001) 233.
[128] R. Zwicky, *A brief Introduction to Dispersion Relations and Analyticity*, in *Quantum Field Theory at the Limits: from Strong Fields to Heavy Quarks*, pp. 93–120, 2017, DOI [1610.06090].
[129] S. Pacetti, *Nucleon form factors and dispersion relations*, *Eur. Phys. J. A* **32** (2007) 421.
[130] A. Mangoni, S. Pacetti and E. Tomasi-Gustafsson, *The first exploration of the physical Riemann surfaces of the ratio G_E^Λ/G_M^Λ*, *Phys. Rev. D* **104** (2021) 116016.
[131] V.A. Matveev, R.M. Muradyan and A.N. Tavkhelidze, *Automodelity in strong interactions*, *Theor. Mat. Fiz.* **15** (1973) 332.
[132] S.J. Brodsky and G.R. Farrar, *Scaling Laws at Large Transverse Momentum*, *Phys. Rev. Lett.* **31** (1973) 1153.
[133] G. Gakh and E. Tomasi-Gustafsson, *General analysis of polarization phenomena in $e^+e^- \to n^+n^-$ for axial parametrization of two-photon exchange*, *Nuclear Physics A* **771** (2006) 169.
[134] H. Czyż, A. Grzelińska and J.H. Kühn, *Spin asymmetries and correlations in Λ-pair production through the radiative return method*, *Phys. Rev. D* **75** (2007) 074026.
[135] G. Fäldt, *Entanglement in joint $\Lambda\bar{\Lambda}$ decay*, *Eur. Phys. J. A* **51** (2015) 74.
[136] G. Fäldt, *Polarization observables in the $e^+e^- \to \bar{\Lambda}\Lambda$ reaction*, *Eur. Phys. J. A* **52** (2016) 141.
[137] G. Fäldt and A. Kupsc, *Hadronic structure functions in the $e^+e^- \to \bar{\Lambda}\Lambda$ reaction*, *Phys. Lett. B* **772** (2017) 16.
[138] E. Perotti, G. Fäldt, A. Kupsc, S. Leupold and J.J. Song, *Polarization observables in e^+e^- annihilation to a baryon-antibaryon pair*, *Phys. Rev. D* **99** (2019) 056008.
[139] BaBar collaboration, *Study of $e^+e^- \to \pi^+\pi^-\pi^0$ process using initial state radiation with BaBar*, *Phys. Rev. D* **70** (2004) 072004.
[140] BaBar collaboration, *Study of $e^+e^- \to \Lambda\bar{\Lambda}$, $\Lambda\bar{\Sigma}^0$, $\Sigma^0\bar{\Sigma}^0$ using initial state radiation with BABAR*, *Phys. Rev. D* **76** (2007) 092006.
[141] S. Dobbs, K.K. Seth, A. Tomaradze, T. Xiao and G. Bonvicini, *Hyperon Form Factors & Diquark Correlations*, *Phys. Rev. D* **96** (2017) 092004.
[142] BESIII collaboration, *Measurement of the cross section for $e^+e^- \to \Lambda\overline{\Lambda}$ and evidence of the decay $\psi(3770) \to \Lambda\overline{\Lambda}$*, *Phys. Rev. D* **104** (2021) L091104.
[143] BESIII collaboration, *Observation of a cross-section enhancement near mass threshold in $e^+e^- \to \Lambda\overline{\Lambda}$*, *Phys. Rev. D* **97** (2018) 032013.
[144] BESIII collaboration, *Complete Measurement of the Λ Electromagnetic Form Factors*, *Phys. Rev. Lett.* **123** (2019) 122003.
[145] BESIII collaboration, *Measurement of Λ baryon polarization in $e^+e^- \to \Lambda\overline{\Lambda}$ at $\sqrt{s} = 3.773$ GeV*, *Phys. Rev. D* **105** (2022) L011101.
[146] BESIII collaboration, *Σ^+ and $\overline{\Sigma}^-$ Polarization in the J/ψ and $\psi(3686)$ Decays*, *Phys. Rev. Lett.* **125** (2020) 052004.
[147] C. Yu et al., *BEPCII Performance and Beam Dynamics Studies on Luminosity*, in *Proc. of International Particle Accelerator Conference (IPAC'16), Busan,*

Korea, May 8-13, 2016, pp. 1014–1018.
[148] B. Liu, M. Gu, C. Zhang and Y. Chi, *New Electron Gun System for BEPCII*, in *Proceedings of the 2005 Particle Accelerator Conference*, pp. 1–3, 2005, DOI.
[149] G. Pei, *Progress of the BEPCII Linac Upgrade*, in *Proceedings of the 2005 Particle Accelerator Conference*, pp. 2416–2418, 2005.
[150] C. Zhang and G. Pei, *BEPCII-The Second Phase Construction of Beijing Electron Positron Collider*, in *Proceedings of the 2005 Particle Accelerator Conference*, pp. 131–135, 2005.
[151] BESIII collaboration, *Future Physics Programme of BESIII*, *Chin. Phys. C* **44** (2020) 040001.
[152] Q. Qin et al., *Beam Dynamic Issues in the BEPCII Luminosity Commissioning*, *Conf. Proc. C* **100523** (2010) TUPEB020.
[153] BESIII collaboration, *Design and Construction of the BESIII Detector*, *Nucl. Instrum. Meth. A* **614** (2010) 345.
[154] *Introduction to the BESIII Experiment* , BESIII Website: `http://english.ihep.cas.cn/bes/doc/2124.html`. Accessed 2021-12-20.
[155] *BESIII MDC Tracking Parameters* , `http://bes.ihep.ac.cn/bes3/internal/software/offline/SofPro/zhangyao/Bes3_trk_par.pdf`.
[156] D.M. Asner et al., *Physics at BES-III*, *Int. J. Mod. Phys.* **A24** (2009) S1.
[157] C.-J. Chen et al., *The BESIII drift chamber*, *2007 IEEE Nuclear Science Symposium Conference Record* **3** (2007) 1844.
[158] Z. Liu et al., *Trigger System of BESIII*, in *2007 15th IEEE-NPSS Real-Time Conference*, pp. 1–4, 2007, DOI.
[159] C.-D. Fu et al., *Study of the online event filtering algorithm for BESIII*, *Chin. Phys. C* **32** (2008) 329.
[160] N. Berger et al., *Trigger efficiencies at BES III*, *Chin. Phys. C* **34** (2010) 1779.
[161] BESIII collaboration, *Study of BESIII trigger efficiencies with the 2018 J/ψ data*, *Chin. Phys. C* **45** (2021) 023002.
[162] M. Xiang et al., *Determination of event start time at BESIII*, *Chin. Phys. C* **32** (2008) 744.
[163] A. Balla et al., *Status of the Cylindical-GEM project for the KLOE-2 Inner Tracker*, *Nucl. Instrum. Meth. A* **628** (2011) 194.
[164] F. Sauli, *GEM: A new concept for electron amplification in gas detectors*, *Nucl. Instrum. Meth.* **386** (1997) 531.
[165] F. Sauli, *The gas electron multiplier (GEM): Operating principles and applications*, *Nucl. Instrum. Meth.* **805** (2016) 2.
[166] R. Farinelli et al., *Preliminary results from the cosmic data taking of the BESIII cylindrical GEM detectors*, *JINST* **15** (2020) C08004.
[167] BESIII collaboration, *BESIII Cylindrical GEM Inner Tracker* , *BESIII Conceptual Design Report* (2014). `http://www.lnf.infn.it/esperimenti/bes3/bes3_tdr_cgem.pdf`.
[168] W. Li et al., *The Offline Software for the BESIII Experiment*, in *Proceedings of the International Conference on Computing in High Energy and Nuclear Physics, vol. 225, Mumbai, India, 13-17 Feb 2006*.
[169] G. Barrand, I. Belyaev, P. Binko, M. Cattaneo, R. Chytracek, G. Corti et al.,

GAUDI — A software architecture and framework for building HEP data processing applications, *Comput. Phys. Comm.* **140** (2001) 45.
[170] R. Brun and F. Rademakers, *ROOT: An object oriented data analysis framework*, *Nucl. Instrum. Meth. A* **389** (1997) 81.
[171] L. Lönnblad, *CLHEP—a project for designing a C++ class library for high energy physics*, *Comput. Phys. Comm.* **84** (1994) 307.
[172] *CERNLIB - CERN Program Library Short Writeups*, *CERN* (1995) .
[173] S. Jadach, B.F.L. Ward and Z. Was, *The precision Monte Carlo event generator K K for two fermion final states in e+ e- collisions*, *Comput. Phys. Commun.* **130** (2000) 260.
[174] E. Richter-Was, *QED bremsstrahlung in semileptonic B and leptonic tau decays*, *Phys. Lett. B* **303** (1993) 163.
[175] R.-G. Ping, *Event generators at BESIII*, *Chin. Phys. C* **32** (2008) 599.
[176] EvtGen Website: `https://evtgen.hepforge.org/`.
[177] R.-G. Ping and C.-Y. Pang, *Monte Carlo Generators for Tau-Charm Physics at BESIII* , BAD 522 V6 (2007). `http://bes.ihep.ac.cn/bes3/phy_book/book/phy/generators_ping.pdf`.
[178] R.-G. Ping, *An exclusive event generator for e^+e^- scan experiments*, *Chin. Phys. C* **38** (2014) 083001.
[179] E.A. Kuraev and V.S. Fadin, *On Radiative Corrections to e^+e^- Single Photon Annihilation at High-Energy*, *Sov. J. Nucl. Phys.* **41** (1985) 466.
[180] R.-L. Yang, R.-G. Ping and H. Chen, *Tuning and Validation of the Lundcharm Model with J/ψ Decays*, *Chin. Phys. Lett.* **31** (2014) 061301.
[181] Z.-Y. Deng et al., *Object-Oriented BESIII Detector Simulation System*, *Chin. Phys. C* **30** (2006) 371.
[182] GEANT4 collaboration, *GEANT4: A Simulation toolkit*, *Nucl. Instrum. Meth. A* **506** (2003) 250.
[183] Y.-T. Liang et al., *A uniform geometry description for simulation, reconstruction and visualization in the BESIII experiment*, *Nucl. Instrum. Meth. A* **603** (2009) 325.
[184] R. Chytracek, J. Mccormick, W. Pokorski and G. Santin, *Geometry Description Markup Language for Physics Simulation and Analysis Applications*, *IEEE Transactions on Nuclear Science* **53** (2006) 2892.
[185] G. Cao et al., *Test of hadronic interaction models in GEANT4 at low energy using the BESIII data*, *Nucl. Instrum. Meth. A* **606** (2009) 700.
[186] H. Bethe and W. Heitler, *On the Stopping of fast particles and on the creation of positive electrons*, *Proc. Roy. Soc. Lond. A* **146** (1934) 83.
[187] Z. Yao, L. Qiuguang, W. Jike and W. Linghui, *The Reconstruction and Calibration of the BESIII Main Drift Chamber*, in *Proceedings of Computing in High Energy in Nuclear Physics, CHEP2007, Victoria, British Columbia, Canada, 2-7 Sep 2007*, 2007.
[188] Q.-G. Liu et al., *Track reconstruction using the TSF method for the BESIII main drift chamber*, *Chin. Phys. C* **32** (2008) 565.
[189] J. Zhang et al., *Low transverse momentum track reconstruction based on the Hough transform for the BESIII drift chamber*, *Radiat. Detect. Technol. Methods* **2** (2018) 20.
[190] J.-K. Wang et al., *BESIII track fitting algorithm*, *Chin. Phys. C* **33** (2009) 870.

[191] Y.-T. Liang et al., *Study of BESIII MUC offline software with cosmic-ray data*, *Chin. Phys. C* **33** (2009) 562.
[192] K. He, G. Qin, B. Huang, J. Hu, X. Ji and Y. Mao, *Particle identification* , (2006). `http://bes.ihep.ac.cn/bes3/phy_book/book/phy/ParticleID.pdf`.
[193] P. Avery, *Applied Fitting Theory I: General Least Squares Theory*, *Colliding Beam Experiment Reports CBX* **91** (1991) 72.
[194] Z.-Y. Zhang, L.-Q. Qin and S.-S. Fang, *Event generators for η/η' rare decays into $\pi^+\pi^- l^+ l^-$ and $e^+e^-\mu^+\mu^-$*, *Chin. Phys. C* **36** (2012) 926.
[195] Z.-R. Xu and K.-L. He, *A photon conversion finder at BESIII*, *Chin. Phys. C* **36** (2012) 742.
[196] BESIII collaboration, *Determination of the number of J/ψ events with inclusive J/ψ decays*, *Chin. Phys.* **C41** (2017) 013001.
[197] J. Bennett, *A study of the photon detection efficiency of the BESIII detector: $J/\psi \to \pi^+\pi^-\pi^0$*, *BESIII Document* **168-v8** (2015) .
[198] BESIII collaboration, *Branching fraction measurements of χ_{c0} and χ_{c2} to $\pi^0\pi^0$ and $\eta\eta$*, *Phys. Rev.* **D81** (2010) 052005.
[199] V. Prasad, C. Liu, X. Ji, W. Li, H. Liu and X. Lou, *Study of photon detection efficiency and position resolution of BESIII electromagnetic calorimeter*, *Springer Proc. Phys.* **174** (2016) 577.
[200] W.-L. Yuan et al., *Study of tracking efficiency and its systematic uncertainty from $J/\psi \to p\bar{p}\pi^+\pi^-$ at BESIII*, *Chin. Phys. C* **40** (2016) 026201.
[201] BESIII collaboration, *Measurement of $\mathcal{B}(J/\psi \to \eta' e^+e^-)$ and search for a dark photon*, *Phys. Rev. D* **99** (2019) 012013.
[202] M.-G. Zhao and X.-Q. Hao, *Systematic uncertainty of electron / pion / kaon / proton PID for J/ψ data*, *BESIII Document* **393-v1** (2015) .
[203] BESIII collaboration, *Search for hadronic transition $\chi_{cJ} \to \eta_c\pi^+\pi^-$ and observation of $\chi_{cJ} \to K\overline{K}\pi\pi\pi$*, *Phys. Rev. D* **87** (2013) 012002.
[204] BESIII collaboration, *Precision Measurement of the Branching Fractions of η' Decays*, *Phys. Rev. Lett.* **122** (2019) 142002.
[205] B.-X. Zhang et al., *Luminosity Measurement for the 2015 R-QCD data from 2.000 to 3.080 GeV*, *BESIII Document* **653-v3** (2017) .
[206] R.-G. Ping, X.-A. Xiong, L. Xia, Z. Gao, Y.-T. Li, X.-Y. Zhou et al., *Tuning and validation of hadronic event generator for R value measurements in the tau-charm region*, *Chinese Physics C* **40** (2016) 113002.
[207] H. Zhang et al., *Cross section measurement of the process $e^+e^- \to \Lambda\bar{\Sigma}^0 + c.c$ from threshold to 3.08 GeV*, *BESIII Internal Document* **983** (2021) .
[208] R. Barlow, *Systematic errors: Facts and fictions*, in *Conference on Advanced Statistical Techniques in Particle Physics*, M.R. Whalley and L. Lyons, eds., University of Durham, 2002 [hep-ex/0207026].
[209] S. Pacetti, R. Baldini Ferroli and E. Tomasi-Gustafsson, *Proton electromagnetic form factors: Basic notions, present achievements and future perspectives*, *Physics Reports* **550-551** (2015) 1.
[210] J. Jiao and X. Zhang, *Study of J/ψ and $\psi(2S) \to \Lambda\bar{\Lambda}$ and $\Sigma^0\bar{\Sigma}^0$ decays*, *BESIII Analysis Memo* **00175** (2015) .
[211] J. Song, A. Kupsc, C. Yuan, X. Zhang and L. Ma, *Helicity amplitude analysis of $\psi(2S) \to \Omega^-\bar{\Omega}^+$*, *BESIII Analysis Memo* **00369** (2020) .

[212] R. Barlow, R. Cahn, G. Cowan et al., *Recommended Statistical Procedures for BABAR* , *BABAR Analysis Document # 318, Version 1* (2002). `https://babar.heprc.uvic.ca/BFROOT/www/Statistics/Report/report.pdf`.
[213] X.-H. Sun et al., *Track segment finding with CGEM-IT and matching to outer drift chamber tracks in the BESIII detector*, *Chin. Phys. C* **40** (2016) 096203.
[214] BESIII collaboration, *Observation of* $\eta' \to \pi^+\pi^-\mu^+\mu^-$, *Phys. Rev. D* **103** (2021) 072006.
[215] D.S.M. Alves, *Signals of the QCD axion with mass of* 17 MeV$/c^2$*: Nuclear transitions and light meson decays*, *Phys. Rev. D* **103** (2021) 055018.
[216] R. Barlow, *SLUO Lectures on Statistics and Numerical Methods in HEP Lecture 6: Resampling and the Bootstrap* , (2000). `https://www-group.slac.stanford.edu/sluo/Lectures/stat_lecture_files/sluolec6.pdf`.
[217] E.B. Levichev, A.N. Skrinsky, G.M. Tumaikin and Y.M. Shatunov, *Electron–positron beam collision studies at the Budker Institute of Nuclear Physics*, *Phys.-Usp.* **61** (2018) 405.
[218] Q. Luo and D. Xu, *Progress on Preliminary Conceptual Study of HIEPA, a Super Tau-Charm Factory in China*, in *Proc. 9th International Particle Accelerator Conference (IPAC'18), Vancouver, BC, Canada, April 29-May 4, 2018*, no. 9 in International Particle Accelerator Conference, (Geneva, Switzerland), pp. 422–424, JACoW Publishing, June, 2018, DOI.
[219] Z.-Y. Li, A.-X. Dai and J.-J. Xie, *Electromagnetic form factors of* Λ *hyperon in the vector meson dominance model and a possible explanation of the near-threshold enhancement of the* $e^+e^- \to \Lambda\bar{\Lambda}$ *reaction*, *Chin. Phys. Lett.* **39** (2022) 011201.

Acta Universitatis Upsaliensis
Uppsala Dissertations from the Faculty of Science
Editor: The Dean of the Faculty of Science

1–11: 1970–1975

12. *Lars Thofelt*: Studies on leaf temperature recorded by direct measurement and by thermography. 1975.
13. *Monica Henricsson*: Nutritional studies on Chara globularis Thuill., Chara zeylanica Willd., and Chara haitensis Turpin. 1976.
14. *Göran Kloow*: Studies on Regenerated Cellulose by the Fluorescence Depolarization Technique. 1976.
15. *Carl-Magnus Backman*: A High Pressure Study of the Photolytic Decomposition of Azoethane and Propionyl Peroxide. 1976.
16. *Lennart Källströmer*: The significance of biotin and certain monosaccharides for the growth of Aspergillus niger on rhamnose medium at elevated temperature. 1977.
17. *Staffan Renlund*: Identification of Oxytocin and Vasopressin in the Bovine Adenohypophysis. 1978.
18. *Bengt Finnström*: Effects of pH, Ionic Strength and Light Intensity on the Flash Photolysis of L-tryptophan. 1978.
19. *Thomas C. Amu*: Diffusion in Dilute Solutions: An Experimental Study with Special Reference to the Effect of Size and Shape of Solute and Solvent Molecules. 1978.
20. *Lars Tegnér*: A Flash Photolysis Study of the Thermal Cis-Trans Isomerization of Some Aromatic Schiff Bases in Solution. 1979.
21. *Stig Tormod*: A High-Speed Stopped Flow Laser Light Scattering Apparatus and its Application in a Study of Conformational Changes in Bovine Serum Albumin. 1985.
22. *Björn Varnestig*: Coulomb Excitation of Rotational Nuclei. 1987.
23. *Frans Lettenström*: A study of nuclear effects in deep inelastic muon scattering. 1988.
24. *Göran Ericsson*: Production of Heavy Hypernuclei in Antiproton Annihilation. Study of their decay in the fission channel. 1988.
25. *Fang Peng*: The Geopotential: Modelling Techniques and Physical Implications with Case Studies in the South and East China Sea and Fennoscandia. 1989.
26. *Md. Anowar Hossain*: Seismic Refraction Studies in the Baltic Shield along the Fennolora Profile. 1989.
27. *Lars Erik Svensson*: Coulomb Excitation of Vibrational Nuclei. 1989.
28. *Bengt Carlsson*: Digital differentiating filters and model based fault detection. 1989.
29. *Alexander Edgar Kavka*: Coulomb Excitation. Analytical Methods and Experimental Results on even Selenium Nuclei. 1989.
30. *Christopher Juhlin*: Seismic Attenuation, Shear Wave Anisotropy and Some Aspects of Fracturing in the Crystalline Rock of the Siljan Ring Area, Central Sweden. 1990.

31. *Torbjörn Wigren*: Recursive Identification Based on the Nonlinear Wiener Model. 1990.
32. *Kjell Janson*: Experimental investigations of the proton and deuteron structure functions. 1991.
33. *Suzanne W. Harris*: Positive Muons in Crystalline and Amorphous Solids. 1991.
34. *Jan Blomgren*: Experimental Studies of Giant Resonances in Medium-Weight Spherical Nuclei. 1991.
35. *Jonas Lindgren*: Waveform Inversion of Seismic Reflection Data through Local Optimisation Methods. 1992.
36. *Liqi Fang*: Dynamic Light Scattering from Polymer Gels and Semidilute Solutions. 1992.
37. *Raymond Munier*: Segmentation, Fragmentation and Jostling of the Baltic Shield with Time. 1993.

Prior to January 1994, the series was called *Uppsala Dissertations from the Faculty of Science*.

Acta Universitatis Upsaliensis

Uppsala Dissertations from the Faculty of Science and Technology
Editor: The Dean of the Faculty of Science

1–14: 1994–1997. 15–21: 1998–1999. 22–35: 2000–2001. 36–51: 2002–2003.

52. *Erik Larsson*: Identification of Stochastic Continuous-time Systems. Algorithms, Irregular Sampling and Cramér-Rao Bounds. 2004.
53. *Per Åhgren*: On System Identification and Acoustic Echo Cancellation. 2004.
54. *Felix Wehrmann*: On Modelling Nonlinear Variation in Discrete Appearances of Objects. 2004.
55. *Peter S. Hammerstein*: Stochastic Resonance and Noise-Assisted Signal Transfer. On Coupling-Effects of Stochastic Resonators and Spectral Optimization of Fluctuations in Random Network Switches. 2004.
56. *Esteban Damián Avendaño Soto*: Electrochromism in Nickel-based Oxides. Coloration Mechanisms and Optimization of Sputter-deposited Thin Films. 2004.
57. *Jenny Öhman Persson*: The Obvious & The Essential. Interpreting Software Development & Organizational Change. 2004.
58. *Chariklia Rouki*: Experimental Studies of the Synthesis and the Survival Probability of Transactinides. 2004.
59. *Emad Abd-Elrady*: Nonlinear Approaches to Periodic Signal Modeling. 2005.
60. *Marcus Nilsson*: Regular Model Checking. 2005.
61. *Pritha Mahata*: Model Checking Parameterized Timed Systems. 2005.
62. *Anders Berglund*: Learning computer systems in a distributed project course: The what, why, how and where. 2005.
63. *Barbara Piechocinska*: Physics from Wholeness. Dynamical Totality as a Conceptual Foundation for Physical Theories. 2005.
64. *Pär Samuelsson*: Control of Nitrogen Removal in Activated Sludge Processes. 2005.

65. *Mats Ekman*: Modeling and Control of Bilinear Systems. Application to the Activated Sludge Process. 2005.
66. *Milena Ivanova*: Scalable Scientific Stream Query Processing. 2005.
67. *Zoran Radovic´*: Software Techniques for Distributed Shared Memory. 2005.
68. *Richard Abrahamsson*: Estimation Problems in Array Signal Processing, System Identification, and Radar Imagery. 2006.
69. *Fredrik Robelius*: Giant Oil Fields – The Highway to Oil. Giant Oil Fields and their Importance for Future Oil Production. 2007.
70. *Anna Davour*: Search for low mass WIMPs with the AMANDA neutrino telescope. 2007.
71. *Magnus Ågren*: Set Constraints for Local Search. 2007.
72. *Ahmed Rezine*: Parameterized Systems: Generalizing and Simplifying Automatic Verification. 2008.
73. *Linda Brus*: Nonlinear Identification and Control with Solar Energy Applications. 2008.
74. *Peter Nauclér*: Estimation and Control of Resonant Systems with Stochastic Disturbances. 2008.
75. *Johan Petrini*: Querying RDF Schema Views of Relational Databases. 2008.
76. *Noomene Ben Henda*: Infinite-state Stochastic and Parameterized Systems. 2008.
77. *Samson Keleta*: Double Pion Production in dd→αππ Reaction. 2008.
78. *Mei Hong*: Analysis of Some Methods for Identifying Dynamic Errors-invariables Systems. 2008.
79. *Robin Strand*: Distance Functions and Image Processing on Point-Lattices With Focus on the 3D Face-and Body-centered Cubic Grids. 2008.
80. *Ruslan Fomkin*: Optimization and Execution of Complex Scientific Queries. 2009.
81. *John Airey*: Science, Language and Literacy. Case Studies of Learning in Swedish University Physics. 2009.
82. *Arvid Pohl*: Search for Subrelativistic Particles with the AMANDA Neutrino Telescope. 2009.
83. *Anna Danielsson*: Doing Physics – Doing Gender. An Exploration of Physics Students' Identity Constitution in the Context of Laboratory Work. 2009.
84. *Karin Schönning*: Meson Production in pd Collisions. 2009.
85. *Henrik Petrén*: η Meson Production in Proton-Proton Collisions at Excess Energies of 40 and 72 MeV. 2009.
86. *Jan Henry Nyström*: Analysing Fault Tolerance for ERLANG Applications. 2009.
87. *John Håkansson*: Design and Verification of Component Based Real-Time Systems. 2009.
88. *Sophie Grape*: Studies of PWO Crystals and Simulations of the $\bar{p}p \to \bar{\Lambda}\Lambda, \bar{\Lambda}\Sigma^0$ Reactions for the PANDA Experiment. 2009.
90. *Agnes Rensfelt*. Viscoelastic Materials. Identification and Experiment Design. 2010.
91. *Erik Gudmundson*. Signal Processing for Spectroscopic Applications. 2010.
92. *Björn Halvarsson*. Interaction Analysis in Multivariable Control Systems. Applications to Bioreactors for Nitrogen Removal. 2010.
93. *Jesper Bengtson*. Formalising process calculi. 2010.
94. *Magnus Johansson*. Psi-calculi: a Framework for Mobile Process Calculi. Cook your own correct process calculus – just add data and logic. 2010.
95. *Karin Rathsman*. Modeling of Electron Cooling. Theory, Data and Applications. 2010.

96. *Liselott Dominicus van den Bussche*. Getting the Picture of University Physics. 2010.
97. *Olle Engdegård*. A Search for Dark Matter in the Sun with AMANDA and IceCube. 2011.
98. *Matthias Hudl.* Magnetic materials with tunable thermal, electrical, and dynamic properties. An experimental study of magnetocaloric, multiferroic, and spin-glass materials. 2012.
99. *Marcio Costa.* First-principles Studies of Local Structure Effects in Magnetic Materials. 2012.
100. *Patrik Adlarson*. Studies of the Decay $\eta \rightarrow \pi^+\pi^-\pi^0$ with WASA-at-COSY. 2012.
101. *Erik Thomé.* Multi-Strange and Charmed Antihyperon-Hyperon Physics for PANDA. 2012.
102. *Anette Löfström.* Implementing a Vision. Studying Leaders' Strategic Use of an Intranet while Exploring Ethnography within HCI. 2014.
103. *Martin Stigge.* Real-Time Workload Models: Expressiveness vs. Analysis Efficiency. 2014.
104. *Linda Åmand.* Ammonium Feedback Control in Wastewater Treatment Plants. 2014.
105. *Mikael Laaksoharju.* Designing for Autonomy. 2014.
106. *Soma Tayamon.* Nonlinear System Identification and Control Applied to Selective Catalytic Reduction Systems. 2014.
107. *Adrian Bahne.* Multichannel Audio Signal Processing. Room Correction and Sound Perception. 2014.
108. *Mojtaba Soltanalian.* Signal Design for Active Sensing and Communications. 2014.
109. *Håkan Selg.* Researching the Use of the Internet — A Beginner's Guide. 2014.
110. *Andrzej Pyszniak*. Development and Applications of Tracking of Pellet Streams. 2014.
111. *Olov Rosén*. Parallel Stochastic Estimation on Multicore Platforms. 2015.
112. *Yajun Wei*. Ferromagnetic Resonance as a Probe of Magnetization Dynamics. A Study of FeCo Thin Films and Trilayers. 2015.
113. *Marcus Björk*. Contributions to Signal Processing for MRI. 2015.
114. *Alexander Madsen*. Hunting the Charged Higgs Boson with Lepton Signatures in the ATLAS Experiment. 2015.
115. *Daniel Jansson*. Identification Techniques for Mathematical Modeling of the Human Smooth Pursuit System. 2015.
116. *Henric Taavola*. Dark Matter in the Galactic Halo. A Search Using Neutrino Induced Cascades in the DeepCore Extension of IceCube. 2015.
117. *Rickard Ström*. Exploring the Universe Using Neutrinos. A Search for Point Sources in the Southern Hemisphere Using the IceCube Neutrino Observatory. 2015.
118. *Li Caldeira Balkeståhl.* Measurement of the Dalitz Plot Distribution for $\eta \rightarrow \pi^+\pi^-\pi^0$ with KLOE. 2015.
119. *Johannes Nygren.* Input-Output Stability Analysis of Networked Control Systems. 2016.
120. *Joseph Scott.* Other Things Besides Number. Abstraction, Constraint Propagation, and String Variable Types. 2016.
121. *Andrej Andrejev*. Semantic Web Queries over Scientific Data. 2016.

122. *Johan Blom*. Model-Based Protocol Testing in an ERLANG Environment. 2016.
123. *Liang Dai*. Identification using Convexification and Recursion. 2016.
124. *Adriaan Larmuseau*. Protecting Functional Programs From Low-Level Attackers. 2016.
125. *Lena Heijkenskjöld*. Hadronic Decays of the ω Meson. 2016.
126. *Delphine Misao Lebrun*. Photonic crystals and photocatalysis. Study of titania inverse opals. 2016.
127. *Per Mattsson*. Modeling and identification of nonlinear and impulsive systems. 2016.
128. *Lars Melander*. Integrating Visual Data Flow Programming with Data Stream Management. 2016.
129. *Kristofer Severinsson*. Samarbete = Samverkan? En fallstudie av AIMday vid Uppsala universitet. 2016.
130. *Nina Fowler*. Walking the Plank of the Entrepreneurial University. The little spinout that could? 2017.
131. *Kaj Jansson*. Measurements of Neutron-induced Nuclear Reactions for More Precise Standard Cross Sections and Correlated Fission Properties. 2017.
132. *Petter Bertilsson Forsberg*. Collaboration in practice. A multiple case study on collaboration between small enterprises and university researchers. 2018.
133. *Andreas Löscher*. Targeted Property-Based Testing with Applications in Sensor Networks. 2018.
134. *Simon Widmark*. Causal MMSE Filters for Personal Audio. A Polynomial Matrix Approach. 2018.
135. *Damian Pszczel*. Search for a new light boson in meson decays. 2018.
136. *Joachim Pettersson*. From Strange to Charm. Meson production in electron-positron collisions. 2018.
137. *Elisabeth Unger*. The Extremes of Neutrino Astronomy. From Fermi Bubbles with IceCube to Ice Studies with ARIANNA. 2019.
138. *Monica Norberg*. Engagerat ledarskap för att skapa förutsättningar för allas delaktighet. Utgångspunkter i kvalitetsarbetet. 2019.
139. *Peter Backeman*. Quantifiers and Theories. A Lazy Aproach. 2019.
140. *Walter Ikegami Andersson*. Exploring the Merits and Challenges of Hyperon Physics. with PANDA at FAIR. 2020.
141. *Petar Bokan*. Pair production of Higgs bosons in the final state with bottom quarks and τ leptons in the ATLAS experiment. Search results using LHC Run 2 data and prospect studies at the HL-LHC. 2020.
142. *Carl Kronlid*. Engineered temporary networks. Effects of control and temporality on inter-organizational interaction. 2020.
143. *Alexander Burgman*. Bright Needles in a Haystack. A Search for Magnetic Monopoles Using the IceCube Neutrino Observatory. 2020.
144. *Eleni Myrto Asimakopoulou*. Search for charged Higgs bosons with tau-lepton signatures at the ATLAS experiment of the Large Hadron Collider and development of novel semiconductor particle detectors. 2021.
145. *Oscar Samuelsson*. Sensor Fault Detection and Process Monitoring in Water Resource Recovery Facilities. 2021.
146. *Helena Fornstedt*. Innovation Resistance. Moving Beyond Dominant Framings. 2021.

147. *Jenny Regina.* Time for Hyperons. Development of Software Tools for Reconstructing Hyperons at PANDA and HADES. 2022.
148. *Viktor Thorén.* Hadron Physics in a Polarized World.Exploring Electromagnetic Interactions with Spin Observables. 2022.